Electrical Manipulation and Detection of Single Electron Spins in Quantum Dots

Electrical Manipulation and Detection
of Single Electron Spins
in Quantum Dots

Proefschrift

ter verkrijging van de graad van doctor
aan de Technische Universiteit Delft,
op gezag van de Rector Magnificus prof. dr. ir. J.T. Fokkema,
voorzitter van het College voor Promoties,
in het openbaar te verdedigen op dinsdag 15 december 2009 om 12:30 uur

door

Katja Carola NOWACK

Diplom-Physikerin, RWTH Aachen, Duitsland
geboren te Krefeld, Duitsland.

Dit proefschrift is goedgekeurd door de promotor:
  Prof. dr. ir. L. M. K. Vandersypen

Samenstelling van de promotiecommissie:
  Rector Magnificus   voorzitter
  Prof. dr. ir. L. M. K. Vandersypen   Technische Universiteit Delft, promotor
  Prof. dr. ir. L. P. Kouwenhoven   Technische Universiteit Delft
  Prof. dr. Yu. V. Nazarov   Technische Universiteit Delft
  Prof. dr. C. M. Marcus   Harvard University, Cambridge, Verenigde Staten
  Prof. dr. K. Mølmer   Aarhus University, Aarhus, Denemarken
  Prof. dr. ir. W. G. van der Wiel   Universiteit Twente, Enschede
  Prof. dr. L. D. A. Siebbeles   Technische Universiteit Delft

Preface

Throughout my studies almost until the end I considered theoretical physics the *true* physics and experimental physics the thing the people with the bad grades do. Essentially I was very focussed on theory because I was good at it and it was fun. But then it dawned on me that I was lured into a terrible misconception. One of the key moments was, when in a lecture, I was faced with wildly speculative assumptions, "based on intuition" the professor assured, which were necessary to do anything practically relevant (or maybe still irrelevant, but at least it would give an analytical result) with the very elegant equations we had derived throughout a couple of previous lectures. And when he mentioned something like "To calculate the fourth order contribution to the self-energy might be a challenging PhD project..." an alarm bell started to ring softly in the back of my head. Somehow this doubt became stronger and by the end of my diploma thesis I had a feeling that I would be missing out on a great adventure, if I stayed with the equations. And that is why I applied as PhD candidate at QT. Lieven, thank you for giving me the chance to actually take on this adventure!

In August 2005 I started as a PhD student in QT and actually I already had a taste of the group from the 'QT uitje' I joined in July 2005. All of QT went on a boat trip to Vlieland, and since I was going to start in August, I was invited to join. During this trip I made sure to behave well and also not to drink too much, very worried what my future colleagues would think about me... But to be honest, I think, I was the only person trying to keep up appearances. People were enjoying themselves, partying wildly and I even saw Prof. dr. ing. Kouwenhoven, ok, Leo (coming from a German university I needed to get used to that) being thrown off the boat into the water!!! In the past 4 years QT was much more than a place to learn and do exciting physics. It was also a place of fun, great pleasure and friendship. And there are many, many people I need to thank for this, so here we go...

My PhD research took place in the spin qubit team, which, at the moment I joined, consisted of Laurens Willem van Beveren, Frank Koppens, Tristan Meunier, Ivo Vink and Lieven Vandersypen. Lieven, I don't only thank you for having me in Delft, but also for being the advisor you have been. I got all the support, guidance and help a PhD student can dream of, while still having the freedom to choose what I wanted to do. Thanks for your patience and for all the things I learned from you about physics, experiments, the importance of staying focussed and even about

sailing a 38 feet yacht across the channel, though for manoeuvring the boat into the box in the harbor I still trust the skipper better :)... Frank has been my mentor in the beginning of the PhD, since I joined the experiment he had set up together with Christo, a master student when I started. And to put it in Dutch (or Flemish?) terms: Ik ben met mijn gat in de boter gevallen. Frank, you taught me nearly everything I know about measuring double dots, helped me with my first babysteps in an experimental lab and thanks to you I obtained nice results already early on in my PhD. I certainly had to get used to your somewhat pushy way of doing science, but with this you make things work and happen. I really appreciate it. Thank you for the fun we had and also for introducing me to a whole new dimension of the German language. All the best in Barcelona! Ivo, it was a great pleasure to work with you and I also enjoyed the great fun we had outside the lab! After you left, the spin qubit team was never quite the same. I am trying to keep the tradition of the happy dance alive! Thanks for all the enthusiasm, happiness and great team-work. And, if you dont mind, I would still really like to learn this specific dance... Tristan, discussions with you were always interesting and exciting, regardless if it was on physics or any other topic (5 minutes???). I also had the pleasure to briefly overlap with Laurens, which kindly still answered all my questions about the art of fabricating our devices, when he already left for down under.

Apart from Lieven, everybody I started with has left by now and new people joined the spin qubit team. Lars, I appreciate that you're a true team-player and I really enjoyed the conference with you in Pisa. Floris, it was fun to work with you in the cleanroom and see the triple dot sample taking shape. I wish you and Lars good luck with getting the electrons to shuttle! Martin, I am happy you enthusiastically joined in, to make the current experiment happening. Let's do this read-out now! And who knows, perhaps optimal control of spin qubits is just around the corner?

Several students joined the team during the last four years: Christo, Klaas-Jan, Tjitte, Machiel, Shi-Chi, Han, Ryan, Victor, Irene, Guen(evere) and Lukas. Thanks to all of you for investing so much time. Especially a few I got to know closer. Christo, I guess, you are a true explorer by now, digging holes somewhere in greenland. I am still amazed by the variety of things you chose to do during the past years. It was nice to have you as a roommate for some months. Han, you are a weirdo sometimes, conversations with you can be very confusing, but I truly enjoy them! Good luck with the rest of your PhD. Machiel, I am sure the composite pulses will be used sooner or later. Victor, you made a big impression on me after you fell dead asleep on our couch after only having started three days with your master project. I enjoyed working with you. All the best with the graphene (graphane, grephane, grephene??). Finally, Guen, at the time we proposed a project for your masters it was uncertain whether I would be around the entire time, nevertheless you decided to take the risk and chose to tango with us. Thanks a lot for mastering python and for all the enthusiasm you bring to the lab.

Of course QT wouldn't be such a great place, if it wasn't for Leo and Hans. In

one group you bring people together with very different backgrounds, ambitions and ideas, that all share an enthusiasm about science. Leo, I am deeply impressed by your scientific instinct and sharpness. Hans, you are an inspiring person. I actually believe that you will never retire. You only used this whole retiring thing to have a great party and an even greater symposium. How about retiring every year from now on? My gratitude also goes to all other members of the scientific staff. Kees, thank you for all the valuable advice. Our last 5-minute discussion led to finally bring the fridge back to base temperature. Ad, I hope the phase slips soon! Thanks for also being a nice neighbor. Val, all the best with your steadily expanding empire in the basement. Ronald, with you the diamond age has also arrived at QT. Did you know, that the first time I learned about spin qubits was from a talk of yours at a conference in Bad Honneff?

Scientists cannot be trusted to run a research group on their own. When they are away with the fairies, blowing helium in the atmosphere or on the point of electrifying themselves while trying to find a groundloop, the QT technicians come to the rescue. Bram, thanks for your virtuous whistling and your way of not promising anything, but in the end fixing it all. Bram, Remco and Peter, thank you all for companionship at the 'koffietafel' and many, many, *many* liters of helium. Raymond, not a single thing in this thesis could have been accomplished without your help. Thank you for your patience when explaining things, even if you had already done so earlier the same day, and for showing me, that electronics is a science in itself. I am amazed by your creativity and look forward to all 'vrijdag-middag-experimentjes' yet to come. Angèle and Yuki, many thanks to keep everybody as much free of paperwork as possible. Angèle, I am still convinced, that you deserved the price for the person which slept the least during the last QT uitje.

When the sample you are measuring is giving confusing signals, it is good to have smart people around to ask for an explanation. Discussions with Mark Rudner, Daniel Klauser and Daniel Loss helped a lot to understand the electron and nuclear spin dynamics better. Especially, I would like to thank Jeroen Danon and Yuli Nazarov, which in addition to the hyperfine interaction also introduced me to the spin-orbit interaction. Jeroen, I enjoyed working with you. I really appreciate your dry humor! I hope you like in Berlin.

During my PhD I had the chance to attend many conferences and also visit a few other labs, which was extremely inspiring. Therefore I would like to especially thank Charles Marcus and his group, as well as Jonathan Baugh, Adrian Lupascu and many others from IQC for their hospitality.

QT hosts a lot of remarkable and friendly people. Some already moved on to other places and jobs and some only joined very recently. I would like to thank all of them to have contributed to making my last four years such a pleasant time. Of course, there are several, I would like to thank on a more personal note.

Special thanks go to my housemates, Lan, Pol and Umberto for the wonderful years we spend together, the numerous parties and barbecues and for not getting

tired when I was again talking too much. All initial concerns to live in a "QT house" were nonsense, I had a great time! Also thanks to Roser and Maksym for the nice weekends. I want you all to know that wherever I will end up living in the future: mi casa es su casa! Also thanks to the temporary housemates we accommodated, Christo, Marcel and Andres.

At QT I shared the 'Bond' office B007 with first Sami and Juriaan, and when Sami left, Sander and later Moïra joined in. Thanks for being my officemates! Especially to Juriaan I am thankful for his patience, when I was again talking too much (Am I repeating myself??). I appreciate that you most of the time forget that I am actually German, but I deeply disapprove that you do your data analysis in Excel!! I really enjoyed my time in the office! Pieter, Jelle, the escalator, and also Karin: if it wasn't for you, my beer consumption during the last years would have been less than a quarter of what it actually was. Although it got somewhat more quiet the past 2 years, I have plenty of memories of enjoyable parties and evenings. We should soon go to the 'Feest' again, and actually I wouldn't mind to watch the complete Britney Spears DVD all over again.

I want to thank Gary for being a true Gary-pedia and Susan for telling me how to interpret the information correctly ('mind the hand'). On the physics side I thank you for all the things you explained to me and your advice, which was always a good one. I thank both of you for all the great times, fanstastic food and a nice trip to Dublin. I am already looking forward to babysit the little squirt. Special thanks also goes to Susan's father for valuable advice about my dancing style. Floris, it is amazing how you still manage to be up to date about all what is going on here. Thanks for your directness about everything. Since you left, the coffee table is quite a bit emptier. Floor, thanks for the good times we had. If you are willing to explain the rules once more, I would be very interested in doing a round of klaverjassen again. Also thanks for exemplifying how to dress for the defense as a girl. Maarten van Kouwen, thanks for entertainment with the wide variety (and quality :)) from your source of jokes that never dries out. Maarten van Weert, thanks for helping me out with annealing at Phillips. I hope the vertical wires will shine brightly! Stevan (although you almost killed Pieter with imported alcohol) and Sergey, good luck with the wires. And I thought nuclei in GaAs are complicated! Georg, I always enjoyed training my slightly degrading German with you. Thomas, all the best to survive your clash of the titans. Arkady, all the best in Switzerland.

Many thanks also to all former group members making QT the enjoyable place it is today. Especially Jorden van Dam, Hubert Heersche, Alexander ter Haar, Pablo Jarillo-Herrero (thanks for the hospitality in Boston) and Silvano de Franceschi.

And than there is of course the newer generation of PhDs and postdocs. Reinier, you are the only corp-ball, which is a die-hard Linux-nerd and plays chess. You got my respect! Toeno -Johnny-, I hope you are up to join team cube for a few bike rides next year! Gijs, I had never realized that the nuclear spins have an orgy in our samples... Stijn, many thanks for showing me around in New York. Lucio,

thanks for the enjoyable bike ride to Texel. Michael 'the windshield' Reimer, your endurance is truly astonishing. Finally, I wish all PhD students and postdocs great results and a lot of pleasure obtaining them!

Very close to QT, just down the corridor, the molecular biophysics group can be found and I would like to thank the members of 'MB', for the great fun during Wednesday night dinners: Igor, Christine (I know, you both already knew, long before me :)), Irene, Fernando, Derek, Bryan, Diego, Adam, Daniel, Francesco and Barbara, Edgar and Liz, Peter, Pradyumna, Matt, Jaan, Juan and Jan. Thanks to Marcel for the advice that got me through the bureaucracy maze and for help in-designing. Special thanks to Jacob Kerssemakers for making such splendid drawings for the cover of my booklet, you did a fantastic job, thanks!

Thanks to the Moortgat brewery for Duvel which provided me with mental support and inspiration during the late hours of thesis-writing.

Back in Aachen there are still many friends, which I visited too few times the past years. I am sorry for this. And I hope that this will get better in the future. Everytime I did come back, I immediately felt at home again. For this I want to thank Max and Caro, Henning and Astrid, Benno and Vanessa, Jarjar, Patrick and Maria (all the best for the little one), Sebastian and Daniel, Thomas and the two Philips. I would like to thank Maarten Wegewijs for being a great supervisor during my diploma thesis and also for supporting me in finding such a nice PhD position afterwards. Maarten, I am always happy to see you again and I hope we manage to keep in touch also in the future. Claas, it is always great fun to meet you, however I refuse to ever play "Mensch ärger Dich nicht!" with you and Iwijn again. I was embarrassed before all of Kobus Kuch *and* we missed a train! All the best for Julchen and you! Monni, I am sorry I didn't reply to too many of your emails. I hope I can compensate that next year.

Many apologizes to everybody who had big expectations, when I opened a face-book account. I am just not good at this sort of stuff. I guess, logging on once in half a year, is not quite how this thing works. Please don't take it personal, if I still didn't confirm, that I want to be your friend...

I thank my parents and my sister for their unconditional and continuous support and love whatever I decide to do. Stephan, thank you for being part of the family too :) and 'helping' me during my defense. Finally, I want to thank Iwijn, for the most important thing I learned in Delft: how pleasant it is, if you share your life with someone. I am looking forward to our future with confidence, excitement and joy.

<div align="right">Katja Nowack, November 2009</div>

Contents

Chapter 1

Introduction

"It is safe to say that nobody understands quantum mechanics." with these words Richard Feynman describes the counter intuitive nature of quantum mechanics that is as difficult to grasp for a first year physics student as it is for anybody already thinking about quantum mechanics for many decades. The reason nobody *understands* quantum mechanics is not related to its complexity, but to its very fundamental consequences and predictions.

In classical mechanics, if the forces acting on a particle are known, by solving the equation of motion, given its position and velocity at time $t = 0$, the position and velocity of that particle are known for all times. In quantum mechanics the behavior of a particle is not described by a trajectory, but by a wavefunction $\Psi(x, t)$. The wavefunction describes the particle's spatial spread and it gives the probability density to find the particle at position x at time t as $|\Psi(x, t)|^2$. The wavefunction evolves in time according to Schroedinger's equation and can in principle also be determined for all times, if known at time $t = 0$. If however an observer measures, e.g. the position of the particle, its wavefunction is postulated to collapse or to be reset to a wavefunction which gives a 100% chance of finding the particle at the measured position. There are elegant ways to describe this in a mathematical formalism. The difficulty however to *understand* quantum mechanics does not lie in learning this formalism, but rather in accepting its implications.

Describing a particle as a wave rather than a particle has strange consequences, for example that a particle can be in more than one place at a time, that it can tunnel through a classically impermeable barrier and that its momentum and position cannot be determined simultaneously. From what is postulated about the measurement process and the description of two particles by a joint wavefunction another property, which lies at the heart of quantum mechanics, follows: entanglement. Measuring a property of one of two entangled particles instantaneously reveals information about the other particle even if they are far apart. This is what Einstein called a "spooky" interaction at a distance.

There were and still are debates over the interpretation of quantum mechan-

ics and its philosophical implications. But regardless of these, quantum mechanics provides a way to describe the world at the atomic scale and explained many phenomena in physics, for example why an electron in an atom does not simply crash into the atomic core, the observation of the photoelectric effect and the spectrum of blackbody radiation, which could not be understood through any other theory.

Apart from answering fundamental physical questions, the ability to explain and predict quantum mechanical effects enabled many technological advances such as the development of the laser, magnetic resonance imaging (MRI) and the CMOS technology you find in every computer nowadays.

1.1 Information processing in a quantum world

In the past few decades the research field of quantum information processing has emerged. Rather than developing a new technology on the basis of an ensemble quantum effect it aims at controlling and engineering *individual* quantum systems to manipulate and store information. Present day information processing is based on bits, which encode a logical 0 or 1 by taking two distinct states. Examples are a charged or uncharged capacitor, the direction of the magnetization of a magnetic domain or simply a switch being in either the upper or lower position. In quantum information processing the information is carried by a quantum bit or 'qubit'. In contrast to a classical bit, a qubit cannot only be $|0\rangle$ *or* $|1\rangle$ but it can be in fact both at the same time, as it can be in a so-called superposition of both: $\alpha|0\rangle + \beta|1\rangle$ with $|\alpha|^2 + |\beta|^2 = 1$. The possibility of creating superposition states combined with entanglement of many qubits are the properties which promise to make quantum information processing more efficient than classical information processing. The idea of using these properties to encode and process information was first proposed for efficiently simulating complex quantum systems [1, 2] such as high temperature superconductors. It has led to the invention of futuristic applications, for example unfailing cryptography of messages [3]. Several quantum algorithms have been developed, for example for factoring large integer numbers [4] and searching databases [5]. In a nutshell, these algorithms exploit the fact that if a qubit is in a superposition of $|0\rangle$ and $|1\rangle$, any computational operation f is simultaneously evaluated for both input values: the outcome of a computation is a superposition of $f(|0\rangle)$ and $f(|1\rangle)$. For multiple qubits this implies that the computation can be simultaneously carried out on all possible input states. A measurement of the superposition will however only yield one possible outcome. A quantum algorithm is specially designed to exploit the possibility of parallel processing on a superposition state in a way that the final measurement of the qubits will yield an answer to the posed problem.

However, quantum information processing faces a major challenge. Manipulating a classical bit requires switching it between its two possible states and is associated with an (at least temporary) energy cost, which protects the information stored in

the bit. Reading out the bit requires distinguishing these two states. The binary nature of the bit restricts the type of possible errors which can be made during the manipulation and efficient ways to compensate for these are available. A quantum bit can be in any superposition of $|0\rangle$ and $|1\rangle$ and each superposition carries different information. Preparing such a superposition requires full and accurate control of the quantum system rather than merely a way to switch the qubit. Interaction with its environment can lead to so-called decoherence of the qubit, an unwanted and unknown evolution of the qubit. Even in case no energy is exchanged with the environment, the information of the relative phase between the states in the superposition can be lost and with it the information stored in the qubit. Algorithms for detecting and correcting these errors have been developed [6]. However, for these algorithms to work, the error when operating a single qubit has to pass below a threshhold: one has to be able to perform at least 10^4 gate operations during the timescale on which the phase information is erased through the environment. This results in two conflicting properties which are desirable for a physical qubit: it needs to be well isolated from the environment, in order to avoid fast decoherence and on the other hand, it should also allow for efficient control and read-out, which implies that it has to be sufficiently coupled to the outside world to allow for external manipulation and read-out. The search for a physical system which provides a good balance between these two properties is briefly sketched in the following section.

1.2 Searching for a physical qubit

Next to the mentioned constraints, which are related to decoherence, a physical implementation of a qubit has to meet another requirement. It needs to be scalable, since the minimum number of qubits needed to perform a useful computation is of the order of 100. Many proposals exist to physically realize a quantum processor and at present several of these are pursued experimentally. Among them are systems that find their origin in atomic physics, such as ions in electrostatic traps [7], atoms in optical lattices [8], cavity quantum electrodynamics systems [9] and ensembles of nuclear spin in a molecule dissolved in a liquid [10] and purely quantum optical approaches [11, 12]. Advances in nanotechnology and lithographic techniques have made it possible to also engineer devices in the solid state such as superconducting circuits containing josephson junctions [13], nuclei of implanted phosphorus in silicon [14] and single electrons confined in lithographically defined [15] or self-assembled quantum dots [16], impurities in Si [17] and nitrogen-defects in diamond [18]. Every candidate has its own advantages and disadvantages. Some already achieved a high level of control, e.g. with nuclear magnetic resonance techniques a quantum algorithm has been realized using 7 qubits, but this specific approach has little prospective of being scaled up. Ion trap experiments have also shown impressive

progress, such as the demonstration of error correction [19] and multi-qubit entanglement [20], and efforts are made to realize scalable architectures [21]. Especially in the lithographically defined solid state systems scaling looks more promising, however decoherence processes are more difficult to overcome, since the qubit is embedded in a host material.

At this point it is not clear which physical implementation holds the biggest promise to eventually build a useful quantum processor. The research going on at this point is mostly explorative and many ideas are still generated and assessed. In a broad range of physical systems a deeper understanding of the decoherence processes, the measurement process and a high level of control over the quantum mechanical degrees of freedom is gained. It is clear that the benefit of this will not only be the potential realization of a quantum processor, but also many other technological advances and a lot of exciting physics. Due to the sensitivity to its environment any qubit is an extremely sensitive probe. For instance nitrogen-defects in diamond in combination with techniques coming from quantum information processing are also explored for applications in magnetometry [22, 23]. The strength of quantum information processing is that it is an extremely interdisciplinary research field bringing together researchers that in the past did not have a motivation to talk to each other. In this way it stimulates different areas in physics to learn from each other and to interface very different physical systems.

1.3   Do not charge - spin

In today's electronic devices it is the electron charge which is used to store and transport information. However each electron also has a small magnetic moment, called spin, which is a purely quantum mechanical property. The field of "spintronics" explores how semiconductor devices, such as diodes and transistors, can be given added functionality and be improved by actively manipulating the spin degree of freedom. An effect based on the spin of the electrons in metallic systems is the giant magnetoresistance, which was only discovered in 1988 [24, 25], but is already today used in every hard disk to store and read-out bits.

Spintronics constitutes the control of the average spin of an ensemble of electrons, manifesting itself in a spin density or magnetization. Advances in nanotechnology make it possible to even isolate single electrons in a semiconductor by confinement within a so-called quantum dot. A quantum dot is a small electrostatically defined box, which can be used to trap electrons. Quantum dots can be defined for example in carbon nanotubes, in nanowires, via self-assembled growth and in a two-dimensional electron gas using surface gates. The last approach is taken in this thesis. At the level of a single electron the spin is a natural quantum mechanical two-level system.

In 1998 Daniel Loss and David DiVincenzo realized the combined power of the elec-

4

tron charge, which is easy to control, and the spin, which is much more protected from the environment, and they formulated a road-map for experimentalists on how to implement a qubit encoded in the two spin states ('up' and 'down') of a single electron confined in a semiconductor quantum dot [15]. The beauty of this approach is that (at least on paper) two conflicting requirements for building a quantum bit can be met. Since the magnetic moment of a single electron is very small it only weakly interacts with its environment, but at the same time the charge of the electron allows to isolate the qubit and to electrically control the exchange interaction between two adjacent electrons.

Since their proposal several experimental groups throughout the world have pursued this idea, and by now all the basic building blocks to realize electron spin qubits in gated quantum dots have been demonstrated. Firstly, gate designs were developed to isolate a single electron in each of two coupled quantum dots. The development of fast gate pulsing [26] and charge sensing techniques [27] allowed for the observation of single electron tunneling events [28, 29] and measurements of the spin relaxation time [26, 30]. In combination with spin-dependent tunneling events, this enabled single-shot read-out of a single electron spin [31, 30]. By means of fast control over the exchange interaction between two neighboring spins a two-qubit gate was demonstrated allowing for the first time the observation of the coherent evolution of electron spins in quantum dots [32]. Finally, manipulation of a single electron spin has been achieved by a technique known as electron spin resonance, which enabled the observation of coherent rotations of a single electron spin [33].

1.4 Outline of this thesis

The experiments presented in this thesis are performed on spins in quantum dots that are defined by surface gates on top of a two-dimensional GaAs/AlGaAs electron gas. Building on the progress made on controlling electron spins in these structures, this thesis presents experiments on further understanding the interaction of the electron spin with its environment and how these interactions can be harnessed to control the environment and to actually manipulate the electron spin itself. The outline of this thesis is as follows.

In **chapter 2** we start by explaining basic properties of gate defined (double) quantum dots used to isolate single electron spins in our experiments. We proceed to discuss the electron spin states in double quantum dots leading us to the Pauli spin blockade regime, which forms the basis for the detection method used in the reported experiments. The second part of the chapter provides a description of the most important interactions coupling the electron spin to its environment: the spin-orbit interaction and the hyperfine interaction with the nuclear spins in the host lattice.

Chapter 3 outlines briefly the fabrication process of few-electron lateral quan-

tum dot devices and provides a description of the measurement set-up and techniques.

In **chapter 4** we present measurements of the coherence properties of the electron spin. First we discuss the realization of coherent control of the electron spin by electron spin resonance. The generation of ac magnetic field bursts at the location of the quantum dot allows for observing Rabi oscillations of the electron spin. The coherent control is then employed to implement sequences of bursts, which enable us to measure the free induction decay time, which is well-understood from the interaction with the nuclear spins. We reverse to a large extent the electron-nuclear dynamics via spin-echo, and find a Hahn echo time of $0.5\,\mu$s at 70 mT. **Chapter 5** reports a study of the electron-nuclear feedback observed when continuously driving electron spin resonance. The electron spin resonance frequency remains locked to the frequency of the ac magnetic field, even when the external magnetic field or the excitation frequency are changed. This is understood by an adjustment of the nuclear field such that the electron spin resonance condition remains satisfied. General theoretical arguments indicate that this spin resonance locking is accompanied by a significant reduction of the randomness in the nuclear field.

We demonstrate in **chapter 6** that coherent control of the electron spin can also be achieved with ac electric fields. Our analysis and measurements of the magnetic field dependence of the driving strength indicate that the driven spin transitions are mediated by the spin-orbit interaction. These results pave the way for all-electrical control of electron spin qubits.

Chapter 7 presents the status of an experiment aiming at the implementation of a single-shot read-out of all four spin states in a double quantum dot.

Concluding remarks, outlook and possible future directions will be presented in **chapter 8**.

Chapter 2

Spins in GaAs few-electron quantum dots

In this chapter we first introduce laterally defined quantum dots in GaAs and touch on some basic properties. We focus on the case of a double quantum dot and discuss the so called Pauli spin blockade, which will be employed in chapters 4-6 to detect electron spin resonance. For realizing an electron spin qubit in a quantum dot it is crucial to understand the mechanisms leading to the loss of the quantum information stored in the electron spin state. We therefore proceed by examining a simple model, which illustrates how the interaction of a qubit with its environment can erase the quantum information stored in the qubit's state, followed by discussing the most important interactions coupling a confined electron spin to its environment. These are the spin-orbit coupling and the hyperfine interaction with the nuclear spins in the host material. This chapter mainly focuses on aspects relevant for the experiments reported in this thesis, let us therefore mention two excellent reviews covering the physics of double dots [34] and spin qubits in few-electron quantum dots [35].

2.1   Laterally defined quantum dots

2.1.1   Creation of a lateral quantum dot

In a quantum dot the motion of an electron is confined in all three spatial directions. The confinement can be achieved in several ways in a semiconductor in the form of self-assembled structures, nanocrystals, nanowires or semiconducting carbon nanotubes for instance. Another convenient starting point is a two-dimensional electron gas (2DEG) realized in a semiconductor heterostructure, in which the motion of electrons is already constrained to the heterointerface. Fig. 2.1a schematically shows the layer structure of a typical heterostructure. These layers, in our case GaAs and AlGaAs (a typical value for the compositon is $Al_{0.3}Ga_{0.7}As$), are grown on top of each other using molecular beam epitaxy (MBE), resulting in very clean

crystals. By doping the n-AlGaAs layer with Si, free electrons are introduced and a 2DEG forms at the heterointerface as depicted in Fig. 2.1 b and c [36]. In case that the electrons remain bound at their donors the conduction band is flat apart from the discontinuity ΔE_c at the interface (Fig. 2.1 b). However, the electrons diffuse through the structure and some reach the GaAs region whose conduction band lies lower. There they get trapped because, once they lost their energy they cannot cross the barrier imposed by ΔE_c. An attracting electric field results from the now positively charged dopants that counteracts further diffusion of these electrons and accumulates them at the GaAs/AlGaAs heterointerface resulting in the formation of a two dimensional electron gas. The potential landscape in which the electrons are trapped is typically triangular and gives rise to a quantization of the electron motion perpendicular to the interface. At low temperature only the lowest mode of the triangular well is populated and therefore the electrons can be thought of moving freely in a two dimensional sheet in the plane at the interface. The 2DEG can have high mobility (typically $10^5 - 10^6$ cm^2/Vs), since the electrons are separated from the dopants, which are a dominant source for scattering (the additional spacer layer of undoped AlGaAs in Fig. 2.1a further increases the distance between electrons and donors leading to an additional increase of the mobility). The electron density in a 2DEG is relatively low (typically $\sim 3 \times 10^{11}$ cm^{-2}) resulting in a large fermi wavelength (~ 40nm) and a large screening length, which allows us to locally deplete the 2DEG with an electric field as discussed below.
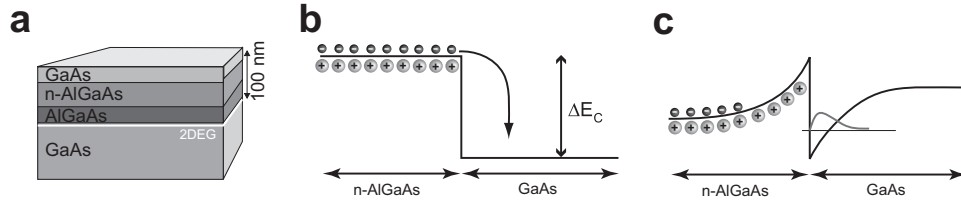
Figure 2.1: Formation of a two-dimensional electron gas. (a) Semiconductor heterostructure containing a 2DEG (indicated in white) approximately 100 nm below the surface, at the interface between GaAs and AlGaAs. The electrons in the 2DEG originate from Si donors in the n-AlGaAs layer. (The thickness of the different layers is not to scale.) (b,c) Conduction band around the GaAs/AlGaAs interface in the case that (a) the electrons remain at their donors and (b) after the 2DEG has formed.

To further constrain the motion of the electrons in the 2DEG surface gates are fabricated on top of the heterostructure using lithography methods (see chapter 3 for the fabrication). These gates are used to locally deplete the underlying 2DEG as shown schematically in Fig. 2.2a. To probe the induced structure ohmic contacts are made to electrically contact the 2DEG (gray columns in Fig. 2.2b). Depending on the chosen geometry of the surface gates the electrons can be confined to one (e.g. a channel) or zero (e.g. a quantum dot) dimensions. For example using the

gate geometry shown in Fig. 2.2c, a double quantum dot can be made in which the number of electrons in each dot can be controlled down to a single electron, a crucial requirement for realizing a spin qubit in this structure.
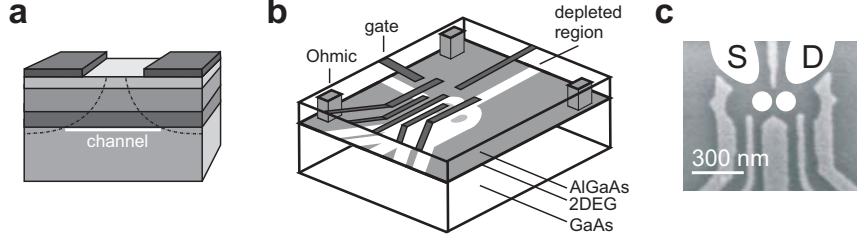
Figure 2.2: Forming a quantum dot by surface gates. (a) By applying negative voltages to the metal electrodes on the surface of the heterostructure, the underlying 2DEG can be locally depleted. In this way, electrons can be confined to one or even zero dimensions. (b) Schematic view of a lateral quantum dot device. Negative voltages applied to metal gate electrodes (dark gray) lead to depleted regions (white) in the 2DEG (light gray). Ohmic contacts (light gray columns) enable bonding wires (not shown) to make electrical contact to the 2DEG reservoirs. (c) Scanning electron microscope image of an actual device, showing the gate electrodes (light gray) on top of the surface (dark gray). The two white dots indicate two quantum dots, connected via tunable tunnel barriers to a source (S) and drain (D) reservoir, indicated in white.

2.1.2 Charge states of a double quantum dot

Here we briefly describe a few basic electronic properties of a lateral double quantum dot in the few-electron regime. A detailed review can be found in [34].

A double quantum dot consists of two quantum dots each coupled to a reservoir and coupled to each other via a tunnel barrier, as schematically shown in Fig. 2.3a,b. The electrochemical potential in the two dots can be adjusted separately by changing the potential on two independent gates V_{gL} and V_{gR}, thereby controlling the number of electrons on the left and right dot respectively. For a fixed voltage on these gates the charge state (N_L, N_R) of the double dot is given by the equilibrium electron number N_L and N_R on the left and right dot respectively. The charge configuration of a double dot can be probed in two ways. First, by measuring the current through the double dot with a bias applied across the double dot (Fig. 2.3a). At small applied bias the current reveals at which values of the gate voltages transport can occur via a cycle $(N_L, N_R) \rightarrow (N_L + 1, N_R) \rightarrow (N_L, N_R + 1) \rightarrow (N_L, N_R)$ through the double dot. This cycle is only energetically allowed at the so-called triple points, where the electrochemical potentials of the three transitions $(N_L, N_R) \rightarrow (N_L + 1, N_R)$,$(N_L + 1, N_R) \rightarrow (N_L, N_R+1)$ and $(N_L, N_R+1) \rightarrow (N_L, N_R)$ line up with the electrochemical potential of the electron reservoirs (Fig. 2.3c). Measuring the current therefore allows mapping out where as a function of the two gate voltages the equilibrium charge state
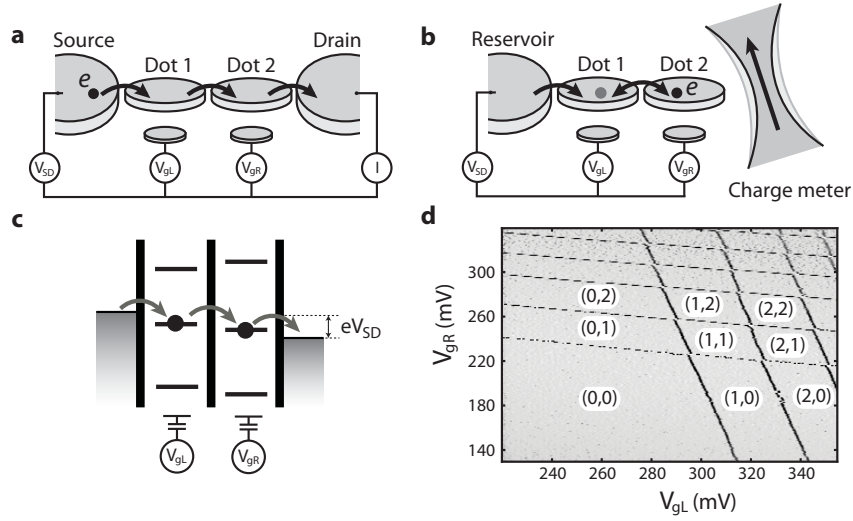
Figure 2.3: (a),(b) Schematic picture of a lateral double quantum dot probed by (a) a transport measurement and (b) charge sensing. In (a) both dots are coupled to a reservoir and to each other via a tunnelbarrier, allowing for the current through the device, I, to be measured in response to a bias voltage V_{SD} and the gate voltages $V_{g,L}, V_{g,R}$. In (b) the charge on the double dot is monitored by measuring the current through a close by quantum point contact (QPC), used as a charge meter. The resistance of the QPC (or the width of the channel) depends on the charge on the double quantum dot. In this scenario the charge meter is more sensitive to a charge on the right than on the left dot. (c) Schematic diagrams showing the electrochemical potentiall on the left and right dot. A small bias V_{SD} is applied. Transport can only occur if the electrochemical potential are lined up and lie in the bias window. (d) Stability diagram of a double dot measured by charge sensing. Displayed is the differentiated current through the QPC dI_{qpc}/dV_{gL} as a function of the gate voltages V_{gL}, V_{gR}. A change in I_{qpc} (and hence a peak in the differentiated current) occurs when an electron is added to the double dot. Labels (N_L, N_R) indicate the number of electrons in left and right dot. The region $(0,0)$ is identified by the absence of lines in the lower left region. A finite cross capacitance between the left (right) dot and V_{gR} (V_{gL})) causes the slope of the lines.

of the double dot changes. This map is called charge stability diagram (Fig. 2.3d). At high applied bias, transport can occur via the same cycle when the electrochemical potentials of the transition $(N_L+1, N_R) \rightarrow (N_L, N_R+1)$ lies within the bias window. Together with the fact that transitions in between the dots are also possible while emitting energy to the environment (e.g. phonons) we can understand that at high applied bias the triple points extend and become transport triangles in the (V_{gL}, V_{gR}) plane. A second way to measure the charge stability diagram is to directly detect the charge state of the double quantum dot using an adjacent charge sensor (Fig. 2.3b). Charge sensing overcomes two disadvantages the transport measurement is facing: (i) transport only occurs at the triple points, whereas charge sensing is sensitive to

all changes in the charge configuration and (ii) charge sensing is possible even when the tunnelbarrier to the reservoir is so opaque, that the resulting transport current is no more measurable. Charge sensing in lateral quantum dots can be realized e.g. by using a quantum point contact adjacent to the double dot (see Fig. 2.3c).

2.2 Two-electron spin states in a double dot and Pauli spin blockade

In double quantum dots, interdot charge transitions conserve spin and obey spin selection rules, which can lead to a phenomenon called Pauli spin blockade. Spin blockade occurs in the regime where the occupancy of the double quantum dot can be (0,1), (1,1), or (0,2), with (N_L, N_R) the occupations of the left and right dots. In the (1,1) and (0,2) charge state, the four possible spin states are the singlet state ($S = \uparrow\downarrow - \downarrow\uparrow$, normalization omitted for brevity)) and the three triplets states $T^0 = \uparrow\downarrow - \downarrow\uparrow, T^+ = \uparrow\uparrow, T^- = \downarrow\downarrow$. Due to a finite tunnel coupling t between the two dots, the (1,1) and (0,2) singlet states can hybridize close to the degeneracy of these two states. Around this degeneracy, the energy difference between the (0,2) and (1,1) triplet states is much larger than t, and therefore, we can neglect hybridization between these states and charge transitions to the (0,2) triplet state. We calculate the energy of the eigenstates via the system Hamiltonian, which is written in the basis states S_{11}, T_{11}^+, T_{11}^-, T_{11}^0 and S_{02}. In the description, we neglect the thermal energy kT, which is justified when the (absolute) energy difference between the eigenstates and the Fermi energy of the left and right reservoir is larger than kT. The Hamiltonian is given by

$$
\begin{aligned}
H_0 = & -\Delta_{\mathrm{LR}}|S_{02}\rangle\langle S_{02}| + \sqrt{2}t\Big(|S_{11}\rangle\langle S_{02}| + |S_{02}\rangle\langle S_{11}|\Big) \\
& - g\mu_{\mathrm{B}}B_{\mathrm{ext}}\Big(|T_{11}^+\rangle\langle T_{11}^+| - |T_{11}^-\rangle\langle T_{11}^-|\Big),
\end{aligned}
\tag{2.1}
$$

where Δ_{LR} is the energy difference between the S_{11} and S_{02} state (level detuning, see Fig. 2.4a), t is the tunnel coupling between the S_{11} and S_{02} states, and B_{ext} is the external magnetic field in the z-direction. The eigenstates of the Hamiltonian (2.1) for finite external field are shown in Fig. 2.4c. For $|\Delta_{\mathrm{LR}}| < t$, the tunnel coupling t causes an anti-crossing of the S_{11} and S_{02} states.

Using this energy diagram, we can analyze the current-carrying cycle via the charge transitions: $(1,1) \to (0,2) \to (0,1) \to (1,1)$. For $\Delta_{\mathrm{LR}} < 0$, transport is blocked by Coulomb blockade, because the (0,2) state S_{02} is at a higher energy than the (1,1) state S_{11}. For $\Delta_{\mathrm{LR}} \geq 0$, two possible situations can occur. First, an electron that enters the left dot can form a double-dot singlet state S_{11} with the electron in the right dot. It is then possible for the left electron to move to the right dot because the right dot singlet state S_{02} is energetically accessible. Transitions

from S_{02} to S_{11} are governed by coherent coupling between the states (Fig. 2.4b) or inelastic relaxation (Fig. 2.4a). From S_{02}, one electron tunnels from the right dot to the right lead and another electron can again tunnel into the left dot. The second possibility is that an electron entering the left dot forms a triplet state T_{11} with the electron in the right dot. In that case, the left electron cannot move to the right dot, as the right dot triplet state T_{02} is much higher in energy (due to the relatively large singlet-triplet splitting in a single dot). The electron can also not move back to the lead due to fast charge relaxation in the reservoir, and therefore, further current flow is blocked as soon as any of the (1,1) triplet states is formed (see schematic below Fig. 2.5a). The key experimental signature of Pauli spin blockade is the strong dependence of current flow on bias direction. For forward bias, current flow is strongly suppressed because as soon as one the triplet states is occupied, the current-carrying cycle is interrupted (Fig. 2.5a). For reverse bias, only singlet states can be loaded and a current can always flow (Fig. 2.5b). The second experimental signature of Pauli spin blockade is visible when the voltage bias is larger than the energy splitting Δ_{ST} between the states T_{02} and S_{02}. Spin blockade is lifted when the relative dot alignment is such that the transition from the T_{11} state to T_{02} state is energetically allowed (Fig. 2.5a).

2.2.1 Singlet-Triplet mixing due to the nuclear field

Spin blockade only occurs if at least one of the eigenstates of the system Hamiltonian is a pure triplet state. If processes are present that induce transitions from all the three triplet states T_{11}^i to the singlet state S_{11}, spin blockade is lifted and a
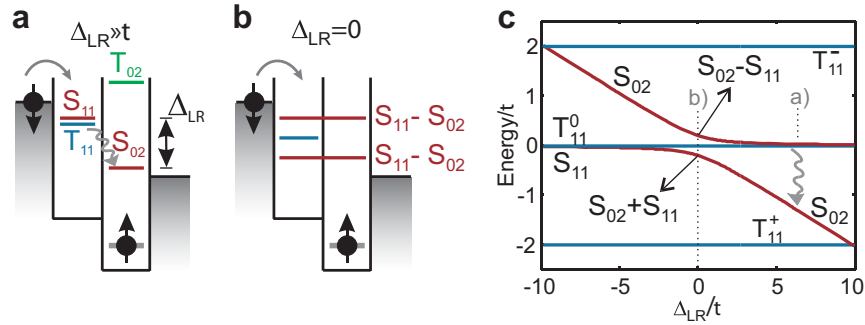
Figure 2.4: (a) A schematic of the double dot and the electro-chemical potentials (energy relative to the (0,1) state) of the relevant two-electron spin states. For $\Delta_{\mathrm{LR}} > t$, transitions from the S_{11} state to the S_{02} state are possible via inelastic relaxation with rate Γ_{in}. Spin blockade occurs when one of the T_{11}^i states is occupied. (b) Similar schematic for $\Delta_{\mathrm{LR}} = 0$, where the singlet states are hybridized. Also in this case, spin blockade occurs when one of T_{11}^i states is occupied. (c) Energy levels as a function of detuning. At $\Delta_{\mathrm{LR}} = 0$, the singlet states hybridize into bonding and anti-bonding states. The splitting between the triplet states corresponds to the Zeeman energy $g\mu_B B_{\mathrm{ext}}$.
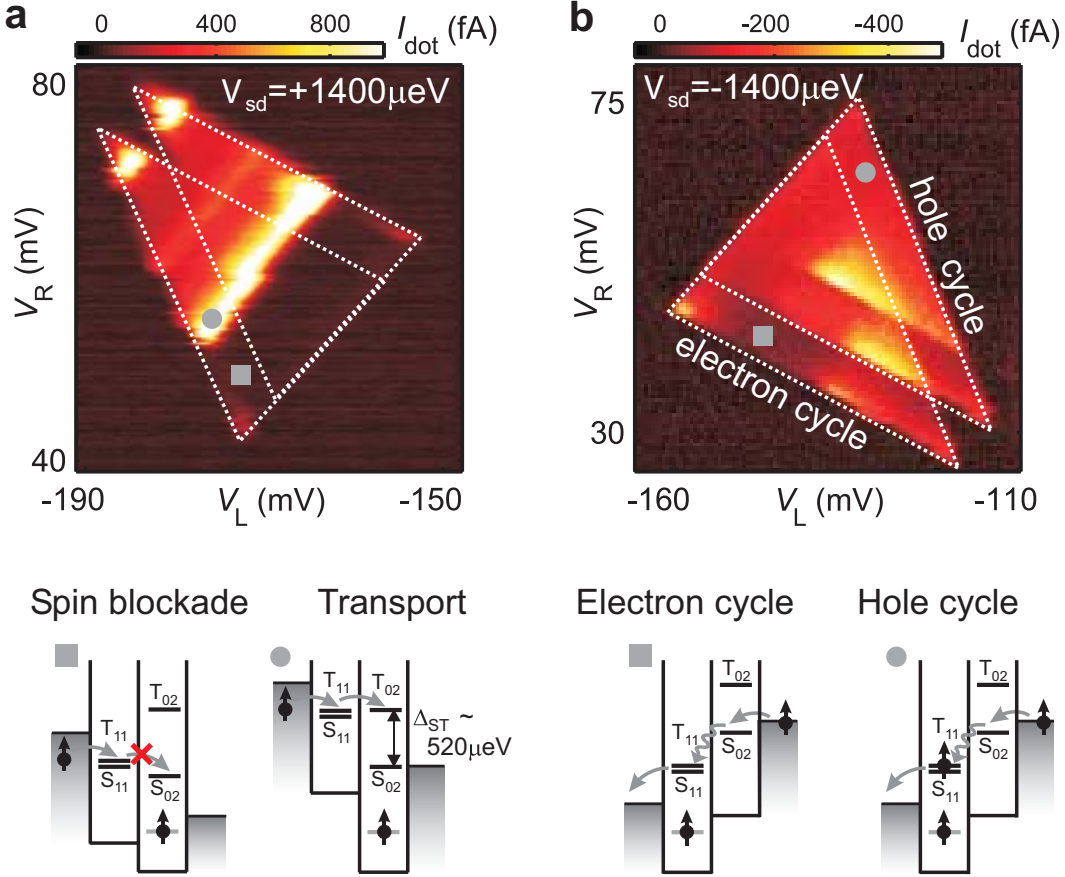
Figure 2.5: High bias transport measurements in the spin blockade regime. (a) Color-scale plot of the current through the double quantum dot under forward bias ($1400\mu eV$) as a function of the gate voltages controlling the left and right dot potential (V_L and V_R) at $B_{ext} = 100$ mT. The white dotted triangles define the region in gate space where transport is energetically allowed. Outside these triangle, the number of electrons is fixed by Coulomb blockade. Transport is suppressed due to spin blockade in part of the triangles (gray rectangle). Spin blockade is lifted (and transport is allowed) when the T_{02} state becomes energetically accessible from the T_{11} state (depicted by the gray circle). The two triangles correspond to two different current cycles, commonly known as the electron cycle and hole cycle. The schematics depict transport by the electron cycle, $(1,1) \rightarrow (0,2) \rightarrow (0,1) \rightarrow (1,1)$. The hole cycle $(1,2) \rightarrow (1,1) \rightarrow (0,2) \rightarrow (1,2)$, exhibits features similar to those visible in the electron cycle, although slight differences can exist. The horizontal black line in the schematics depict the electrochemical potential for transitions from the (0,1) state to the (0,2) and (1,1) singlet (S) and triplet (T) states. (b) Similar measurement as in (a), but for reverse bias (-1400 μeV). Current flows in the entire region in gate space where it is energetically allowed (within the white dotted triangles).

current will flow. As we will see below, the presence of the nuclear spins in the host semiconductor can give rise to such transitions.

The effect of the hyperfine interaction with the nuclear spins can be described in approximation [37] by adding a static (frozen) effective nuclear field $\mathbf{B}_N^L$ ($\mathbf{B}_N^R$) at the left (right) dot to the system Hamiltonian (for more details on the origin of the nuclear fields see section 2.5):

$$
\begin{aligned}
H_{\text{nucl}} &= -\frac{g\mu_B}{\hbar}\left(\mathbf{B}_N^L \cdot \mathbf{S}_L + \mathbf{B}_N^R \cdot \mathbf{S}_R\right) \\
&= -\frac{g\mu_B}{\hbar}(\mathbf{B}_N^L - \mathbf{B}_N^R) \cdot (\mathbf{S}_L - \mathbf{S}_R)/2 \\
&\quad -\frac{g\mu_B}{\hbar}(\mathbf{B}_N^L + \mathbf{B}_N^R) \cdot (\mathbf{S}_L + \mathbf{S}_R)/2,
\end{aligned}
\tag{2.2}
$$

with $\mathbf{S}_{L(R)}$ the spin operator for the left (right) electron.

For the sake of convenience, we separate the inhomogeneous and homogeneous contribution, for reasons which we will discuss later. Considering the nuclear field as static is justified since the tunneling rates and electron spin dynamics are expected to be much faster than the dynamics of the nuclear system [38, 39, 40]. Therefore, we will treat H_{nucl} as time-independent. The effect of nuclear reorientation will be included later by ensemble averaging.

We will show now that triplet states mix with the S_{11} state if the nuclear field is different in the two dots (in all three directions). This mixing will lift spin blockade, visible as a finite current running through the dots for $\Delta_{\text{LR}} \geq 0$. The effective nuclear field can be decomposed in a homogeneous and an inhomogeneous part (see right-hand side of (2.2)). The homogeneous part simply adds vectorially to the external field B_{ext}, changing slightly the Zeeman splitting and preferred spin
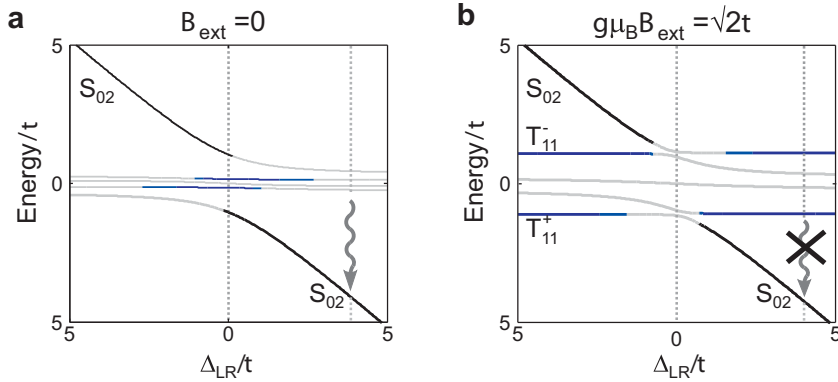
Figure 2.6: Energies corresponding to the eigenstates of $H_0 + H_{\text{nucl}}$ as a function of Δ_{LR} for (a) $B_{\text{ext}} = 0$ and (b) $B_{\text{ext}} = \sqrt{2}t$. Singlet and triplet eigenstates are denoted by dark gray lines. Hybridized states (of singlet and triplet) are denoted by light gray lines. For $\Delta_{\text{LR}} \gg t$ and $B_{\text{ext}} \gg |\Delta\mathbf{B}_N|$, the split-off triplets (T_{11}^+ and T_{11}^-) are hardly perturbed and current flow is blocked when they become occupied. Parameters: $t = 0.2\,\mu\text{eV}$, $g\mu_B\mathbf{B}_{N,L}=(0.03,0,-0.03)\mu\text{eV}$, $g\mu_B\mathbf{B}_{N,R}=(-0.03,-0.06,-0.06)\mu\text{eV}$.

orientation of the triplet states. The inhomogeneous part $\Delta \mathbf{B}_\mathrm{N} \equiv \mathbf{B}_\mathrm{N}^L - \mathbf{B}_\mathrm{N}^R$ on the other hand couples the triplet states to the singlet state, as can be seen readily by combining the spin operators in the following way

$$
\begin{aligned}
S_\mathrm{L}^x - S_\mathrm{R}^x &= \frac{\hbar}{\sqrt{2}} \Big(|S_{11}\rangle \langle T_{11}^-| - |S_{11}\rangle \langle T_{11}^+| + h.c. \Big) \\
S_\mathrm{L}^y - S_\mathrm{R}^y &= \frac{\hbar}{\sqrt{2}} \Big(i|S_{11}\rangle \langle T_{11}^-| - i|S_{11}\rangle \langle T_{11}^+| + h.c. \Big) \\
S_\mathrm{L}^z - S_\mathrm{R}^z &= \hbar \Big(|S_{11}\rangle \langle T_{11}^0| + |T_{11}^0\rangle \langle S_{11}| \Big).
\end{aligned}
\tag{2.3}
$$

The first two expressions reveal that the inhomogeneous field in the transverse plane ΔB_N^x, ΔB_N^y mixes the T_{11}^+ and T_{11}^- states with S_{11}. The longitudinal component ΔB_N^z mixes T_{11}^0 with S_{11} (third expression). The degree of mixing between two states will depend strongly on the energy difference between them [41].

This is illustrated in Fig. 2.6 where the energies corresponding to the eigenstates of the Hamiltonian $H_0 + H_\mathrm{nucl}$ are plotted as a function of Δ_LR. We first discuss the case where $\Delta_\mathrm{LR} \gg t$. For $g\mu_\mathrm{B} B_\mathrm{ext} < g\mu_\mathrm{B} \sqrt{\langle \Delta B_\mathrm{N}^2 \rangle}$ (Fig. 2.6a), the three triplet states are close in energy to the S_{11} state. Their intermixing will be strong, lifting spin blockade. For $g\mu_\mathrm{B} B_\mathrm{ext} \gg g\mu_\mathrm{B} \sqrt{\langle \Delta B_\mathrm{N}^2 \rangle}$ (Fig. 2.6b) the T_{11}^+, the T_{11}^- states are split off in energy by an amount of $g\mu_\mathrm{B} B_\mathrm{ext}$. Consequently the perturbation of these states caused by the nuclei will be small. Although the T_{11}^0 remains mixed with the S_{11} state, the occupation of one of the two split-off triplet states can block the current flow through the system. The situation for $\Delta_\mathrm{LR} \sim 0$ is more complicated due to a three-way competition between the exchange interaction and nuclear and external magnetic fields. In contrast to the previous case, increasing B_ext from 0 to $\sqrt{2} t / g\mu_\mathrm{B}$ gives an increase of singlet-triplet mixing, as illustrated in Fig. 2.6. Theoretical calculations of the nuclear-spin mediated current flow, obtained from a master equation approach, are discussed in [37, 42].

2.3 Relaxation and decoherence of a spin - a simple model

Every real life two-level quantum system possibly representing a qubit interacts with its environment which disturbs its quantum state. Since the interaction with the environment is uncontrolled this can be seen as a loss of the information stored in the quantum state of the qubit. The dominant interactions coupling a spin of an electron isolated in a GaAs quantum dot to its environment are thought to be the spin-orbit interaction and the hyperfine interaction with the host nuclei. Before describing these specific interactions, we present in this section a simple model applicable to any qubit to illustrate how the coupling to its environment results in relaxation and
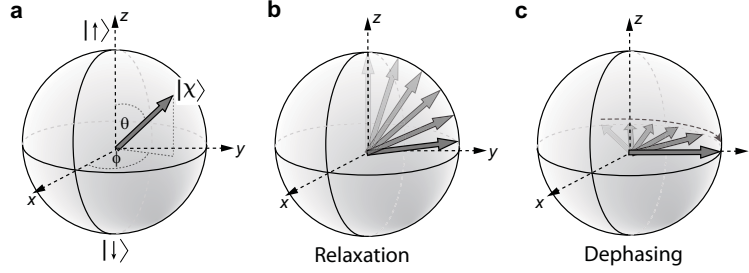
Figure 2.7: (a) Bloch sphere representation of the qubit state eq. 2.4. (b) Relaxation and (c) dephasing correspond to a loss of information of the angles θ, see (b), and ϕ, see (c), respectively. Note that during relaxation also the angle ϕ is randomized (not included in (b)).

dephasing. The state of a qubit can be written, up to a global phase, as

$$|\chi\rangle = \cos(\theta/2)|\uparrow\rangle + \sin(\theta/2)e^{i\phi}|\downarrow\rangle \tag{2.4}$$

The two angles θ and ϕ unambiguously define a point on the so-called Bloch sphere whose poles than correspond to the qubit excited state $|\uparrow\rangle$ and ground state $|\downarrow\rangle$ as depicted in Fig. 2.7a. The coupling to the environment can lead to two distinct processes: relaxation and decoherence. If the qubit is coupled to a dissipative environment it relaxes after some time from the excited state to the ground state. This requires an energy transfer from the qubit to the environment and can be seen as a loss of information about the angle θ as shown in Fig. 2.7b. The time scale of the associated decay is referred to as T_1. Relaxation can also be viewed as a decay of the initial longitudinal polarization $\langle\hat{\sigma}_z\rangle$ to its equilibrium state ($\hat{\sigma}_{x,yz}$ are the Pauli matrices). Decoherence than refers to the decay of an initial transversal polarization $\langle\hat{\sigma}_\perp\rangle$ ($\hat{\sigma}_\perp$ can include both $\hat{\sigma}_{x,y}$) and is associated with a timescale T_2.[1] Decay of a transversal polarization can result from pure dephasing meaning a loss of information of the azimuthal angle ϕ, see Fig. 2.7c. The energy stored in the qubit remains conserved in this process, therefore no energy is exchanged with the environment. However, relaxation also contributes to the decay of a transversal polarization and it can be shown that $1/T_2 = 1/2T_1 + 1/T_\phi$ where T_ϕ is the timescale of pure dephasing [43].

The combined dynamics of a qubit and its environment leading to dephasing and relaxation can be a complex problem [44, 38]. However both these processes already arise when considering only a fluctuating environment coupling to the qubit in the

---

[1]The notation for this timescale varies widely in the literature and is also dependent on how it is obtained experimentally. Below we will therefore follow the common practice of introducing notation specific to the pulse sequence used to measure the decay.

following way [45, 46][2]:

$$\hat{H} = \frac{\hbar}{2}[\omega_z \hat{\sigma}_z + \delta\omega_z(t)\hat{\sigma}_z + \delta\omega_x(t)\hat{\sigma}_x + \delta\omega_y(t)\hat{\sigma}_y], \qquad (2.5)$$

Here $\hbar\omega_z$ is the energy splitting between the qubit's ground and excited state and $\hbar\delta\omega_{x,y,z}(t)$ are fluctuations in the x, y, z-direction that couple to the qubit. These fluctuations can have different noise sources depending on the qubit under consideration and its specific environment. A convenient way to characterize these noise sources is to consider their noise spectral density $S_i(\omega) = \frac{1}{2\pi}\int_{-\infty}^{\infty} e^{i\omega\tau}C_i(\tau)d\tau$, where $C_i(t-t') = \langle\delta\omega_i(t)\delta\omega_i(t')\rangle$ is the autocorrelation function of $\delta\omega_i(t)$ ($i = x, y, z$).

Relaxation and in principle excitation of the qubit is induced via the x, y components of $\delta\omega_i$, since these two terms couple the qubit excited and ground state. Due to energy conservation in the combined system, the qubit and its environment, only the $\pm\omega_z$ frequency components of the power spectral density will contribute to these processes. In the case that the noise sources couple weakly to the qubit ($\omega_z >> \delta\omega_{x,y}$) the following idenitities can be found for the relaxation and excitation rates: $\Gamma_{\uparrow\to\downarrow} \propto S_x(\omega_z) + S_y(\omega_z)$ and $\Gamma_{\downarrow\to\uparrow} \propto S_x(-\omega_z) + S_y(-\omega_z)$ respectively. If the noise source is in thermodynamic equilibrium the excitation and relaxation rates satisfy the detailed balance $\Gamma_{\uparrow\to\downarrow}/\Gamma_{\downarrow\to\uparrow} = e^{\hbar\omega_z/(k_B T)}$ with k_B the Boltzmann constant and T temperature implying that $S_{x,y}(\omega_z) = e^{\hbar\omega_z/(k_{BT})}S_{x,y}(-\omega_z)$. At low temperatures $\hbar\omega_z >> k_{BT}$ the excitation rate $\Gamma_{\downarrow\to\uparrow}$ is therefore exponentially suppressed and we obtain a characteristic relaxation time T_1 with $1/T_1 \propto \Gamma_{\uparrow\to\downarrow}$ [47].

The longitudinal fluctuations $\delta\omega_z$ lead to dephasing or the loss of information about the azimuthal angle ϕ. A qubit in a superposition state undergoes due to ω_z a Larmor precession in the xy-plane of the Bloch-sphere. The Larmor precession frequency is changed by the fluctuations $\delta\omega_z$ resulting in an extra unknown phase $\Delta\phi = \int_0^\tau \delta\omega_z(t')dt'$ in a time τ. In contrast to relaxation where only one frequency component of the noise spectrum contributes, a wide range of frequency components of $S_z(\omega)$ contributes to the loss of phase coherence (see below for a more precise definition).

The dephasing during free evolution can be experimentally probed by measuring the decay of the average transverse polarization, e.g. $\langle\hat{\sigma}_x\rangle$, of the qubit via a Ramsey sequence illustrated in Fig. 2.8. In the following, we will reason in a rotating frame which rotates at the Larmor precession frequency of the electron spin around the $\hat{z}$-axis. The sequence starts with the qubit initialized into one of its eigenstates e.g. $|\uparrow\rangle$, then application of a $\pi/2$ pulse around e.g. the $\hat{y}$-axis aligns the spin with the $\hat{x}$-axis in the Bloch sphere, thus $\langle\hat{\sigma}_x\rangle = 1$ at that moment. The qubit then evolves freely for the time τ. Another $\pi/2$ pulse is applied after the free evolution again around the $\hat{y}$-axis. If no dephasing has taken place during τ, we will find

---

[2]Note that in the following I will mainly refer to [45, 46] and [47], since I found these references very clearly written and insightful. However there are older and more extensive references, as e.g. [43], where the same concepts can be found
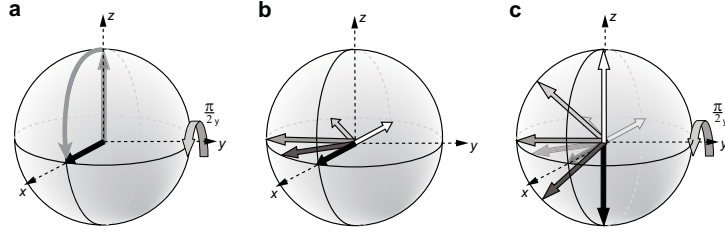
Figure 2.8: A Ramsey sequence seen from the rotating frame starting with (a) a $\pi/2$ pulse, followed by (b) free evolution during τ and (c) a final $\pi/2$ pulse. The differently gray shaded arrows represent the qubit state after the free evolution for different values of $\delta\omega_z$.

the qubit in the state $|\downarrow\rangle$ after the sequence. In contrast, if the qubit has for instance rotated in the xy-plane by π, we will find the qubit in the state $|\uparrow\rangle$ after the sequence. Altogether the average decay of the transversal polarization due to information loss of the phase ϕ is mapped onto decay of the longitudinal polarization via the $\pi/2$-pulses, which is directly measurable (assuming that the read-out basis is $\{|\uparrow\rangle, |\downarrow\rangle\}$).

The form and characteristic of the decay depends on the noise distribution of $\delta\omega_z$. For gaussian distributed noise one can find that the average transversal polarization decays as (see e.g. in [46])

$$\langle\hat{\sigma}_x\rangle(\tau) \propto \exp\left(-\frac{\tau^2}{2}\int_{-\infty}^{\infty}S_z(\omega)W_{\mathrm{R}}(\omega\tau)d\omega\right) \tag{2.6}$$

where the spectral weight function is given by $W_{\mathrm{R}}(\omega\tau) = \sin^2(\omega\tau/2)/(\omega\tau/2)^2$. In the case that low frequency fluctuations of $\delta\omega_z$ are dominant (implying that $S_z(\omega)$ is sharply peaked) the contribution from the low frequencies $\omega \ll 1/\tau$ in the expression above can be evaluated[3]: $\langle\hat{\sigma}_x\rangle(\tau) \propto \exp\left(-(\tau/T_2^*)^2\right)$ with $(1/T_2^*)^2 = 1/2\int_{-\infty}^{\infty}S_z(\omega)d\omega$. For a white noise source having an auto-correlation function $C_z \propto \delta(t)$ with a vanishing correlation time (the environment has 'no memory') the transversal polarization decays exponentially: $\langle\hat{\sigma}_x\rangle(\tau) \propto \exp\left(-\Gamma\tau\right)$ often referred to as Markovian dynamics.

The loss of spin coherence that is caused by the low frequency components of $S_z(\omega)$ is often referred to as pure dephasing or inhomogeneous broadening. The last term was used in traditional NMR experiments on ensembles of spins. Then, each spin experiences a different but static $\delta\omega_z$ and therefore, the coherence decay is an effect of the ensemble average over the $\delta\omega_z$ distribution. For single qubit experiments, dephasing can still occur when coherence measurements are averaged over long times. Therefore, the dephasing time does not characterize well the coherence of the qubit.

---

[3]$\sin x/x \approx 1$ for $x \ll 1$
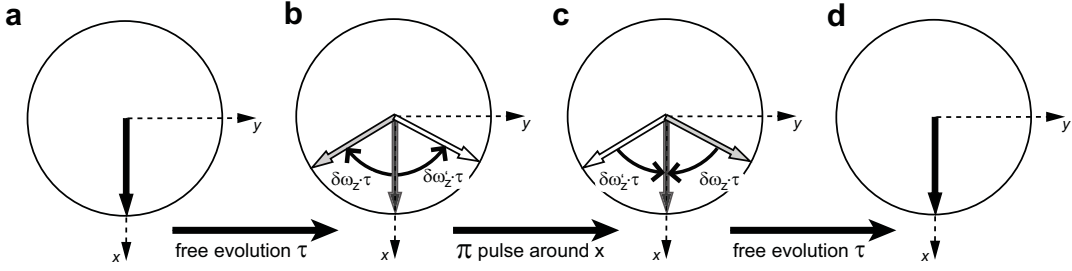
Figure 2.9: Spin echo sequence.

An improved characterization of the qubit coherence is provided by a Hahn echo decay time and can similarly to the Ramsey decay time be obtained experimentally by applying a pulse sequence. Again a $\pi/2$ pulse aligns the spin with e.g. the $\hat{x}$-axis in the Bloch sphere, it evolves freely during a time $\tau/2$ after which a π pulse is applied which effectively interchanges $|\uparrow\rangle$ and $|\downarrow\rangle$ and thus leads to a refocusing of the transverse spin polarization after another time $\tau/2$ in the case that $\delta\omega_z$ stayed constant during both free evolutions (see Fig. 2.9). A final $\pi/2$ pulse allows measurement of the transversal spin polarization. The random phase acquired during an echo experiment is given by $\Delta\phi = \int_0^{\tau/2} \delta\omega_z(t')dt' - \int_{\tau/2}^{\tau} \delta\omega_z(t')dt'$. The spin echo decay for a gaussian noise spectral density is given as well by eq. 2.6 with the spectral weight function W_R replaced by $W_{\text{Echo}} = \tan^2(\omega\tau/2)W_R(\omega\tau)$. The additional term $\tan^2(\omega t/2)$ cancels the low frequency contributions to the spin echo decay. It is very illustrative to generalize to an echo experiment using $(2N-1)$ π-pulses within the total time τ (so-called Carr-Purcel pulses, see e.g. [48]), which further changes the spectral weight to $W'_{\text{Echo}} = \tan^2(\omega\tau/2N)W_R(\omega\tau)$ and reveals that repeated echo-pulses render the decay more and more insensitive to lower frequencies. The decay time scale inferred from a spin-echo experiment is often referred to as $T_{2,\text{echo}}$. From the above expressions it is clear that $T_{2,\text{echo}}$ can exceed T_2^* by orders of magnitude, especially in the case that low-frequency components of $S_z(\omega)$ are dominant. In the other extreme case of white noise the spin echo decay is exponential with the same time constant as the Ramsey decay, since the noise is uncorrelated in time. For other specific shapes of the noise spectral density direct relations between $T_{2,\text{echo}}$ and T_2^* can be established. This is however beyond the scope of this section and examples can be found for instance in [43].

The effect of $\delta\omega_{x,y,z}$ on the coherence can also be evaluated for a driven qubit. By investigating the dynamics of the qubit in the rotating frame similar time scales T_1', T_2' can be obtained describing the dynamics in the rotating frame. If the driving field is on resonance with the Larmor precession it can be shown that instead of $S_z(0)$ the component $S_z(\omega_R)$ of the noise power spectrum contribute mainly to the coherence decay [46, 45], where ω_R is the Rabi precession frequency of the qubit. This implies that driving the qubit faster results in a longer decay time, provided

19

that $S_z(\omega)$ decreases with ω, which is often the case and will be of relevance when investigating the driven oscillations of a spin under the influence of a slowly fluctuating nuclear field in chapter 4.

As we will see below, relaxation of an electron spin in a GaAs quantum dot is dominated by electric field fluctuations from phonons which couple to the electron spin via the spin-orbit interaction (SOI). The associated effective field fluctuations point in the longitudinal direction only (see next section) with a more significant contribution at higher frequencies. Therefore, this mechanism contributes mainly to spin relaxation. In contrast, a fluctuating effective field due to the interaction with the nuclear spins points in all three directions, and contains mostly low-frequency components. Therefore, the contribution from the nuclei to spin relaxation is very small, but instead, the nuclei do cause very rapid spin dephasing (see section 2.5).

2.4 A localized spin and the environment - Spin-orbit coupling

2.4.1 Origin

In atomic physics spin-orbit coupling is together with the (spin-independent) Darwinian term the origin of the so-called fine structure in atomic spectra. In a nutshell, the electron in the atom is orbiting with velocity $\mathbf{p}/m$ in the electric field $\mathbf{E}$ of the proton. Looking in the rest frame of the electron the motion in the electric field gives rise to a magnetic field $\mathbf{B}_{\text{int}} = -\frac{1}{mc}\mathbf{p} \times \mathbf{E}$ with c the velocity of light. This internal magnetic field interacts with the electron spin resulting in the spin-orbit Hamiltonian $H_{\text{SO}} = -\boldsymbol{\mu}_{\text{S}}\mathbf{B}_{\text{int}}$ with $\boldsymbol{\mu}_{\text{S}} \propto \mathbf{S}$ the magnetic moment associated with the electron spin $\mathbf{S}$. Making use of the fact that the Coulomb potential of the proton is spherical symmetric (implying that $\mathbf{E} = -\nabla\Phi(r) = -\frac{d\Phi}{dr}\frac{\mathbf{r}}{r}$) one can find the familiar dependence $H_{\text{SO}} \propto \mathbf{L}\cdot\mathbf{S}$ where $\mathbf{L} = \mathbf{r} \times \mathbf{p}$ is the orbital angular momentum of the electron. To predict the right magnitude of the spin-orbit coupling, a correction term related to the electron moving on a curved orbit and hence being accelerated has to be included in the transformation to the rest frame above [49]. Later, the spin-orbit coupling was derived as a first order relativistic correction from the Dirac equation describing a relativistic electron. In a general potential $V(\mathbf{r})$ an electron experiences the following spin-orbit interaction:

$$H_{\text{SO}} = -\frac{\hbar}{4m_0^2c^2}\boldsymbol{\sigma} \cdot (\mathbf{p} \times (\nabla V)) \tag{2.7}$$

here m_0 is the mass of the free electron and $\boldsymbol{\sigma} = (\sigma_x, \sigma_y, \sigma_z)$ are the Pauli matrices. It is important to realize that due to the strong Coulomb potential, the largest contributions to the spin-orbit coupling result from the regions close to the atomic core, where the electric field and the electron momentum (orbital angular momentum is preserved) take the largest values.

2.4.2 Spin-orbit interaction in a bulk zinc-blende structure

For an electron in a crystal lattice spin-orbit coupling arises from the same microscopic origin, since it feels the electric fields from the charged atoms in the lattice. The Hamiltonian eq. 2.7 can be viewed as an internal magnetic field $\propto \mathbf{p} \times (\nabla V)$ and hence it is expected to result in a splitting of the spin states even at zero external magnetic field. This splitting modifies the bandstructure, which describes the electronic spectrum in the crystal. How strongly spin-orbit coupling influences the band structure depends, among other parameters, on the symmetry of the underlying crystal, as will be explained in the following. We focus on a s-type band (referring to the fact that the symmetry of the corresponding Bloch function is that of an orbital with angular momentum $l = 0$). As will be noted a few times below, the s-type character simplifies a few argumentations, because an s-type orbital is spherical symmetric. The s-type band is, luckily, the most relevant to us, because
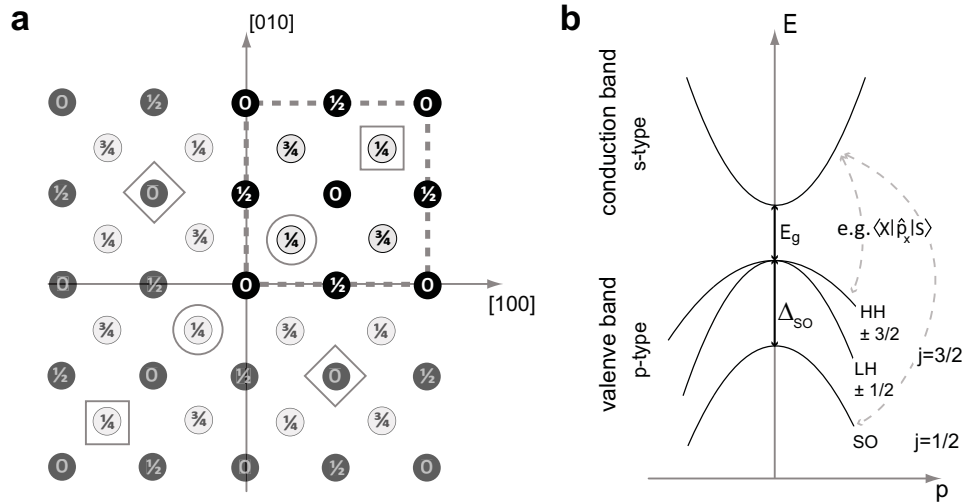
Figure 2.10: (a) The zinc blende structure is shown seen from the [001] direction. The numbers give the height of the atoms in units of the lattice constant and the two colors encode the two different type of atoms. From this sketch it becomes clear that the [001] direction, which is pointing out of the plane is a twofold rotational axis. For an electron moving along the [001] direction the electric field components perpendicular to the direction of its motion cancel out, which is exemplified by pointing out a few pairs of atoms whose field components cancel out by encircling them with a square, circle or diamond. Note that it is important that the electron is in a s-type orbital. If it is in e.g. a p-type orbital the contributions do not cancel, since the orbital is not spherical symmetric. (b) Shown is the bandstructure of GaAs as it is approximated in the 8×8 Kane model. E_g is the bandgap, Δ_{SO} the spin-orbit gap and $\langle X | \hat{p}_x | S \rangle$ is an example for the matrix elements which couple the valence and conduction bands. Here $\hat{p}_x$ is momentum operator along the x-direction, $|X\rangle$ is one of the p-type Bloch functions and $|S\rangle$ is the s-type Bloch function.

the 2DEG forms in the s-type conduction band of GaAs. In a crystal with inversion symmetry (like diamond) all electronic states described by the bandstructure are at least doubly degenerate. This is a consequence of the requirements imposed by time reversal (Kramers) symmetry and inversion symmetry. Let $E_{\uparrow,\downarrow}(\mathbf{k})$ denote the energy dispersion of the lowest conduction band and $\uparrow, \downarrow$ the two possible (pseudo-)spin species[4]. Spatial inversion symmetry implies $E_\uparrow(\mathbf{k}) = E_\uparrow(-\mathbf{k})$, while time reversal symmetry implies $E_\uparrow(\mathbf{k}) = E_\downarrow(-\mathbf{k})$ (the time reversal operation changes not only $\mathbf{k}$ to $-\mathbf{k}$, but also flips the spin), see e.g. [50]. Both combined result in the requirement of spin degeneracy $E_\uparrow(\mathbf{k}) = E_\downarrow(\mathbf{k})$. If however the crystal lacks inversion symmetry, the first condition is no more imposed and a spin splitting at zero magnetic field can occur.(Note that the spin-orbit coupling does conserve time reversal symmetry, hence Kramers degeneracy, $E_\uparrow(\mathbf{k}) = E_\downarrow(-\mathbf{k})$, is still preserved.) The zinc-blende structure of GaAs lacks inversion symmetry (or as it is mainly called, it exhibits bulk inversion asymmetry) and Dresselhaus derived from symmetry arguments that the spin-orbit coupling in eq. 2.7 results in lowest order of p/mc in an internal spin splitting for the s-type conduction band described by [51]

$$H_\mathrm{D}^{3D} \propto p_x(p_y^2 - p_z^2)\sigma_x + p_y(p_z^2 - p_x^2)\sigma_y + p_z(p_x^2 - p_y^2)\sigma_z \tag{2.8}$$

Here x, y, z correspond to the main crystallographic directions $[100], [010], [001]$. For $\mathbf{k} = 0$ and along high-symmetry directions as for instance $\mathbf{k}\|[001]$ the spin splitting vanishes. The role of symmetry becomes here less abstract: since the $[001]$ direction is a twofold rotational symmetry axis of the crystal, the electric fields perpendicular to $\mathbf{k}$ cancel (see Fig. 2.10a). As a result $\mathbf{p} \times (\nabla V) = 0$ which implies that the spin-orbit coupling in eq. 2.7 vanishes.

While symmetry considerations allow to derive the functional form of the spin-orbit interaction, a bandstructure calculation is needed to estimate the coupling strength. The bandstructure describes the electronic spectrum in a semiconductor and the electronic states are given by $\Psi(\mathbf{r}) = e^{i\mathbf{k}\mathbf{r}}u_{n\mathbf{k}}(\mathbf{r})$ where $u_{n\mathbf{k}}(\mathbf{r})$ is the Bloch part labeled by the $\mathbf{k}$-vector and the band index n. In the $\mathbf{k} \cdot \mathbf{p}$ method equations which determine solely the Bloch part are derived and expanded around a specific value of $\mathbf{k}$. Of special interest is the bandstructure around the Γ-point, $\mathbf{k} = 0$. From tight binding considerations it is known that in zinc-blende structures the Bloch functions $u_{n\mathbf{0}}$ for the lowest conduction and highest valence band have s- and p-type character, respectively. In the so-called Kane models only a restricted number of bands (or Bloch functions $u_{n\mathbf{0}}$) are taken into account to calculate the bandstructure around $\mathbf{k} = 0$ in the respective bands (higher and lower bands can still be taken into account perturbatively) as schematically shown in Fig. 2.10b. The strength of these models is that they take measurable quantities of the bandstructure as e.g.

---

[4]Here we use the labels $\uparrow, \downarrow$. However due to spin orbit coupling the eigenstates are not spin eigenstates and the wavefunction does not factorize into a pure spin and orbital component. Therefore often the expression pseudo-spin is used.

the bandgap, the spin-orbit gap (see below) and transition matrix elements between the bands (measurable as the oscillator strength in optical experiments) as an input and can be used to compute for e.g. the effective mass m^* and the effective g-factor as a function of these parameters [52].

While above we mainly focused on the conduction band, we note here that due to the p-type character of the valence band the effect of spin-orbit coupling is much more pronounced for holes in GaAs. The arguments invoking time reversal and inversion symmetry are more complex for p-type orbitals, because an additional orbital degree of freedom, the angular momentum, is relevant. In the bandstructure of a zincblende structure the most prominent effect of the spin-orbit interaction is the splitting of the topmost valence bands by the spin-orbit gap Δ_{SO}, see Fig. 2.10b. This originates from their p-type character implying that without spin-orbit coupling they are six-fold (including spin) degenerate at $\mathbf{k} = 0$. In the presence of spin-orbit coupling they get split corresponding to their total angular momentum number $j = l + 1/2 = 3/2$ and $j = l - 1/2 = 1/2$, which is directly understood when remembering that the spin-orbit coupling is $\propto \mathbf{L} \cdot \mathbf{S}$ in a atom. Accordingly, the effect of spin-orbit coupling in the s-type conduction band is expected to be weak, since it is s-type and hence $l = 0$. A bandstructure calculation yields that the strength of the spin-orbit interaction given in eq. 2.8 is actually determined by the mixing of the valence band with the conduction band, which depends on the size of the band gap and the transition matrix elements coupling conduction and valence bands, see Fig. 2.10b. Note that this matrix element depends through the Bloch functions on the details of the atomic structure of the crystal unit cell.

So far we only discussed bulk inversion asymmetry and hence internal electric fields as a origin for spin-orbit interaction in a semiconductor. Structure inversion asymmetry refers to symmetry breaking by an externally applied or built-in asymmetric potential as for instance is the case for a 2DEG whose confinement potential is triangular shaped at the heterointerface. The corresponding electric fields also result in spin-orbit coupling which is called Rashba spin-orbit interaction [53, 54]. We will discuss the Rashba spin-orbit interaction further in the following section.

2.4.3 Spin-orbit interaction in 2D

To obtain the Dresselhaus spin-orbit interaction in two dimensions we take the expectation value of the Hamiltonian in eq. 2.8 with respect to the lowest mode of the potential confining the electron motion to two dimensions. Assuming the confinement direction to be [001] (note that the result for an [011] grown structure is quite different) we can use that $\langle p_z \rangle = 0$ and that $\langle p_z^2 \rangle$ is non-zero but determined by the specifics of the heterostructure. With that we find

$$\tilde{H}_D^{2D} \propto [\langle p_z^2 \rangle(-p_x \sigma_x + p_y \sigma_y) + p_x p_y^2 \sigma_x - p_y p_x^2 \sigma_y] \tag{2.9}$$

The first two terms are referred to as the linear Dresselhaus term, whereas the last two are called cubic terms. Since the confinement is typically very strong along the growth direction and hence $\langle p_z^2 \rangle \gg p_x^2, p_y^2$, the linear terms are considered dominant. This yields the well-known Dresselhaus term in two-dimensions:

$$H_D^{2D} = \beta(-p_x\sigma_x + p_y\sigma_y) \tag{2.10}$$

Eq. 2.10 describes an in-plane internal magnetic field which is experienced by an electron with momentum $p_{x,y}$. A convenient way to characterize the magnitude of this field is the spin-orbit length, defined to be the length after which a spin has undergone a π-rotation when moving under influence of the internal field. Note that this length is independent of the momentum, if the electron moves faster, its spin rotates faster, but the electron crosses a given distance in a shorter time. The spin-orbit length is given by $l_{SO}^D = \hbar/\beta m^*$. While the direction of the internal magnetic field originating from the Dresselhaus term is anisotropic in the x-y plane, it points along the momentum for motion along [010] but opposite to momentum for motion along [100] (see Fig. 2.11a), its magnitude and thus the spin-orbit length is isotropic. In GaAs estimates of the coupling strength β range from 10^3 to 3×10^3 m/s [52], in agreement with experimentally reported values of $1-10\mu$m for the spin-orbit length [55].

The Rashba spin-orbit coupling originating from the confinement potential can be understood in an intuitive way: the electric field originating from the confinement is oriented along the growth direction $\mathbf{E} = (0, 0, E_z)$. Substituting this electric field in the Hamiltonian in eq. 2.7 yields the following form:

$$H_R^{2D} = \alpha(-p_y\sigma_x + p_x\sigma_y) \tag{2.11}$$

with $\alpha \sim \langle E_z \rangle$. While this way to derive the Rashba term results in the correct functional form (only for the s-type conduction band though) it is important to note
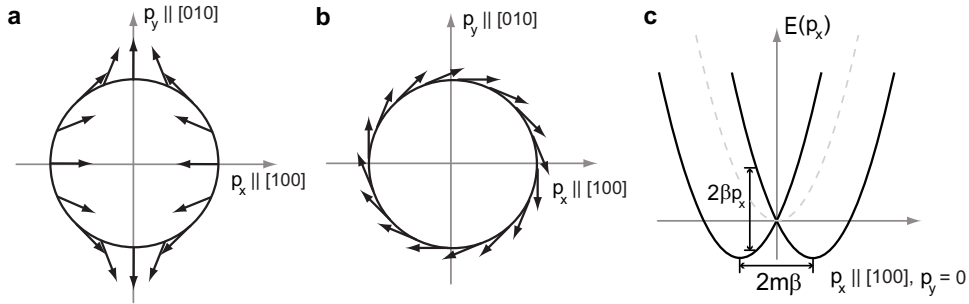
Figure 2.11: 2D Dresselhaus and Rashba spin-orbit coupling. Shown are the direction of the internal magnetic field originating from (a) the Dresselhaus and (b) the Rashba spin-orbit coupling for an electron moving with momentum $\mathbf{p}$ in the 2DEG. (c) The dispersion of a free electron in a 2DEG with (solid lines) and without (gray-dashed line) the Dresselhaus term included is shown for a cut at $p_y = 0$. The p_x-dependent spin splitting is indicated.

that the strength of α is not determined solely by the strength of the electric field but depends strongly on the microscopic details of the heterostructure, since the largest momentum with which the electrons move in the electric field is acquired in the strong Coulomb potential of the atomic cores. In a bandstructure calculation it can be shown that the Rashba spin-orbit coupling also originates from the coupling of the conduction band to the valence band. This reconciles the surprise that there is at all a net spin-orbit coupling in the conduction band resulting from the confinement, since the average electric field in the conduction band has to be zero considering that the electrons are confined along the growth direction [52].

Different from the Dresselhaus term the Rashba term is isotropic also concerning the direction of the corresponding internal magnetic field, it always points perpendicular to the momentum, see Fig. 2.11b. Note however that an interplay of Rashba and Dresselhaus spin-orbit coupling results in an anisotropy of the direction and magnitude of the internal magnetic field and accordingly of the spin-orbit length, which is for example given by $l_{SO} = \hbar/(\alpha + \beta)m^*$ along the [110] and $l_{SO} = \hbar/(\alpha - \beta)m^*$ along [1$\bar{1}$0].

There is a vast amount of experimental and theoretical literature available studying effects of spin-orbit coupling in 2D and 3D. Here we only mention a few. The zero field splitting in 2DEGs arising from the spin-orbit terms has been studied through beatings in the Shubnikov de Haas oscillations [56], antilocalization in magnetoresistance measurements [57, 58, 55] and spin-flip Raman scattering [59]. Time- and spatially resolved Faraday rotation spectroscopy allowed for directly observing the precession of the electron spin polarization due to the internal spin-orbit fields in the presence of an electric field [60] enabling a direct measurement the anisotropy of the spin-orbit fields in the presence of Rashba - and Dresselhaus spin-orbit coupling [61]. The spin-orbit coupling in combination with momentum scattering gives rise to several spin relaxation mechanisms in a 2DEG (for a review see especially [62] and also [63]). The so-called D'yakonov-Perel mechanism considers the effect that a change of the momentum of an electron by a scattering event changes the internal magnetic field around which the electron spin precesses in between scattering events [64]. A mechanism discussed by Elliot and Yaffet is based on actual spin-flips during a scattering event [65]. In the next section we will see that the situation in a quantum dot is very different, because the average momentum of the electron is zero.

2.4.4 Spin-orbit interaction in a quantum dot

A lateral few-electron quantum dot in GaAs is typically much smaller than the spin-orbit length and it is therefore reasonable to expect that the spin-orbit interaction only weakly affects the electron spin states. In fact since the electron is bound in a quantum dot, it does not have net momentum $\langle p_{x,y} \rangle = 0$. Hence the spin-orbit coupling does not directly couple the Zeeman split sublevels of a quantum dot,

because $\langle n \downarrow | H_{\text{SO}} | n \uparrow \rangle \propto \langle n | p_{x,y} | n \rangle \langle \downarrow | \sigma_{x,y} | \uparrow \rangle = 0$, here n labels the orbitals in the dot and $H_{\text{SO}} = H_D^{2D} + H_R^{2D}$. However the spin-orbit Hamiltonian does couple states with different orbital and spin: $\langle n \downarrow | H_{\text{SO}} | n' \uparrow \rangle \neq 0$ for $n \neq n'$. As a result, an electric field which couples to the electron orbital can also couple to the spin. As we will discuss in the following, this can lead to spin relaxation [66, 67, 68, 69], but can also serve as a means to drive spin transitions coherently [70, 71, 72, 73]

A convenient way to study the effect of spin-orbit coupling in a quantum dot is to derive an effective Hamiltonian by applying a spin-dependent canonical transformation (Schrieffer Wolff transformation) to the Hamiltonian describing the quantum dot including the spin orbit coupling and the Zeeman term. This yields in lowest order of the spin-orbit coupling for the spin-dependent part of the Hamiltonian [72, 70]:

$$H = \frac{1}{2} g \mu_{\mathbf{B}} \left(\mathbf{n} \times \mathbf{B}_{\text{ext}} + \mathbf{B}_{\text{ext}} \right) \boldsymbol{\sigma} \tag{2.12}$$

$$n_x = \frac{2m^*}{\hbar} \left(-\alpha y - \beta x \right) ; n_y = \frac{2m^*}{\hbar} \left(\alpha x + \beta y \right) ; \ n_z = 0 \tag{2.13}$$

The spin-orbit coupling results in a position-dependent correction of the Zeeman term, which has several implications. Due to the outer product the effective magnetic field $\mathbf{n} \times \mathbf{B}_{\text{ext}}$ is orthogonal to the direction of $\mathbf{B}_{\text{ext}}$ (which has important influence on the spin dephasing due to spin-orbit coupling, see below) and depends linearly on the external magnetic field. The latter is a consequence of Kramers degeneracy, which requires that the spin states at zero magnetic field are degenerate and hence also the effective magnetic field has to vanish at zero field. It is interesting to note that both characteristics are very different compared to the effect of spin-orbit coupling in a 2DEG, in which the internal magnetic field lies always in the plane of the 2DEG and does not depend on the external magnetic field[5]. While normally electric fields cannot couple two spin states, we see that due to the dependence of the internal magnetic field on the electron position a electric field can cause transitions by modulating the electron position. In chapter 6, we use this effect to coherently drive electron spin transitions by an externally applied electric field. However in the same way uncontrolled fluctuating electric fields can couple to the spin and give rise to spin relaxation. Several sources of uncontrolled fluctuating electric fields are present in semiconductor quantum dots, like fluctuations

---

[5]A note of caution is appropriate. In a quantum dot a reasoning analogous to the 2D case is very tempting, but gives the wrong result concerning these two characteristics. Assuming that an electric field adiabatically displaces the equilibrium position of the confined electron results in a time varying position $\mathbf{x}(t)$. One can associate this with a net momentum $\mathbf{p}(t) = \dot{\mathbf{x}}(t)$. Inserting this net momentum directly in the 2D spin-orbit Hamiltonian yields an effective magnetic field which is in-plane and does not vanish at zero external field, hence Kramers degeneracy is not respected. When driving the electron spin, this approach however predicts correctly what the optimum orientation of electric and external magnetic field are and on resonance even the magnitude of the effective field is predicted correctly, since on resonance $h f_{\text{ac}} = g \mu_{\text{B}} B_{\text{ext}}$ and $\mathbf{p}(t) \propto f_{\text{ac}}$.

of the gate potentials [74], background charge fluctuations [74], noise in an adjacent point contact [75] or lattice phonons [69, 67]. The latter is believed to be the dominant source for spin relaxation and is therefore extensively studied in theory and experiments. Due to the fact that the coupling of the spin states via spin-orbit coupling and electric fields involves virtual transitions to higher orbitals, since $\langle n \downarrow | H_{\mathrm{SO}} | n' \uparrow \rangle \neq 0$ only for $n \neq n'$, the relaxation rate due to spin-orbit coupling can be extraordinary small, especially when approaching zero field. The dependence on the Zeeman splitting E_Z can be understood in the following way. Along with the spin-flip a phonon with energy E_Z and wave vector $q \propto E_Z$ (considering only acoustic phonons [76]) is emitted. The relaxation rate depends on (i) the phonon density of states, which increases quadratically with energy ($\propto E_Z^2$) [76], (ii) the coupling of the phonon to the dot, which depends on the phonon wavelength ($\propto E_Z$), (iii) the electric field strength associated with a single phonon, which scales also with the wavelength resulting in $\propto E_z^{\pm 1/2}$ for piezo-electric or deformation phonons respectively and (iv) how strongly spin-orbit coupling admixes the spin states ($\propto E_Z$, see eq.2.12). Taking into account that (ii)-(iv) contribute quadratically to the relaxation rate [6], T_1^{-1} is expected to vary as E_Z^7 for coupling to deformation phonons and E_Z^5 for coupling to piezoelectric phonons [67]. In experiments the predicted E_Z^5 dependence could be observed (see [35]). Measured relaxation times range from 120 μs at 14 T to a value exceeding a second at 1 T [30, 77, 78].

In general, energy relaxation processes will also lead to decoherence, and therefore by definition $T_2 \leq 2T_1$. However, in leading order the field correction due to the spin-orbit interaction given in eq. 2.12 is always perpendicular to the quantization axis B_{ext}, and therefore, there is no pure phase randomization of the electron spin (see section 2.3). This implies that T_2 is limited by T_1 giving $T_2 = 2T_1$ [69]. This prediction has so far not been verified experimentally because decoherence due to the nuclear spin bath was dominant.

2.5 A localized spin and the environment - Hyperfine interaction

2.5.1 Origin

While the spin-orbit coupling is a result of the interaction of the magnetic moments associated with the electron spin and the electron's orbital angular momentum as discussed in the previous section, the hyperfine interaction is a consequence of the interaction of these two magnetic moments with the nuclear magnetic moment. The name hyperfine interaction originates from atomic physics where the interaction

---

[6](ii)-(iv) describe the strength of the coupling matrix element, which goes quadratically into the relaxation rate which can be derived using Fermi's golden rule or, as in the last section, using the noise spectral density.

manifests itself in the hyperfine structure observed in atomic spectra, which in atoms is typically a few orders of magnitude weaker compared to the fine structure. The coupling between the magnetic moment of the nucleus $\boldsymbol{\mu}_\mathrm{N}$ and the magnetic moment associated with the electron spin $\boldsymbol{\mu}_\mathrm{e}$ is described by the Hamiltonian [79]:

$$H = \frac{\boldsymbol{\mu}_\mathrm{e}\boldsymbol{\mu}_\mathrm{N}}{r^3} - \frac{3(\boldsymbol{\mu}_\mathrm{e}\mathbf{r})(\boldsymbol{\mu}_\mathrm{N}\mathbf{r})}{r^5} \tag{2.14}$$

where $\mathbf{r}$ is the vector pointing from the nucleus to the electron. If the electron has no overlap with the nucleus, which is the case for an electron with non-zero orbital angular momentum (e.g. electrons in p- or d- orbitals), this interaction can be readily evaluated by averaging over the electron wave function. For an electron in a s-type orbital, as the conduction band electrons in GaAs, there is however a finite probability to find the electron at the position of the nucleus $\mathbf{r} = 0$, since its wavefunction is non-zero at that point. The large electrostatic potential at the position of the nucleus causes in this case a relativistic correction, the so-called Fermi contact hyperfine interaction [80], which dominates the coupling between electron and nuclear spin and is given by [79, 40]:

$$H_\mathrm{HF} = \frac{2\mu_0}{3}g_0\mu_\mathrm{B}\gamma_\mathrm{N}\hbar|\psi(0)|^2\mathbf{I}\cdot\mathbf{S} \tag{2.15}$$

here g_0 is the free-electron g factor, γ_N the nuclear gyromagnetic ratio and $|\psi(0)|^2$ is the magnitude of the electronic wave function $\psi(\mathbf{r})$ at the position of the nucleus. In contrast to an atom an electron in a quantum dot interacts with many nuclear spins in the host material. In that case the Hamiltonian for the Fermi contact hyperfine interaction is given by the sum over the contributions from all N nuclei:

$$H_{HF} = \frac{2\mu_0}{3}g_0\mu_\mathrm{B}\gamma_\mathrm{N}\hbar\sum_{i=1}^{N}|\psi(\mathbf{r}_i)|^2\mathbf{I}_i\cdot\mathbf{S} \tag{2.16}$$

where $\mathbf{I}_i$ denotes the nuclear spin at position $\mathbf{r}_i$. In a crystal the electron wave-function can be written as a product of a Bloch function $u(\mathbf{r})$, which depends on the specifics of the crystal unit cell and is periodic with respect to the crystal lattice, and an envelope wave function $\Psi(\mathbf{r})$, which depends on the macroscopic confinement potentials. This allows us to define the hyperfine coupling strength as $A = \frac{2\mu_0}{3}g_0\mu_\mathrm{B}\mu_\mathrm{B}\gamma_\mathrm{N}\hbar|u(0)|^2/v_0$ with v_0 the volume of the crystal unit cell [81]. If the electron density was smeared out homogeneously over the unit cell in the crystal, we would have $|u(0)|^2 = 1$ [7]. However the electron density has a sharp maximum at the nucleus. In [40] it is estimated that $|u(0)|^2 = 2.7\times 10^3$ for Ga and $|u(0)|^2 = 4.5\times 10^3$ for As yielding that $A \sim 90\mu eV$ in GaAs, which is weighted by the natural abundances of the three isotopes ^{69}Ga, ^{71}Ga and ^{75}As (of respectively 1,0.6 and 0.4). We

---

[7]Here the following normalization is assumed: $\int|\Psi(\mathbf{r})|^2 d^3r = 1$ and $\int_{v_0}|u(\mathbf{r})|^2 d^3r = v_0$.

can rewrite eq. 2.16 by using the coupling constant A:

$$H_{HF} = \sum_{i=1}^{N} A_i \mathbf{I}_i \cdot \mathbf{S} \tag{2.17}$$

here $A_i = v_0 A |\Psi(r_i)|^2$.

2.5.2 Electron spin time evolution in the presence of the nuclear field

The hyperfine interaction can give rise to very complex dynamics. Since both the electron spin and the nuclear spins are quantum objects the electron spin state is not only affected by the nuclear spins, but also the electron spin affects the dynamics of each nuclear spin. For instance, if the nuclear spins can be prepared in a state which is not fully mixed, the hyperfine interaction can in principle generate entanglement between the two [82]. Making however use of the fact that the time scales governing the evolution of the nuclear spin system are slow compared to the evolution of the electron spin, we can approximate the effect of the nuclear spin bath on the electron spin evolution as an effective magnetic field acting on the electron spin [83]:

$$H_{HF} = \sum_{i=1}^{N} A_i \mathbf{I}_i \cdot \mathbf{S} = g\mu_{\mathrm{B}} \mathbf{B}_{\mathrm{N}} \mathbf{S} \tag{2.18}$$

here we introduced $\mathbf{B}_{\mathrm{N}} = \sum_i^N A_i \mathbf{I}_i / g\mu_{\mathrm{B}}$ as the nuclear field, the so-called Overhauser field, which in this approximation is no more considered an operator, but rather a random, classical field which is added vectorial to the external magnetic field. When all nuclear spins are fully polarized, we have $|\mathbf{B}_N| \sim 5$ T independent of N [40]. However, given the temperatures ($\geq 10\,\mathrm{mK}$) and magnetic fields ($\leq 12\,\mathrm{T}$) typical in an experiment, the thermal energy $k_{\mathrm{B}}T$ dominates the nuclear Zeeman energy as well as H_{HF}. Therefore only a small average polarization is present according to the Boltzmann distribution. In addition the nuclear field undergoes statistical fluctuations around this average, which in the limit of large N (N being the number of nuclei the electron interacts with) follow a Gaussian distribution in all three directions with spread $\sigma_N \sim A/\sqrt{N}$ [84, 83, 85]. For a typical number of $N = 10^6$ nuclei interacting with an electron confined in a quantum dot this results in $\sigma_N \sim 5\,\mathrm{mT}$. The statistical nuclear field distribution has been measured in both optical [86, 87] and electrical dots [88, 41]; all were in the range of a few mT. We remark that this statistical nuclear field is much stronger for electrons localized in dots or bound to impurities than for free electrons in a 2DEG which overlap with a much larger number of nuclei.

In section 2.3 we saw that an unknown offset adding to the externally applied magnetic field leads to dephasing of the electron spin by changing its Larmor precession frequency. In a typical nuclear field in a quantum dot with $B_{\mathrm{N},z} \sim 2\,\mathrm{mT}$

the electron spin picks up an extra phase of π within $\sim 50\,\mathrm{ns}$ (assuming $g = 0.35$ and $\mathbf{B}_{\mathrm{ext}}$ to be along $\hat{z}$). The dephasing can be described by averaging the spin precession over the nuclear field, which obeys a Gaussian distribution, yielding: $\int_{-\infty}^{\infty} \frac{1}{\sqrt{2\pi}\sigma} e^{(-B_{\mathrm{N},z}^2/2\sigma^2)} \cos(g\mu_b B_{\mathrm{N},z} t/\hbar) dB_{N,z} = e^{-(t/T_2^*)^2}$, with $T_2^* = \sqrt{2}\hbar/g\mu_b\sigma \sim 20\,\mathrm{ns}$ [83, 89] (assuming $\sigma = 2\,\mathrm{mT}$, $g = 0.35$). At large external magnetic field ($B_{\mathrm{ext}} \gg B_{\mathrm{N}}$) the transverse components of the nuclear field only have a negligible effect on the spin dephasing. They slightly tilt the precession axis by an angle $\sim B_{\mathrm{N}}/B_{\mathrm{ext}}$ and change the precession frequency by $g\mu_{\mathrm{B}} B_{\mathrm{N}}^2/B_{\mathrm{ext}}$ [90]. For this reason we will mainly consider the longitudinal component.

Some ways have been proposed to suppress the dephasing due to the nuclear magnetic field. First of all, one can perform Hahn echo sequences, which will be discussed in the next section. Polarizing the nuclear system by a fraction p suppresses the field distribution by a factor $1/\sqrt{N(1 - p^2)}$ [91, 38]. However, to enhance T_2^* by a factor of 100 a very large, and therefore difficult to realize, polarization of 99.99% is needed. Several proposals explore the idea to reduce the nuclear field uncertainty by performing measurements of the nuclear field in the z-direction [92, 93, 94, 95]. More recently an experiment using a gate voltage controlled pumping cycle demonstrated that the difference of the nuclear fields in two adjacent quantum dots can be reduced, resulting in a 70-fold increase of the dephasing time between the singlet and the $m_z = 0$ triplet states in the double quantum dot [96]. In chapter 5 we present measurements employing electron-nuclear feedback, which imply a reduction of the nuclear field distribution in one dot of more than a factor of 10.

Finally, we remark that the instantaneous value of the nuclear field depends on the position of the electron, since it is determined by the position dependent coupling constants $A_i \propto \Psi(\mathbf{r}_i)$. Changing the position of the electron therefore changes the nuclear field experienced by the electron. As a result an applied electric field at the frequency of the electron spin splitting together with the transverse nuclear field $B_{N,x,y}$ can induce spin transitions [97]. Similarly, uncontrolled electric field fluctuations, like phonons [98, 99, 100, 101] in combination with the nuclear field can lead to spin relaxation. This process is relatively weak and is only expected to be dominant over relaxation processes due to the combination of spin-orbit coupling and phonons at low magnetic fields.

2.5.3 Dynamics of the nuclear field

The electron spin dynamics due to the statistical nuclear field can be reversed by a Hahn echo technique (see section 2.3) to the extent that the nuclear field is static. However, the nuclear field is also subject to a slow evolution limiting the spin-echo coherence time $T_{2,\mathrm{echo}}$. The evolution of the nuclear spins is mainly attributed to the hyperfine interaction and the dipole interaction between neighboring nuclear spins.

We first consider the hyperfine interaction. From the Hamiltonian in eq.2.17 we see that each nucleus experiences a small magnetic field $\sim A/N$, known as the

Knight field, from the hyperfine interaction with the electron spin. At low external magnetic field $B_\mathrm{ext} \ll B_\mathrm{N}$ this causes a precession and accordingly a change of the nuclear field. At large magnetic field $B_\mathrm{ext} \gg B_\mathrm{N}$ electron and nuclear spins precess around the external magnetic field and the longitudinal component of the nuclear field is preserved, since the change due to precession in the knight field is strongly suppressed. The quantum mechanical analogue of this picture can be understood by rewriting the hyperfine interaction Hamiltonian 2.17 in the following way:

$$H = \sum_i^N A_i (\sigma_z I_{z,i} + \sigma_+ I_{i-} + \sigma_- I_{i+}). \tag{2.19}$$

The last two terms represent electron-nuclear flips-flops that cause fluctuations of the nuclear field. However, due to the difference in Zeeman energy between electron and nuclear spin, this process is not energy conserving and therefore efficiently suppressed by an external magnetic field B_ext. However, virtual processes involving two electron-nuclear flip-flops can result in a nuclear-nuclear flip-flop: a flip-flop between the electron spin and nucleus i followed by a flip-flop between the electron spin and nucleus j effectively results in a flip-flop between nucleus i and nucleus j. In the total process the electron spin polarization is preserved and thus the energy cost ($\sim A_i - A_j$) is small. For $A_i \neq A_j$ this process changes the nuclear field. While the rate of direct electron-nuclear flip-flops is reduced efficiently with $1/B_\mathrm{ext}^2$, the rate of the first order virtual processes scales with $1/B_\mathrm{ext}$ and therefore, these are much harder to suppress.

Calculating the dynamics due to the hyperfine-mediated nuclear-nuclear flip-flop is a complex many body problem, especially for inhomogeneous A_i which suppresses this process due to the energy cost $\sim A_i - A_j$ of a flip-flop. Furthermore, because the nuclear dynamics are not independent of the electron spin, the coupled electron-nuclear system can lead to coherence decay characteristics different than the usual exponential decay. These so-called non-Markovian dynamics are extensively discussed in [38]. In general, the predicted coherence time due to this process is in the range 1-100 μs [38, 84, 102, 103, 104] for magnetic fields below 3 T.

A second process governing the nuclear dynamics is the dipole-dipole interaction between neighboring nuclei, which is given in the secular approximation (valid for Zeeman energies larger than the interaction strength D):

$$H_{i,j} = D(I_i^+ I_j^- + I_i^- I_j^+ - 4I_i^z I_j^z)/2, \tag{2.20}$$

with $D \sim 1/100\,\mu s$ [105]. The first two terms give rise to flip-flops of nuclear pairs which changes $B_{N,z}$ and therefore affects the electron spin coherence. The timescale of the drift in $B_{N,z}$ is difficult to evaluate due to a combination of complications. First of all, the flip-flop rate is suppressed when $A_i - A_{i+1} > D$ due to the associated energy mismatch [104]. From this it is expected that $B_{N,x,y}$ evolve on a $100\,\mu s$ timescale, the drift in the longitudinal component $B_{N,z}$ due to the dipole interaction

may be much longer. The contribution from the dipole-dipole interaction to the electron coherence time is estimated theoretically as $\sim$10-100 μs [39, 106, 103, 107], much faster than the $B_{N,z}$ drift time. We only note here that the time scale on which the spin decoheres is not only dependent on the typical correlation time of the nuclear spin bath, but also on the amplitude and the stochastics of the nuclear field fluctuations and, as we have seen in section 2.3, on the specific shape of the corresponding noise spectral density.

Chapter 3

Device fabrication and experimental setup

3.1 Device fabrication

Fabrication of a lateral gated quantum dot starts with a semiconductor heterostructure as described in chapter 2. The surface gates which electrostatically define the quantum dot are made by means of electron-beam lithography. The lithography process consists in general of the following steps. First, we spin a layer of organic resist (poly-methyl-methacrylate, PMMA) on the heterostructure surface (Fig. 3.1a). Then the pattern is defined by writing with a focused electron-beam in the electron-sensitive resist. This locally breaks up the polymer chains, so that the exposed parts can be removed by a developer (solution of methyl isobutyl ketone, MIBK, and iso-propyl alcohol, IPA), see Fig. 3.1b. The undercut is caused by electrons backscattered from the substrate during electron beam exposure. In the next step (Fig. 3.1c), metal is evaporated. The metal is only deposited on the heterostructure at the places where the resist has been exposed and removed. The last step is the removal of the remaining resist by acetone (Fig. 3.1d). In this process, the metal on top of the resist is removed as well, the so-called 'lift-off'. The lift-off process is facilitated by the undercut in the resist layer. Now metal electrodes are left at the places that were exposed to the electron-beam. For the fine gate pattern which is used to form the quantum dot and therefore has the smallest lateral dimension ($\sim$ 20 nm), we use a 10 nm layer of Ti serving as 'sticking' layer followed by 20 nm of gold.

To probe the quantum dot, ohmic contacts are fabricated which make electrical contact between the 2DEG and metal bonding pads on the surface. The pattern is also defined by electron-beam lithography. Considering the dimensions of $\sim$ 100 μm $\times$ 100 μm optical lithography would also be possible, however the e-beam pattern generator offers great flexibility for design changes, since no optical mask is required. The ohmic contacts are diffused into the substrate by rapid

thermal annealing (at 440°C for 60 sec) of an evaporated sandwich of Ni/AuGe/Ni (5/150/25 nm). Typically the ohmic contacts have a resistance of about 1 kΩ at helium temperature with a fabricated mesa. Metal wires bonded to these pads run toward the current or voltage probes, enabling us to perform transport measurements. For the experiments reported in chapter 4 and 5 an ac magnetic field is generated on-chip to induce electron spin resonance. In order to achieve a strong enough ac magnetic field a coplanar stripline (CPS) is fabricated on top of the fine gate structure. To electrically isolate the CPS and the gate pattern, calixarene is used as a dielectric [108], which is an organic material that can be dissolved in chlorobenzene. The solution is spin coated on the device. When writing on calixarene with an electron-beam using a high exposure dose the calixarene molecules cross-link with each-other and form a solid layer. This is used for defining the pattern.

A more detailed description of all steps of the fabrication process can be found in [109] and in [110] in particular an extensive account on the coplanar stripline. An updated fabrication recipe can be found in appendix 9.1.
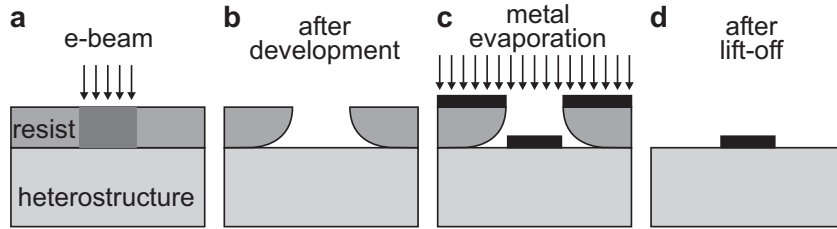
Figure 3.1: Fabrication of metal electrodes on the surface of the heterostructure. (a) Writing a pattern in the resist layer with an electronbeam. (b) After developing, the resist has been locally removed. (c) Evaporating metal. (d) After lift-off, a metal electrode remains.

3.2 Measurement setup

The measurement setup for performing the experiments discussed in chapters 4-6 of this thesis has been extensively discussed in [110]. Therefore we restrict ourselves to a concise description that includes the changes and additions made in order to perform the experiment described in chapter 7.
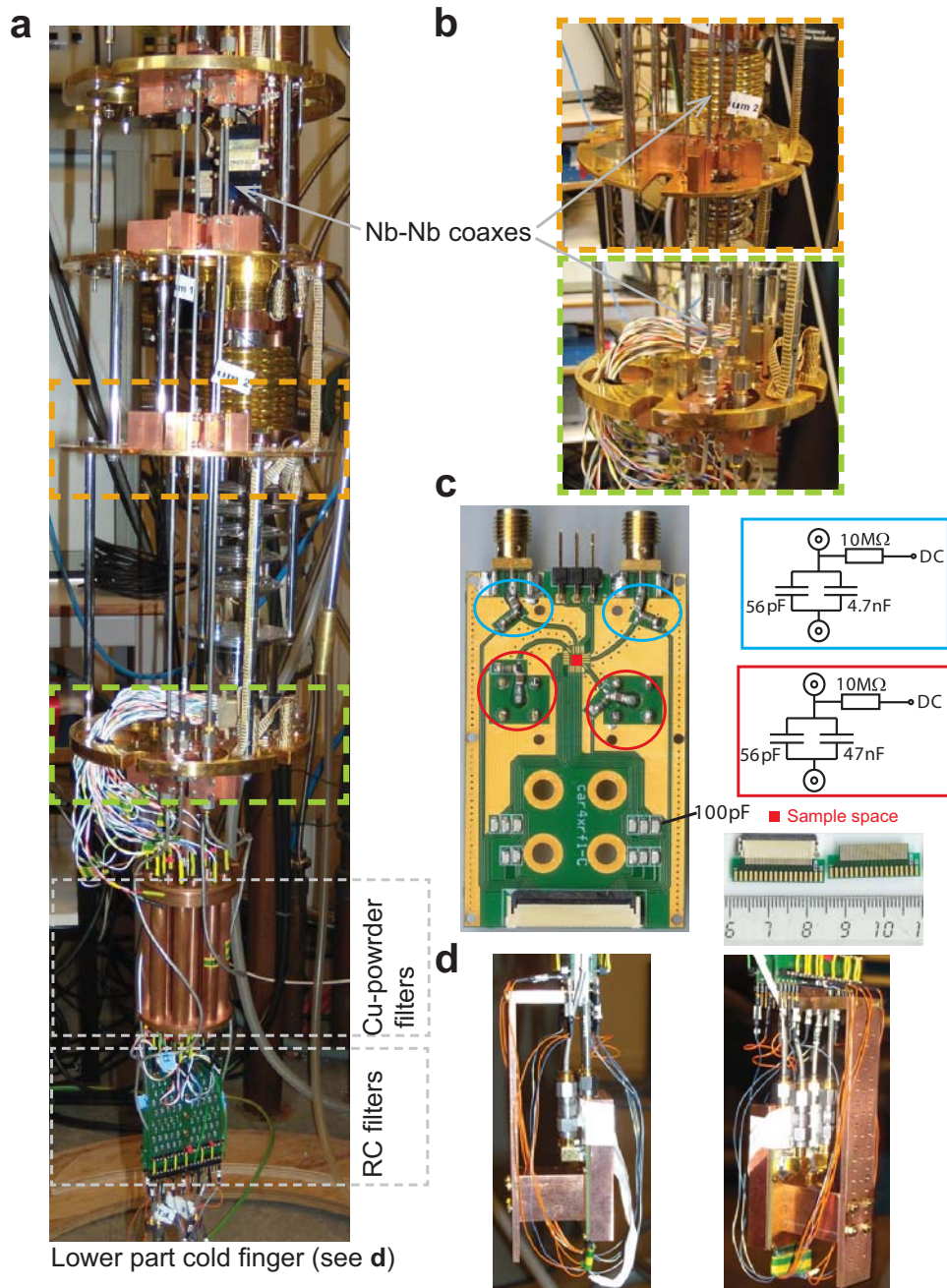
Figure 3.2: Insert of the Kelvinox 400 with device, RC-filters and copper powder filters. (a) Insert from the 1K pot stage to the bottom of the RC filters. (b) Zoom in on thermal anchoring of the coax lines. (c) PCB board with 4 bias-tees and SMA connectors. The dc-connector with a small PCB board to make a connector to the RC filters is shown (see blue and orange wires in (d)). (d) Mounted PCB board with 4 coaxes connected.

3.2.1 Dilution refrigerator and device cooling

In order to isolate an electron spin in a quantum dot well enough from the electrons in the reservoirs (of the 2DEG), the device temperature should be well below 1K. We use a Kelvinox 400 dilution refrigerator to cool down the device to a temperature of about 10-40 mK (with a cooling power of 400μW at 100 mK). Although phonons in the semiconductor lattice will have a similar temperature as the base temperature of the refrigerator, the electron temperature of the 2DEG is higher, around 100 mK. Due to weak electron-phonon coupling, the electrons are mostly cooled via DC wires which are connected to the source/drain contacts. The DC wires are thoroughly thermally anchored at several temperature stages including the mixing chamber. However, the electrons are heated up by noise that couples in via the DC wires, comes from the DC wires and radiation. In order to suppress the noise in the DC wires, we use different filtering stages at different temperatures and covering different frequency ranges. This will be discussed in section 3.2.3. In order to suppress radiation, the device is mounted in a copper can which is cooled to base temperature, protecting the device from the 4 K radiation of the inner vacuum chamber (IVC). The cold finger, which connects the device to the dilution stage of the refrigerator,and different filtering stages are shown in Fig. 3.2.

3.2.2 Measurement electronics and grounding

A typical measurement involves applying a source-drain bias over either the quantum dots or an adjacent quantum point contact and measuring the resulting current as a function of source-drain voltage and the applied voltages to the gates. The electrical circuit for implementing voltage-biased current measurements and applying voltages onto the gates of the device in the dilution fridge is shown in Fig. 3.3. The measurement electronics that are connected to the device, i.e. the current-to-voltage (IV) converter, voltage sources and digital-to-analog converters (DACs), were designed and built by Raymond Schouten at Delft University of Technology. In order to avoid interference coming from external measurement devices and data-acquisition equipment to couple to the device optical isolation is used at both sides of the measurement chain, i.e. in the voltage source, in the isolation amplifier as well as in the DACs. In this way, there is no galvanic connection between the two sides. The electrical signals are passed through analog optocouplers, which first convert these to an optical signal using an LED, and then convert the optical signal back using a photodiode. All circuitry at the sample side is analog, battery-powered and can use a ground separate from the ground of the power grid.

The measurements are controlled by a computer running LabView and more recently QTlab, a text-oriented measurement environment in Python developed by Reinier

Heeres and Pieter de Groot [1]. Commands are sent via a fiber link to the DAC box which contains 16 digital-to-analog converters. All other equipment described in this section is also remotely controlled and/or read-out from the measurement computer.

The experiments discussed in chapters 4-6 of this thesis are performed at low bandwidth (DC - 10Hz), therefore the current coming from the drain reservoir is fed to a low bandwidth IV converter. The IV converter has a noise floor of 5 fA/$\sqrt{\text{Hz}}$. The used value for the feedback resistor is 1 GΩ. The amplifier gain A can be chosen to be either 10^4 or 10^3 for lower effective input resistance of the IV converter (and thus higher bandwidth) or lower noise[2]. The bandwidth depends on the input impedance of the IV-converter and is approximately 50 Hz for an amplifier gain of 1000. More detailed information about the IV-converter can be found in [110]. The signal from the IV converter is sent to an isolation amplifier to provide optical isolation and possible gain. The voltage from the isolation amplifier is finally measured by a digital multimeter (Keithley 2700). In most measurements an additional passive 10Hz filter is used between the isolation amplifier and the multimeter.

The experiment described in chapter 7 is performed at higher bandwidth to measure the real-time response of a quantum point contact (QPC) current to electrons tunneling on/off an adjacent quantum dot. The IV converter used in the experiment [3] is the same as described in [29]. It has a bandwidth of about 150kHz and an input voltage noise measured to be 0.8 nV/$\sqrt{\text{Hz}}$. The feedback resistor is 10 MΩ and the amplifier gain is 10^4, corresponding to an input impedance of the IV converter of about 1kΩ. The actual rms current noise resulting from the input voltage noise and the measurement bandwidth depend on the total capacitance C_L of the connection of the drain (including filtering) to ground. The measurement bandwidth is limited by the low-pass filter formed by C_L and the input impedance of the IV converter to approximately 100kHz for $C_L = 1.5$ nF. The rms current noise resulting from the input voltage noise increases with frequency due to the capacitive load formed by C_L, which already at low frequencies has a lower impedance than the feedback resistor. It is therefore crucial to reduce C_L as much as possible, which implies removing parts of the filtering on the line coming from the drain of the QPC. This is clearly a trade-off. In Fig.3.3 the connection to the source and the drain of the QPC is shown. The source is connected to a 'slow line' and is the same as used for all ohmic contacts in chapters 4-6. In the 'fast line' of the drain mainly three changes were made: (i) The ground wire of the twisted pair is grounded at the top of

---

[1]QTlab is available at http://qtlab.sf.net .

[2]Via the feedback loop, the voltage noise of the amplifier is sent back to the device. This so-called "kickback" drops partially over R_f/A, and therefore, lower noise is achieved with smaller amplification. To prevent "kickback"' over a large bandwidth, A is frequency dependent with a cutoff around 85 Hz.

[3]In fact two IV converters are used to measure both the response of the left and right quantum point contact. One is the actual IV converter used in [29], the other is a copy of that one using the same JFET (Interfet 3602).

the copper powder. This reduces C_L due to the cross-capacitance between different wires in the copper powder filters ($\sim 0.4\,\mathrm{nF}$). (ii) No RC filter is used. (iii) The pi-filter at room temperature is replaced with a 'feedthrough capacitor' of $\sim 100\,\mathrm{pF}$. In total the remaining capacitance of the connection to ground is measured to be about $1.3\,\mathrm{nF}$ with additional contribution from e.g. the cable connecting the room-temperature electronics and the fridge. An external low-pass filter set at $40\,\mathrm{kHz}$ is used in between the IV converter and the digital oscilloscope (LeCroy Waverunner 44Xi) used for the data-acquisition. In the first cool-down of the experiment described in chapter 7 the electron temperature was fairly high ($\sim 350\,\mathrm{mK}$). We now added an RC filter also to the 'fast line' which is on the same board as visible in Fig.3.2 and schematically in the 'slow line' in Fig. 3.3. A high cut-off frequency is chosen ($\sim 1\,\mathrm{MHz}$) with filter values of $470\,\Omega$ for the resistor and $270\,\mathrm{pF}$ for the capacitor, in order not to increase C_L too much.

3.2.3   Wires and filtering

In order to connect the source/drain contacts and the gates of the device to the room temperature electronics, 2 times 12 twisted pairs of wires run from room temperature down to the plate at the mixing chamber of the dilution refrigerator. The diameter of the wires is very small ($\sim 100\,\mu m$), and the material (constantan) is chosen such that the heat conduction of the wires is small (resulting in a relative high electrical resistance of $168\,\Omega$). For the faster lines connecting the QPC drains in chapter 7 wires made of copper which perform worse regarding heat conductivity, but have a lower resistance ($57\,\Omega$) are used in order to reduce the Johnson noise in the wires. For the electrical circuits that carry a current, like the connection to the source/drain contacts of the device, two twisted pairs are used as depicted in Fig. 3.3. One side of a twisted pair is connected to the differential output of the voltage source. At the other side of the pair, one wire is connected to the cold finger (defining a "cold-ground"), and the other wire is connected to the source contact of the device. Another twisted pair is connected at one side to the differential input of the IV-converter, and one wire at the other side is connected to the cold finger and another one to the drain contact of the device (see Fig. 3.3). As a result the surface of the loop that carries a current is very small, and therefore also the noise that couples to the wires via magnetic induction. No current flows through the wires that connect to a gate and therefore, both wires from a pair are separately used to connect to two different gates. All the wires are thermally anchored to the fridge by wrapping them around copper posts at several temperature stages ($4\,\mathrm{K}$, $1\,\mathrm{K}$ and $\sim 10\,\mathrm{mK}$). This anchoring is causing a parasitic capacitance to ground of about $0.5\,\mathrm{nF}$.

The wires connecting the device to the measurement electronics have to be filtered carefully to reduce electron heating and uncontrolled excitations of the device disturbing the measured signal. We use three types of filters, which together cover
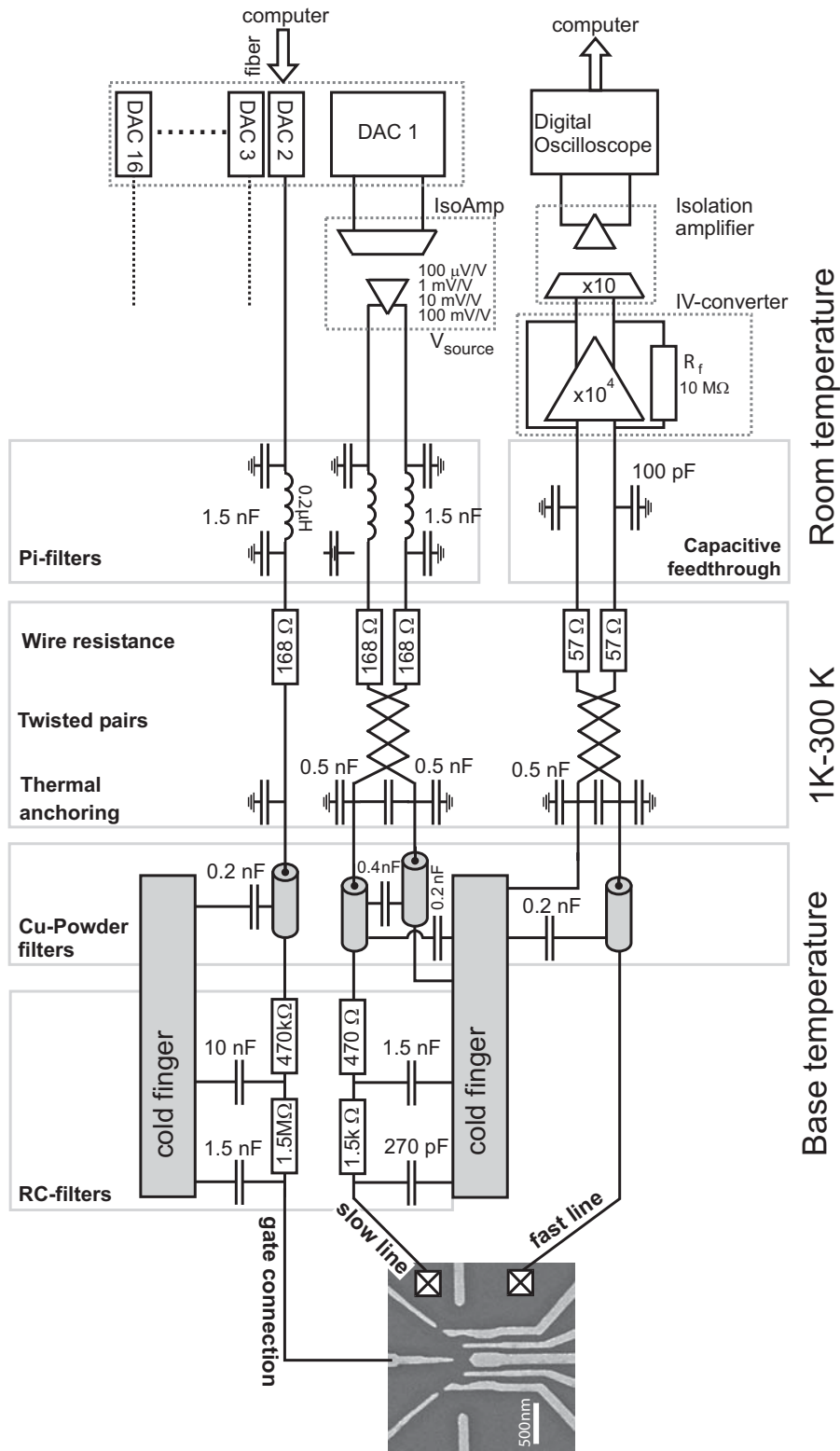
Figure 3.3: Electrical circuit for applying voltages to the gate electrodes, and for performing a voltage-biased current measurement with high bandwidth.

the required frequency range. At room temperature, so-called Pi-filters (combination of two capacitors and an inductor) filter noise in the middle frequency range, which is above 10 MHz (attenuation is 5 dB at 10 MHz, and 45 dB at 100 MHz), but they perform worse above 1 GHz. Therefore, at base temperature, the signal wires run through copper tubes filled with copper powder in which about 2 meters of wire is wound. Via eddy currents, the high-frequency noise is absorbed in the powder very effectively (attenuation of more than 60 dB from 1 GHz up to more than 50 GHz). The remaining low-frequency noise is removed by two types of two-stage RC-filters with a cut-off at 20 Hz for the wires connecting the gates, and a cut-off at 150 kHz for wires connecting ohmic contacts. The ground plane of the filterboard is carefully designed to minimize leaking of high frequency signals through the resistors. The 'fast lines' have significantly less filtering as visible in Fig. 3.3.

3.2.4 High frequency signals

High frequency lines are needed in order to apply fast voltage pulses to one of the gates, or microwave signals to the coplanar stripline. The configuration of the two high frequency lines used in chapters 4-6 are described in [110]. For the experiment in chapter 7 we added two more coaxial lines. These two are identical to the ones which were already built-in apart from the connectors, which were chosen to be 2.92 mm rather than 2.4 mm. All four lines are connected via a SMA feedthrough at room temperature specified up to 18 GHz. Each line consists of three segments all of which are produced by Keycom: (i) From room temperature to 1 Kelvin we use Keycom ULT-05 cables (outer diameter 2.2 mm; inner conductor: silver-plated brass; outer conductor: stainless steel (SUS304) with a 5 μm layer of copper). This choice is a compromise between lower heat conductivity and insertion loss. A thinner cable or silver plated beryllium copper for the inner conductor would give a lower heat conductivity, but a higher insertion loss. (ii) From 1 Kelvin to the mixing chamber, we use Keycom 085A semi-rigid coax lines with both inner and outer conductor made of Nb. The coax is superconducting at these temperatures, which suppresses heat conduction. (iii) From the mixing chamber to the sample holder, we use tin plated Cu coaxial cables which are flexible and therefore convenient in use. The outer conductors of the coaxial lines are thermally anchored to the dilution unit at 4K, 1K, ∼800 mK and ∼40 mK. In order to anchor the inner conductor of the coaxial lines as well, we use attenuators which are anchored at 1 K (all -20 dB; Agilent and Weinschel for the 2.4 mm lines; XMA corporation[4] for the 2.92 mm lines) and at the mixing chamber (all -10 dB Weinschel for the 2.4 mm lines; XMA corporation for the 2.92 mm lines). Note that in chapters 4-6 the attenuation of the coax line used for excitation of the stripline was only 9 dB (Agilent -10 dB at 1 K, Weinschel -3 dB at the mixing chamber) because high power excitation is required and the cooling

---

[4]Order number: 2682-6460-xx with xx the attenuation value in dB

power of the mixing chamber is limited. Finally, when applying fast pulses and/or microwaves we use home-made and commercially available DC blocks (Picosecond model:5505) which intersect both inner and outer conductor of the coaxial lines with capacitors to avoid low-frequency noise coming from the high frequency generators into the electrical circuit of the device. For the longer pulses used in chapter 7 we optically isolate the waveform generator from the electrical circuit of the device by using analog optocouplers which support a bandwidth from DC up to 200MHz to avoid common mode noise from the generator coupling to the sample.

The phase-controlled RF burst sequences used for magnetic ESR are generated with a vector source (Rohde&Schwarz SM300, 9 kHz to 3 GHz) with RF modulator, controlled by two channels of a Tektronix arbitrary waveform generator (see Fig. 3.4a for a block diagram). Voltage pulses are applied to the right side gate through a bias-tee, so that the gate can remain biased with a DC voltage as well. The bias-tee was home-made, with a rise time of 150 ps and RC charging time of 10 ms at 77 K (R=10 MΩ, C=3.3 nF). For generation of RF bursts at higher frequencies (see Fig. 3.4b), we use a HP 83650A source (10 MHz to 50 GHz) or Rohde&Schwarz SMR40 source (1-40 GHz). The bursts are created by sending this signal through a high isolation GaAs RF switch (Minicircuits ZASWA-2-50DR, typical rise time 3 ns), gated by rectangular pulses from an arbitrary waveform generator (Tektronix AWG520, channel rise time $\leq$2.5 ns, marker rise time 0.5-2 ns). The coplanar stripline is contacted via a modified microwave probe (GGB Industries, Picoprobe model 50A, loss <1 dB, DC-50 GHz), which is shown in Fig. 3.2b. For the frequency range 5-20 GHz we cannot use the RF switch, and instead, we use microwave mixers. Two mixers are connected in series in order to suppress the leakage, whereas the extra loss is compensated by an Hittite amplifier (Fig. 3.4c).

In chapter 7 four cryogenic bias-tees are used to enable fast pulsing and microwave excitation of four of the gates. Different from what is described above these four bias-tees are on the same PCB board (printed by Eurocircuits, material: FR4) which also carries the sample (see Fig.3.2c). The PCB board is fitted with 4 SMA connectors from which waveguides run towards the sample. The waveguides are tapered in the end to make bonding to the sample possible. By interconnecting two of the waveguides with a bonding wire the transmission could be measured. Up to 10 GHz the response is flat and the waveguides including the bias-tees have less than 2 dB losses. The back side of the PCB is the ground plane, which is connected with the ground planes on the front by via-holes. All dc lines on the board are fitted with a 100 pF capacitor to ground, few of which are on the back side, to reduce cross-talk between the waveguides and the lines. For additional shielding and also mechanical protection of the sample the PCB board is capped with a copper box, see Fig. 3.2d. For the experiment in chapter 7 a new waveform generator, Tektronix AWG5014 is used.
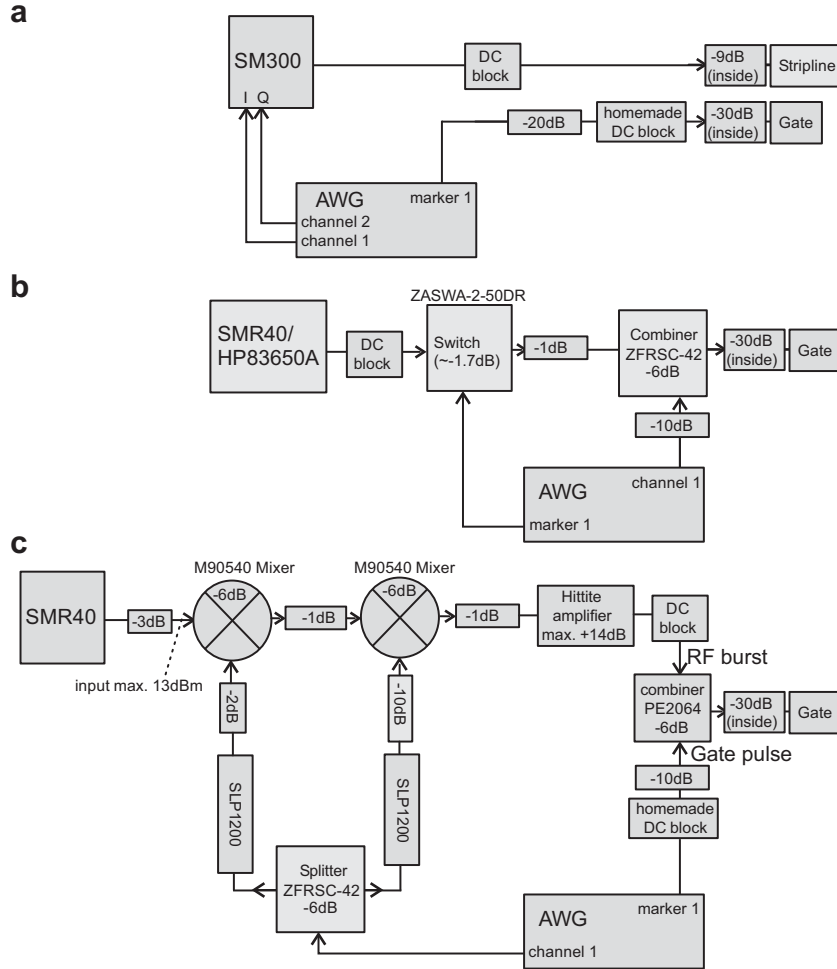
Figure 3.4: (a) Block diagrams depicting generation of gate voltage pulse ($\sim 1\mu s$) and phase-controlled RF burst sequences for magnetic ESR. (b) Block diagrams depicting generation of RF bursts for electrically driven ESR (1-5 GHz), combined with generation of gate pulse ($\sim 1\mu s$). (c) Similar as (b) for the frequency range 1-5 GHz.

Chapter 4

Coherence of a single spin in a quantum dot

We report time-resolved coherence measurements of a single electron spin confined in a semiconductor quantum dot. Coherent control is realized via electron spin resonance which is discussed in the first part of this chapter. This allows us to perform a Ramsey-style experiment showing that the free evolution decay time T_2^* is about 37 ns, set by the nuclear field distribution. Via a spin-echo technique we reverse to a large extent the electron-nuclear dynamics, and find a coherence time $T_{2,\mathrm{echo}}$ of about $0.5\,\mu$s at 70 mT, which is more than a factor of ten longer than the Ramsey decay time. These results are close to the range of theoretical predictions of the electron spin coherence time governed by the dynamics of the electron-nuclear system.

4.1 Introduction

Isolated electron spins in a semiconductor can have very long coherence times, which permits studies of their fundamental quantum mechanical behavior, and holds promise for quantum information processing applications [15, 90]. For ensembles of isolated spins, however, the slow intrinsic decoherence is usually obscured by a much faster systematic dephasing due to inhomogeneous broadening [87, 111]. The actual coherence time must then be estimated using a spin echo pulse that reverses the fast dephasing [112, 113].

For a single isolated spin there is no inhomogeneous broadening due to averaging over a spatial ensemble. Instead, temporal averaging is needed in order to collect sufficient statistics to characterize the spin dynamics. In some cases, this averaging can also lead to fast apparent dephasing that can be (largely) reversed using a spin-echo technique. This is possible when the dominant influence on the electron spin coherence fluctuates slowly compared to the electron spin dynamics, but fast compared to the required averaging time. Such a situation is common for an electron spin in a GaAs quantum dot where the hyperfine interaction with the nuclear spins gives rise to a slowly fluctuating nuclear field, resulting in a dephasing time of tens of nanoseconds [84, 83, 88, 41, 32]. The effect of the low-frequency components of the nuclear field can be reversed to a large extent by a spin-echo technique. For two-electron spin states, this was demonstrated by rapid control over the exchange interaction between the spins [32]. The application of a spin-echo technique on a single electron spin is required when using the spin as a qubit. Furthermore, erasing the fast dephasing allows for a more detailed study of the remaining decoherence processes, including those caused by the electron-nuclear spin dynamics [39, 38, 102, 104, 103, 107, 114].

We first discuss the realization of coherent control by electron spin resonance and than apply it to probe the coherence of single electron spin confined in an electrostatically defined GaAs quantum dot. We find that the spin-echo decay time $T_{2,\text{echo}}$ is about 0.5 μs at 70mT, more than a factor ten longer than the dephasing time T_2^* obtained from a Ramsey-style experiment. This indicates that the echo pulse reverses the dephasing to a large extent. These findings are consistent with (extrapolations of) theoretical predictions for this system [103, 107, 104], as well as with earlier echo measurements on two-electron spin states in a similar quantum dot system [32], and with mode locking measurements of single spins in an ensemble of self-assembled quantum dots [115].

4.2 Electron spin resonance

The most commonly used technique for driving coherent transitions between Zeeman split levels is electron spin resonance (ESR) [116]. In ESR a rotating magnetic
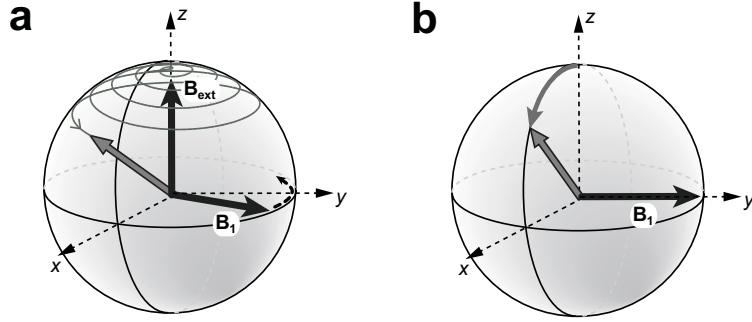
Figure 4.1: Electron trajectory during spin resonance. (a) Seen from the laboratory frame the spin spirals over the surface of the Bloch sphere. (b) Seen from the rotating frame which rotates with the RF frequency f_{ac} around the $\hat{z}$-axis. The field $\mathbf{B}_1$ lies along a fixed axis around which the spin precesses. In the case that the resonance condition is not exactly fulfilled an offset field along the $\hat{z}$-axis will be present.

field B_1 is applied perpendicular to the external magnetic field B_{ext} evolving on resonance with the spin precession frequency: $f_{ac} = g\mu_B B_{ext}/h$ (μ_B is the Bohr magneton, g the electron spin g-factor and f_{ac} the excitation frequency at which B_1 evolves). Fig. 4.1 shows the trajectory of the electron spin during ESR both in the lab and the rotating frame. Experimentally, a rotating magnetic field is difficult to produce. However, an oscillating magnetic field B_{ac} can be decomposed into two counter rotating components with amplitude $B_1 = B_{ac}/2$. One component rotates with the spin and results in ESR, whereas the other rotates in the opposite way thus being far off-resonant (assuming that $B_{ext} \gg B_1$)and therefore having a negligible effect on the spin. Magnetic resonance of a single electron spin in a solid has been reported in a few specific cases [117, 18, 118] and has also been proposed for a single semiconductor quantum dot [119, 120]. The scheme to detect ESR in a single quantum dot is conceptually simple: the electrochemical potential in the dot is tuned such that only spin-up electrons can tunnel out, but not spin-down electrons. Therefore, Coulomb blockade only gets lifted when the electron spin gets repeatedly flipped. Technically this scheme turned out to be hard to implement: it requires that the Zeeman splitting must be larger than the thermal broadening of the electron reservoir, and therefore the excitation frequency is in the microwave regime. Furthermore, the electric field components, unavoidably generated along with the driving field B_1, can lead to photon-assisted tunneling (PAT) processes, lifting Coulomb blockade regardless of the spin state.

4.3 Device and detection concept

Here, magnetically induced ESR of a single electron is realized in a double quantum dot and coherent control of the spin state is demonstrated. Instead of using lifting
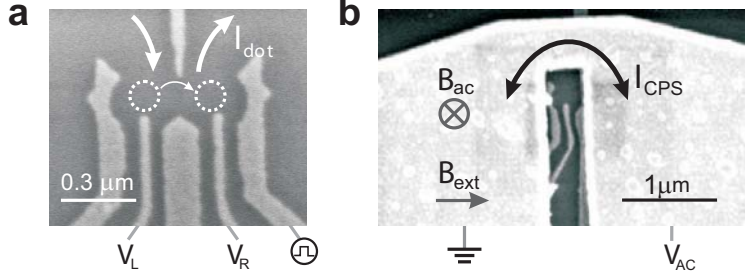
Figure 4.2: (**a**) Scanning electron microscope (SEM) image of a device with the same gate pattern as used in the experiment. The Ti/Au gates are deposited on top of a GaAs/AlGaAs heterostructure containing a two-dimensional electron gas 90 nm below the surface. White arrows indicate current flow through the two coupled dots (dotted circles). The right side gate is fitted with a homemade bias-tee (rise time 150 ps) to allow fast pulsing of the dot levels. (**b**) SEM image of a device similar to the one used in the experiment. The termination of the coplanar stripline is visible on top of the gates. The gold stripline has a thickness of 400 nm and is designed to have a 50 Ω characteristic impedance, Z_0, up to the shorted termination. It is separated from the gate electrodes by a 100-nm-thick dielectric (Calixerene). More details about the design of the stripline can be found in [110, 33].

of Coulomb blockade as proposed for detection in a single quantum dot [119], we use electrical transport measurements through the two dots in series in the spin blockade regime (see chapter 2) where current flow depends on the relative spin state of the electrons in the two dots [121, 122]. In brief, the device is operated so that current is blocked owing to spin blockade, but this blockade is lifted when spin-flips are induced by ESR. In this scheme the relevant transitions are not to the temperature broadened leads, but the transition from one dot to the other. The experiment can thus be performed at a smaller static magnetic field, and consequently with lower, technically less demanding, excitation frequencies. Furthermore, by applying a large bias voltage across the double dot, the spin detection can be made much less sensitive to electric fields (generated along with the ac magnetic field) than is possible in the single-dot case.

The double quantum dot is defined by surface gates (Fig. 4.2a) on top of a two-dimensional electron gas. By applying the appropriate negative voltages to the gates, the dots can be tuned to the few-electron regime [123]. The oscillating magnetic field, that drives the spin transitions, is generated by applying a radio-frequency (RF) signal to an on-chip coplanar stripline (CPS), which is terminated in a narrow wire, positioned near the dots and separated from the surface gates by a 100-nm-thick dielectric (Fig. 4.2b). The current through the wire generates an oscillating magnetic field B_{ac} at the dots, perpendicular to the static external field B_{ext} and slightly stronger in the left dot than in the right dot.

More specifically ESR is detected as follows (see Fig. 4.3). The double dot is tuned

to the spin-blockade regime in which transport occurs via the following sequence of charge states $(0,1) \rightarrow (1,1) \rightarrow (0,2) \rightarrow (0,1)$, where (n,m) denotes the charge state with $n(m)$ electrons in the left (right) dot. Since energetically only the singlet is accessible in the $(0,2)$ charge state, the transition $(1,1) \rightarrow (0,2)$ can only occur, if the spin state of the electrons in the $(1,1)$ state have a $S(1,1)$ component. As a result, occupation of the triplet states $|T_+(1,1)\rangle = |\uparrow\uparrow\rangle$ and $|T_-(1,1)\rangle = |\downarrow\downarrow\rangle$ block transport. In principle the triplet state $|T_0(1,1)\rangle = 1/\sqrt{2}(|\uparrow\downarrow\rangle - |\downarrow\uparrow\rangle)$ also blocks transport, it is however coupled to $S(1,1)$ by the nuclear field, as discussed in chapter 2. In summary, the states with even spin parity (parallel spins) block transport, while the states with odd spin parity (anti-parallel spins) allow transport. An oscillating magnetic field resonant with the Zeeman splitting, $hf_{ac} = g\mu_B B_{ext}$, can flip the spin in the left or the right dot. If the double dot is initially blocked in $|\uparrow\uparrow\rangle$ (or $|\downarrow\downarrow\rangle$) the spin state then changes to $\uparrow\downarrow$ (or $\downarrow\uparrow$) due to ESR. If both spins are flipped, transitions occur between $|\uparrow\uparrow\rangle$ and $|\downarrow\downarrow\rangle$ via the intermediate state $|\uparrow \pm \downarrow\rangle|\uparrow \pm \downarrow\rangle/2$. In both cases, states with odd spin parity are created owing to ESR, as a result the spin blockade is lifted and the occurring transport can be directly related to induced spin transitions.

4.4 ESR spectroscopy

In Figs. 4.4b,c the resonant ESR response is clearly observed in the transport measurements as a function of magnetic field, where satellite peaks develop at the resonant field $B_{ext} = \pm h f_{ac}/g\mu_B$ when the RF source is turned on (the zero-field peak arises from the inhomogeneous nuclear field, which admixes all the triplets with the singlet (see chapter 2 and refs [41, 37]). The key signature of ESR is the linear dependence of the satellite peak location on the RF frequency, which is clearly seen in the data of Fig. 4.4c, where the RF frequency is varied from 10 to 750 MHz. From a linear fit through the top of the peaks we obtain a g-factor of 0.35±0.01, which lies within the range of reported values for confined electron spins in GaAs quantum dots [124, 125, 126, 127]. We also verified explicitly that the resonance we observe is magnetic in origin and not caused by the electric field that the CPS generates as

| (0,1) | (1,1) | (1,1) | (0,2) | (0,1) |

Spin
blockade

Spin
manipulation

Projection
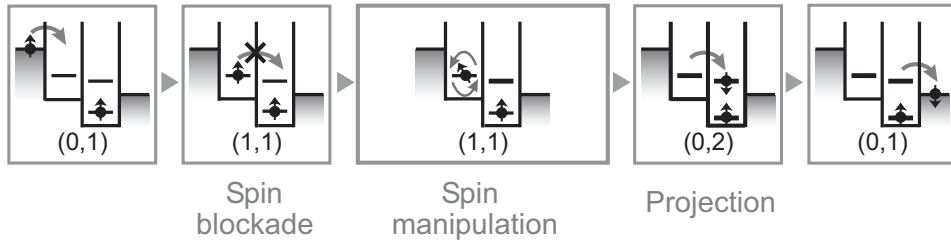
Figure 4.3: Schematic of the double dot tuned into the spin blockade regime. The spin blockade gets lifted by electron spin flips in one of the two dots.

well; negligible response was observed when RF power is applied to the right side gate, generating mostly a RF electric field (see Fig. 4.4d)[1].
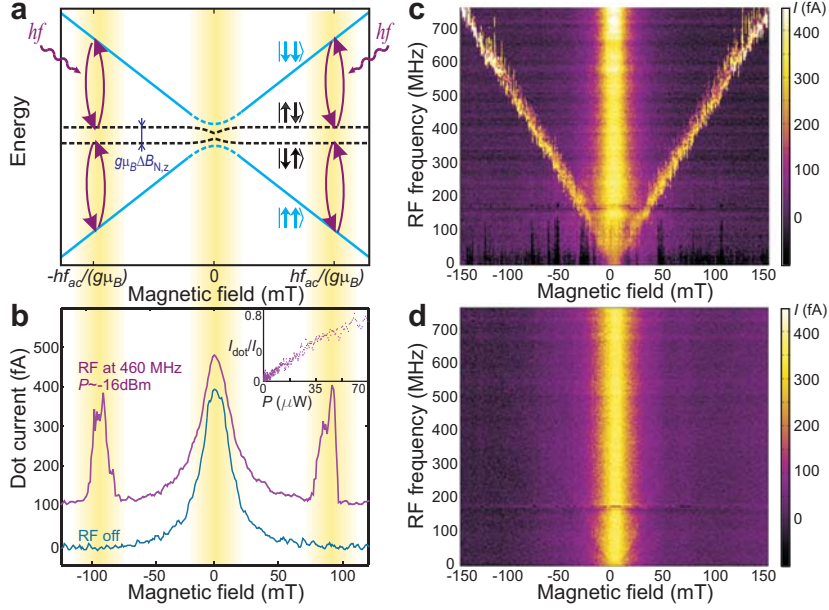
Figure 4.4: ESR spin state spectroscopy. (a) Energy diagram showing the relevant eigenstates of two electron spins in a double-dot, subject to an external magnetic field and nuclear fields. Because $B_{N,z}$ is in general different in the two dots, the energy for ↑↓ and ↓↑ is different. ESR induces transitions between states with parallel spin and states with anti-parallel spin, thereby lifting spin blockade. At zero external magnetic field spin blockade is lifted due to the nuclear field.(b) Current measured through the double-dot in the spin blockade regime, with (red trace, offset by 100 fA for clarity) and without (blue trace) a RF magnetic field. Satellite peaks appear as the external magnetic field is swept through the spin resonance condition. Each measurement point is averaged for one second, and is therefore expected to represent an average response over many nuclear configurations. The RF power P applied to the CPS is estimated from the power applied to the coax line and the attenuation in the lines. Inset, satellite peak height versus RF power ($f = 408$ MHz, $B_{\text{ext}} = 70$ mT, taken at slightly different gate voltage settings). The current is normalized to the current at $B_{\text{ext}} = 0$ (=I_0). (c) Current through the dots when sweeping the RF frequency and stepping the magnetic field. (d) Similar data as in (c), but now with the RF signal applied to the right side gate instead of to the ESR stripline. The amplitude of the RF signal (-50 dBm at the gate) was chosen such that the electric field is equally strong as in the ESR measurements of (c) (determined from the measured PAT broadening).

---

[1]A very faint line is still present at the same position as the ESR response in Fig. 4.4c. It could also be due to the coupling of the electric field to the electron spin, through Rashba or Dresselhaus spin-orbit interaction (see chapter 6 and [73]). A final possibility is that spins are flipped when the electron wave function is moved back-and-forth in the inhomogeneous nuclear field [97]. In any case, it is clear that in our experiment, all these mechanisms are much less efficient than magnetic excitation via the CPS at the generated electric field amplitude.

The amplitude of the peaks in Fig. 4.4b increases linearly with RF power ($\sim B_{\mathrm{ac}}^2$) before saturation occurs, as predicted [119] (Fig. 4.4b, inset). The ESR satellite peak is expected to be broadened by either the excitation amplitude B_{ac} or incoherent processes, like cotunnelling, inelastic transitions (to the S(0,2) state) or the statistical fluctuations in the nuclear field, whichever of the four has the largest contribution. No dependence of the width on RF power was found within the experimentally accessible range ($B_{\mathrm{ac}} < 2$ mT). Furthermore, we suspect that the broadening is not dominated by cotunnelling or inelastic transitions because the corresponding rates are smaller than the observed broadening.The observed ESR peaks are steeper on the flanks and broader than expected from the nuclear field fluctuations. In many cases, the peak width and position are even hysteretic in the sweep direction, suggesting that the resonance condition is shifted during the field sweep. We speculate that dynamic nuclear polarization due to feedback of the electron transport on the nuclear spins plays a central part here [37, 128, 129, 42].

4.5   Coherent oscillations
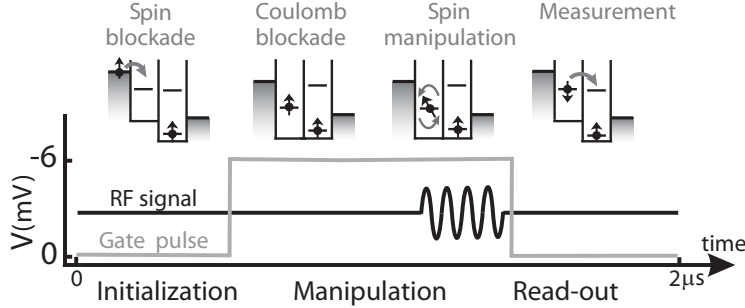
Figure 4.5: The control cycle for coherent manipulation of the electron spin. During the 'initialization' stage the double-dot is tuned in the spin blockade regime. Electrons will move from left to right until the system is blocked with two parallel spins (either ↑↑ or ↓↓; in the figure only the ↑↑ case is shown). For the 'manipulation' stage, the right dot potential is pulsed up so none of the levels in the right dot are accessible (Coulomb blockade), and a RF burst with a variable duration is applied. 'Read-out' of the spin state at the end of the manipulation stage is done by pulsing the right dot potential back; electron tunnelling to the right lead will then take place only if the spins were anti-parallel. The duration of the read-out and initialization stages combined was 1 μs, long enough (1 $\mu s \gg 1/\Gamma_{\mathrm{L}}, 1/\Gamma_{\mathrm{M}}, 1/\Gamma_{\mathrm{R}}$) to have parallel spins in the dots at the end of the initialization stage with near certainty (this is checked by signal saturation when the pulse duration is prolonged). The duration of the manipulation stage is also held fixed at $1\mu s$ to keep the number of pulses per second constant. The RF burst is applied just before the read-out stage starts.

Following the observation of magnetically induced spin flips, we next test whether we can also coherently rotate the spin by applying RF bursts with variable length.
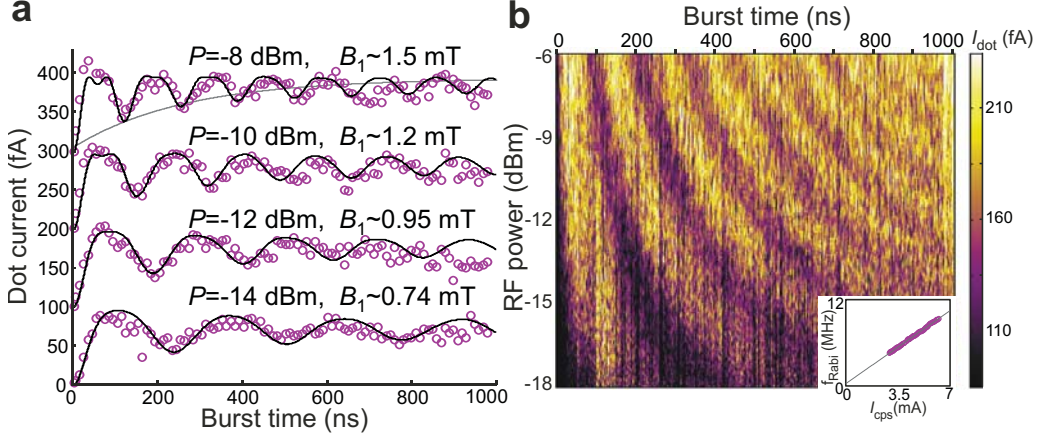
Figure 4.6: Coherent spin rotations. (a) The dot current-reflecting the spin state at the end of the RF burst-oscillates as a function of RF burst length (curves offset by 100 fA for clarity). The frequency of B_{ac} is set at the spin resonance frequency of 200 MHz ($B_{ext} = 41$ mT). The period of the oscillation increases and is more strongly damped for decreasing RF power. The RF power P applied to the CPS is estimated from the power applied to the coax line and the attenuation in the lines and RF switch. From P, the stripline current is calculated via the relation $P = \frac{1}{2}(\frac{I_{CPS}}{2})^2 Z_0$ assuming perfect reflection of the RF wave at the short. Each measurement point is averaged over 15 s. We correct for a current offset which is measured with the RF frequency off-resonance (280 MHz). The solid lines are obtained from numerical computation of the time evolution, as discussed in the text. The grey line corresponds to an exponentially damped envelope. (b) The oscillating dot current (represented in colourscale) is displayed over a wide range of RF powers (the sweep axis) and burst durations. The dependence of the Rabi frequency f_{Rabi} on RF power is shown in the inset. f_{Rabi} is extracted from a sinusoidal fit with the current oscillations from 10 to 500 ns for RF powers ranging from -12.5 dBm up to -6 dBm.

In contrast to the continuous-wave experiment, where detection and spin rotation occur at the same time, we pulse the system into Coulomb blockade during the spin manipulation. This eliminates decoherence induced by tunnel events from the left to the right dot during the spin rotations. The experiment consists of three stages (Fig. 4.5): initialization through spin blockade in a statistical mixture of ↑↑ and ↓↓, manipulation by a RF burst in Coulomb blockade, and detection by pulsing back for projection (onto S(0,2)) and tunnelling to the lead. When one of the electrons is rotated over $(2n + 1)\pi$ (with integer n), the two-electron state evolves to ↑↓ (or ↓↑), giving a maximum contribution to the current (as before, when the two spins are anti-parallel, one electron charge moves through the dots). However, no electron flow is expected after rotations of $2n\pi$, where one would find two parallel spins in the two dots after the RF burst.

We observe that the dot current oscillates periodically with the RF burst length (Fig. 4.6). This oscillation indicates that we performed driven, coherent electron spin rotations, or Rabi oscillations. A key characteristic of the Rabi process is a linear

dependence of the Rabi frequency on the RF burst amplitude, B_{ac} ($f_{Rabi} = g\mu_B B_1/h$ with $B_1 = B_{ac}/2$ due to the rotating wave approximation). We verify this by extracting the Rabi frequency from a fit of the current oscillations of Fig. 4.6b with a sinusoid, which gives the expected linear behaviour (Fig. 4.6b, inset). From the fit we obtain B_{ac}=0.59 mT for a stripline current I_{CPS} of ∼1 mA, which agrees well with predictions from numerical finite element simulations (see in [33, 110]). The maximum B_1 we could reach in the experiment before electric field effects hindered the measurement was 1.9 mT, corresponding to $\pi/2$ rotations of only 27 ns (that is, a Rabi period of 108 ns, see Fig. 4.6b). If the accompanying electric fields from the stripline excitation could be reduced in future experiments (for example, by improving the impedance matching from coax to CPS), considerably faster Rabi flopping should be attainable.

The oscillations in Fig. 4.6b remain visible throughout the entire measurement range, up to 1 μs. This is striking, because the Rabi period of ∼100 ns is much longer than the time-averaged coherence time T_2^* of 10-20 ns (refs [32, 87, 88, 41]) caused by the nuclear field fluctuations. The slow damping of the oscillations is only possible because the nuclear field fluctuates very slowly compared to the timescale of spin rotations and because other mechanisms, such as the spin-orbit interaction, disturb the electron spin coherence only on even longer timescales [30, 77, 69]. We also note that the decay is not exponential (grey line in Fig. 4.6a), which is related to the fact that the correlation time of the nuclear bath is longer than the Rabi period (see [38, 130]).

4.6 Modeling of the electron spin time evolution

4.6.1 Full time dependent Hamiltonian

To understand the amplitudes and decay times of the oscillations better, we model the time evolution of the spins throughout the burst duration. The time evolution of the electron spin in the left and right dot is described by the following Hamiltonian (in the rest of this section the index $i = \{L, R\}$ refers to the left and right dot respectively and accordingly $\hat{\mathbf{S}}^i, i = L, R$ denote the left and right electron spin):

$$\hat{H}^i = g\mu_B(\mathbf{B}_{ext} + \mathbf{B}_{ac}\cos(\omega_{ac}t + \varphi) + \mathbf{B}_N^i) \cdot \hat{\mathbf{S}}^i \tag{4.1}$$

where $\mathbf{B}_{ext}$ is the external magnetic field, $\mathbf{B}_{ac}\cos(\omega_{ac}t + \varphi)$ is the ac magnetic field generated by the coplanar waveguide[2] and $\mathbf{B}_N^i$ corresponds to a single frozen configuration of the nuclear field in the left and right dot (see chapter 2). This is justified because the electron spin dynamics considered here is much faster than the dynamics

---

[2]For simplicity we assume the RF field to be of equal amplitude in both dots. From numerical finite element simulations we expect the fields in the two dots to differ from each other by no more than 20% [110].

of the nuclear system. The correlation time of the fluctuations in the nuclear-spin system due to the dipole-dipole and hyperfine interaction between the nuclear spins, which is predicted to be $\gtrsim 10-100\mu s$, is much larger than the timescale for electron spin dynamics considered here (up to $1\mu s$) (see chapter 2). We also assume that the exchange interaction between the two spins is negligible during the manipulation, which is appropriate due to the small tunnel coupling and the finite detuning when the microwave bursts are applied.

From the Hamiltonian we can numerically obtain the time evolution of the two spins during the RF burst. Assuming that the initial state is a statistical mixture of $|\uparrow\uparrow\rangle$ and $|\downarrow\downarrow\rangle$, we can compute the probability P_{odd} for having anti-parallel spins after the RF burst. This is also the probability that the left electron tunnels to the right dot during the read-out stage.

In the measurements of Fig. 4.6a, each data point is averaged over 15 s, which presumably represents an average over many nuclear configurations. We include this averaging over different nuclear configurations in the model by taking 2,000 samples from a gaussian distribution of nuclear fields (with standard deviation $\sigma = \sqrt{\langle B_N^2 \rangle}$), and computing the probability that an electron tunnels out after the RF burst. When the electron tunnels, one or more additional electrons, say m, may subsequently tunnel through before $\uparrow\uparrow$ or $\downarrow\downarrow$ is formed and the current is blocked again. Taking m and σ as fitting parameters, we find good agreement with the data for $m = 1.5$ and $\sigma = 2.2$ mT (solid black lines in Fig. 4.6a). This value for σ is comparable to that found in refs [88, 41]. The value found for m is different from what we would expect from a simple picture where all four spin states are formed with equal probability during the initialization stage, which would give $m = 1$. We do not understand this discrepancy, but it could be due to different tunnel rates for $\uparrow$ and $\downarrow$ or more subtle details in the transport cycle that we have neglected in the model [131].

4.6.2 Simplifications in the case $B_{\text{ext}} >> B_1, B_N$

In the Hamiltonian of eq. 4.1 all components of the nuclear field and the ac magnetic field were included. While this is suitable for numerical calculations, it is insightful to simplify the Hamiltonian. In the experiments reported here, it is $B_{\text{ext}} >> B_{\text{ac}}$ and $B_{\text{ext}} >> B_N$ allowing us to neglect components of the nuclear field and the ac magnetic field. In the following, we choose the external magnetic field to be along the $\hat{z}$-axis, $\mathbf{B}_{\text{ext}} = B_{\text{ext}}\hat{z}$, and the microwave field to be along the $\hat{x}$-axis, $\mathbf{B}_{\text{ac}} = 2B_1 \cos(\omega_{\text{ac}}t + \varphi)\hat{x}$. For an external magnetic field $B_{\text{ext}} \gg B_N$, we may neglect the transverse components $B_{N,x}$ and $B_{N,y}$ of the nuclear field (see also section 2.5), since owing to the fast precession of the electron spin only transverse components evolving on-resonant (as for instance the driving field) affect the electron spin dynamics noticeably. The effect of off-resonant transverse components averages out. Similarly, considering that $B_{\text{ext}} >> B_1$ we can apply the rotating wave approximation meaning

that we neglect the rotating component of the ac magnetic field, which precesses contrary to the electron spin (see section 4.2), and thus is also far off-resonant. Furthermore, the dynamics of the electron spins in the left and right dot ($i = L, R$) is most conveniently studied in a rotating frame evolving with the RF frequency ω_{ac} around the $\hat{z}$-axis. The Hamiltonian including the discussed simplifications in the rotating frame is given by ($i = \{L, R\})$[3]:

$$\hat{H}^i = \frac{\hbar}{2}(\Delta\omega + \delta\omega_i)\hat{\sigma}_z^i + \frac{\hbar}{2}\omega_R(\cos\varphi\hat{\sigma}_x^i - \sin\varphi\hat{\sigma}_y^i) \tag{4.2}$$

here $\hbar\Delta\omega = (g\mu_B B_{ext} - \hbar\omega_{ac})$, $\hbar\delta\omega_i = g\mu_B B_{N,z}^i$, $\hbar\omega_R = g\mu_B B_1$ and $\hat{\sigma}_{x,y,z}^i$ are the Pauli matrices acting on the left and right spin state respectively. $\hbar\Delta\omega$ is the offset of the RF field with respect to the electron spin precession. The z-component of the nuclear field adds to this offset by an amount $\delta\omega_i$. Note that the direction of the driving field B_1 in the rotating frame depends on the phase φ of the RF field in the laboratory. While this phase is uncontrolled and therefore meaningless for a single applied burst, it can be changed in between two subsequent RF bursts, thereby changing the rotation axis of the second rotation with respect to the first. This will be relevant for the Ramsey and spin echo experiments discussed below. Since however the phase of the first burst (and in the case of a Rabi oscillation that is the only one) is not relevant, we will use $\varphi = 0$ unless stated otherwise.

As discussed in the previous section the nuclear field and hence $\delta\omega_i$ is considered to be static during the electron spin evolution. The time evolution of the left and right spin during a microwave burst of length τ, for a static value of the nuclear field, is then given by the evolution operator $U_n^i = \exp\left(-i\hat{H}^i\tau/\hbar\right) = \exp\left(-i\mathbf{n}^i(\tau)\hat{\boldsymbol{\sigma}}/2\right)$ with $\mathbf{n}^i(\tau) = (\cos(\varphi)\omega_R\tau, -\sin(\varphi)\omega_R\tau, (\Delta\omega + \delta\omega_i)\tau)$. If the spin is initially in the state $|\chi\rangle$, it evolves into $U_n^i|\chi\rangle$ during the time τ. The evolution operator describes a rotation of the spin by an angle $|\mathbf{n}|$ around the axis $\mathbf{n}/|\mathbf{n}|$. On resonance, $\Delta\omega = 0$, we consider two special cases. For $\omega_R = 0$ the Hamiltonian in eq. 4.2 describes the free evolution of the electron spin. The evolution operator in this case is given by $U_{free}^i(\delta\omega_i\tau) = \exp\left(-i\delta\omega_i\tau\hat{\sigma}_z/2\right)$. The electron spin undergoes a precession around the nuclear field. During an RF burst the effect of the nuclear field is to tilt the rotation axis out of the $\hat{x}$-$\hat{y}$ plane, $\mathbf{n}^i(\tau) = (\omega_R\tau, 0, \delta\omega_i\tau)$ (here $\varphi = 0$). Effectively this causes an error in the rotation. For later purposes we introduce for this case the notation $U_\theta^i(\delta\omega_i)$ with $\theta = \omega_R\tau$ being the intended rotation angle around the $\hat{x}$-axis. By applying $U_\theta^i(\delta\omega_i)$ to a spin initialized in $|\uparrow\rangle$ we obtain the probability to find the spin in $|\downarrow\rangle$ after the RF burst[4].

$$P_\downarrow^i(\tau) = |\langle\downarrow|U_n^i|\uparrow\rangle|^2 = \omega_R^2/(\omega_R^2 + \delta\omega_i^2)\sin^2(\sqrt{\omega_R^2 + \delta\omega_i^2}\tau) \tag{4.3}$$

---

[3]See for instance [48] for transforming to the rotating frame.

[4]Note that the identity $\exp\left(-i\mathbf{n}^i(\tau)\hat{\boldsymbol{\sigma}}/2\right) = \mathbb{1}\cos(|\mathbf{n}|/2) - i\hat{\boldsymbol{\sigma}}\mathbf{n}/|\mathbf{n}|\sin(|\mathbf{n}|/2)$ is very convenient to evaluate the evolution-operator, here $\mathbb{1}$ is the $2x2$ unity matrix.

In [130] an analytical analysis employing the Rabi formula eq. 4.3 averaged over a gaussian distributed nuclear field shows that the observed coherent oscillations exhibit a $\pi/4$ phase shift and decay according to a power law. These predictions are verified by a careful fit of data similar as in Fig. 4.6 and are a direct consequence of the slow dynamics of the nuclei.

To obtain the average probability of finding the two electrons with anti-parallel spins, $<P_{\text{odd}}> = <P_\uparrow^L P_\downarrow^R + P_\downarrow^L P_\uparrow^R>$, after an RF burst is applied, we proceed as described above. The electrons are initialized in a statistical mixture of $|\uparrow\uparrow\rangle$ and $|\downarrow\downarrow\rangle$, however the resulting value of P_{odd} is equal for both initial states (only the spin parity is important). Therefore in the discussion we assume to initialize in $|\uparrow\uparrow\rangle$. Applying the time evolution operator described above, P_{odd} is computed and averaged for many static values of $\delta\omega_{\text{L,R}}$ drawn from a gaussian distribution with standard deviation $\tilde{\sigma} = g\mu_B\sigma_z/\hbar$, with $\sigma_z = \sqrt{<B_{\text{N,z}}^2>} = \sigma/\sqrt{3}$ the rms z-component of nuclear field. This yields $<P_{\text{odd}}>$. Assuming that the nuclear fields are independent in the two dots[5], we can write $<P_{\text{odd}}> = <P_\uparrow^L><P_\downarrow^R> + <P_\downarrow^L><P_\uparrow^R>$. This allows us to discuss some properties of the read-out based on spin blockade for detecting the induced single spin rotations. If the RF field amplitude in both dots and the width of the nuclear field distribution [6] are very similar in the two dots, the average probabilities in the two dots are approximately equal $<P_{\uparrow,\downarrow}^L> \approx <P_{\uparrow,\downarrow}^R>$. In this case $<P_{\text{odd}}>$ does not exceed 0.5, which reduces the contrast of the detection. In the case that the driving field is much larger than the nuclear field $\omega_R \gg \tilde{\sigma}$, the RF is most of the time on resonance with both spins, such that the single-spin rotations take place for both spins simultaneously. Since the current through the dots is proportional to P_{odd} we see that in this case, the current through the dots will oscillate twice as fast as when only one spin is excited. This can be understood by looking at the evolution of the two spins:

$$|\uparrow\uparrow\rangle \to \frac{|\uparrow\rangle + |\downarrow\rangle}{\sqrt{2}}\frac{|\uparrow\rangle + |\downarrow\rangle}{\sqrt{2}} \to |\downarrow\downarrow\rangle \to \frac{|\uparrow\rangle - |\downarrow\rangle}{\sqrt{2}}\frac{|\uparrow\rangle - |\downarrow\rangle}{\sqrt{2}} \to |\uparrow\uparrow\rangle$$

After a π-rotation the spins evolved into $|\downarrow\downarrow\rangle$, indeed yielding $<P_{\text{odd}}> = 0$. In the case $\omega_R \approx \tilde{\sigma}$ most of the time only one of the two spins is on-resonance. $<P_{\text{odd}}>$ resembles then directly the single spin probabilities $<P_\downarrow^{L,R}>$. Finally, we note that by assuming the RF field and the width of the nuclear field distribution to be exactly the same in both dots, we can further simplify to $<P_{\text{odd}}> = 2<P_\uparrow><P_\downarrow> = 2<P_\uparrow>(1 - <P_\uparrow>)$, where $<P_{\uparrow,\downarrow}^L> = <P_{\uparrow,\downarrow}^R> \equiv <P_{\uparrow,\downarrow}>$.

---

[5] Note that there are experimental situations in the spin blockade regime, where this might not be appropriate, because the nuclear fields in both dots become coupled through the dynamics of the two electron spin states, e.g. [96].

[6] A difference in the probability distribution of the nuclear field can arise, if the two dots are very different in size, since $B_N \propto A/\sqrt{N}$ (see section 2.5) with A the hyperfine constant and N the number of nuclei the electron wavefunction overlaps with. From the orbital splittings in the left and right dot we can however conclude that the two dots are similar in size, such that we consider this to be a small effect.

In the experiment, the excitation is on-resonance with only one spin at a time for most of the frozen nuclear configurations. Only at the highest powers ($\omega_R/\tilde{\sigma} > 1$), both spins may be excited simultaneously (but independently) and a small double Rabi frequency contribution is expected, although this could not be observed, owing to the measurement noise.

4.6.3 Implications for the quantum gate fidelity

Based on our knowledge of B_1 and the nuclear field fluctuations in the z-direction from the fits performed above we can estimate the angle over which the electron spins are rotated in the Bloch sphere. For the maximum ratio of $\omega_R/\tilde{\sigma} = 1.5$ reached in the present experiment, we achieve an average tip angle of $131°$ for an intended $180°$ rotation, corresponding to a fidelity of 73%. Apart from using a stronger B_1, the tip angle can be increased considerably by taking advantage of the long timescale of the nuclear field fluctuations. First, application of composite pulses, widely used in nuclear magnetic resonance to compensate for resonance off-sets [48], can greatly improve the quality of the rotations. A second solution comprises a measurement of the nuclear field (nuclear state narrowing [92, 95, 93]), so that the uncertainty in the nuclear field is reduced, and accurate rotations can be realized for as long as the nuclear field remains constant.

4.7 Free evolution decay

4.7.1 Measurement of the free evolution decay

We now use the coherent control which was described in the previous sections to measure the dephasing of the spin via a Ramsey-style experiment (see inset Fig. 4.7a and Fig. 2.8 in chapter 2). After a $\pi/2$-pulse that creates a coherent superposition between $|\uparrow\rangle$ and $|\downarrow\rangle$, the spin is allowed to freely evolve for a delay time τ (for now, we reason just in a single-spin picture). Subsequently, a $3\pi/2$-pulse is applied, with a variable phase. Ideally, if both RF pulses have the same phase (implying the same rotation axis in the rotating frame), the spin is rotated back to $|\uparrow\rangle$, and the system returns to spin blockade. If the phases of the two pulses are $180°$, the spin is rotated to $|\downarrow\rangle$, and the blockade is lifted. Fig. 4.7c shows, that for small τ, the signal indeed oscillates sinusoidally as a function of the relative phase between the two RF pulses, analogous to the well-known Ramsey interference fringes. We remark that this also demonstrates our ability to rotate the electron spin on the Bloch-sphere about any arbitrary axis, which provides universal control over the spin state. For large τ, however, the spin completely dephases during the delay time, and the fringes disappear (Fig. 4.7c). When the two pulses are applied with the same phase (Fig. 4.7a), we find that the signal saturates on a timescale of
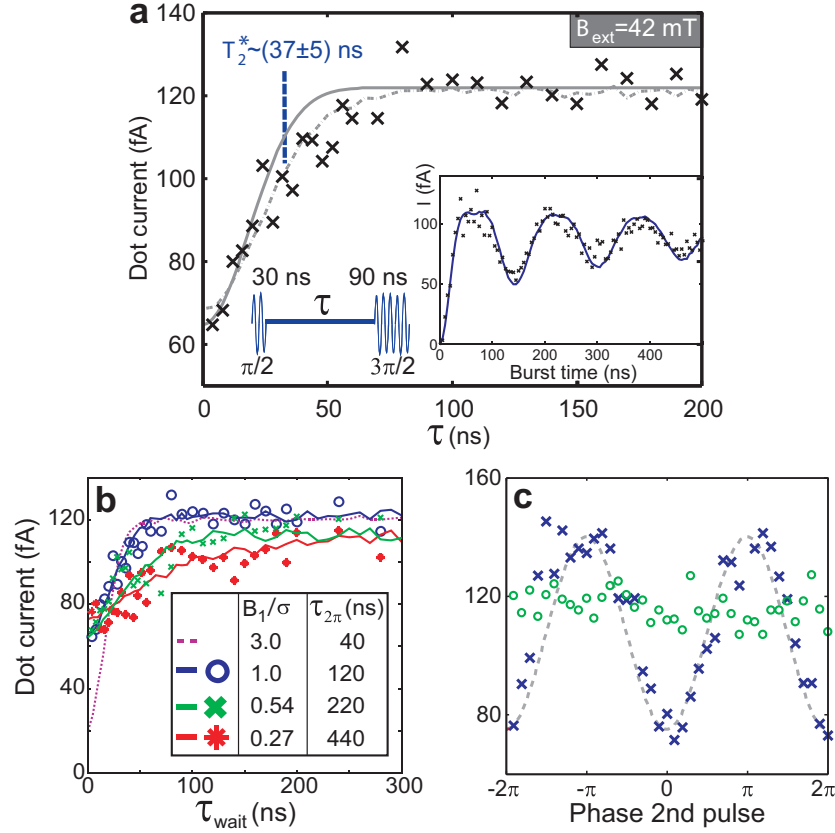
Figure 4.7: (a) Ramsey signal as a function of free-evolution time τ (each point averaged over 20 seconds at constant $B_{\text{ext}} = 42$ mT, $f_{\text{ac}} = 210$ MHz, $B_{\text{ac}} = 3$ mT). As shown in the inset, this gives a Rabi period $\tau_{2\pi}$ of 120 ns; see [33] for further details. In order to optimize the visibility of the decay, the second pulse is a $3\pi/2$-pulse instead of the usual $\pi/2$-pulse (the measured signal depends on P_{odd}, see main text). Solid line: Gaussian decay with $T_2^* = 30$ ns, corresponding to $\sigma = 1.5$ mT. Dotted line: numerically calculated current. First P_{odd} is computed taking $\sigma = 1.5$ mT, and then the current is derived as $I_{\text{dot}} = P_{\text{odd}}(m+1)80 + 23$ fA (m and offset due to background current obtained from fit). A current of 80 fA corresponds to one electron transition per 2 μs cycle, and m is the additional number of electrons that tunnels through the dot on average before the current is blocked again. Here, we find $m = 1.44$; the deviation from the expected $m = 1$ is not understood and discussed in [33]. (b) Measured and numerically calculated Ramsey signal for a wide range of driving fields. The simulations assume $\sigma = 1.5$ mT, and estimate the current as $P_{\text{odd}}(m+1)80 + 23$ fA ($m = 1.5$) for $\tau_{2\pi}$=40-220 ns, and as $P_{\text{odd}}(m+1)80 + 43$ fA ($m = 1.5$) for $\tau_{2\pi}$=440 ns. c) Ramsey signal as a function of the relative phase between the two RF bursts for $\tau = 10$ (crosses) and 150 ns (circles). Gray dashed line is a best fit of a cosine to the data.

$T_2^* \sim 37$ ns (obtained from a Gaussian fit, see below), which gives a measure of the dephasing time.

The observed Ramsey decay time is the result of the z-component of the nuclear field, $B_{N,z}$, which during the free evolution modifies the Larmor precession frequency of the electron spin by $\delta\omega = g\mu_B B_{N,z}/\hbar$. Averaging the precession about $B_{N,z}$ during time τ over a Gaussian distribution of nuclear fields (with width σ), gives a Gaussian coherence decay

$$\int_{-\infty}^{\infty} \frac{1}{\sqrt{2\pi}\sigma} e^{-B_{N,z}^2/2\sigma^2} \cos(g\mu_b B_{N,z}\tau/\hbar) dB_{N,z} = e^{-(\tau/T_2^*)^2}, \tag{4.4}$$

with $T_2^* = \sqrt{2}\hbar/g\mu_b\sigma \sim 30$ ns [84, 83] (assuming $\sigma = 1.5$ mT, extracted from the Rabi oscillations, see [130]). This decay is plotted in Fig. 4.7a (solid line). However, the observed Ramsey signal cannot be compared directly with this curve because we have to take into account that the nuclear field also introduces errors to the $\pi/2$ and $3\pi/2$-pulses.

4.7.2 Modeling of the free evolution decay

We can include these effects by a simulation of the spin dynamics, as described in section 4.6. At the end of the sequence, the two-spin state is given by

$$|\psi(\tau, \delta\omega_{L,R})\rangle = \tag{4.5}$$
$$U_{\frac{3\pi}{2}}^L(\delta\omega_L)U_{\frac{3\pi}{2}}^R(\delta\omega_R)U_{\text{free}}^L(\delta\omega_L, \tau)U_{\text{free}}^R(\delta\omega_R, \tau)U_{\frac{\pi}{2}}^L(\delta\omega_L)U_{\frac{\pi}{2}}^R(\delta\omega_R)|\uparrow\uparrow\rangle$$

Here, $U_\theta^{L,R}(\delta\omega_{L,R}))$ is the single spin time-evolution operator for an intented θ-rotation, as defined in section 4.6, resulting from the driving field and the offset $\delta\omega_{L,R} = g\mu_B B_{N,z}^{L,R}/\hbar$ caused by the z-component of the nuclear fields in the left and right dot. The operator $U_{\text{free}}^{L,R}(\delta\omega_{L,R}\tau)$ describes the single spin evolution during a time τ in the presence of the nuclear field only. We can then compute P_{odd} at the end of the pulse sequence, averaging over two independent Gaussian distributions of nuclear fields in the left and right dot:

$$<P_{\text{odd}}(\tau)> = \frac{1}{2\pi\sigma^2}\iint e^{-((B_{N,z}^R)^2+(B_{N,z}^L)^2)/2\sigma^2} P_{\text{odd}}(\tau, \delta\omega_{L,R}) \, dB_{N,z}^L dB_{N,z}^R \; ;$$
$$P_{\text{odd}}(\tau, \delta\omega_{L,R}) = |\langle\psi(\tau, \delta\omega_{L,R})|\uparrow\downarrow\rangle|^2 + |\langle\psi(\tau, \delta\omega_{L,R})|\downarrow\uparrow\rangle|^2 .$$

This numerically calculated $P_{\text{odd}}(\tau)$ is plotted in Fig. 4.7a (dotted line), after rescaling in order to convert P_{odd} to a current flow I_{dot} (see caption). We see that the predicted decay time is longer when the rotations are imperfect due to resonance offsets. This is more clearly visible in Fig. 4.7b, where the computed curves are shown together with Ramsey measurements for a wide range of driving fields. The experimentally observed Ramsey decay time is longer for smaller B_1, in good agreement with the numerical result. This effect can be understood by considering that a burst does not (much) rotate a spin when the nuclear field pushes the resonance condition outside the Lorentzian lineshape of the excitation with width B_1. If the spin

is not rotated into a superposition, it cannot dephase either. As a result, the cases when the nuclear field is larger than the excitation linewidth do not contribute to the measured coherence decay. The recorded dephasing time is thus artificially extended when long, low-power RF bursts are used ($\omega_R/\tilde{\sigma} \lesssim 1$). However, in Fig. 4.7a, this is only a small effect.

The fact that the rotations are inaccurate due to the nuclear field also determines the contrast of the fringe in Fig. 4.7c and the value it saturates to for $\tau \gg T_2^*$, which we discuss here briefly. For a single spin initialized into $|\uparrow\rangle$, in the case of perfect $\pi/2$ and $3\pi/2$ rotations, the average probability $<P_\uparrow>_\varphi$ oscillates between 1 and 0 for $\tau = 0$ as a function of the relative phase φ of the two pulses. For $\tau \gg T_2^*$ the average probability is given by $<P_\uparrow> = 0.5$ independent of φ. Accordingly, $<P_{odd}>$ oscillates between 0.5 and 0 for $\tau = 0$ and the fringe saturates to $<P_{odd}> = 0.5$ for $\tau \gg T_2^*$ (see section 4.6) and not to the average value of the fringe observed for $\tau \ll T_2^*$. For non-perfect pulses, $\omega_R/\tilde{\sigma} \lesssim 1$, the contrast of the fringe is reduced and the average probability does not take the value 0.5 for large τ. For a single spin the value of $<P_\uparrow>$ saturates to the average probability measured at $\tau = 0$: $<P_\uparrow(\tau \gg T_2^*)> = 1/2\pi \int_0^{2\pi} <P_\uparrow(\tau = 0)>_{\varphi'} d\varphi'$. The value differs from 0.5, because the fringe at $\tau = 0$ does not oscillate symmetrically around 0.5. This is related to the fact that the combined fidelity of a $\pi/2$ and a $3\pi/2$ rotation which are both subject to the same offset error around the e. g. $\hat{x}$-axis is higher than that of a $\pi/2$ rotation around $\hat{x}$ followed by a $3\pi/2$ rotation around $-\hat{x}$ (see e.g. [48] for a discussion of two subsequent π-rotations). Here this causes $<P_\uparrow(\tau \gg T_2^*)> > 0.5$. Another way to see this, invokes the same argument which was used to explain the artificially extended Ramsey decay time for low power RF bursts (see above). For the cases that the nuclear field is larger than the excitation linewidth, the RF bursts fail to rotate the spin, leaving the spin in the initial state. This causes the probability to find the spin in the initial state after the sequence, $<P_\uparrow>$, to saturate to a value higher than 0.5 at $\tau \gg T_2^*$. Since $<P_{odd}> \approx 2<P_\uparrow>(1 - <P_\uparrow>)$ we see that $<P_{odd}>$ will saturate to a value smaller than 0.5, which is the maximum value of the fringe for $\tau \ll T_2^*$. This can be seen in Fig. 4.7c.

4.8 Measurement of the spin echo decay

We now test to what extent the electron spin dephasing is reversible using a spin-echo pulse. The pulse sequence we apply is depicted in the inset of Fig. 4.8a, and the measured signal as a function of the total free-evolution time $\tau_1 + \tau_2$ is shown in the main panel of Fig. 4.8a. We see immediately that the spin-echo decay time, $T_{2,echo}$, is much longer than the dephasing time, T_2^*. This is also clear from the data in Fig. 4.8c, which is taken in a similar fashion as the Ramsey data in Fig. 4.7c, but now with an echo pulse applied halfway through the delay time. Whereas the fringes were fully suppressed for a 150 ns delay time without an echo pulse, they
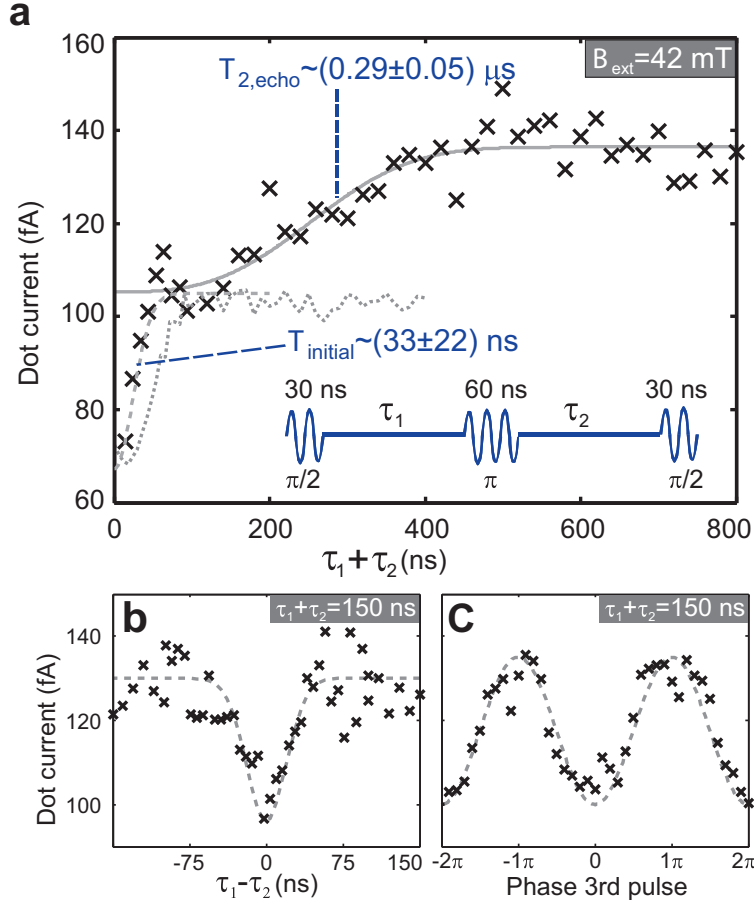
Figure 4.8: (color online) a) Spin-echo signal as a function of total free-evolution time $\tau_1 + \tau_2$ (each point averaged over 20 seconds at constant $B_{ext} = 42$ mT, $f_{ac} = 210$ MHz, $B_{ac} = 3$ mT). Dashed line: best fit of a Gaussian curve to the data in the range $\tau_1 + \tau_2 = 0 - 100$ ns. Solid line: best fit of $e^{-((\tau_1+\tau_2)/T_{2,echo})^3}$ to the data in the range $\tau_1 + \tau_2 = 100 - 800$ ns. Dotted line: numerically calculated dot current $P_{odd}(m+1)80 + 25$ fA, taking $\sigma = 1.5$ mT in both dots and $m = 1.83$. The scatter in the data points is not due to the noise of the measurement electronics (noise floor about 5 fA), but is caused by incomplete averaging over the statistical nuclear field. b) Spin-echo signal as a function of $\tau_1 - \tau_2$. Dashed line: best fit of a Gaussian curve to the data. c) Spin-echo signal for $\tau_1 + \tau_2 = 150$ ns as a function of the relative phase between the first two and third pulse. Dashed line is the best fit of a cosine to the data.

are still clearly visible after 150 ns if an echo pulse is used. As a further check, we measured the echo signal as a function of $\tau_1 - \tau_2$ (Fig. 4.8b). As expected, the echo is optimal for $\tau_1 = \tau_2$ and deteriorates as $|\tau_1 - \tau_2|$ is increased. The dip in the data at $\tau_1 - \tau_2 = 0$ has a half width of ~27 ns, similar to the observed T_2^*.

Upon closer inspection, the spin-echo signal in Fig. 4.8a reveals two types of

decay. First, there is an initial decay with a typical timescale of 33 ns (obtained from a Gaussian fit), which is comparable to the observed Ramsey decay time when using the same B_{ac}. This fast initial decay occurs because the echo pulse itself is also affected by the nuclear field. As a result it fails to reverse the electron spin time evolution for part of the nuclear spin configurations, in which case the fast dephasing still occurs, similar as in the Ramsey decay. To confirm this, we calculate numerically the echo signal, including the effect of resonance offsets from the nuclear fields, similar as in the simulations of the Ramsey experiment. We find reasonable agreement of the data with the numerical curve (dotted line in Fig. 4.8a), regarding both the decay time and the amplitude.
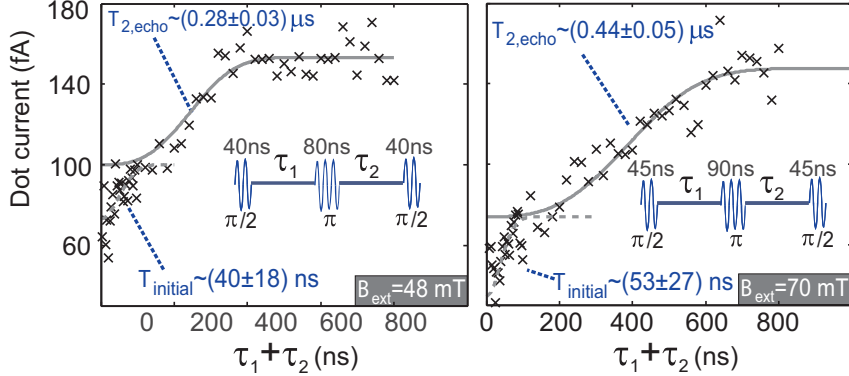
Figure 4.9: (a) Spin-echo signal at $B_{\mathrm{ext}} = 48$ mT ($f_{\mathrm{ac}} = 280$ MHz) and (b) 70 mT ($f_{\mathrm{ac}} = 380$ MHz). Pulse sequence depicted in the insets. Solid and dashed lines are best fits to the data as in Fig. 4.8a.

The slower decay in Fig. 4.8a corresponds to the loss of coherence that cannot be reversed by a perfect echo pulse. We extract the spin-echo coherence time $T_{2,\mathrm{echo}}$ from a best fit of $a + be^{-((\tau_1+\tau_2)/T_{2,\mathrm{echo}})^d}$ to the data ($a, b, T_{2,\mathrm{echo}}$ are fit parameters and d is kept fixed) and find $T_{2,\mathrm{echo}} = (290 \pm 50)$ ns at $B_{\mathrm{ext}}=42$ mT for $d = 3$ (see Fig. 4.8a, solid line). We note that the precise functional form of the decay is hard to extract from the data, but we find similar decay times reasonable fits for the range $d = 2 - 4$.

Measurements at higher B_{ext} are shown in Fig. 4.9a,b. Here, experiments were only possible by decreasing the driving field and as expected, we thus find a longer initial decay time, similar as seen in Fig. 4.7b for Ramsey measurements. The longer decay time from which we extract $T_{2,\mathrm{echo}}$ tends to increase with field, up to 0.44 μs at $B_{\mathrm{ext}}=70$ mT. This is roughly in line with the spin echo decay time of 1.2 μs observed for two-electron spin states at $B_{\mathrm{ext}}=100$ mT [32].

The field-dependent value for $T_{2,\mathrm{echo}}$ we find is more than a factor of 10 longer than T_2^*, which is made possible by the long correlation time of the nuclear spin bath. We now examine what mechanism limits $T_{2,\mathrm{echo}}$. The z-component of the nuclear

field can change due to the spin-conserving flip-flop terms $H_{ff} = \frac{1}{2}(S_+ h_- + S_- h_+)$ in the hyperfine Hamiltonian $\mathbf{S} \cdot \mathbf{h}$, and due to the dipole-dipole interaction between neighbouring nuclear spins. Direct electron-nuclear flip-flop processes governed by H_{ff} are negligible at the magnetic fields used in this experiment, because of the energy mismatch between the electron and nuclear spin Zeeman splitting. However, the energy-conserving higher-order contributions from H_{ff} can lead to flip-flop processes between two non-neighboring nuclear spins mediated by virtual flip-flops with the electron spin [38, 102, 104, 103, 114]. It is predicted that this hyperfine-mediated nuclear spin dynamics can lead to a field dependent free-evolution decay of about 1-100 μs for the field range 1-10 T [104, 103, 114]. Interestingly, some theoretical studies [102, 103] have predicted that this type of nuclear dynamics is reversible (at sufficiently high field) by an echo-pulse applied to the electron spin. The coherence decay time due to the second possible decoherence source, namely the dipole-dipole interaction, is theoretically predicted to be 10-100 μs [107, 103], independent of magnetic field (once B_{ext} is larger than ~ 0.1 mT, which is the dipole field of one nucleus seen by its neighbor).

Also decoherence mechanisms other than the interaction with the nuclear spin bath must be considered. One possibility is spin-exchange with electrons in the reservoir via higher order tunneling processes. However, we expect that the typical timescale of this process is very long because (during the manipulation stage) the energy required for one of the electrons to be promoted to a reservoir ($> 100 \, \mu$eV) is much larger than the tunnel rate ($< 0.1 \, \mu$eV). In principle, the exchange coupling between the spins in the two quantum dots could spoil the spin-echo effect, but we estimate this coupling to be much smaller than $1/T_{2,echo}$. Altogether, the most likely limitation to the observed $T_{2,echo}$ is hyperfine-mediated flip-flops between any two nuclear spins.

4.9   Conclusions

To conclude, we have performed time-resolved measurements of the dephasing of a single electron spin in a quantum dot caused by the interaction with a quasi-static nuclear spin bath. We have largely reversed this dephasing by the application of a spin-echo technique. The echo pulse extends the decay time of the electron spin coherence by more than a factor of ten. We obtain a $T_{2,echo}$ of 0.29 μs and 0.44 μs at magnetic fields of 42 and 70 mT respectively. While even longer coherence times are expected at higher magnetic fields and multiple pulse sequences [132, 133], the observed decay times are already sufficiently long for further exploration of electron spins in quantum dots as qubit systems.

This work has been performed in collaboration with F. H. L. Koppens, C. Buizert,

K. J. Tielrooij, I. T. Vink, T. Meunier, L. P. Kouwenhoven and L. M. K. Vandersypen.

Chapter 5

Locking electron spins into magnetic resonance by electron-nuclear feedback

Quantum information processing requires accurate coherent control of quantum mechanical two-level systems but is hampered by their coupling to an uncontrolled environment. For electron spins in III-V quantum dots, the random environment is mostly given by the nuclear spins in the quantum dot host material; they collectively act on the electron spin through the hyperfine interaction, much like a random magnetic field. Here we show that the same hyperfine interaction can be harnessed such that partial control of the normally uncontrolled environment becomes possible. In particular, we observe that the electron spin resonance frequency remains locked to the frequency of an applied microwave magnetic field, even when the external magnetic field or the excitation frequency are changed. The nuclear field thereby adjusts itself such that the electron spin resonance condition remains satisfied. General theoretical arguments indicate that this spin resonance locking is accompanied by a significant reduction of the randomness in the nuclear field.

5.1 Introduction

Individual electron spins in semiconductor quantum dots are attractive for applications in quantum information processing, as demonstrated by the considerable progress that has been made towards this goal [90]. Nearly all experiments in this direction have been realized in III-V materials where all isotopes carry nuclear spin. In thermodynamic equilibrium, the nuclear spins in the quantum dot host material are randomly oriented, even at dilution refrigerator temperatures and in magnetic fields of a few Tesla. An electron spin confined in the quantum dot interacts via the hyperfine coupling with $N \sim 10^6$ nuclear spins and as a result experiences a random nuclear field B_N. This random nuclear field is sampled from a distribution with a root mean square width $\propto IA/g\mu_B\sqrt{N}$, where g is the electron g-factor, μ_B the Bohr magneton, I the nuclear spin and A the hyperfine coupling constant ($IA \approx 135\mu$eV in GaAs). Measurements typically give a width of ~ 1 mT. As a result, we lose track of the phase of a freely evolving electron spin within a time T_2^* of a few tens of nanoseconds [84, 83, 32, 134, 115]. Similarly, when the spin evolves under an oscillating driving field, the nuclear field leads to a random offset in the resonance condition which has a comparable amplitude to presently achievable driving fields. This results in poorly controlled spin rotations [33].

It is therefore of great importance to develop the ability to control and manipulate the nuclear field with great precision. In particular, it would be highly desirable to set the nuclear field to a narrow distribution of values at the start of every experiment [135, 92, 95, 93]. This would immediately reduce the rapid dephasing, and the electron spin would lose phase coherence only from the slow subsequent evolution of the nuclear field, giving a predicted spin coherence time of $1 - 10\mu$s [107, 38]. Such narrowing has been achieved in an ensemble of self-assembled quantum dots by synchronizing the precessing spins with a series of laser pulses [136]. Also, the spread of the difference in nuclear fields in two neighbouring quantum dots was reduced via a gate voltage controlled pumping cycle, giving a 70-fold increase in the T_2^* for states in the two-electron $m_z = 0$ subspace [137].

Here we exploit electron-nuclear feedback in order to control and manipulate the nuclear fields in two coupled quantum dots during continuous wave (CW) driving of the electron spins in the dots. We observe that each nuclear field adjusts itself such that the electron spin in the corresponding quantum dot remains in resonance with a fixed driving frequency, even when we sweep the external magnetic field away from the nominal resonance condition. Similarly, the electron spin resonance frequency remains locked to the excitation frequency when the excitation frequency is swept back and forth. These distinctive features set our observations apart from the many previous observations of dynamic nuclear spin polarization in quantum dots, both in transport [128, 41, 138, 139, 140] and optical measurements [141, 142, 143]. We investigate the origin of this feedback by studying its dependence on the amplitudes of the applied *ac* magnetic and electric fields and on the sweep rates. Furthermore,

we show theoretically that the spin resonance locking must be accompanied by a narrowing of the nuclear field distribution, in the present experiment by more than a factor of 10.

The measurements are performed on an electrostatically defined double quantum dot tuned to the Pauli spin blockade regime [121], with effectively one excess electron on each dot (the actual electron number is small but unknown). We measure the dc current through the double quantum dot device, which depends on the spin states of the electrons residing on the dots. When the two electrons have parallel spins, the electron flow through the dots is blocked. When one of the spins is flipped, the spin blockade is lifted and electrons flow through the two dots until the system returns to a state with parallel spins on the two dots. As previously demonstrated [33], it is possible to flip the electron spins via magnetic resonance, by ac excitation of an on-chip wire which generates an oscillating magnetic field at the dots: when the excitation frequency, f, matches the electron spin resonance (ESR) frequency, $|g|\mu_B B_0/h$, a finite current flows through the device. Here h is Planck's constant, and B_0 the external magnetic field. In addition, current can flow at zero magnetic field, where the electron spins can flip-flop with the nuclear spins in the substrate [41]. We use this zero-field feature to determine and adjust for small magnetic field offsets present in our setup. The zero-field peak and the ESR response are seen in current measurements under CW excitation with increasing excitation frequency at fixed magnetic fields (Fig. 5.1a), similar to the data published in Ref. [33], and taken on the same device but in a different cooldown.

5.2 Locking to the spin resonance condition

Surprisingly, when we reverse the sweep direction, a distinctly different behavior is observed over a wide range of dot settings (see section 5.9.1 for details of the tuning parameters). Current starts flowing when the driving frequency hits the spin resonance frequency but *remains* high even as the frequency is swept well below the nominal resonance condition (Fig. 5.1b). The fact that the current remains high implies that the electron spin is still on resonance with the excitation frequency, and that an effective field, B_{eff}, counteracts the external magnetic field B_0: $hf = |g|\mu_B(B_0 + B_{\mathrm{eff}})$. From the fact that the current is strongly reduced when we simultaneously excite any of the three nuclear spin species in the substrate (data not shown), we conclude that this effective field is created by dynamical nuclear spin polarization, i.e. $B_{\mathrm{eff}} = B_N$. This nuclear field builds up exactly at the right rate in order to keep the electron spin in resonance with the changing driving frequency, which implies there is a built-in electron-nuclear feedback mechanism.

Similar dragging of the resonance is observed when sweeping the magnetic field for a fixed excitation frequency. In Fig. 5.2a we show typical data obtained from measurements where the magnetic field is swept from -33 mT to 97 mT (right
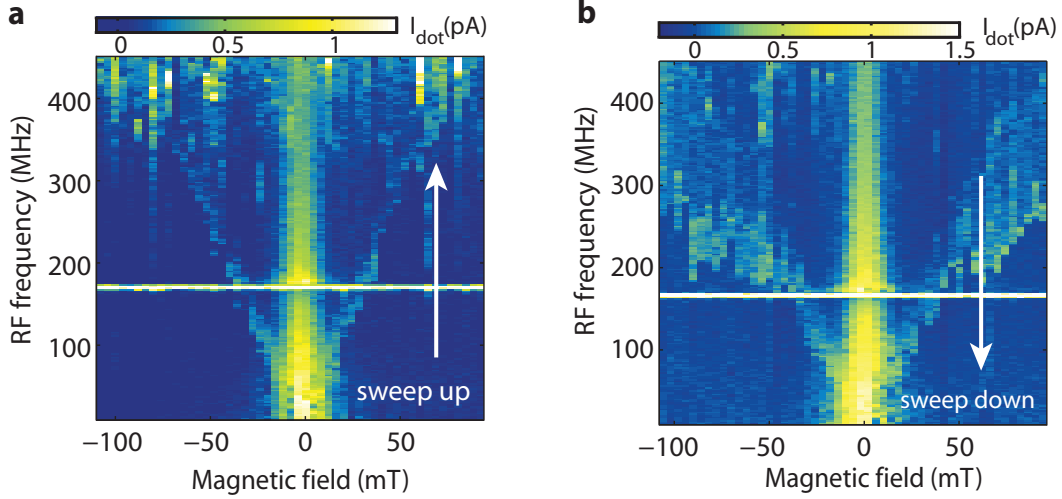
Figure 5.1: Electron spin resonance locking during frequency sweeps. a, Current through the double dot (colorscale) subject to CW magnetic excitation, when sweeping the frequency up at fixed magnetic fields. The bright fork indicates the position of the ESR condition. **b**, Similar to **a** but sweeping the frequency down. The ESR frequency remains locked to the excitation frequency when the excitation frequency is swept past the nominal resonance condition. The feature at 180 MHz is due to a resonance in the transmission line in our dilution refrigerator.

vertical axis) in about 25 seconds. We first see the zero-field peak, as expected, and next the current jumps up around $B_0 = 67$ mT, which is slightly below the nominal resonance condition ($f = 400$ MHz, $|g| = 0.36$). The current remains high as the field is swept further to 97 mT, which is well outside the ESR linewidth in the absence of feedback (see Fig. 5.4b). Similar to the case of the frequency sweeps, a nuclear field builds up exactly in such a way as to maintain the ESR frequency locked to the excitation frequency. When we subsequently keep the field fixed at 97 mT, we observe that the electron spin can remain locked into magnetic resonance for well over a minute.

It is even possible to drag the nuclear field back and forth under fixed-frequency excitation. In Figs. 5.2b and 5.2c, B_0 is ramped up from -33 mT to 117 mT, and is subsequently swept back and forth between 117 mT and 87 mT in a triangular pattern. The current again jumps up as we sweep through resonance and subsequently remains high independent of the sweep direction, implying that after the system is locked on resonance the sign of dB_0/dt (df/dt) does not matter as long as the condition $B_0 > B^{res} = hf/g\mu_B$ ($f < f^{res} = g\mu_B B_0/h$) remains fulfilled. In Fig. 5.2c the resonance is lost after approximately 1 minute, whereas in Fig. 5.2b the spin remains locked on resonance during the entire experiment (about 2 minutes).

5.3 Locking characteristics
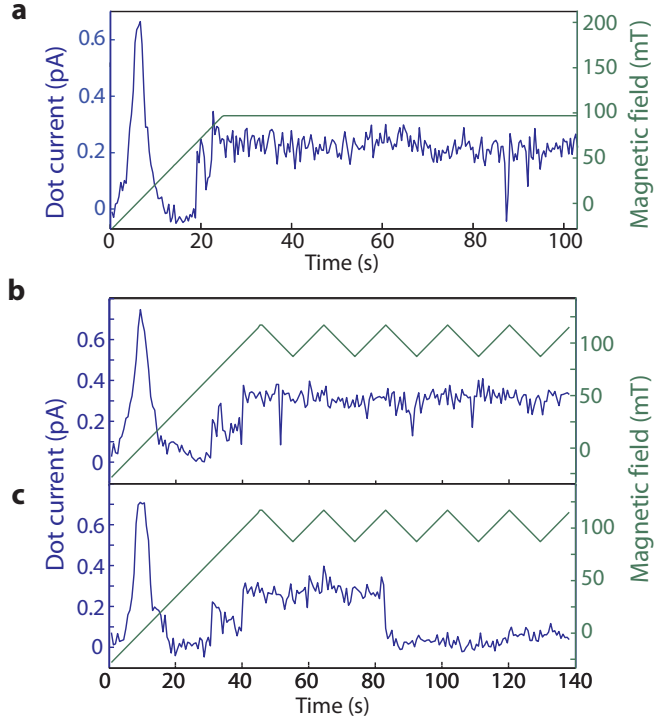
Figure 5.2: Electron spin resonance locking during magnetic field sweeps. a, Current through the double dot as a function of time, while the magnetic field is first ramped up (right axis) and subsequently held fixed, under CW excitation ($f = 400$ MHz). **b-c**, Two current traces similar to **a**, but after the magnetic field is ramped up, it is repeatedly swept down and back up over a 30 mT range (right axis). After the ESR condition is first met, the electron spin remains locked into magnetic resonance for up to two minutes, even though the resonance condition is shifted back and forth.

These remarkable observations of spin resonance locking due to electron-nuclear feedback are characterized by a number of common features. First, the current jumps up abruptly, in many cases in less than a few 100 ms, at a field value that varies over 10-30 mT around the nominal resonance condition (see the green circles in Fig. 5.4 below). This is a further indication that the system is actively pulled into resonance – without feedback a current peak with smooth flanks and a width of a few mT is expected [144]. Second, the resonance dragging generally occurs only for fields larger than the nominal resonant field, or for frequencies lower than the nominal resonance frequency. This is opposite to the case of the usual Overhauser effect, as discussed further below. Third, the initial current jump is usually followed by a second current jump, before the current drops back to zero. A possible explanation for this double step is that the first current plateau corresponds to a situation where

both dots are on-resonance, and that only one dot remains on resonance after the second jump (see section 5.9.2 for a discussion of the current levels). When the resonance is lost in this last dot too, the current returns to zero.

5.4   Pump-probe measurements
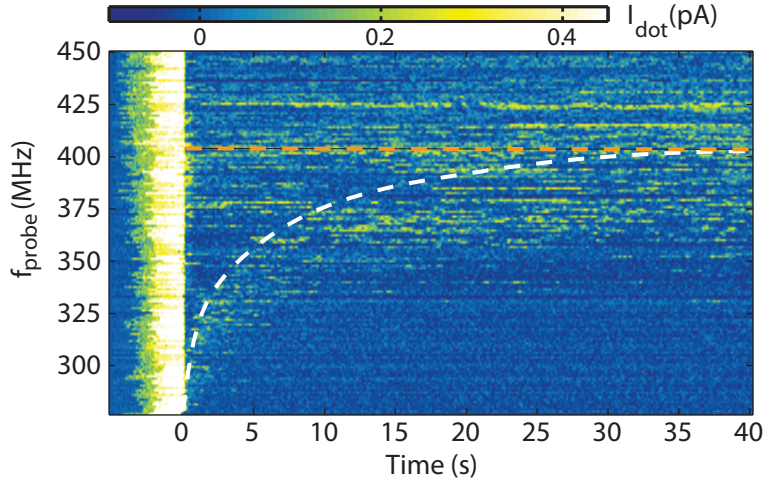
Figure 5.3: Pump-probe measurement of the relaxation of the nuclear spin polarization. At a fixed magnetic field of $B_0 = 80$ mT, we apply CW excitation ($P = -13$ dBm) sweeping the frequency from 500 MHz to 276 MHz at 43 MHz/s, and dragging the nuclear field along (pump phase). Next we turn off the CW excitation and apply 140 ns microwave bursts every 2 μs at frequency f_{probe} throughout a 40 s probe phase. This pump-probe cycle is repeated for different probe frequencies, 277 MHz $\leq f_{probe} \leq$ 450 MHz (see vertical axis). The horizontal axis indicates the time t into the probe phase; the data for $t < 0$ correspond to the pump phase. In the pump phase, the current (plotted in colorscale) jumps up twice, reaching the highest current plateau (traces where the resonance is lost by the end of the pump phase are left out). When the frequency is switched to f_{probe} at $t = 0$, the current drops to zero since the excitation is now off-resonance. As the nuclear spin polarization relaxes, the resonance condition $|g|\,\mu_B(B_0 + B_N(t)) = hf_{probe}$ will be fulfilled at some point in time at which the current sets on again. Varying f_{probe} reveals then the nuclear spin relaxation as indicated by the white dashed line (guide to the eye) marking the onset of the current, where the probe pulses have had the least effect on the nuclear polarization. The orange dashed line marks an additional signal at the nominal resonance frequency already present from the start of the probe phase.

This interpretation of the double current step is supported by pump-probe measurements shown in Fig. 5.3. Starting from the second current plateau with $B_0 = 80$ mT and $f = 276$ MHz, we switch off the CW excitation and probe the position of the ESR frequency as the nuclear field returns to equilibrium (we use short bursts

for probing in order to minimize feedback during the probe phase). We see that the ESR frequency returns to its nominal value, slightly above 400 MHz, within 20 seconds, corresponding to the relaxation time of the local nuclear spin polarization (white dashed line). This signal must originate from a dot that is still locked into magnetic resonance at the end of the pump phase. In addition, we see a response at the nominal resonance frequency already from the start of the probe phase (red dashed line). Presumably, this signal arises from the other dot, where the resonance was lost during the pump phase and the nuclear field has (nearly) relaxed by the time the probe phase starts. We note that the signal in the pump phase is much stronger than the signal in the probe phase, since during the pump phase a strong (-13dBm) continuous microwave excitation is applied, whereas during the probe phase, the excitation is applied only in bursts with a duty cycle of less than 10%. Even though the excitation is applied only in bursts, the electron spin sometimes remains locked into resonance during the probe phase as well, stalling the nuclear spin relaxation.

5.5 Dependence on sweep and excitation parameters

In order to better understand the locking mechanism, we study how far the nuclear spin polarization can be dragged by performing magnetic field sweeps as a function of the applied microwave power, the microwave frequency and the magnetic field sweep rate. Specifically, we repeatedly ramp the magnetic field from -28 mT upwards and record (i) the field at which the current jumps up (circle in Fig. 5.4a), (ii) the field where the current jumps to a still higher value (diamond), and (iii) the field where the current drops back to zero (cross). The resulting data points are shown as scatter plots in Figs. 5.4c-e, using the same symbols.

The first current jump always occurs as the nominal resonant field (in the absence of feedback) is first approached. The second jump and the current drop occur at fields that increase with driving amplitude over the range that we could explore (for still stronger driving, spin blockade was lifted by photon assisted tunneling so that we lost sensitivity to spin flips). For the highest powers accessible in the experiment, the electron spin is maintained on resonance over a magnetic field range of a few 100 mT. As the power is reduced, the locking effect vanishes. Furthermore, the field that can be reached before the resonance is lost, increases with excitation frequency. Earlier measurements on the same sample showed that along with the *ac* magnetic field an *ac* electric field is generated whose amplitude for a fixed power (and magnetic field amplitude) increases roughly linearly with the excitation frequency [33]. The dependence on driving frequency can therefore also be interpreted as stronger locking for higher electric field amplitudes. Finally, we see that for higher magnetic field sweep rates the resonance is lost at lower fields.
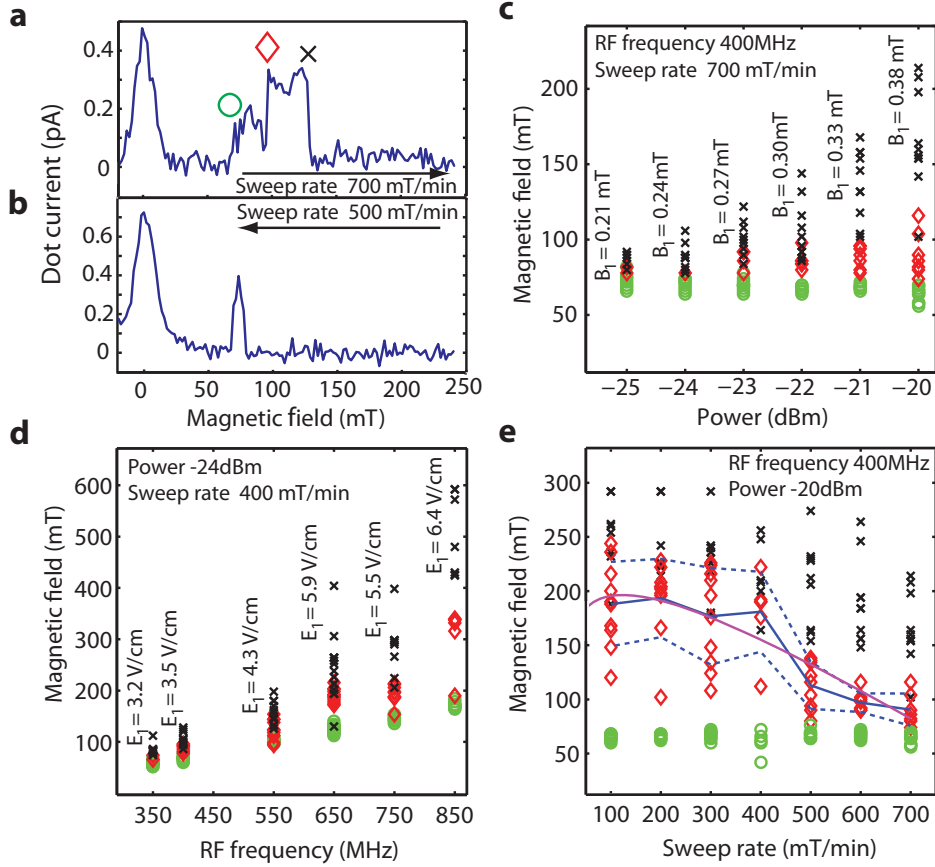
Figure 5.4: ESR locking dependence on excitation power, frequency and sweep rate. a, Current through the double dot as the magnetic field is swept up ($f = 400$ MHz). **b**, Similar to **a** but now B_0 is swept down. No dragging effects are observed; the narrow peak gives the position of the nominal resonant field. **c**, Scatter plot of the switching fields as indicated by the symbols in **a**, as a function of the power applied to the on-chip wire, obtained from multiple sweeps as in **a**. The corresponding resonant magnetic field amplitude B_1 at the dot is given as well. **d**, Scatter plot similar to **c**, as a function of f. The electric field amplitude E_1 estimated from photon assisted tunneling generally increases with f, and is shown in the figure. **e**, Scatter plot similar to **c** as a function of magnetic field sweep rate. Blue lines: average and standard deviation of the magnetic fields where the second current jump is observed. Purple curve: fit of these average values with a theoretical model (see section 5.9.3). We note that there is no build-up of B_N in the limit of zero sweep rate, so the predicted switching field first increases with sweep rate, before decreasing.

5.6 A phenomenological model

A few basic considerations give insight into the mechanism behind our observations. To describe the nuclear spin dynamics we construct a phenomenological model di-
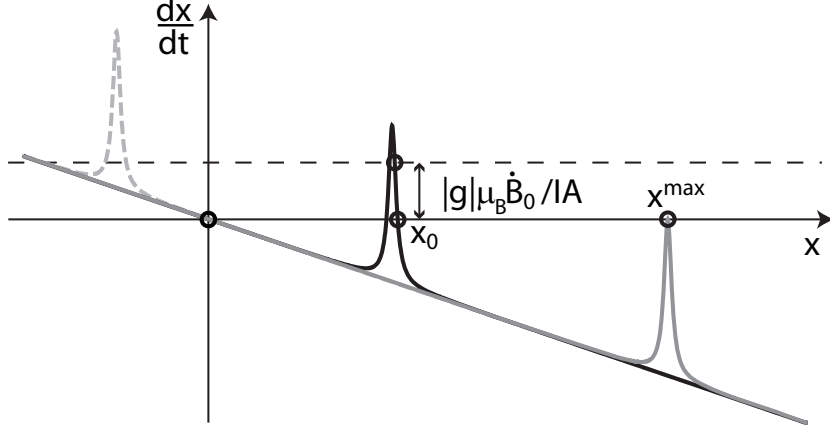
Figure 5.5: Nuclear spin pumping curves. The nuclear spin polarization rate for one dot (dx/dt) is shown as a function of its polarization x for three different values of x^{res} (the dashed gray, black and solid gray curve). The overall negative slope is due to nuclear spin relaxation and the resonant peak is due to the external driving. Circles indicate stable points in nuclear spin polarization and are found whenever the curve crosses the x-axis with a negative slope. During a field (or frequency) sweep, a dynamic equilibrium is reached where $dx/dt = |g|\mu_B \dot{B}_0/IA$.

rectly from the experimental data. For clarity we discuss the nuclear spin dynamics in one of the dots; the results for two dots are qualitatively similar [145] and the fact that the tunnel coupling is small (smaller than the typical nuclear field in equilibrium) justifies considering the electron spins as independent. First we describe in general terms a mechanism which explains the observed locking and the dragging of the nuclear polarization, and afterwards we turn to the origin of this mechanism.

The nuclear spin polarization x in the dot is felt as an effective magnetic field by the electron spin: $IAx = g\mu_B B_N$ (x is defined as dimensionless $-1 \leq x \leq 1$; in our experiments, $|x| \ll 1$). In the absence of any excitation, the polarization naturally relaxes to zero on a characteristic time scale τ_n, due to nuclear spin diffusion. However, the nuclear spin dynamics will be altered by hyperfine-mediated electron-nuclear flip-flops when the electron spins are brought out of equilibrium [128, 41, 138]. In the spin blockade regime at finite B_0, such non-equilibrium dynamics is induced when the electron spins are resonantly excited by an external microwave magnetic or electric field. This occurs when the nuclear polarization is close to x^{res} with $IAx^{\mathrm{res}} = g\mu_B B_N^{\mathrm{res}} = |g|\mu_B B_0 - hf$ such that the electron spin is in resonance with the excitation. Regardless of the relevant microscopic processes, we thus expect in very general terms a polarization-dependent pump rate Γ_p, which is non-zero only close to the resonance condition. The dynamics of the polarization in the dot is then described by

$$\frac{dx}{dt} = \Gamma_p(x - x^{res}) - \frac{1}{\tau_n}x, \tag{5.1}$$

where Γ_p peaks when its argument $(x - x^{res})$ is 0. Fig. 5.5 qualitatively visualizes Eq. (5.1) in the form of a pumping curve for three different values of x^{res}, where we have (for now arbitrarily) chosen the resonant contribution to be positive. From the figure we can see that stable points of nuclear polarization occur when dx/dt crosses zero with a negative slope: if x is higher (lower) than the stable polarization x_0, dx/dt is negative (positive) and x gets pushed back to x_0. Due to nuclear spin relaxation there is almost always a stable point at $x = 0$. Depending on the particular shape of Γ_p, hence on the specific experimental regime, there can be one or more additional stable points [145, 146, 147].

We now interpret the field sweep experiments within this simple picture. First, given that the current remains high in field sweeps, a stable point must exist close to resonance, in agreement with our expectation of a resonant peak in Γ_p. Next, since dragging is generally observed only for $x > 0$, Γ_p must be positive, as in Fig. 5.5. Finally, from the maximum nuclear field B_N^{max} that can be achieved by dragging, we can estimate the height of Γ_p: when the maximum of the pumping peak falls below zero, i.e. when nuclear spin relaxation exceeds the resonant pumping, the stable point at $x > 0$ disappears and B_N relaxes to zero (Fig. 5.5, red curve).

During actual field sweeps, the resonance is lost at fields below B_N^{max}: since a dynamic equilibrium is reached when $dx/dt = |g|\mu_B \dot{B}_0/IA$ instead of $dx/dt = 0$, the stable operating point moves up the pumping curve (see Fig. 5.5) and disappears when the sweep rate exceeds the maximum of the pumping peak. In practice we will lose the resonance even earlier, because intrinsic nuclear field fluctuations can drive the nuclear field across the maximum. We model the average switching field taking into account such fluctuations by assuming an exponential dependence of the switching rate on the "barrier height". The result is illustrated in Fig. 5.4e. This combined picture captures very well the experimental observation that for higher sweep rates the resonance is more easily lost, but not at exactly the same field every time.

5.7 Relevant microscopic processes

We next turn to the nature of the extrinsic pumping process, Γ_p and subsequently sketch the findings of [145] which are closely related to the observations reported here. Fig. 5.6 summarizes relevant microscopic processes affecting the electron and nuclear spin polarization. Excitation of the electron spin by magnetic resonance (Fig. 5.6a) combined with relaxation back from ↓ to ↑ by flip-flopping with the nuclear spins (Fig. 5.6b2) creates a nuclear spin polarization in the direction of the electron spin excited state and therefore gives rise to the usual Overhauser effect.
[1] However in the experiment described here the stable points generally occur for

---

[1]Let us clarify the term usual Overhauser effect. In his original work Overhauser [148] described a build-up of nuclear spin polarization resulting from non-equilibrium electron spin dynamics
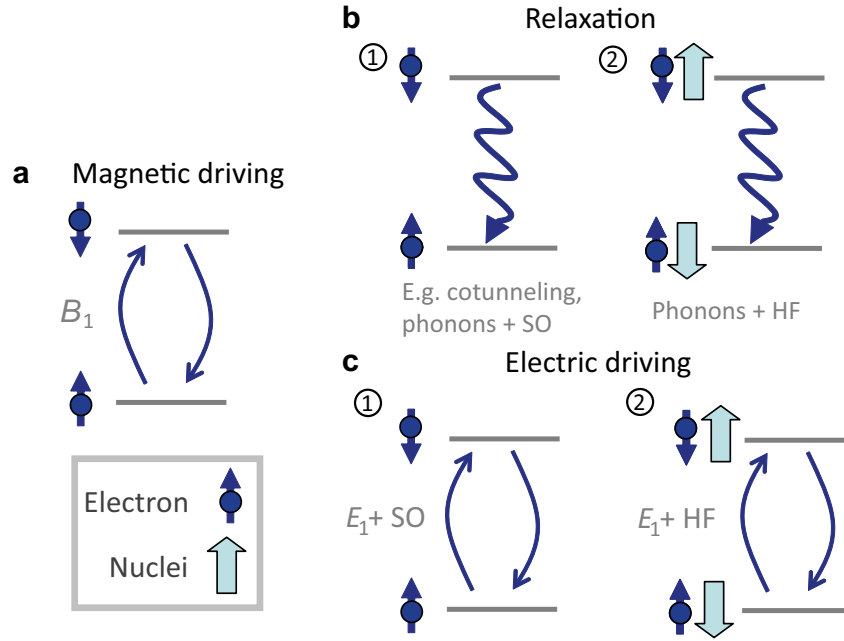
Figure 5.6: Microscopic processes. a, The resonant magnetic driving field B_1 induces electron spin transitions from ↑ to ↓ and vice versa. **b**, Electron spin relaxation (1) without and (2) with an accompanying electron-nuclear spin flip-flop. In (1) relaxation can be e.g. due to cotunneling processes with the leads and the combination of phonons and spin-orbit interaction (SO). In (2) relaxation results from the hyperfine interaction (HF) while the energy mismatch between electron and nuclear Zeeman splitting is dissipated in the environment (e.g. by phonons). Therefore this process has a preferential direction. **c**, The resonant electric field E_1 induces electron spin transitions from ↑ to ↓ and vice versa (1) without and (2) with an accompanying electron-nuclear spin flip-flop. As indicated in (1) spin-orbit interaction (SO) can mediate the coupling between electron spin and electric field (see chapter 6). In the present experiment this mechanism is however expected to much less efficient than magnetic driving (see also 4). An electric field moves the electron with respect to the nuclei resulting in a modulation of the hyperfine coupling. This gives rise to transitions as depicted in (2) [147, 97]. The energy mismatch between electron and nuclear Zeeman splitting is in this case compensated for by resonant photons. Therefore this process does not have a preferential direction in itself. As explained in the main text the combination of **a** and **b**2 gives rise to the usual Overhauser effect, whereas a combination of **a,b**1 and **c**2 results in 'reverse pumping' building up a nuclear field pointing against the external magnetic field.

---

caused by electron spin resonance. An excited electron can, while relaxing to its ground state (GS), transfer its angular momentum to one of the nuclei by the hyperfine interaction. The sign of the resulting nuclear polarization is thereby determined as parallel to the spin of the electron excited state (ES). A build-up of nuclear spin polarization that points in the direction of the GS electron spin, we therefore denote as opposite to usual Overhauser effect.

$x > 0$, i.e. the nuclear field points against the external magnetic field. Therefore the nuclear spin pumping cannot be explained by the usual Overhauser effect and consequently the mechanism described above cannot be the dominant one.

The observed 'reverse' pumping is possible when there is an excess of ↑ electrons, which are excited to ↓ by resonant electric fields, whereby the nuclear spins absorb the angular momentum [147, 97] (Fig. 5.6c2). Spin relaxation (Fig. 5.6b1) in general creates an excess of ↑ electrons, which favors reverse pumping. In our experiment, we believe the dominating electron spin relaxation process to be spin-exchange with the leads due to photon assisted tunneling (estimated to be $10 - 100$ kHz). Second, the locking effect gets stronger, hence Γ_p becomes larger, not only with stronger driving in general (Fig. 5.4c), but also with stronger electric excitation by itself (higher f, Fig. 5.4d). Based on these observations, we suggest that electric-field assisted electron-nuclear flip-flops combined with electron spin relaxation are mainly responsible for the resonant pumping in line with the analysis in [145].

The focus in [145] is on strong magnetic driving ($g\mu_B B_1/\hbar >> \Gamma_R$ with Γ_R denoting the rate at which the electron spin relaxes). Interestingly in this case even more stable points are predicted. Without giving details (which can be found in [145]) this can be understood in the following way. Exactly at resonance ↑ and ↓ are equally occupied due to saturation of the transition. As a result the transitions induced by the ac electric field have no more a preferential direction hence no net pumping of the nuclear spins occurs. Accordingly the corresponding pumping curve exhibits a dip exactly at resonance. In fact the nuclear spin relaxation even gets resonantly enhanced considering that the process of Fig. 5.6c2 contributes to possible nuclear spin flips. Therefore Γ_p as defined above can take a negative value exactly at resonance such that the value of dx/dt falls below the line corresponding to nuclear spin relaxation due to diffusion. The dip in the pumping curve gives rise to an additional stable point as illustrated in Fig.5.7. Therefore up to three (depending on x^{res}) stable points are predicted for one dot, and it can be anticipated that for the double system up to nine stable points are possible. Because the current through the double dot in the spin blockade regime is very sensitive to how close both dots are to resonance these stable points are associated with different current values. This might explain the observation of switching between multiple stable values of the current (see Fig. 5.7b) through the double dot observed in time-resolved measurements in which all external parameters (detuning of the double dot, microwave frequency and power, external magnetic field) are kept fixed.

5.8 Implications for electron spin dephasing and conclusion

Finally, we analyze theoretically the implications of our observations for the width of the nuclear field distribution. We define $\Gamma_\pm(x)$ as the total positive and negative
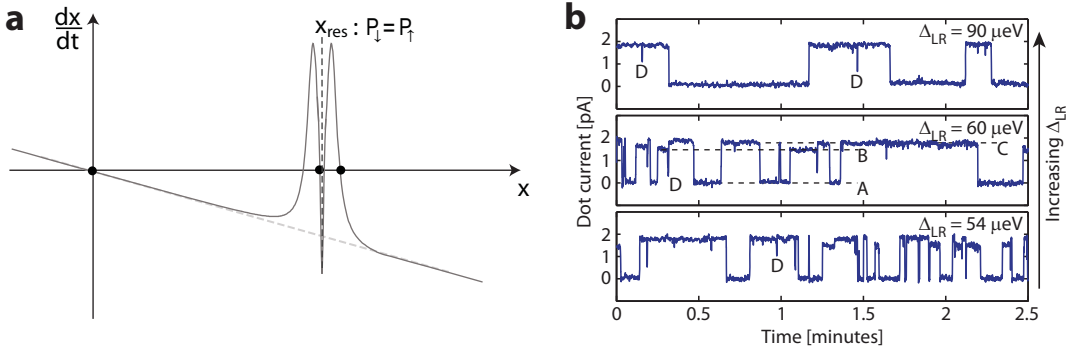
Figure 5.7: Multiple stable points in the case of strong driving. a, Similar to Fig. 5.5 a sketch of the nuclear spin polarization rate for one dot (dx/dt) is shown as a function of its polarization x now in the case of strong driving (see [145] for details). The dip at x^{res} due to saturation of spin resonance causes an extra stable point to occur compared to Fig. 5.5. (The three stable points are indicated by black dots.) In a double dot this can result in up to nine stable points for the nuclear spin polarization (x_L, x_R) where the indices refer to left and right dot respectively. **b**, Time resolved measurement of the current through the double dot approximately at resonance for different values of the energy level detuning in the left and right dot Δ_{LR}. (Reproduced from [145].) Multiple stable values of the current are visible labeled as $A - D$. D is only visible as current dips, which are thought however too big to be statistical fluctuations. The observation of four stable states is consistent with the fact that in this measurement $x_{res} \sim 0$ (the system is approximately on resonance) and thus the stable point $x = 0$ disappears for both dots, leaving two stable points per dot and therefore four for the combined system. Note that this measurement is done on the same sample but in a different cooldown as the one measured in this chapter. Especially the $(0, 2)$ singlet-triplet splitting was larger, allowing to access higher microwave power and therefore stronger driving (at even higher power photon-assisted tunneling lifts spin blockade irrespective of the spin states of the two electrons).

nuclear spin flip rates that result from the intrinsic relaxation and resonant response combined, so $dx/dt = \frac{2}{N}(\Gamma_+ - \Gamma_-)$, where N denotes the total number of nuclei. We also define $\gamma(x)$ as the total rate of nuclear spin flips, $\gamma = \frac{2}{N}(\Gamma_+ + \Gamma_-)$. Using the fact that the pumping curve exhibits a resonant peak at $|x_0| \ll 1$, we can then approximate the variance of the nuclear polarization distribution around x_0 as (see section 5.9.4)

$$\sigma^2 \approx \frac{1}{N} \frac{\gamma(x_0)}{\left(-\frac{\partial}{\partial x}\frac{dx}{dt}\right)|_{x_0}} . \tag{5.2}$$

The numerator is the local diffusion rate, and the denominator is the restoring force – the steeper the slope of dx/dt, the stronger the restoring force. When labelling the number of nuclei with spin up (down) by $N_{+(-)}$ we get for the case without pumping $\Gamma_\pm = N_\mp/2\tau_n$, so Eq. (5.2) gives us the usual result $\sigma^2 = 1/N$. (Note that we assume

here for simplicity nuclear spin $I = 1/2$. For higher values of spin, e.g. $I = 3/2$ as in GaAs, the results do not change qualitatively.) For a stable point $x_0 > 0$ near resonance, we take as a rough estimate for the local slope the maximum of Γ_p divided by its width. This gives $\sigma^2 \approx B_1/NB_N^{\max}$ (see Supplementary Information). Since $B_N^{\max}$ was several 100 mT with $B_1 < 1$ mT, these arguments imply that the nuclear field distribution was narrowed by more than a factor of 10. Future experiments will aim at a quantitative study of the impact of this narrowing on the electron spin dephasing time via Ramsey-style experiments.

Narrowing of the nuclear field distribution would greatly enhance our level of control of the electron spin dynamics. Furthermore, the observed locking effect allows us to accurately set the spin resonance frequency of an electron in a quantum dot to a value determined only by the externally controlled excitation frequency. Finally, our measurements suggest that we can selectively control the ESR frequency in one of the dots, which could be exploited for independent addressing of electron spins in quantum dots that are less than 100 nm apart.

5.9 Additional material

5.9.1 Tuning of the dot parameters in order to observe a pronounced electron-nuclear feedback

The conditions for observing a pronounced electron-nuclear feedback are as follows. Qualitatively, the interdot tunnel coupling and the tunnel coupling to the outgoing lead are increased compared to the regime of Ref. [33]. Furthermore, the potentials of the double dot are tuned such that the interdot transition occurs without energy loss: at low power, the configuration of the dot potentials is such that electrons can tunnel elastically from the left to the right dot when spin blockade is lifted. Thereby, the interdot transition is made from the $(1, 1)$ singlet to the $(0, 2)$ singlet, where (m, n) represent the effective electron numbers on the two dots. This working point cannot be used at strong driving, since the electric field component of the excitation causes photon assisted tunneling to the $(0, 2)$ triplet, thereby lifting spin blockade irrespective of the spin states of the two electrons. Instead, the double

dot must be tuned such that the $(0,2)$ singlet electrochemical potential is higher than that of the $(1,1)$ singlet. This is nominally in the Coulomb blockade regime, but photon-assisted tunneling now provides the missing energy in order to make the transition from the $(1,1)$ to the $(0,2)$ singlet.

5.9.2   Analysis of ESR current levels
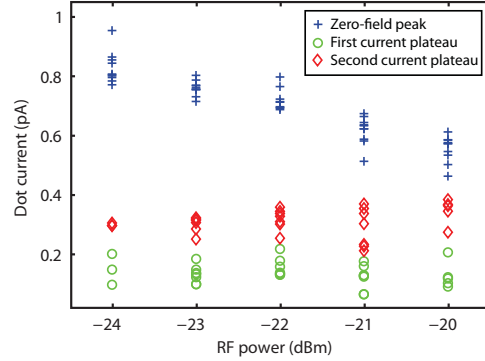
Figure 5.8: Current levels of the zero-field peak and the two plateaus. An offset is subtracted from all current levels given by the average current between the tail of zero-field peak and the ESR resonance. The height of the zero-field peak is determined by averaging 3 points around the position of its maximum, which is determined by first averaging 10 consecutive measurements and determining the maximum current in the averaged trace. The current levels of the first plateau are obtained by averaging individual traces between the magnetic field values where the first step occurs (indicated by green circles in Fig. 5.4a) and the field where the second step occurs or the field value where the current drops to zero, if that occurs before the second step (red diamonds and black crosses in Fig. 5.4a in the main text). We require these magnetic field intervals to be longer than 10 measurement points (corresponding to 20mT) in order not to be omitted. The height of the second plateau is determined in a similar way but now by averaging between the magetic field values where the second step occurs and the field where the current drops to zero. The resulting heights of the zero-field peak, first and second current plateaus are represented here by respectively blue crosses, green circles and red diamonds for different excitation powers.

Next to the *position* of the current jumps, we also analyzed the *height* of the current plateaus between the jumps as function of driving amplitude. For different microwave powers we repeatedly swept the external magnetic field from low to high with a sweep speed of $\dot{B}_0 = 400$ mT/min, keeping the driving frequency fixed at $f = 400$ MHz. For each trace we averaged the current of the first plateau and the current of the second plateau, and we determined the height of the zero-field peak. The result is plotted in Fig. 5.8 as a scatter plot for the different microwave powers. We clearly observe that in all traces the highest current was measured in the zero-

field peak, and that the second plateau exhibited higher current than the first. As to the dependence of the current levels on driving power, we see that (i) the height of the zero-field peak tends to decrease with increasing excitation power and (ii) the height of the ESR current plateaus seems nearly constant. As we attribute the observed double step feature to dragging of the nuclear field, first in two and then only in one dot, we here give some general considerations concerning the current levels during resonant electron transport in double quantum dot ESR experiments.

Let us first consider the limit of strong microwave driving with a saturated ESR, i.e. $g\mu_B B_1/h$ much larger than all relaxation and decay rates. If *both* dots are exactly on resonance, the driving causes the electrons to evolve entirely within the triplet subspace [149], i.e. in the cycle $|T_+\rangle \rightarrow \frac{1}{2}\left\{|T_+\rangle + \sqrt{2}|T_0\rangle + |T_-\rangle\right\} \rightarrow |T_-\rangle \rightarrow \frac{1}{2}\left\{|T_+\rangle - \sqrt{2}|T_0\rangle + |T_-\rangle\right\} \rightarrow |T_+\rangle$. As all three $(1,1)$ triplet states are Pauli spin blockaded, current can only flow to the extent there is relaxation from the triplets to the singlet. If only *one* of the two dots is on resonance, the system will evolve due to driving in the cycle $|T_\pm\rangle \rightarrow \frac{1}{\sqrt{2}}\left\{|T_0\rangle \pm |S\rangle\right\} \rightarrow |T_\pm\rangle$, where in the course of every cycle the state $\frac{1}{\sqrt{2}}\left\{|T_0\rangle \pm |S\rangle\right\}$ can decay via the $(0,2)$ singlet to the outgoing lead, giving rise to a current. Therefore, we expect in this limit of strong driving to observe the highest current when only one dot is on resonance. Since the resonance is saturated in the strong driving regime, we expect to first approximation no dependence of the current on microwave power.

In the limit of very weak driving, with $g\mu_B B_1/h$ much smaller than the relevant rates, one would expect quite the opposite. In this case the system spends most time in a Pauli spin blockaded state. The blockade can be lifted by spin relaxation in one of the two dots or by a spin flip in either of the dots caused by the driving field B_1. In this limit we therefore expect increasing current with increasing driving power, and furthermore that current will be highest when both dots are on resonance, simply because more spin flips take place.

During a field or frequency sweep, it is in principle possible that a nuclear field builds up in only one dot when the nominal ESR condition is first reached, subsequently locking the dot to the ESR condition. However, it is very unlikely that a nuclear field would build up in the other dot at a later time, when the ESR frequency in that dot is very far away from the driving frequency. A much more likely scenario is that a nuclear field builds up in both dots when the ESR condition is first reached (first plateau, low current), and that at the second current jump, the polarization in one dot relaxes to zero and only the other dot polarizes further (second plateau, high current). This would suggest that our experiments were performed in the regime of strong driving.

However, there is an issue which does not fit in this simple picture. The decrease of the zero-field peak height for increasing power suggests that the electric field component of the excitation smears out the current peak in gate voltage space due to photon-assisted tunneling (at high frequencies, discrete sidebands are visible, at low frequencies, the sidebands overlap). This could account for the decrease of the zero-

field current, but should presumably affect the ESR current levels in the same way since the ESR transition is saturated at strong driving. However, experimentally, the current levels at the two ESR plateaus are roughly independent of power, rather than decreasing with power. This point remains at present unresolved.

In order to develop a coherent picture of electron transport at zero-field and at spin resonance, a more systematic and detailed study of the dependence of the current levels on driving power and on the tuning of the double dot (tunnel coupling, detuning) is needed. This is quite involved, since the behavior of even the zero-field peak varies widely with tuning parameters.

5.9.3 Statistics of switching

Here we explain how we calculated the purple curve in Fig. 4e in the main text. We suggest that the second current jump (red diamonds in the Figure) corresponds to the resonance being lost in one of the two dots. This occurs when the effective barrier between the polarized and unpolarized states becomes small enough for a typical nuclear field fluctuation to overcome. If we assume a simple linear decrease of this effective barrier for increasing B_N and include the effect of the finite sweep rate $\dot{B}_0$, we find the polarization-dependent switching rate

$$\Gamma_{\mathrm{sw}}(B_N) = \Gamma_0 \exp\left\{ \gamma \left(\frac{B_N}{B_N^{\mathrm{max}}} + \frac{\dot{B}_0}{\dot{B}_0^{\mathrm{max}}} \right) \right\}, \tag{5.3}$$

where $\dot{B}_0^{\mathrm{max}}$ is the maximal sweep rate to observe any locking at all. From this expression we can derive the standard deviation in B_N where the second jump is observed, σ_{sw}, and the average switching field $\langle B_N^{\mathrm{sw}} \rangle$. Explicitly, we find

$$\sigma_{\mathrm{sw}} = \frac{B_N^{\mathrm{max}}}{\gamma} \qquad \text{and} \qquad \langle B_N^{\mathrm{sw}} \rangle = \sigma_{\mathrm{sw}} \ln \frac{\dot{B}_0^{\mathrm{max}}}{\sigma_{\mathrm{sw}} \Gamma_0} + \sigma_{\mathrm{sw}} \ln \frac{\dot{B}_0}{\dot{B}_0^{\mathrm{max}}} - B_N^{\mathrm{max}} \frac{\dot{B}_0}{\dot{B}_0^{\mathrm{max}}}. \tag{5.4}$$

We analyzed the set of red diamonds in Fig. 4e in the main text. From (5.4) we expect σ_{sw} to be constant in first approximation, which is indeed observed for lower sweep rates (100-400 mT/min). The decrease of σ_{sw} for sweep rates above 400 mT/min could be a consequence of the average switching field lying too close to the resonance condition. Therefore we averaged the standard deviation over the first four values to find $\sigma_{\mathrm{sw}} = 39$ mT. Using this value for the standard deviation, we fitted equation (5.4) to the data in Fig. 4e. This resulted in the fitting parameters $B_N^{\mathrm{max}} = 289.6$ mT, $\dot{B}_0^{\mathrm{max}} = 920.7$ mT/min and $\gamma = 6.946 \cdot 10^{-4}$ s^{-1}, giving a sample correlation coefficient of $R = 0.948$. The resulting fitting curve is plotted in purple in Fig. 4e. Another way to estimate B_N^{max} and $\dot{B}_0^{\mathrm{max}}$ is to extrapolate the set of red diamonds in Fig. 4e to the two axes. In this way one finds the estimates $B_N^{\mathrm{max}} \approx 300$ mT and $\dot{B}_0^{\mathrm{max}} \approx 900$ mT/min, both in reasonable agreement with the results of the fit.

5.9.4 Suppression of fluctuations

In this section we derive an estimate for the typical magnitude of nuclear field fluctuations around a stable point close to resonance. For the sake of argument we show here the derivation for a *single* quantum dot, although a similar argument holds for a double dot setup and the results are qualitatively similar as well. (in the double dot case, a *two dimensional* Fokker-Planck equation must be considered, where stable points correspond to zeros of $\{\partial_t x_1, \partial_t x_2\}$ in the plane (x_1, x_2))

We consider all possible configurations of the nuclear spin system in the dot as discrete points, labeled n, defining $n \equiv \frac{1}{2}(N_+ - N_-)$, where $N_{+(-)}$ denotes the number of nuclei with spin up(down) . We assume here for simplicity nuclear spin $I = 1/2$. For higher values of spin, e.g. $I = 3/2$ as in GaAs, the results do not change qualitatively. This results in $N \equiv N_+ + N_-$ possible values for n, ranging from $-N/2$ to $N/2$. To investigate the stochastic properties we derive a Fokker-Planck equation for the probability distribution function $\mathcal{P}(n)$, starting from a simple master equation

$$\frac{\partial \mathcal{P}(n)}{\partial t} = -\mathcal{P}(n)[\Gamma_+(n) + \Gamma_-(n)] + \mathcal{P}(n-1)\Gamma_+(n-1) + \mathcal{P}(n+1)\Gamma_-(n+1). \quad (5.5)$$

In this equation $\mathcal{P}(n)$ gives the chance of finding the system in state n, and $\Gamma_\pm(n)$ is the rate at which the spin bath flips from the configuration n to $n \pm 1$. We go over to the continuous limit, justified by the large number of nuclei $N \sim 10^6$ [150], and expand all functions around n up to second order. We find

$$\frac{\partial \mathcal{P}}{\partial t} = \frac{\partial}{\partial n}\left\{(\Gamma_- - \Gamma_+)\mathcal{P} + \frac{1}{2}\frac{\partial}{\partial n}(\Gamma_- + \Gamma_+)\mathcal{P}\right\}, \quad (5.6)$$

a Fokker-Planck equation where all rates $\Gamma_\pm$ are still functions of n. Due to the large number of nuclei, the spin flip rates $\Gamma_\pm$ do not change on their full scale when increasing n by only ± 1 (the features of $\Gamma_\pm$ occur on the scale of the width of the resonance ~ 1 mT, whereas changing n by ± 1 corresponds to $IA/N \sim 5$ μT). This implies that $|\partial_n \Gamma_\pm| \ll \Gamma_\pm$, which allows us to neglect one of the cross terms resulting from the last term in (5.6).

In the resulting continuity equation, the right-hand side corresponds to the derivative of a probability flux. In equilibrium this probability flux must vanish, which enables us to write down a general equilibrium solution of (5.6). In terms of the bath polarization $x \equiv 2n/N$ this solution reads

$$\mathcal{P}(x) = \exp\left\{\int^x N\frac{\Gamma_+ - \Gamma_-}{\Gamma_+ + \Gamma_-}dx'\right\}. \quad (5.7)$$

Maxima and minima of this distribution are found at the zeros of the derivative of the exponent. Suppose the point x_0 is one of these solutions corresponding to a maximum of $\mathcal{P}(x)$ (i.e. the second derivative in the point x_0 is negative). We then

expand the exponent of $\mathcal{P}(x)$ up to second order around the maximum, giving a Gaussian approximation for $\mathcal{P}(x)$,

$$\mathcal{P}(x) \approx \exp\left\{ \int^{x_0} N\frac{\Gamma_+ - \Gamma_-}{\Gamma_+ + \Gamma_-}dx' + \frac{N}{2}\frac{\partial}{\partial x}\frac{\Gamma_+ - \Gamma_-}{\Gamma_+ + \Gamma_-}\bigg|_{x_0}(x - x_0)^2 \right\} \tag{5.8}$$

$$\equiv \mathcal{P}(x_0)\exp\left\{ -\frac{(x - x_0)^2}{2\sigma^2} \right\}, \tag{5.9}$$

where σ gives the width of the distribution. So we find that

$$\sigma^2 = \frac{1}{N}\left(-\frac{\partial}{\partial x}\frac{\Gamma_+ - \Gamma_-}{\Gamma_+ + \Gamma_-}\bigg|_{x_0} \right)^{-1} = \frac{1}{N}\frac{\Gamma_+ + \Gamma_-}{\frac{\partial}{\partial x}(\Gamma_- - \Gamma_+)}\bigg|_{x_0}, \tag{5.10}$$

where we used that $(\Gamma_+ - \Gamma_-)|_{x_0} = 0$. We now only still want to translate this expression in terms of the 'pumping curve'. We use the relation $dx/dt = (2/N)(\Gamma_+ - \Gamma_-)$ and define $\gamma(x) = (2/N)(\Gamma_+ + \Gamma_-)$. In the limit of small polarizations, i.e. $|x| \ll 1$, we can write

$$\frac{dx}{dt} = L(x) - \gamma(x)x. \tag{5.11}$$

In this notation the effect of Γ_p (main text) is separated into two parts: (i) a polarization-dependent net spin pumping contribution, $L(x)$, and (ii) a polarization-dependent contribution to the relaxation, which together with the intrinsic relaxation rate $1/\tau_n$ is written as $\gamma(x)$. One can rewrite equation (5.10) in terms of dx/dt and $\gamma(x)$ using the relations given above. This gives us finally the expression

$$\sigma^2 \approx \frac{1}{N}\frac{\gamma(x_0)}{\left(-\frac{\partial}{\partial x}\frac{dx}{dt}\right)\big|_{x_0}}. \tag{5.12}$$

To get an idea of the magnitude of this variance, we approximate the derivative of the pumping curve at the stable point as roughly the height of $L(x)$ over the width (see Fig. 5 in the main text), i.e. $-\partial_x(dx/dt)|_{x_0} \approx L^{\max}/\tilde{x}$, where $\tilde{x}$ is the width of $L(x)$. From equation (5.11) we see that we can write for the absolute maximum of achievable polarization $x^{\max} = L^{\max}/\gamma(x^{\max})$. Combining these two expressions and using that $\gamma(x^{\max}) \sim \gamma(x_0)$, we find the order of magnitude of the variance σ^2 to be

$$\sigma^2 \sim \frac{1}{N}\frac{\tilde{x}}{x^{\max}}. \tag{5.13}$$

In terms of the effective nuclear field B_N, this variance reads

$$\sigma_{B_N}^2 \sim \Omega^2\frac{B_1}{|B_N^{\max}|}, \tag{5.14}$$

where $\Omega \equiv IA/g\mu_B\sqrt{N}$ are the diffusive fluctuations around the unpolarized state, and B_1 is the scale of the width of the pumping term L, in our case given by the strength of the microwave driving field.

Chapter 6

Coherent control of a single spin with electric fields

Manipulation of single spins is essential for spin-based quantum information processing. Electrical control instead of magnetic control is particularly appealing for this purpose, since electric fields are easy to generate locally on-chip. We experimentally realize coherent control of a single electron spin in a quantum dot using an oscillating electric field generated by a local gate. The electric field induces coherent transitions (Rabi oscillations) between spin-up and spin-down with 90° rotations as fast as ∼55 ns. Our analysis indicates that the electrically-induced spin transitions are mediated by the spin-orbit interaction. Taken together with the recently demonstrated coherent exchange of two neighboring spins, our results demonstrate the feasibility of fully electrical manipulation of spin qubits.

6.1 Introduction

Spintronics and spin-based quantum information processing provide the possibility to add new functionality to today's electronic devices by using the electron spin in addition to the electric charge [151]. In this context, a key element is the ability to induce transitions between the spin-up and spin-down states of a localized electron spin, and to prepare arbitrary superpositions of these two basis states. This is commonly accomplished by magnetic resonance, whereby bursts of a resonant oscillating magnetic field are applied [116]. However, producing strong oscillating magnetic fields in a semiconductor device requires specially designed microwave cavities [152] or microfabricated striplines [33], and has proven to be challenging. In comparison, electric fields can be generated much more easily, simply by exciting a local gate electrode. In addition, this allows for greater spatial selectivity, which is important for local addressing of individual spins. It would thus be highly desirable to control the spin by means of electric fields.

Although electric fields do not couple directly to the electron spin, indirect coupling can still be realized by placing the spin in a magnetic field gradient [153] or in a structure with a spatially varying g-tensor, or simply through spin-orbit interaction, present in most semiconductor structures [53, 51]. Several of these mechanisms have been employed to electrically manipulate electron spins in two dimensional electron systems [60, 154, 155, 156], but proposals for coherent electrical control at the level of a single spin [73, 70, 153, 71, 157] have so far remained unrealized.

We demonstrate coherent single spin rotations induced by an oscillating electric field. The electron is confined in a gate-defined quantum dot (see Fig. 6.1a) and we use an adjacent quantum dot, containing one electron as well, for read-out. The ac electric field is generated through excitation of one of the gates that forms the dot, thereby periodically displacing the electron wavefunction around its equilibrium position (Fig. 6.1b).

6.2 Electrically driven spin resonance

The experiment consists of four stages (Fig. 6.1c). The device is initialised in a spin-blockade regime where two excess electrons, one in each dot, are held fixed with parallel spins (spin triplet), either pointing along or opposed to the external magnetic field (the system is never blocked in the triplet state with anti-parallel spins, because of the effect of the nuclear fields in the two dots combined with the small interdot tunnel coupling, see [144] for full details). Next, the two spins are isolated by a gate voltage pulse, such that electron tunneling between the dots or to the reservoirs is forbidden. Then, one of the spins is rotated by an ac voltage burst applied to the gate, over an angle that depends on the length of the burst [158] (most likely the spin in the right dot, where the electric field is expected to be strongest).

Finally, the read-out stage allows the left electron to tunnel to the right dot if and only if the spins are anti-parallel. Subsequent tunneling of one electron to the right reservoir gives a contribution to the current. This cycle is continuously repeated, and the current flow through the device is thus proportional to the probability of
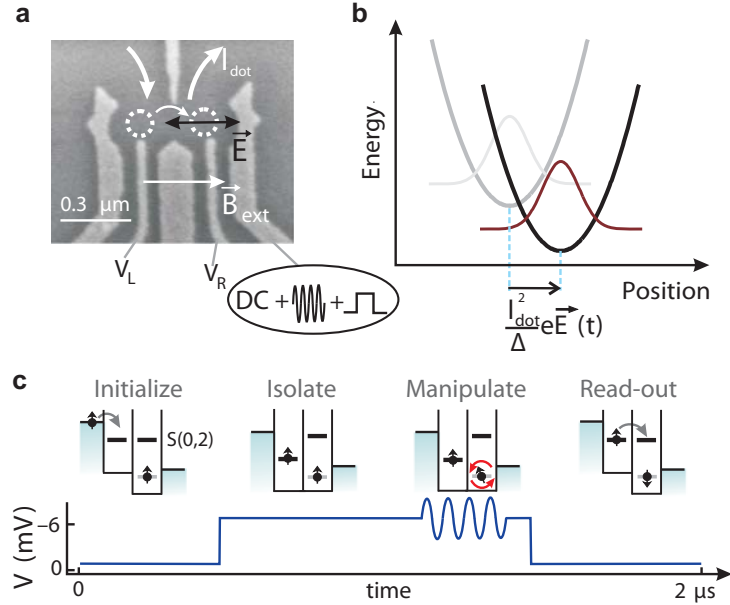
Figure 6.1: (a) Scanning electron microscope image of a device with the same gate structure as the one used in this experiment. Metallic TiAu gates are deposited on top of a GaAs heterostructure which hosts a 2DEG 90 nm below the surface. Not shown is a coplanar stripline on top of the metallic gates, separated by a dielectric (not used in this experiment). In addition to a dc voltage we can apply fast pulses and microwaves to the right side gate (as indicated) through a home made bias-tee. The orientation of the in-plane external magnetic field is as shown. The sample used here is identical to the one used in chapter 4).(b) The electric field generated upon excitation of the gate displaces the center of the electron wavefunction along the electric field direction and changes the potential depth. Here, Δ is the orbital energy splitting, $l_{dot} = \hbar/\sqrt{m^*\Delta}$ the size of the dot, m^* the effective electron mass, $\hbar$ the reduced Planck constant and $\mathbf{E}(t)$ the electric field. (c) Schematic of the spin manipulation and detection scheme, controlled by a combination of a voltage pulse and burst, $V(t)$, applied to the right side gate. The diagrams show the double dot, with the thick black lines indicating the energy cost for adding an extra electron to the left or right dot, starting from $(0,1)$, where (n, m) denotes the charge state with n and m electrons in the left and right dot. The energy cost for reaching $(1,1)$ is (nearly) independent of the spin configuration. However, for $(0,2)$, the energy cost for forming a singlet state (indicated by $S(0,2)$) is much lower than that for forming a triplet state (not shown in the diagram). This difference is exploited for initialization and detection, as explained further in the main text.

having antiparallel spins after excitation.

To demonstrate that electrical excitation can indeed induce single-electron spin flips, we apply a microwave burst of constant length to the right side gate and monitor the average current flow through the quantum dots as a function of external magnetic field $\mathbf{B}_{\text{ext}}$ (Fig. 6.2a). A finite current flow is observed around the single-electron spin resonance condition, i.e. when $|\mathbf{B}_{\text{ext}}| = hf_{\text{ac}}/g\mu_{\text{B}}$, with h Planck's constant, f_{ac} the excitation frequency, and μ_{B} the Bohr magneton. From the position of the resonant peaks measured over a wide magnetic field range (Fig. 6.2b) we determine a g-factor of $|g| = 0.39 \pm 0.01$, which is in agreement with other reported values for electrons in GaAs quantum dots [35].

In addition to the external magnetic field, the electron spin feels an effective
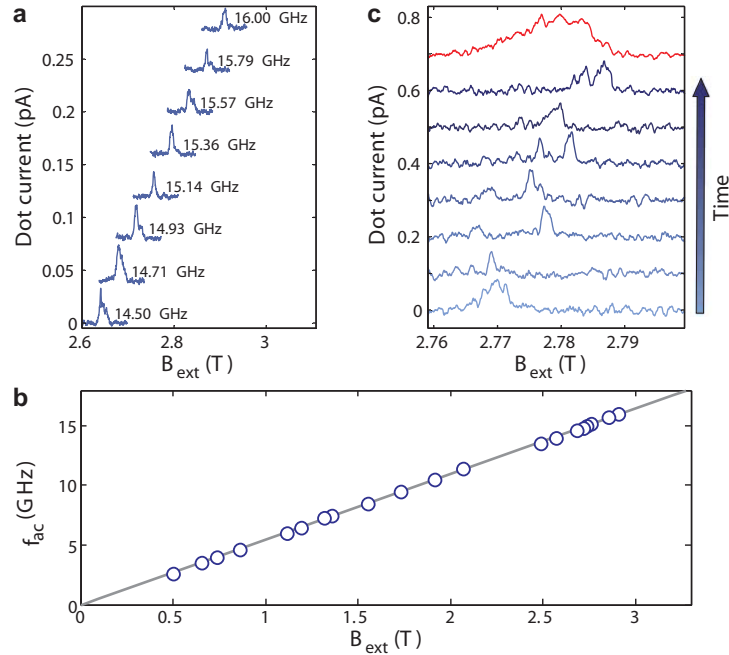
Figure 6.2: (a) The current averaged over 40 magnetic field sweeps is given for eight different excitation frequencies, with a microwave burst length of 150 ns. The traces are offset for clarity. The microwave amplitude V_{mw} was in the range $0.9 - 2.2$ mV depending on the frequency (estimated from the output power of the microwave source and taking into account the attenuation of the coaxial lines and the switching circuit used to create microwave bursts). (b) Position of the resonant response over wider frequency and field ranges. Errorbars are smaller than the size of the circles. (c) Individual magnetic field sweeps at $f_{\text{ac}} = 15.2$ GHz measured by sweeping from high to low magnetic field with a rate of 50 mT/minute. The traces are offset by 0.1 pA each for clarity. The most upper trace is an average over 40 sweeps, including the ones shown and scaled up by a factor of 5.

nuclear field B_N arising from the hyperfine interaction with nuclear spins in the host material and fluctuating in time [84, 83]. This nuclear field modifies the electron spin resonance condition and is generally different in the left and right dot (by ΔB_N). The peaks shown in Fig. 6.2A are averaged over many magnetic field sweeps and have a width of about 10-25 mT. This is much larger than the expected linewidth, which is only 1-2 mT given by the statistical fluctuations of B_N [88, 41]. Looking at individual field sweeps measured at constant excitation frequency, we see that the peaks are indeed a few mT wide (see Fig. 6.2c), but that the peak positions change in time over a range of $\sim$ 20mT. Judging from the dependence of the position and shape of the averaged peaks on sweep direction, the origin of this large variation in the nuclear field is most likely dynamic nuclear polarization [139, 129, 33, 92, 97].

6.3 Electrically driven Rabi oscillations

In order to demonstrate coherent control of the spin, the length of the microwave bursts was varied, and the current level monitored. In Fig. 6.3a we plot the maximum current per magnetic field sweep as a function of the microwave burst duration, averaged over several sweeps (note that this is a more sensitive method than averaging the traces first and then taking the maximum)[158]. The maximum current exhibits clear oscillations as a function of burst length. Fitting with a cosine function reveals a linear scaling of the oscillation frequency with the driving amplitude (Fig. 6.3b), a characteristic feature of Rabi oscillations, and proof of coherent control of the electron spin via electric fields.

The highest Rabi frequency we achieved is $\sim$ 4.7 MHz (measured at $f_{ac} =$
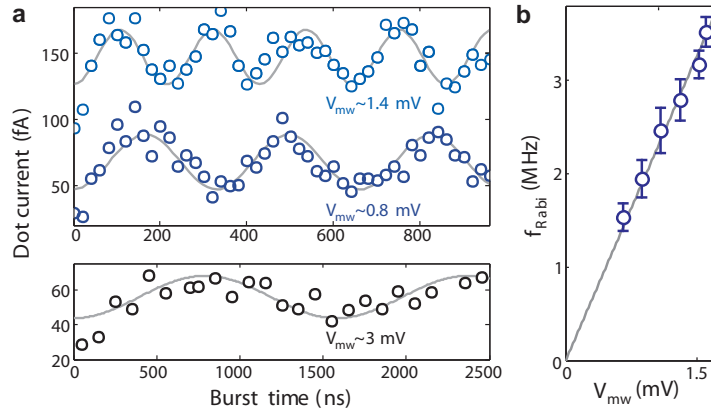
Figure 6.3: (a) Rabi oscillations at 15.2 GHz (upper, average over 5 sweeps) and 2.6 GHz (lower, average over 6 sweeps). The two oscillations at 15.2 GHz are measured at different amplitude of the microwaves V_{mw} leading to different Rabi frequencies. (b) Linear dependence of the Rabi frequency on applied microwave amplitude measured at $f_{ac} = 14$ GHz.

15.2 GHz) corresponding to a 90° rotation in ~ 55 ns, which is only a factor of two slower than those realized with magnetic driving [33]. Stronger electrical driving was not possible because of photon-assisted-tunneling. This is a process whereby the electric field provides energy for one of the following transitions: tunneling of an electron to a reservoir or to the triplet with both electrons in the right dot. This lifts spin-blockade, irrespective of whether the spin resonance condition is met.

Small Rabi frequencies could be observed as well. The bottom trace of Fig. 6.3a shows a Rabi oscillation with a period exceeding 1.5μs (measured at $f_{ac} = 2.6$ GHz), corresponding to an effective driving field of only about 0.2 mT, ten times smaller than the statistical fluctuations of the nuclear field. The reason the oscillations are nevertheless visible is that the dynamics of the nuclear bath is slow compared to the Rabi period, resulting in a slow power law decay of the oscillation amplitude on driving field [130].

6.4 Mechanism coupling the electric field and the electron spin

We next turn to the mechanism responsible for resonant transitions between spin states. First, we exclude a magnetic origin as the oscillating magnetic field generated upon excitation of the gate is more than two orders of magnitude too small to produce the observed Rabi oscillations with periods up to ~ 220 ns, which requires a driving field of about 2mT [158]. Second, we have seen that there is in principle a number of ways in which an ac electric field can cause single spin transitions. What is required is that the oscillating electric field give rise to an effective magnetic field, $\mathbf{B}_{eff}(t)$, acting on the spin, oscillating in the plane perpendicular to $\mathbf{B}_{ext}$, at frequency $f_{ac} = g\mu_B|\mathbf{B}_{ext}|/h$. The g-tensor anisotropy is very small in GaAs so g-tensor modulation can be ruled out as the driving mechanism. Furthermore, in our experiment there is no external magnetic field gradient applied, which could otherwise lead to spin resonance [153]. We are aware of only two remaining possible coupling mechanisms: spin-orbit interaction and the spatial variation of the nuclear field.

In principle, moving the wavefunction in a nuclear field gradient can drive spin transitions [99, 153] as was recently observed [97]. However, the measurement of each Rabi oscillation took more than one hour, much longer than the time during which the nuclear field gradient is constant ($\sim 100\mu$s - few s). Because this field gradient and therefore, the corresponding effective driving field slowly fluctuates in time around zero, the oscillations would be strongly damped, regardless of the driving amplitude [97]. Possibly a (nearly) static gradient in the nuclear spin polarization could develop due to electron-nuclear feedback. However, such polarization would be parallel to $\mathbf{B}_{ext}$ and can thus not be responsible for the observed coherent oscillations.

In contrast, spin-orbit mediated driving can induce coherent transitions [73], which can be understood as follows. The spin-orbit interaction in a GaAs heterostructure is given by $H_{\mathrm{SO}} = \alpha(p_x\sigma_y - p_y\sigma_x) + \beta(-p_x\sigma_x + p_y\sigma_y)$, where α and β are the Rashba and Dresselhaus spin-orbit coefficient respectively, and $p_{x,y}$ and $\sigma_{x,y}$ are the momentum and spin operators in the x and y directions (along the [100] and [010] crystal directions respectively). As suggested in [70], the spin-orbit interaction can be conveniently accounted for up to the first order in α, β by applying a (gauge) transformation, resulting in a position-dependent correction to the external magnetic field. This effective magnetic field, acting on the spin, is proportional and
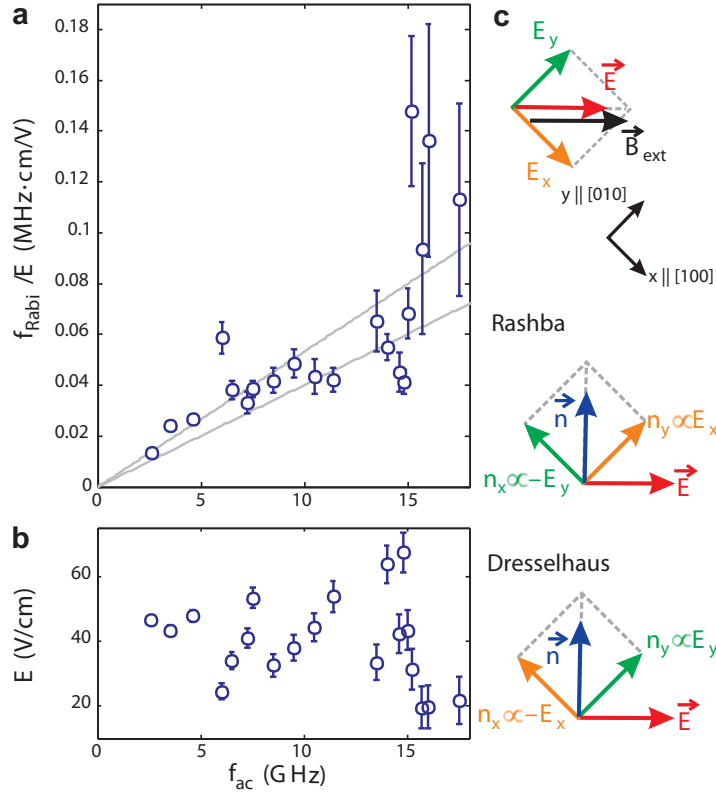
Figure 6.4: (a) Rabi frequency rescaled with the applied electric field for different excitation frequencies. The errorbars are given by $f_{\mathrm{Rabi}}/E \cdot \sqrt{(\delta E/E)^2 + (\delta f_{\mathrm{Rabi}}/f_{\mathrm{Rabi}})^2}$ where δf_{Rabi} and δE are the error in the Rabi frequency and electric field amplitude respectively. The grey lines are the 95% confidence bounds for a linear fit through the data (weighting the datapoints by the inverse error squared). (b) Estimated electric field amplitudes at which the Rabi oscillations of (A) were measured at the respective excitation frequencies [158]. (c) Construction of the direction of **n** resulting from the Rashba and Dresselhaus spin-orbit interaction for an electric field along [110] following equation 1. The coordinate system is set to the crystallographic axis [100] and [010].

orthogonal to the field applied:

$$\mathbf{B}_{\text{eff}}(x,y) = \mathbf{n} \otimes \mathbf{B}_{\text{ext}}$$
$$n_x = \frac{2m^*}{\hbar}\left(-\alpha y - \beta x\right); \ n_y = \frac{2m^*}{\hbar}\left(\alpha x + \beta y\right); \ n_z = 0 \tag{6.1}$$

An electric field $\mathbf{E}(t)$ will periodically and adiabatically displace the electron wave function (see Fig. 6.1b) by $\mathbf{x}(t) = (el_{\text{dot}}^2/\Delta)\mathbf{E}(t)$, so the electron spin will feel an oscillating effective field $\mathbf{B}_{\text{eff}}(t) \perp \mathbf{B}_{\text{ext}}$ through the dependence of $\mathbf{B}_{\text{eff}}$ on the position. The direction of $\mathbf{n}$ can be constructed from the direction of the electric field as shown in Fig. 6.4c and together with the direction of $\mathbf{B}_{\text{ext}}$ determines how effectively the electric field couples to the spin. The Rashba contribution always gives $\mathbf{n}\perp\mathbf{E}$, while for the Dresselhaus contribution this depends on the orientation of the electric field with respect to the crystal axis. Given the gate geometry, we expect the dominant electric field to be along the double dot axis (see Fig. 6.1a) which is here [1$\bar{1}$0] crystallographic direction (see section 6.6). For these orientations, the Dresselhaus contribution is also orthogonal to the electric field (see Fig. 6.4c). This is why both contributions will give $\mathbf{B}_{\text{eff}} \neq 0$ and lead to coherent oscillations in the present experimental geometry, where $\mathbf{E} \parallel \mathbf{B}_{\text{ext}}$. Note that in [97], a very similar gate geometry was used, but the orientation of $\mathbf{B}_{\text{ext}}$ was different, and it can be expected that $\mathbf{E} \perp \mathbf{B}_{\text{ext}}$. In that experiment, no coherent oscillations were observed, which is consistent with the considerations here.

An important characteristic of spin-orbit mediated driving is the linear dependence of the effective driving field on the external magnetic field which follows from Eq. 1 and is predicted in [73, 70, 67]. We aim at verifying this dependence by measuring the Rabi frequency as a function of the resonant excitation frequency (Fig. 6.4a), which is proportional to the external magnetic field. Each point is rescaled by the estimated applied electric field (Fig. 6.4b). Even at fixed output power of the microwave source, the electric field at the dot depends on the microwave frequency due to various resonances in the line between the microwave source and the gate (caused by reflections at the bonding wires and microwave components). However, we use the photon-assisted-tunneling response as a probe for the ac voltage drop across the interdot tunnelbarrier, which we convert into an electric field amplitude by assuming a typical interdot distance of 100 nm. This allows us to roughly estimate the electric field at the dot for each frequency [158]. Despite the large error bars, which predominantly result from the error made in estimating the electric field, an overall upgoing trend is visible in Fig. 6.4a.

For a quantitative comparison with theory, we extract the spin-orbit strength in GaAs, via the expression of the effective field $\mathbf{B}_{\text{eff}}$ perpendicular to $\mathbf{B}_{\text{ext}}$ for the geometry of this experiment [73]

$$|\mathbf{B}_{\text{eff}}(t)| = 2|\mathbf{B}_{\text{ext}}|\frac{l_{\text{dot}}}{l_{\text{SO}}}\frac{e|\mathbf{E}(t)|l_{\text{dot}}}{\Delta}, \tag{6.2}$$

with l_{SO} the spin-orbit length (for the other definitions see Fig. 6.1b). Here, $l_{\mathrm{SO}}^{-1} = m^*(\alpha \mp \beta)/\hbar$ for the case with the gate symmetry axis along $[1\bar{1}0]$ or $[110]$ respectively. Via $f_{\mathrm{Rabi}} = (g\mu_{\mathrm{B}}|\mathbf{B}_{\mathrm{eff}}|)/2h$, the confidence interval of the slope in Fig. 6.4a gives a spin-orbit length of $28 - 37\mu$m (with a level splitting Δ in the right dot of 0.9 meV extracted from high bias transport measurements). Additional uncertainty in l_{SO} is due to the estimate of the interdot distance and the assumption of a homogenous electric field, deformation effects of the dot potential [157] and extra cubic terms in the Hamiltonian [51]. Still, the extracted spin-orbit length is of the same order of magnitude as other reported values for GaAs quantum dots [35].

Both the observed trend of $\mathbf{B}_{\mathrm{eff}}$ with f_{ac} and the extracted range for l_{SO} are consistent with our supposition (by elimination of other mechanisms) that spin transitions are mediated by spin-orbit interaction. We note that also for relaxation of single electron spins in which electric field fluctuations from phonons couple to the spin, it is by now well established that the spin-orbit interaction is dominant at fields higher than a few 100 mT [99, 67, 73, 35]. It can thus be expected to be dominant for coherent driving as well.

6.5 Conlusion

The electrically driven single spin resonance reported here, combined with the so-called $\sqrt{SWAP}$ gate based on the exchange interaction between two neighbouring spins [32], brings all-electrical universal control of electron spins within reach. While the $\sqrt{SWAP}$ gate already operates on sub-nanosecond timescales, single-spin rotations still take about one hundred nanoseconds (the main limitation is photon-assisted-tunneling). Faster operations could be achieved by suppressing photon-assisted-tunneling (e.g. by increasing the tunnel barriers or operating deeper into Coulomb blockade), by working at still higher magnetic fields, by using materials with stronger spin-orbit interaction or through optimized gate designs. Furthermore, the electrical control offers the potential for spatially selective addressing of individual spins in a quantum dot array, since the electric field is produced by a local gate. Finally, we note that the spin rotations were realized at magnetic fields high enough to allow for single-shot read-out of a single spin [30], so that both elements can be integrated in a single experiment.

(NWO).

6.6 Additional material

6.6.1 Extraction of Rabi oscillations from magnetic field sweeps
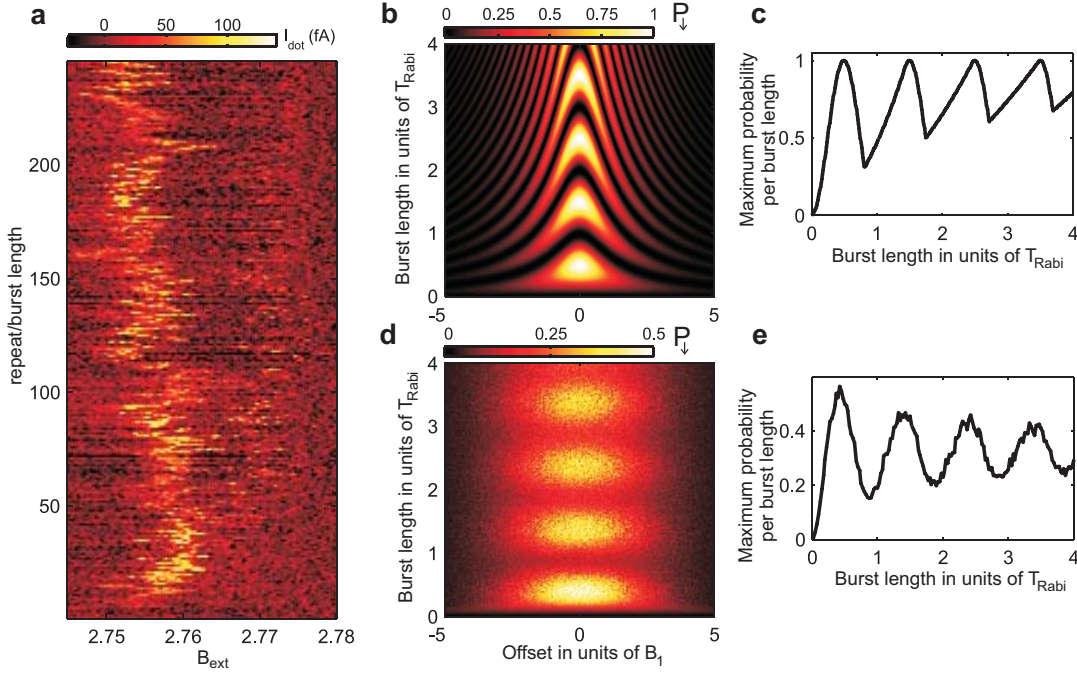
Figure 6.5: (a) Magnetic field sweeps from which the topmost Rabi oscillation in Fig. 6.3A is extracted. The vertical axis is a combination of repeated measurements and microwave burst length (the first 5 traces correspond to a burst length of 0 ns, the following 5 to 20 ns etc.). (b) The simulated probability to find spin down as a function of burst length and detuning from the resonant field assuming spin up as initial state. The detuning is given in units of the driving field $B_1 = B_{\text{eff}}/2$ and the burst length is given in units of the Rabi period $T_{\text{Rabi}} = h/(g\mu_B B_1)$. (c) Maximum probability from (b) for each burst length. (d) Same as in (b) but with each pixel averaged over 75 values of the detuning, sampled from a distribution of width σ, with $\sigma = 1.4B_1$ (which corresponds to the experimental situation in (a) where $B_1 \sim 0.8$ mT). (e) Maximum probability from (d) for each burst length.

In Fig. 6.2c we see that at large external magnetic field, the nuclear field fluctuates over a much larger range than $A/\sqrt{N}$, where A is the nuclear field experienced by the electron spin when the nuclei are fully polarized and N the number of nuclei

overlapping with the electron wave function. This made it impossible in the experiment to record a Rabi oscillation at constant B_{ext}. We therefore chose to sweep the external magnetic field through the resonance. We measured a few magnetic field sweeps per microwave burst length and averaged over the maximum current values reached in each sweep (raw data shown in Fig. 6.5a).

However, when extracting the Rabi oscillation by looking at the absolute maximum per magnetic field sweep, it is not obvious that the correct Rabi period $T_{\text{Rabi}} = 2h/(g\mu_B B_{\text{eff}})$ is found. For instance, a burst which produces a 2π rotation at resonance, gives a tip angle different from 2π away from resonance.

In order to illustrate the effect more fully, Fig. 6.5b shows a map of the probability for flipping a spin, calculated from the Rabi formula [116] as a function of the detuning away from resonance and the microwave burst length. When taking for each fixed burst length the maximum probability, a saw tooth like trace is obtained (Fig. 6.5c). Still the positions of the maxima remain roughly at burst lengths corresponding to odd multiples of π and the distance between maxima corresponds to the Rabi period.

In addition, we note that every data pixel in Fig. 6.5a is integrated for about 50ms, so it presumably represents an average over a number of nuclear configurations. This is additionally taken into account in Fig. 6.5d by averaging each point over a Gaussian distribution of detunings. The width of the distribution used in Fig. 6.5d corresponds to statistical fluctuations of the nuclear field along the direction of the external magnetic field of 1.1mT (at a driving field of $\sim 0.8\,\text{mT}$). This assumes that on top of the large variation of the nuclear field, visible in Fig. 6.2c, which occurs on a minute time scale, the nuclear field undergoes additional statistical fluctuations on a faster time scale. Taking the maximum in Fig. 6.5d for each microwave burst length reveals a rather smooth Rabi oscillation (Fig. 6.5e) with a phase shift [130], and again with the proper Rabi period.

Presumably neither case, with and without averaging over a distribution of detunings, reflects the actual experimental situation in detail. However in the simulation the Rabi period obtained from the periodicity of the maximum probability as a function of the burst length is *independent* of the width of the gaussian distribution.

Finally, we remark that these conclusions are unchanged when considering the maximum current for each burst length (the current measures parallel spins versus anti-parallel spins) instead of the maximum probability for flipping a single spin. On this basis, we conclude that taking the maximum current value for each burst length gives us a reliable estimate of the Rabi period.

6.6.2 Estimate of the electric field amplitude at the dot

The electric field generated at the dot by excitation of a gate is difficult to quantify exactly. While we can estimate the power that arrives at the sample holder from

the output power of the microwave source and the measured attenuation in the line, the power that arrives at the gate is generally somewhat less (the coax is connected to the gate via bonding wires). In addition, it is difficult to accurately determine the conversion factor between the voltage modulation of the gate and the electric field modulation of the dot. We here estimate the voltage drop across the interdot tunnel barrier via photon-assisted-tunneling (PAT) measurements, and extract from this voltage drop a rough indication of the electric field at the dot.
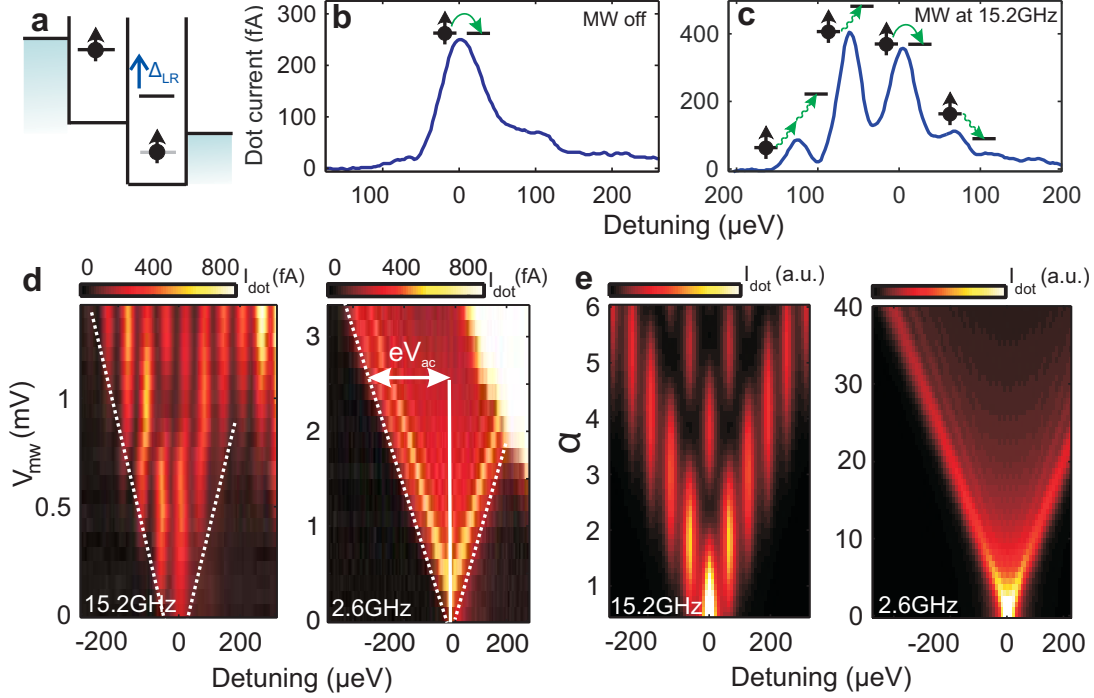
Figure 6.6: (a) Schematic of a double dot with Δ_{LR} (detuning) the difference in the energy the electron needs to access the left or right dot. (b,c) Current through the double dot as a function of detuning with microwaves turned off (b) and on (c). (d)Measured current as a function of detuning Δ_{LR} and microwave amplitude V_{mw} at the gate at $f_{ac} = 15.2\,\text{GHz}$ and 2.6 GHz (applied in continuous wave). The external magnetic field is zero and therefore spin blockade is lifted due to mixing of the spin states through the fluctuating nuclear field [41]. At higher microwave amplitude ($V_{mw} > 0.5\,\text{mV}$ and 1.5 mV respectively), the transition to the right dot triplet state is also visible (in the upper right corner). V_{mw} is determined by the estimated attenuation of the coaxial lines and the switching circuit used to create microwave bursts. (e) Simulated current as a function of detuning and $\alpha = eV_{ac}/(hf_{ac})$ (h Planck's constant) for $f_{ac} = 15.2\,\text{GHz}$ and 2.6 GHz respectively. It reproduces the linear envelope of the measured current as well as, qualitatively, a modulation of the current amplitude in detuning. However the asymmetry with respect to detuning visible in (d) as well as the observed overall increase of the current with V_{mw} is not captured in this model.

The leakage current through the double quantum dot in the spin blockade regime as a function of the detuning Δ_{LR} (defined in Fig. 6.6a) shows at $B_{\mathrm{ext}} = 0\,\mathrm{T}$ a peak at $\Delta_{\mathrm{LR}} = 0$ due to resonant transport and a tail for $\Delta_{\mathrm{LR}} > 0$ due to inelastic transport (emission of phonons) [41] (Fig. 6.6b). Excitation of the right side gate induces an oscillating voltage drop across the tunnel barrier between the two dots, which leads to side peaks at $\Delta_{\mathrm{LR}} = nhf_{\mathrm{ac}}, n = \pm1, \pm2, ...$ away from the resonant peak (Fig. 6.6c). These side peaks are due to electron tunneling in combination with absorption or emission of an integer number of photons, a process which is called photon-assisted-tunneling. In the limit where hf_{ac} is much smaller than the linewidth of the states $h\Gamma$ (Γ is the tunnel rate) the individual sidepeaks cannot be resolved, whereas for higher frequencies they are clearly visible (see Fig. 6.6d).

More quantitatively we describe PAT by following reference [159]. An ac voltage drop $V(t) = V_{\mathrm{ac}}\cos 2\pi f_{\mathrm{ac}} t$ across the interdot tunnel barrier modifies the tunnel rate through the barrier as $\tilde{\Gamma}(E) = \sum_{n=-\infty}^{+\infty} J_n^2(\alpha)\Gamma(E + nhf_{\mathrm{ac}})$. Here, $\Gamma(E)$ and $\tilde{\Gamma}(E)$ are the tunnel rates at energy E with and without ac voltage, respectively; $J_n^2(\alpha)$ is the square of the nth order Bessel function of the first kind evaluated at $\alpha = (eV_{\mathrm{ac}})/hf_{\mathrm{ac}}$, which describes the probability that an electron absorbs or emits n photons of energy equal to hf_{ac} (with $-e$ the electron charge). Fig. 6.5e shows the current calculated from this model including a lorentzian broadening of the current peaks. A characteristic of the n-th Bessel function $J_n(\alpha)$, important here, is that it is very small for $\alpha \ll n$ (i.e. when $eV_{ac} \ll nhf_{\mathrm{ac}}$) and starts to increase around $\alpha \approx n$, implying that the number of side peaks is approximately $eV_{\mathrm{ac}}/hf_{\mathrm{ac}}$. This results in a linear envelope visible in Fig. 6.5e.

We extract eV_{ac} as the width of the region with non-zero current measured at fixed microwave frequency f_{ac} and amplitude V_{mw}. Instead of this width, we can take equivalently the number of side peaks times hf_{ac} (this is possible at frequencies high enough such that individual side peaks are resolved). A reasonable estimate of the error made in determining eV_{ac} is $\pm hf_{\mathrm{ac}}$. Another method to extract V_{ac} is to determine the slope of the envelope (for which a threshold current needs to be chosen) of the PAT response (see Fig.6.6d). Varying the threshold gives a spread in the slope which defines the error of this method. We note that within the error bars both methods give the same result.

In order to estimate from V_{ac} the amplitude of the oscillating electric field at the dot, $|E|$, we assume that this voltage drops linearly over the distance between the two dot centers (a rough approximation), which is approximately 100 nm. This estimate is used in Fig. 6.4a in the main text, and in the approximate determination of the spin orbit length. Note that the uncertainty in this estimate of the spin-orbit length only affects the overall scaling in Fig. 6.4a, but not the fact that there is an up-going trend.

6.6.3 Orientation of the double dot with respect to the crystallographic axis

To determine the orientation of the surface gates with respect to the crystallographic axis of the GaAs/AlGaAs heterostructure, we carry out an anisotropic wet etch. In [160] several wet etchants are described, which result in an anisotropic edge profile, when etching on a [001] GaAs surface. Here we use $HCl : H_2O_2(30\%) : H_2O$ with volume ratio $1 : 4 : 40$ and concentrated HCl. This etchant results in an edge profile as shown in Fig. 6.7a along the [110] direction and as shown in Fig. 6.7b along the [1$\bar{1}$0] direction. We first performed an etch on a wafer with known orientation, which confirmed the information from [160]. We than performed an etch on a sample processed on the same chip and with the identical orientation as the sample used here to find the orientation of the surface gates. This reveals that the double dot axis and given the gate geometry the dominant electric field is along the [1$\bar{1}$0] crystallographic direction. The spin-orbit length relevant in this experiment is hence $l_{SO}^{-1} = m^*(\alpha - \beta)/\hbar$. Note that α and β do not necessarily have the same sign. In fact band structure calculations taking the specifics of our heterostructure into account predict that $|\alpha - \beta| > |\alpha + \beta|$ [161], also in agreement with recent measurements on ballistic spin resonance [162] in a similar heterostructure as the one used here. This suggests, that the electric field in the experiment performed here, was oriented along the crystallographic axis, which corresponds to more efficient coupling between the electron spin and the electric field.
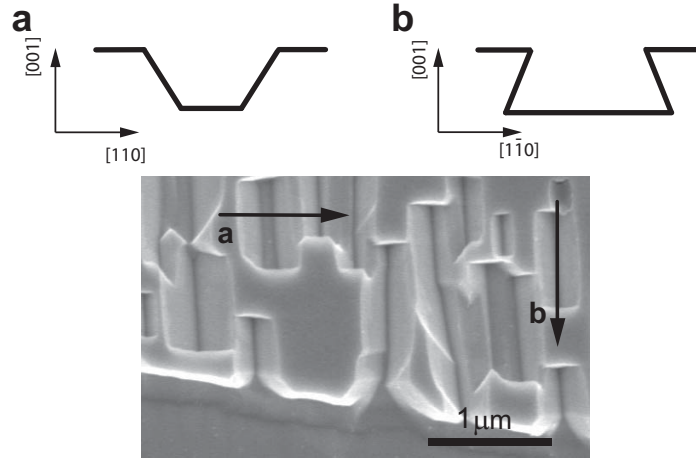
Figure 6.7: (a) and (b) show schematically the edge profiles along the [110] and [1$\bar{1}$0] crystallographic directions respectively. The SEM picture shows an etched [001] surface. A small droplet of the etchant was applied to the surface and rinsed after 20s. The structure as visible in the picture is found at the brim of the droplet.

6.6.4 Upper bound on the ac magnetic field amplitude at the dot

The oscillating gate voltage produces an oscillating electric field at the dot. Here we determine an upper bound on the oscillating magnetic field that is unavoidably generated as well. Since the distance from the gate to the dot is much smaller than the wavelength (20 GHz corresponds to 1.5 cm), we do this in the near-field approximation, where magnetic fields can only arise from currents (displacement currents or physical currents).

An oscillating current can flow from the right side gate to ground via the 2DEG, the coplanar stripline [33], or the neighbouring gates (all these elements are capacitively coupled to the right side gate). We first consider the case of the stripline. The right side gate is about 100nm wide and overlaps with the coplanar stripline over a length of about 10 μm, giving an overlap area of $\approx (1\mu\text{m})^2$. The gate and stripline are separated by a 100 nm thick dielectric (calixerene [108], $\epsilon_r = 7.1$), which results in a capacitance of 0.6 fF. For a maximum voltage of 10 mV applied to the right side gate and a microwave frequency of 20 GHz, this gives a maximum displacement current through this capacitor of $\sim 1\mu$A. This is an upper bound as we neglect all other impedances in the path to ground. Even if this entire current flowed at a distance to the dot of no more than 10 nm (whether in the form of displacement currents or physical currents), it would generate a magnetic field B_{ac} of only $\approx 0.02\,\text{mT}$, more than two orders of magnitude too small to explain the observed Rabi oscillations. In reality, the displacement current is distributed along the length of the gate, and most of the current through the gate and stripline flows at a distance very much greater than 10 nm from the dot, so B_{ac} is still much smaller than 0.02 mT. The maximum magnetic field resulting from capacitive coupling to the other gates and to the 2DEG is similarly negligible.

It is also instructive to compare the power that was applied to the gate for electric excitation of the spin with the power that was applied to the microfabricated stripline for magnetic excitation [33]. For the shortest Rabi periods observed here (220 ns), the power that arrived at the sample holder was less than $\approx -36\,\text{dBm}$ (the output power of the microwave source minus the attenuation of the microwave components in between source and sample holder, measured at 6 GHz – at higher frequencies, the attenuation in the coax lines will be still higher). In order to achieve this Rabi frequency through excitation of the stripline, more than 100 times more power (≈ -14 dBm) was needed directly at the stripline [33].

The upper bounds we find for the oscillating magnetic field generated along with the electric field are thus much smaller than the field needed to obtain the measured Rabi frequencies of a few MHz. We therefore exclude magnetic fields as a possible origin for our observations.

6.6.5 Additional figures: transport triangles with applied microwaves and pulses.
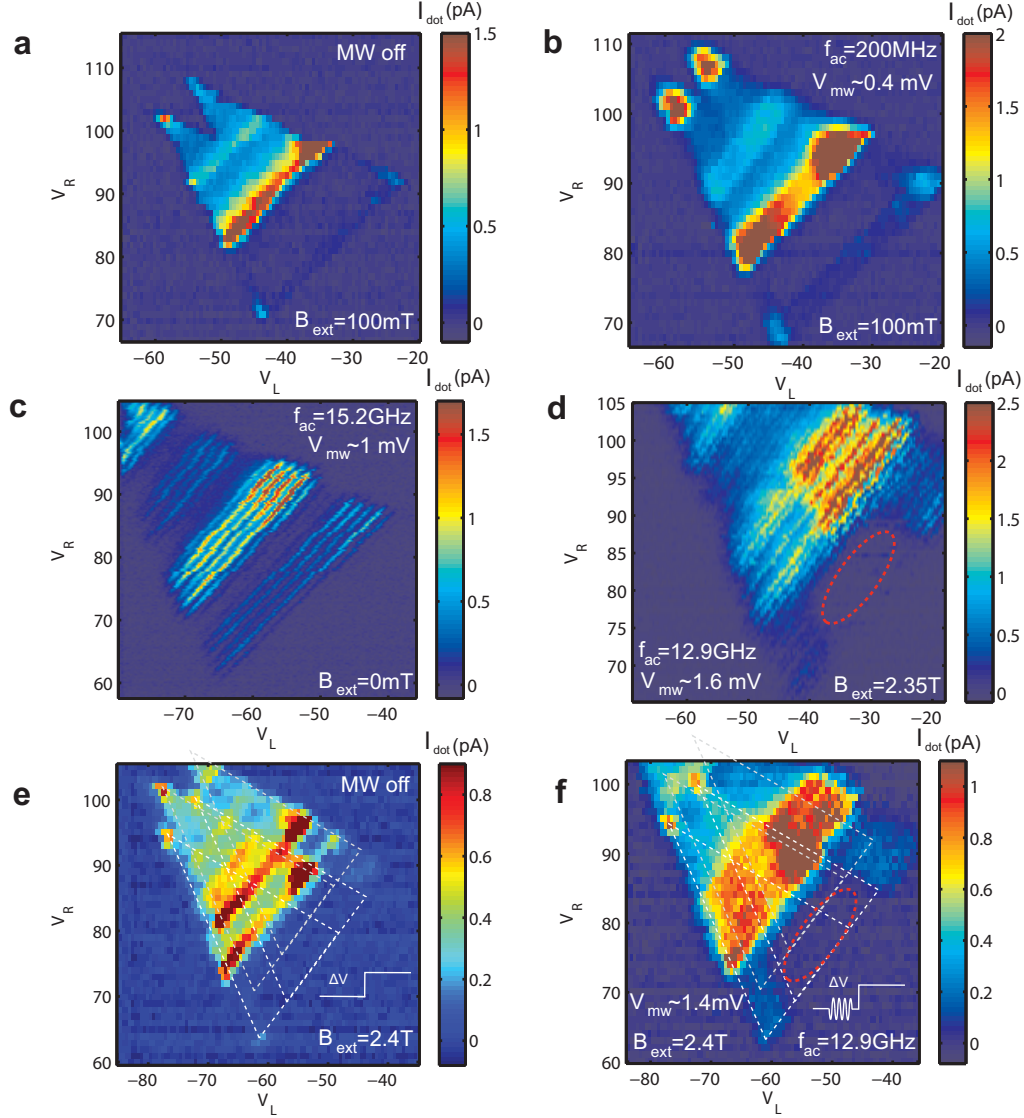
Figure 6.8: (a)-(d) show transport triangles for applied microwaves at different frequencies f_{ac}, applied magnetic field B_{ext} and microwave amplitude V_{mw}. (e)-(f) show transport triangles while only a pulse (e) and additional a microwave burst during the low stage of the pulse (f) is applied. Two 'copies' of the triangle are visible in (e), in (f) the second copy smears out, due to PAT. All parameters are indicated in the figure. The red ellipses show where in a continuous wave measurement (d) and in a pulsed measurement (f) observation of electron spin resonance could be attempted.

Chapter 7

Towards single-shot read-out of two-electron spin states in a double quantum dot

Recent experiments have shown the coherent control of a single electron spin [33], as well as coherent control of the time evolution of two coupled spins in a double quantum dot implementing the SWAP gate [32]. Both experiments however employed a read-out which gives only limited information about the two-electron spin state. Exploring two-spin entanglement or implementing a simple two-qubit algorithm in a double quantum dot requires a read-out which can distinguish four orthogonal spin states of the two-spin system. In this chapter we present the progress of an experiment working towards implementation of single-shot read-out of the four spin states $|\uparrow\uparrow\rangle, |\uparrow\downarrow\rangle, |\downarrow\uparrow\rangle, |\downarrow\downarrow\rangle$ in a double quantum dot by extending the principle used for the single-shot read-out of a single spin [30].

7.1 Introduction

The spin of a single electron is associated with only a tiny magnetic moment, which makes a direct measurement of the spin state, either pointing along $|\uparrow\rangle$ or against $|\downarrow\rangle$ the applied magnetic field, of a single electron very challenging. In a quantum dot it is however easy to measure the charge on the dot. In Ref. [30] single-shot read-out of the spin of a single electron is demonstrated by employing spin-to-charge conversion [31] and detecting the charge in a single shot mode [28]. To achieve spin-to-charge conversion a magnetic field is applied to split the two possible spin states $|\uparrow\rangle$ and $|\downarrow\rangle$ by the Zeeman energy. The electrochemical potentials of the quantum dot are then tuned such that an electron in the spin ground state $|\uparrow\rangle$ cannot tunnel out, whereas an electron in the spin excited state $|\downarrow\rangle$ will leave the dot. Reading out the charge on the dot now reveals the original spin state.

Coherent control of the time evolution of two coupled spins [32] as well as manipulation of a single electron spin (see chapter 4) have been performed in a double quantum dot. In both experiments, the double quantum dot was tuned into the spin blockade regime (see chapter 2) in which the transition from the $(1, 1)$ to the $(0, 2)$ charge state[1] is allowed, if the two electrons form a spin singlet $|S\rangle$, but blocked if they occupy one of the three triplets $|T_{\pm}\rangle$ and $|T_0\rangle$. In the first experiment, the two-electron spin state was restricted to the two dimensional subspace spanned by $|S\rangle$ and $|T_0\rangle$. The two-spins were prepared in e.g. $|\uparrow\downarrow\rangle$ which evolves under influence of the exchange interaction into $|\downarrow\uparrow\rangle$ and back into $|\uparrow\downarrow\rangle$. Coherent oscillations could be measured by rapidly switching the exchange on for a variable time and reading out the spin state after the evolution by measuring the charge state of the double quantum dot. The $(0, 2)$ charge state corresponds to $|S\rangle$ and the $(1, 1)$ charge state corresponds to $|T_0\rangle$. Recently this read-out has also been realized in a single-shot mode [163].

In the second experiment all four spin states were accessed. However, the read-out only revealed information about the spin parity of the two-spin states. The device was configured such that transport occurred via $(0, 1) \rightarrow (1, 1) \rightarrow (0, 2) \rightarrow (0, 1)$. By waiting long enough that a few electrons could go through the double dot, the system initializes in one of the blocked states $|T_{\pm}\rangle$ with even spin parity. The triplet $|T_0\rangle$ with odd spin parity did not block transport, since, for a small energy difference of the $|S\rangle$ and $|T_0\rangle$, the difference in nuclear magnetic field between the two dots rapidly admixes $|T_0\rangle$ and $|S\rangle$ and any occupation of the $|S\rangle$ immediately gets projected due to a fast barrier to the electron reservoir.

In order to explore spin entanglement in a double quantum dot or a two-qubit gate, like the CNOT gate, a read-out is necessary which can distinguish four orthogonal spin states. Here, we aim at extending the read-out scheme applied to a single quantum dot, as described in Ref. [30], such that we can read out the two spins in

---

[1]Here, (n, m) denotes the charge state of the double quantum dot with n electrons in the left and m electrons in the right dot.

a double quantum dot.

7.2 Device and method
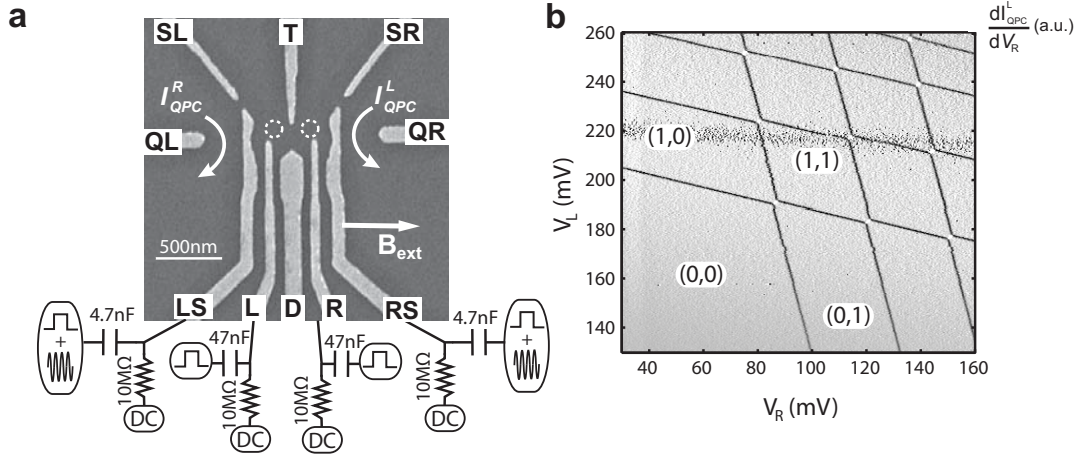
Figure 7.1: (a) Scanning electron micrograph image of a device with the same gate structure as the one used in this experiment. Metallic TiAu gates are deposited on top of a GaAs heterostructure which hosts the 2DEG 90 nm below the surface. The gates LS, RS, T, D are used to form the two quantum dots (white dotted circles). Gates L and R are mainly used to adjust the electrochemical potentials in the dots, but can also be used for fine tuning of the dots. QL and QR are used to form quantum point contacts on the left and right side respectively. Finally, gate SL and SR are used to isolate the electron reservoirs of the quantum dots and the QPC sources. Schematically the four cryogenic bias-tees are shown, which allow us to apply simultaneously a dc voltage, pulses and microwaves to the gates LS, RS, L and R. The values of the resistors and capacitors are indicated. The cut-off frequency for the L and R gate is chosen lower to be able to apply long pulses, necessary for the relaxation measurements (see main text), without differentiating the pulse too strongly. The disadvantage is a longer setting time of the dc voltage on gate L and R. An in-plane magnetic field B_{ext} is applied along the indicated direction. (b) Charge stability diagram of the double quantum dot using the left QPC as charge sensor. Plotted is the differential QPC current dI_{QPC}^L/dV_R.

A scanning electron micrograph of the device is shown in Fig. 7.1a. The gates L, R, T and D are used to form the two quantum dots and to tune them into the few-electron regime, Fig. 7.1b. We measure the current through the left and right quantum point contact (QPC). At a source-drain voltages of 700 μV, $I_{QPC}^{L,R}$ are about 20 nA and an electron tunneling on/off the dot close to the respective QPC changes the current by typically $\sim$ 200 pA. An electron leaving the non-adjacent dot results in a change of the QPC current by a factor of 2 smaller. Note however, that these numbers depend on the tuning of the quantum dots and are subject to change

during the measurement run. The electron reservoirs of the quantum dot itself are grounded.

The QPC currents are sent to room temperature current-to-voltage converters, followed by gain 10 isolation amplifiers and a 40kHz low-pass filter. The data is acquired using a digital oscilloscope (LeCroy Waverunner 44Xi) sampling at typically 5×10^5 samples/s. The rms noise level of this arrangement allows for detection of the step in $I_{QPC}^{L,R}$ resulting from an electron tunneling on/off the quantum dot close to the respective QPC provided that it lasts at least 8μs. In order to also detect the step due to an electron tunneling on/off the non-adjacent dot, the low-pass filter has to be set to approximately 10kHz to further reduce the rms noise level of the measurement. To use the full 40kHz bandwidth, we therefore record the response of both QPCs. More information about the measurement set-up can be found in chapter 3. Pulse spectroscopy, as described in [164], is used to set the tunnel barriers to the electron reservoirs to approximately $\Gamma_{L,R} \approx 1/(0.05\text{ms})$. Real-time detection of the electrons tunneling on and off the quantum dot allows for fine tuning of the tunnel barriers [29].

As indicated in Fig.7.1, fitting of four cryogenic bias-tee allows fast pulsing and microwave excitation of four of the gates. For the read-out it is in principle sufficient to be able to pulse two gates. The possibility to pulse and excite four gates provides more flexibility to combine the read-out later with e.g. performing the SWAP gate as in [32] and microwave excitation to induce spin resonance. Potentially it might also enable direct pulsing of the tunnel coupling. Pulsing the two gates LS and RS to more negative values pushes the two dots towards each other thereby increasing the tunnel coupling. A compensating pulse on gates L and R has to be applied to keep the electrochemical potentials of the quantum dots at the same position.

7.3   Read-out pulse scheme

The read-out scheme used in [30] can be extended in different ways to be applicable to a double quantum dot. Two possibilities are shown in Fig. 7.2. We briefly discuss advantages and disadvantages of these two schemes. In Fig. 7.2 both schemes are shown along with two stages which will be used to initialize the double quantum dot in an unknown spin state. The double dot is first emptied (①), then two electrons with unknown spin state are injected (②) and next the spin states in the left and right dot are measured. In the first scheme, ③ and ④ in the following referred to as read-out I, the left and right dot are brought sequentially into the read-out position, whereas in the second scheme, ❸ in the following referred to as read-out II, both dots are brought simultaneously into the read-out position. In read-out I the signals from the left and right dot are easily distinguished by the timing. In read-out II they have to be distinguished by the height of the QPC responses. In read-out I,
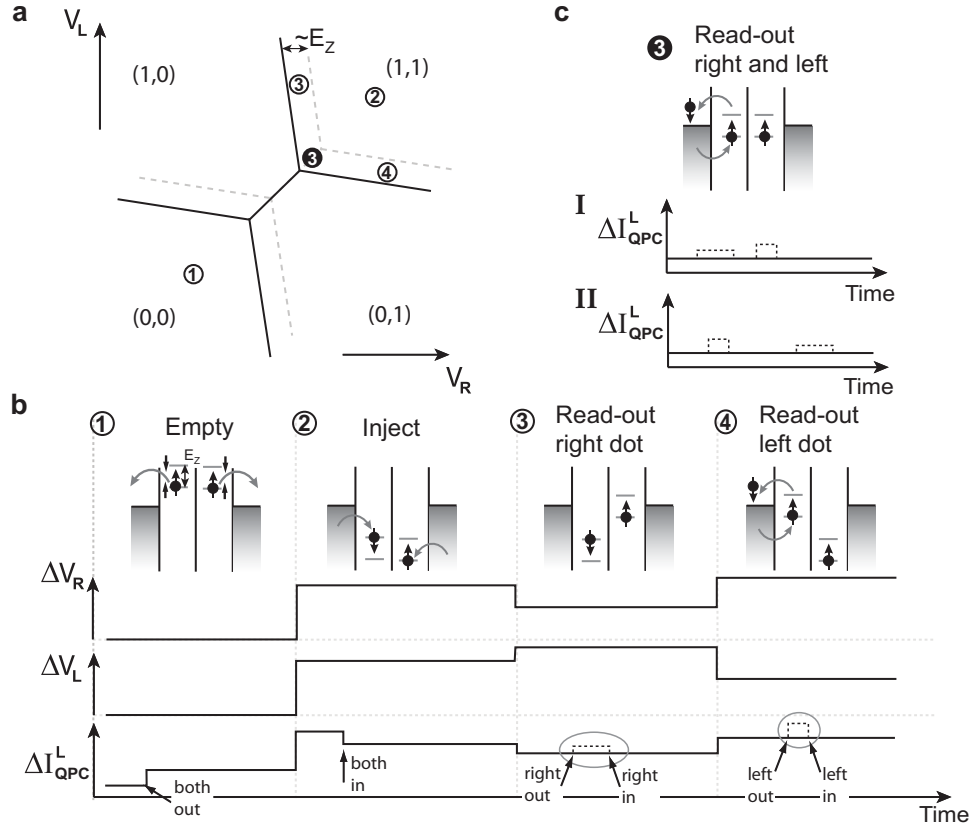
Figure 7.2: (a) Shown is a schematic charge stability diagram containing the $(0,0), (1,0), (0,1)$ and $(1,1)$ charge regions. The dotted lines indicate the Zeeman splitting E_Z. In position ① the double dot is emptied and in ② two electrons are injected. In position ③ and ④ the left and right dot are read out subsequently (read-out I in the main text). Position ❸ can alternatively be used to read out both dots (read-out II in the main text). (b) Schematics of the energy levels of the double quantum dot at position ①-④ together with the shape of the corresponding voltage pulses ΔV_L, ΔV_R applied to gates L and R. For illustration the case of $|\downarrow\uparrow\rangle$ being injected is shown. Also a schematic of the left QPC response is sketched. It mainly follows the pulse applied to gate L. On top of that current changes due to electrons tunneling into the left and right dot as indicated by arrows. For simplicity only one step is shown in the emptying and injecting stage, although two can be observed (two electrons leave and tunnel in). The dotted lines in the read-out stage of the left and right dots are the signature of a spin-down in the left and right dot respectively, which escapes during read-out and is replaced by a spin-up electron, as illustrated for the right electron in the schematics. The different heights account for the difference of contrast in the left QPC for an electron tunneling out of the left or right dot. A corresponding response can be observed in the right QPC. (c) Shown are the energy levels during read-out II in position ❸. I and II illustrate that the same spin state (e.g. $|\downarrow\downarrow\rangle$) can result in different QPC responses depending on which electron tunnels first.

when for instance reading out the left dot, the electron in the right dot will stay in the right dot, due to the detuning between the two dots, whereas in read-out II the electron can tunnel between the dots. In principle, this can be detected by the QPCs, however the analysis of the read-out signal becomes more difficult. How well $|\uparrow\downarrow\rangle, |\downarrow\uparrow\rangle$ can be distinguished will depend crucially on the detection of the potential interdot tunnel events. Note however that it is energetically forbidden to enter the $(0,0)$ charge state during the read-out. The read-out in this sense of left and right dot is also sequential, the order, however, is stochastic. The advantage of read-out II is that the read-out takes place at one position, therefore tuning the read-out will be easier. Also the read-out is potentially faster, since the read-out of the second dot starts immediately after the read-out of the first.

One other important difference is that for read-out I, the exchange interaction between the two electron spins is suppressed during reading out due to the detuning between the two dots. In read-out II the energy levels are aligned, allowing for resonant tunneling. Note however, that by applying a bias voltage over the double quantum dot, a modification of read-out II is possible also featuring detuning of the two dots during read-out. Mainly to avoid tunneling between the left and right dot and the easier way to distinguish the signal from the left and right dot, we pursue implementation of read-out I in the following.

7.4 Tuning the double dot into the read-out position

To perform the read-out, pulses are applied to the gates L and R as sketched in Fig. 7.2b. Note that the bias-tees block any dc-component of these pulses. The dc-voltages applied to L and R need to be fine tuned, such that the position of the electrochemical potentials of the left and right dot during the read-out are as indicated in Fig. 7.2b (③ and ④ respectively). L and R couple not exclusively to the left and right dot, but also (less strongly) to the right and left dot respectively, causing the slopes of the lines in Fig. 7.1b. To make the fine tuning of L and R easier, we compensate for this by not tuning L and R independently, but by using "virtual gates" VL and VR instead. This simply means, that when changing R by ΔV, we compensate by a smaller change $-\gamma \Delta V$ of L to keep the electrochemical potentials in the left dot constant and only shift the right dot potentials. Correspondingly, we proceed for tuning the electrochemical potentials of the left dot. The factor γ and its corresponding value for the left dot can be determined by the slopes of a charge stability diagram as shown in Fig. 7.1b measured as a function of the voltage applied to RP and LP. Fig. 7.3a shows a zoom in on the $(0,1) \leftrightarrows (1,0)$ charge transition measured by sweeping the virtual gates VL and VR, the lines marking an electron tunneling on/off the left and right dot are now vertical and horizontal, respectively. In Fig. 7.3 the (averaged) response of the left QPC for decreasing values of VL is
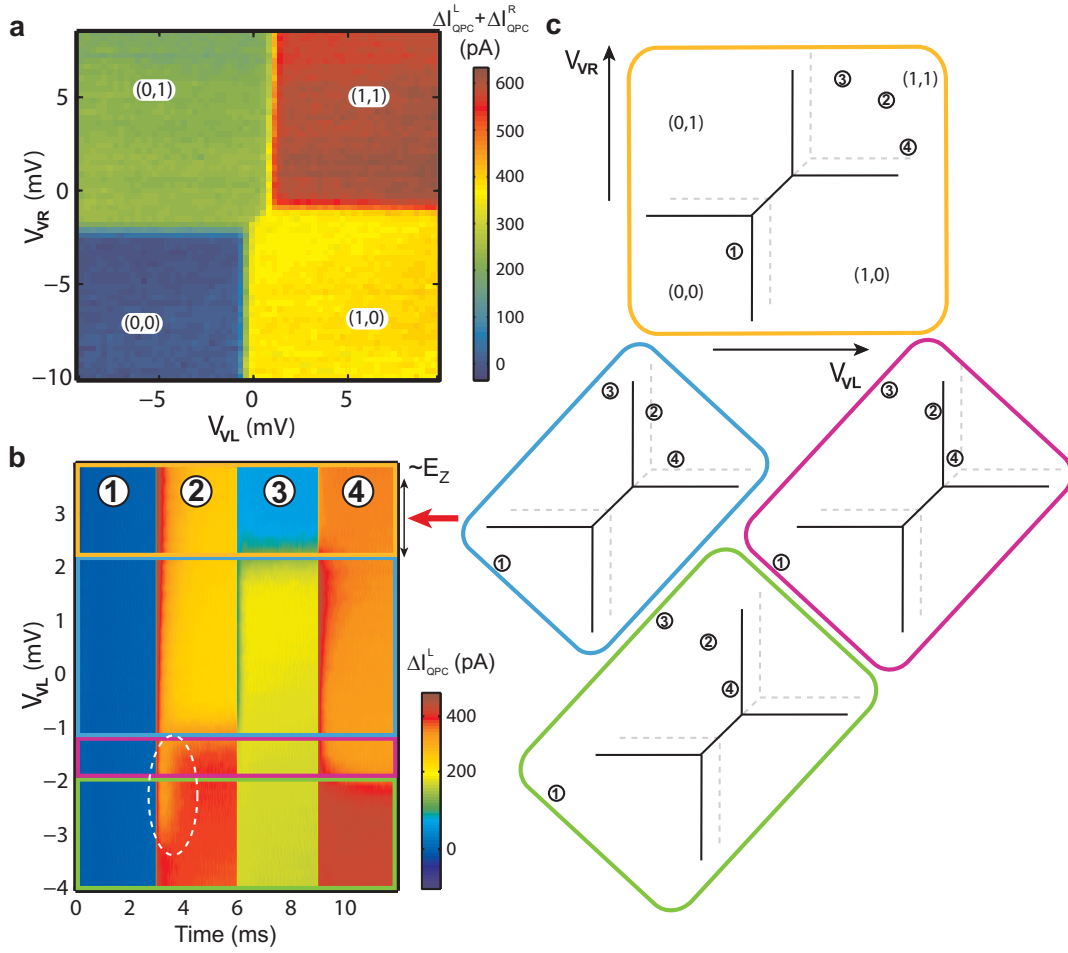
Figure 7.3: (a) Charge stability diagram containing the $(0,0), (1,0), (0,1)$ and $(1,1)$ charge regions measured using the virtual gates VL and VR. Plotted is the sum of the left and right QPC response to enhance the contrast. An offset plane is substracted to compensate for the direct coupling of the gates to the QPCs. (b) Left QPC response ΔI_{QPC}^L to the applied four stage pulse, as discussed in the main text and Fig. 7.2, as a function of the value of VL to find the read-out position of the left dot. An offset is substracted per trace, such that $\Delta I_{QPC}^L = 0$ when the double quantum dot is empty. The response is averaged over 100 repetitions by the digital oscilloscope and mainly follows the applied pulse. On top of that four different regions can be identified, which are further illustrated in (c). The red arrow indicates the optimum value of VL to read out the left dot. The actual read-out will be carried out at higher tunnel rates and shorter duration of the injection and read-out stages. The measurement is taken at $B_{\text{ext}} = 5$T. Note that the 'bump' visible in the injection stage (white dotted ellipse) occurs, because when the injection stage enters the $(0,1)$ charge region the electron in the right dot cannot only be injected directly, but also via $(0,0) \rightarrow (1,0) \rightarrow (0,1)$. $(1,0)$ results in a lower current in the left QPC than $(0,1)$. At more negative values of VL the transition $(0,0) \rightarrow (1,0)$ is no more possible and the bump disappears. (c) Schematic charge stability diagrams. Positions ①-④ indicate the four stages of the applied pulse as in Fig. 7.2. By decreasing the value of VL the stages shift.

105

shown. The value of VR has not yet been set to the read-out position of the right dot, as indicated in Fig. 7.3. Different regions can be identified when changing the value of VL. From this the optimum setting of VL, such that the left dot is in the read-out position during stage ③ of the pulse, can be determined (indicated by the red arrow). The shift in VL corresponding to shifting the energy levels by E_Z is approximately known from measurements using a two step pulse probing the rate at which electrons tunnel into the dots [165]. Once the correct value of VL is found the corresponding scan is done for finding the value of VR. Both scans together yield the setting of VL and VR, such that the energy levels are positioned as shown in Fig. 7.2b.

To test the read-out we aim at measuring the spin relaxation time in the left and right quantum dot by varying the time spent in the injection stage, and monitoring the fraction of spin down events detected from the left and right dot. In preparation for the first attempt, we have addressed a number of problems, which delayed the ongoing experiment, most of them are technical. In a first stage of this experimental run we reproduced the read-out of of a single electron spin by keeping one of the two quantum dots empty. A problem we faced, was, that only very few spin-down electrons were injected during the injection stage. This has also been reported elsewhere [165] and could there be suppressed by lowering the applied magnetic field. However, we were also facing two other problems: the dilution refrigerator did not reach base temperature, it could only be cooled to ~ 100mK and also the electron temperature was as high as ~ 350mK. Therefore, we were only able to lower the field to 5T, which still only gave us very rare spin-down events. Finally, we changed the way how to initialize the single dot. Instead of emptying the dot, we injected two electrons occupying a spin singlet, and let one electron tunnel out in a subsequent stage. Read-out was then done using the difference in energy of the $S \leftrightarrows \uparrow$ and $S \leftrightarrows \downarrow$ transition. This allowed us to measure the relaxation time in a single quantum dot to be ~ 0.7ms at 7.5 T and ~ 4ms at 5T. When attempting the corresponding procedure to read out the double dot, which implies to pulse around the $(1,1), (2,1), (1,2), (2,2)$ charge regions, the measurements got disturbed by a noise band, likely due to an activated charge trap, which is visible in Fig. 7.1b. Though there were still options as using larger amplitude pulses and fill the dot in $(2,2)$, let electrons tunnel out in $(1,1)$ and read-out in the positions indicated in Fig.7.2 we decided to warm up and first solve some of the technical problems before proceeding. Major changes for improving the electron temperature are RC filters at base temperature with a high cut-off frequency (~ 1 MHz, resistor 470Ω, capacitor 270pF) in the fast lines used to carry the current to the room temperature IV converters, interchanging source and drain of the QPCs, so that the fast connection is not directly adjacent to the dot reservoir and grounding the dot reservoirs directly on the cold finger. At this moment the measurements are starting again and the electron and fridge temperatures look promising. This will allow us to attempt the read-out at lower field, which potentially will help to overcome insufficient injection

of spin-down electrons. Also the noise band visible in Fig.7.1 is no more in the region of interest, which gives us greater flexibility in where to carry out the read-out.

7.5 Conclusions

To summarize, we have prepared the measurement set-up and software to be able to perform the read-out of the four possible spin states $|\uparrow\uparrow\rangle, |\uparrow\downarrow\rangle, |\downarrow\uparrow\rangle, |\downarrow\downarrow\rangle$ in a double quantum dot. Our strategy to tune the double dot into the read-out position is already implemented and at the time this thesis has to go into press the mainly technical problems which prevented us up to date from actually performing the read-out seem largely solved.

After testing the read-out, we will attempt to measure an anti-correlation in the measurement outcomes, when a spin-singlet is prepared in the double quantum dot. This can be achieved by pulsing to the $(0, 2)$ charge region and transferring the injected $S(0, 2)$ non-adiabatically into a $S(1, 1)$. In the case that the read-out can be performed at low enough magnetic field also combination with electrically induced spin resonance is feasible. Furthermore, the ability to pulse and excite four gates gives great flexibility and might allow us to pulse the tunnel coupling, perform a SWAP [32] and ultimately to attempt a CNOT gate.

Chapter 8

Conclusions and outlook

In this section we briefly summarize the experiments discussed in this thesis and place them into the context of the general progress made towards implementing qubits using electron spins in quantum dots. For an excellent and extensive review see [35].

Since the initial proposal by Loss and DiVincenzo in 1998 [15] all basic building blocks needed to realize electron spin qubits in quantum dots have been demonstrated. Development of single and double quantum dot designs allowing for controlling the number of electrons down to a single electron enabled experiments resolving the Zeeman splitting of a single electron [124] and showing single-shot read-out of an individual electron spin [30]. The single-shot read-out was realized using spin-to-charge conversion making use of the difference in energy of spin-up and spin-down electrons. More recently a special regime in double quantum dots has been the focus of many experiments (e.g.[121, 88, 122, 41]) and enabled a series of experiments (e.g. [32, 33, 166]): the Pauli spin blockade. The Pauli spin blockade provides a way to convert spin information into charge information, but in contrast to the read-out in [30], the relevant charge transition is not to the electron reservoir but in between the two quantum dots. This regime allowed to observe and to manipulate for the first time the coherent evolution of electron spins in a double quantum dot by electrically controlling the exchange interaction between the two adjacent spins [32]. In doing this, the SWAP gate between two spins in neighboring quantum dots was implemented, one of the main ingredients in the original proposal by Loss and DiVincenzo [15].

Early on it was proposed to induce single spin rotations by magnetically driven electron spin resonance (ESR) and to detect them by employing the single-shot read-out of a single electron spin [119, 120]. This turned out to be technically challenging due to conflicting requirements for the read-out and for driving ESR. The read-out requires a high magnetic field, such that the Zeeman splitting overcomes the temperature broadening of the electron reservoir, whereas for ESR low magnetic fields are desirable, because that allows using an ac magnetic field with relatively low

frequency. At high frequencies the striplines designed to generate the ac magnetic field, needed to drive ESR, were accompanied by strong ac electric field, which made the read-out impossible due to photon assisted tunneling.

Employing the Pauli spin blockade to detect single spin rotations solved this problem, because the temperature broadening in the leads is not relevant and therefore experiments can be performed at comparably low magnetic field. In ref.[33] for the first time coherent control of a single electron spin was realized by magnetically driven ESR in a double quantum dot by generating the ac magnetic field with an on-chip coplanar waveguide. The spin blockade is employed as a means to read-out the spin state of the electron in the double dot. This experiment is described in chapter 4 of this thesis. Using the coherent control a quantitative understanding of the timescales and mechanisms by which the spin loses phase coherence can be gained. This is also explored in chapter 4 of this thesis, which discusses Ramsey and spin echo measurements of a single electron spin in a quantum dot. The measurement of a Ramsey fringe by varying the phase between two subsequent bursts of the ac magnetic field demonstrates the ability to rotate the electron spin about any arbitrary axis, which therefore provides universal control of the electron spin state. The main source of decoherence is identified to be the hyperfine interaction of the localized electron spin with the randomly fluctuating nuclear spins of the host lattice. The coupling of the localized spin to the uncontrolled nuclear spin bath gives rise to rapid dephasing within a few tens of nanoseconds. The dephasing can be reversed by a spin-echo pulse which allowed us to measure the Hahn echo decay time to be 0.5μs at 70mT. Both findings are comparable to the timescales determined by Ramsey and spin echo measurements of the dephasing of a two-electron spin state in a double quantum dot [32]. The nuclear spins are not only dephasing the electron spin, but since the hyperfine interaction acts both ways, the electron spin can act back on the nuclear spin bath. In chapter 5 the observation of electron-nuclear feedback is reported in the case of continuous wave excitation of electron spin resonance. From simple theoretical arguments one can conclude that the randomness of the nuclear field has been reduced at least by a factor of 10 in the discussed experiment.

While the electric fields were considered an experimental nuisance in the successful experiment to magnetically induce electron spin resonance, we show in chapter 6 that electron spin resonance can actually also be induced by ac electric fields in GaAs. Though magnetically induced electron spin resonance for the first time enabled coherent control of a single spin, it is highly desirable to achieve manipulation of the electron spin by means of electric fields only. Electric fields are easier to generate, can be excited locally and exciting them results in less ohmic heating on-chip. The ac electric field used in chapter 6 to induce single spin rotations was generated by applying an ac voltage on one of the local gates used to define the quantum dot. Together with the SWAP gate [32], which was realized by electrically controlling the exchange interaction between two adjacent electron spins, this brings all-electrical control of electron spin qubits into reach. In the experiment reported in chapter

6 the coupling between the electron spin and the ac electric field is mediated by spin-orbit interaction. Coupling of spin and electric fields by spin-orbit coupling is well known in the context of quantum dots as the main spin relaxation mechanism. It is theoretically predicted [84, 67, 69] and supported experimentally [30, 77, 78], that the combination of uncontrolled electric fields from phonons and spin-orbit coupling gives rise to the observed relaxation times, which can be as long as 1s [78]. Other experiments demonstrating electrically driven electron spin resonance have been performed by employing nuclear field gradients [97] and magnetic field gradients generated by an on-chip micromagnet [167]. Since the nuclear field is not controlled, no coherent oscillations could be observed in [97].

The drawback of using spin blockade to read out the spin state in a double quantum dot is that only information about the parity of the two-electron spin state is obtained: parallel spins can be distinguished from anti-parallel spins. To perform two-qubit experiments as e.g. a CNOT gate a read-out of all four possible two-spin states is necessary. Chapter 7 presents the progress of an experiment, which attempts to extend the read-out scheme demonstrated for a single electron spin [30] to a read-out of spins in a double quantum dot.

8.1 Near future and present themes

Here, we give an overview of possible near future themes and discuss potential ways for improving existing manipulation techniques and coherence properties of single spins confined in quantum dots.

8.1.1 Integrating read-out, coherent control and the SWAP gate in a single experiment

All basic building blocks to implement electron spin qubits have been experimentally demonstrated, hence the next natural goal is to combine the developed techniques to read-out, drive single spin rotations and perform the SWAP gate in a single experiment. This would enable for example exploring two-spin entanglement, performing a CNOT gate or running a simple two-qubit algorithm.

However this goal is at present still very challenging: (i) The separate experiments have been performed in different experimental regimes concerning applied magnetic field and tunnel coupling between the two quantum dots. (ii) The two electron spins need to be addressed individually. It is expected that electrically driving spin resonance enable this, since an electric field can be generated locally. However individually addressing of the two spins has been so far only demonstrated by using the magnetic field gradient of a micromagnet, which causes a difference in the resonance frequencies of the two dots [167]. (iii) A read-out distinguishing four orthogonal two-spin states needs to be implemented.

There are different routes towards solving issues (i)-(iii). One route which can be pursued right away with existing double dot devices, is to implement the double dot read-out as attempted in chapter 7. This imposes the requirement of sufficient high magnetic fields, since spin-to-charge conversion in this schemes requires a Zeeman splitting larger than the temperature broadening of the lead. For electrically driving spin resonance based on spin-orbit coupling, this is in principle even beneficial, since the driving becomes more efficient with higher applied magnetic field. In reality for a magnetic field beyond 3T, and hence frequencies above 20GHz, the microwave engineering becomes challenging, which will have strong impact when trying to fulfill requirement (ii). If the electric field is generated through excitation of one of the side gates it is expected, that it mainly shifts the quantum dot adjacent to the gate. Residual coupling to the other dot could be eliminated by applying a lower amplitude ac voltage with a phase shift of π to the other side gate for cancelation. In this way it might be possible to achieve individual control of the two spins in the double quantum dot without using a micromagnet. The success of this route will largely depend on many technical factors. This is among other reasons due to the fact that the energy-selective read-out is very sensitive to the electron temperature and electrostatic fluctuations.

Another route for implementing the read-out via spin-to-charge conversion is by making tunneling of the electron to an adjacent "read-out dot" dependent on its spin state. There are different ways to accomplish this. If the magnetic field is larger in the read-out dot than in the dot holding the spin, for instance due to an on-chip micromagnet or a prepared difference in nuclear magnetic field, energy selective tunneling can be used similar to the read-out involving the electron reservoir. A variation of this scheme, in which the two dots are detuned and the first photon-assisted tunneling sideband is excited, has been recently realized [168]. Due to the difference in magnetic field, tunneling of spin-up and spin-down electron occurs at different frequencies of the applied electric field. However, this scheme is still sensitive to charge noise. Alternatively, the read-out dot could hold an electron initialized in spin-up. Trying to transfer the electron in the other quantum dot to the read-out dot establishes a spin-to-charge conversion due to spin-selective tunneling in the spin blockade regime. Also here a small difference in magnetic field between the two dots is required, which in GaAs is naturally provided by the nuclear fields. Without the nuclear fields the T_0 triplet component does not decay and there is a chance that the electron will not tunnel even though it is a spin-down. Advantage of this read-out scheme is, that it does not require a strong magnetic field gradient. Since it is not based on energy selection, it is also less susceptible to charge noise. The advantage of the scheme employing a micromagnet is, that it is a non-destructive measurement. Both read-outs require ancillary quantum dots, implying that a quadruple dot sample needs to be made to implement a two-qubit experiment. The advantage though compared to the read-out in [30] and chapter 7 is that the schemes are less sensitive to temperature and, in the case of the scheme

112

employing spin blockade also to charge noise. Furthermore they allow to isolate the quantum dots from the surrounding electron reservoirs.

8.1.2   Improving coherence times

The main obstacle to the realization of electron spin qubits in quantum dots is the coupling of the spin to its uncontrolled environment imposed by the host material. While relaxation processes are relatively slow (T_1 1s) and dominated in GaAs by the combination of spin-orbit coupling and phonon emission, much faster decoherence processes result from the hyperfine interaction between the electron spin and the nuclear spins of the host lattice. The randomness of the nuclear field gives rise to dephasing of the electron spin within $10-40$ns [134, 32]. By applying an echo pulse, the Hahn echo decay time was found to be ~0.5μs at 70mT for a single spin [134] and 1μs at 100mT for a two-spin state [32]. Note that the random nuclear field not only leads to dephasing, but also gives rises to offset errors in the single spin rotations reported in chapter 4 and 6 and is one of the limitations for increasing their fidelity.

Reducing the randomness of the nuclear field
The dephasing time can be extended through polarization of the nuclear spins. However, to extend the dephasing time by an order of magnitude, a polarization of above 99% is required, but the best result so far reached is only <90% in quantum dots [139]. Another approach is to exploit feedback from the electron spin to the nuclear spin bath. By tuning the double quantum dot properly close to S/T_+ and S/T_- anti-crossings, spin can be transferred to the nuclear spin bath leading to dynamic nuclear polarization. This polarization process can be made self-limiting by balancing the polarization processes in the two directions. It is predicted that this type of feedback can reduce the fluctuations in the nuclear field significantly [129]. It has been demonstrated that by pulsing repeatedly first adiabatically through and non-adiabatically back through the S/T_+ anti-crossing results in spin-transfer to or pumping of the nuclear spin [169, 170]. In [137] this was used too reduce the difference in nuclear magnetic field between the two quantum dots, extending the $S-T_0$ dephasing time up to a factor of ~70.
Another type of hyperfine induced feedback is present when we continuously drive magnetic resonance. It locks the electron spin into resonance with the microwaves (see chapter 5). This locking is also predicted to reduce the fluctuations of the nuclear spin in (one of the two) dots [145]. An experimentally and theoretically little explored question concerns how the proposed and observed pumping and feedback mechanisms influence the echo decay time.

Other materials
The most successful experiments which study electron spins in laterally gated quantum dots so far have been realized in GaAs/AlGaAs heterostructures. Ga, As and

Al have non-zero nuclear magnetic moment. The only semiconductors that have stable isotopes without nuclear moments are C, Si and Ge. Through isotopic purification nuclear spins could be removed from these materials. In that case, the spin decoherence time is expected to be dominated by the relaxation time originating from spin-orbit interaction (see chapter 2) which in the case of GaAs is beyond one second at 1T [78]. It is likely longer in C and Si due to weaker spin-orbit coupling (smaller atomic number) and differences in the available phonon modes. Experimentally different strategies are pursued to realize electron spin qubits in these alternative materials.

The approach which is the closest to lateral quantum dots defined in a GaAs/AlGaAs heterostructure is to use lateral quantum dots in a Si/SiGe heterostructure. By now it has been demonstrated that it is possible to form single and double quantum dots in Si/SiGe and that they can be probed both by measuring transport[171] and charge sensing [172]. In a double quantum dot the tunability of the center barrier has been demonstrated [173] and more recently the spin relaxation time has been measured to be T_1 160ms at 1.5T for about 6 excess electrons in the dot [174]. Working with Si/SiGe is lithographically more challenging because in order to obtain the same energy splittings as in GaAs, the quantum dot needs to be smaller, due to the higher effective mass. For the same reason tunnel barriers tend to get opaque very easily. Due to the larger g-factor of Si and lower (or even absent) nuclear magnetic field, for instance magnetically driven single spin rotations will likely have a much higher fidelity compared to GaAs. The most important challenge in working with a Si/SiGe heterostructure might be charge noise, which seems still to be stronger compared to GaAs [172, 175], which will make the realization of the SWAP gate as done in ref. [32] more difficult. Another aspect which makes the orbital structure of quantum dots in Si more complex is the six-fold valley degeneracy of bulk Si. This degeneracy can be lifted by confinement and strain, but can still give rise to only small orbital splittings and will influence how clearly for instance spin blockade can be observed in different Si/SiGe structures [175, 171]. Apart from laterally defined quantum dots experimental progress has also been made to create a double quantum dot in Ge/Si nanowires featuring charge sensing [176].

Next to silicon carbon is also a promising material. In the past few years progress has been made to study single electron spins in carbon nanotubes. Experiments have demonstrated gate-defined double quantum dots [177, 178] and explored the spin blockade regime in C^{13} enriched nanotubes [179]. Recent advances in fabrication made it possible to explore ultraclean devices [180], which allowed tuning a double quantum into the few-electron regime [181]. Similar to the case of Si an additional orbital degeneracy is present due to the two possible electronic orbits encircling the nanotube circumference clockwise and anti-clockwise. Also, it has been recently shown that due to the strong curvature of a nanotube spin-orbit interaction is induced [182], which has consequences for the spin relaxation time [183]. Instead of nanotubes also a single layer of graphene might be used [184] and first steps towards

realizing gated dot structures has been made, e.g. [185], although it still remains to be seen what the role of disorder is and how well tunable these devices can be made.

To study single electron spins in a semiconductor also a broad range of other systems apart from gate-defined quantum dots are studied, as e.g. phosphorus donors in Si, N-V centers in diamond and self-assembled quantum dots. It is however beyond the scope of this chapter to discuss these.

Alternative encodings of the logical qubit

Instead of encoding the qubit in the spin of a single electron, it has been proposed to encode a logical qubit in the two-electron singlet S and the unpolarized $m_z = 0$ triplet state T_0 close to the $(1,1) \leftrightarrows (0,2)$ charge transition [186]. At high enough magnetic field, leakage to the triplets $T_{+/-}$ with $m_z = \pm 1$ is suppressed. Dephasing between S and T_0 is induced by a random difference in nuclear magnetic field between the two quantum dots, but can be suppressed by a large enough qubit or exchange splitting J. In addition to this suppression an immediate advantage of this qubit is the built-in non-destructive read-out via charge detection. The SWAP gate [32] interpreted in the context of this $S - T_0$ qubit provides rotation around the qubit quantization axis and recently universal control of this qubit has been demonstrated enabled through a controlled pumping scheme that builds up a controlled difference in nuclear field between left and right dot [166]. The major drawback however of using the $S - T_0$ qubit is its sensitivity to charge noise, which can lead to fluctuations in the qubit splitting J. Also the scheme envisioned to couple two qubits is sensitive to charge noise is [187]. It relies on the capacitive coupling of the electrons in adjacent double quantum dots. First attempts to realize the two-qubit gate are reported in [188].

Higher magnetic fields

The reported Hahn echo decay times of 0.5μs at 70mT for a single spin [134] and 1μs at 100mT for a two-spin state [32] were both measured at relatively low magnetic fields. At higher fields hyperfine mediated nuclear flip-flops are expected to be further suppressed and echo decay times up to 100μs are predicted [189, 190, 103]. Very recently spin echo measurements of the dephasing of the two-electron S and T_0 spin states have been reported to yield echo decay times as long as 30μs at external magnetic fields larger than 400mT [191]. By applying Carr-Purcell-Meiboom-Gill decoupling pulses the echo time could be extended even further [191]. Since the microscopic mechanisms changing the difference in nuclear field between two quantum dots are identical to those changing the nuclear field in a single dot, a similar result is anticipated for a single spin. This actually holds the promise, that decoherence due to the slowly evolving nuclear spin bath might also be overcome by improving the fidelities of single and two qubit gate operations.

8.1.3 Improving single and two spin coherent control

Currently single spin rotations as well as the $\sqrt{SWAP}$ gate have been realized. In principle these two operations are a universal set of quantum gates, i.e. every unitary operation on an arbitrary number of qubits can be decomposed into combinations of only these quantum gates [192]. However to be useful for exploring the possibility to use electron spins in quantum dots for quantum information processing, the fidelities and duration of the gates have to be dramatically improved.

Single spin rotations
The fastest $\pi/2$-rotation of a single electron spin in a gate defined quantum dot realized to date has been performed in 27 ns (see chapter 3) with an estimated fidelity of 75% for a π-rotation starting from initial state $|\uparrow\rangle$. The accuracy of the single spin rotations is limited by the offset error introduced by the nuclear field fluctuations. By reducing the randomness in the nuclear field by a factor of ten (see previous section) the gate fidelity can exceed 99%. In fact due to the slow evolution of the nuclear magnetic field, it might even be sufficient to measure the nuclear magnetic field (by e.g. measuring the ESR resonance position) prior to performing a series of gate operations. This would result in a similar improvement of the single spin rotations, given that the excitation frequency can be adjusted on a fast timescale. However in order to come close to the estimated threshold of being able to perform 10^4 gate operations within the decoherence time, as is required to perform error correction, also the speed of the rotations has to be improved. For a decoherence time of 10μs this would imply performing a single spin rotation in 1ns. In the case of magnetically driven spin resonance that would require an oscillating magnetic field of 75mT, which is unlikely to be achieved among other reasons due to ohmic heating of the chip. Electrically driving spin resonance will be further discussed below.
As an alternative to single spin rotations via spin resonance, it has been proposed to realize single spin rotation through a switchable exchange interaction [193]. However, the proposed scheme requires an ancillary qubit as well as a magnetic field gradient. Considering the progress in fabrication of on-chip micromagnets [167], first efforts towards demonstration of this scheme can be expected in the near future. As already mentioned in a previous section, also in the case of the $S-T_0$ qubit, spin resonance is not required. The single qubit rotations are realized through the switchable exchange interaction and a difference in magnetic field between the two quantum dots. Single spin rotations, induced by a difference in the nuclear magnetic field in the two dots, have been reported to be as fast as 1ns [166]. Another proposed scheme takes advantage of encoding the logical qubit in two of the eight spin states of a triple quantum dot [194]. Arbitrary single qubit rotations as well as two-qubit gates can in principle be performed with a tunable exchange interaction only. First attempts towards an implementation of such a qubit can be found in [188].

Different ways to electrically induce electron spin resonance

In the case of electrically driving the electron spin, the fastest $\pi/2$-rotation has been performed in 55 ns. Increasing the electric field amplitude is necessary to achieve faster spin rotations. The electric field amplitude in the experiment reported in chapter 6 and also in [167] was limited by photon assisted tunneling (PAT) to the electron reservoirs and the $T(0, 2)$. At the highest frequencies, the electric field amplitude was limited by the microwave power we were able to generate at the sample. PAT might, to some degree, be suppressed by canceling out unwanted electric field components (see e.g. supplementary of [33]), which requires better knowledge of the electric field geometry. PAT can be further suppressed by isolating the quantum dots more from the electron reservoirs, which is possible if initialization in future experiments is not done via a transport cycle. From the estimate of the electric fields, we can conclude that in chapter 6 the quantum dot was displaced over a distance $\sim 5\%$ of its own size. When the electric field amplitude is increased much more, the generated effective magnetic field increases no more linearly with the amplitude and direct transitions to higher orbitals in the same dot become possible. Also deformation of the dot potential can start to play a role [157].

In the case where spin-orbit coupling provides the coupling between the spin and the electric field, the speed of the gate operation can be further enhanced by increasing the external magnetic field, with the consequence that excitation will be technically more challenging due to the higher microwave frequencies. In the case where a magnetic field gradient generated by a micromagnet is used [167], the design and material of the micromagnet itself still leaves room for improvement. The downside of strong magnetic field gradients is, that in combination with uncontrolled electric fields, coming from charge noise, gate noise and phonons, additional dephasing is introduced. Using the nuclear magnetic field gradient for coherent control of the electron spin remains challenging. By now control over the longitudinal nuclear field components has been demonstrated [137, 166], but ESR requires a gradient in the transverse field direction. A possibility is to build up a longitudinal gradient and manipulate the nuclear field by means of a NMR pulse. The nuclear spin polarization will however precess in the external magnetic field and dephase slowly.

Which method of coupling electric fields and spin is the most advantageous also depends on the chosen host material. In Si/SiGe for instance spin-orbit coupling is much weaker, which favors the use of a micromagnet. On the other hand, charge noise is presumably stronger, which leads to dephasing in combination with a field gradient. Furthermore a micromagnet adds extra complexity to the devices. For individual addressing of the electron spins it remains still to be seen, wether a micromagnet is necessary or the electric fields can be generated sufficiently localized (potentially also by compensation schemes) to only address a single electron spin. It is difficult to estimate how far one can get by pushing the mentioned improve-

ments. Within existing schemes an improvement by a factor of ~ 5 seems feasible, beyond that it remains speculation.

SWAP gate

The two-qubit SWAP-gate has been performed in 180 ps [32], limited by the rise time of the fast voltage pulses, allowing for 7000 operations within the reported decoherence time of 1.2 μs. Even shorter gate operation times down to 40 ps are in principle possible because a singlet-triplet splitting of 120 μeV can be achieved. The fidelity of the SWAP-gate is limited by nuclear-spin [195] and charge-related dephasing [196]. The latter can be understood from the fact that the singlet-triplet splitting J depends on the level detuning ϵ and tunnel coupling between the two dots; both are susceptible to charge noise. In order to achieve higher fidelity for the two-qubit gate, one should use higher J [195]. Alternatively one could try to exploit potentially present 'sweet-spots' at which J is to first order independent of ϵ [197], or further reduce the charge noise [198].

8.2 Far future - scaling

At this point the first tunable few-electron triple dots in GaAs have been reported [199, 200, 188] and it is likely that with an extension of the current gate design samples with more than three quantum dots will be realized. These experiments will be however technically very challenging. Right now every single dot requires careful and time consuming tuning. The fine tuning of the dots does not always follow a well defined protocol, but is often based on trial and error or an "acquired intuition". Lithographically identical quantum dots can behave very differently due to impurities and disorder in the structure. This also makes ab initio simulations of the structures only useful for qualitative studies rather than predicting the experimentally necessary voltages to be applied to the gates to form a dot. Currently the time needed to form and tune the quantum dots will pose an important bottleneck for the number of qubits which can be realized. Another challenge lies in the necessary equipment to be able to operate each quantum dot as a qubit. This requires a large number of high frequency lines going to the sample, which needs to be at cryogenic temperatures, and the sources for generating pulses and microwaves. With the current status of the materials and an, at the moment, state of the art laboratory it will be very challenging to go beyond 10 qubits.

Another aspect is whether or not long-distance communication can be implemented for electron spin-based qubits. In principle communication between distant qubits in an array can be established via nearest neighbor interaction. This comes however at a cost of an even higher error threshhold (estimated to be 10^2 higher compared to qubit arrays where long distance communication is possible [192]). Numerous proposals are available describing ways to establish long distance communication, as

118

e.g. coupling to a superconducting transmission line making either use of the charge states of the double quantum dot or strong spin-orbit coupling, e.g. [201, 202]. However at this stage it is hard to oversee which of the proposed schemes are likely to be experimentally feasible.

8.3 Conclusion

In the past few years experimental research pursuing the idea of realizing spin-based quantum computation by using single electron spins in quantum dots has produced many exciting results among which are the coherent control of a single spin and the time evolution of two spins. At a modest level, spin qubits in quantum dots satisfy the basic criteria for implementation of quantum information processing as outlined by DiVincenzo [203] (see also [35]). However, whether a quantum computer based on electron spins in quantum dots will ever be build remains an open question. In the near future, experiments will aim at combining all basic building blocks (read-out, ESR, SWAP) in a single experiment, which will allow for exploring quantum coherence in semiconductor structures as for instance entanglement and the quantum measurement process.

Open questions are which material system is the most promising and which way to manipulate the electron spins should be chosen. Both are likely to be decided not only by aspects as the strength of the spin-orbit coupling and the absence or presence of nuclear spins in the material, but to a strong degree also by which material system can be improved the most in terms of charge noise, impurities and disorder to be able to reproducibly create the quantum dots. Furthermore many material systems still need to be explored more detailed to answer questions as, for example in Si/SiGe, what the consequences of the valley degeneracy are.

Currently many ideas are still generated and explored and although final success is not guaranteed, without doubt the ongoing research towards realizing a spin-based quantum computer will yield many useful techniques and exciting physics along the way.

Keep spinning!
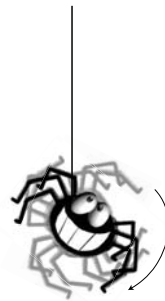
Chapter 9

Appendix

9.1 Fabrication recipe

In this appendix we summarize the current fabrication recipe used to fabricate the device measured in chapter 7. The fabrication recipe for the sample used in chapters 4 - 5, including fabrication of the coplanar waveguide, can be found in [110].

First some general remarks:

- The evaporation rates given in the recipe are mainly determined by the evaporator. For the big structures like the alignment markers and the large gates a higher rate is desirable, to shorten the time the evaporation takes. However a higher rate in the used evaporator could not be reached due to a maximum possible current through the filament.

- For all steps apart from the fine gates the given values for the dose, beam current and spot size only have to be met approximately. The given value for the dose is the lowest value which worked during the recent fabrication. A $100 - 200 \mu C/cm^2$ higher dose can be applied without noticeably changing the structure, the only disadvantage being a longer writing time. A lower dose might result in too much resist residues after development. For the fine gates a dose test is done on a small spare corner of the chip.

- The lift-off is faster if the acetone is warmed up in a au-bain marie. Note that acetone boils at about 56°C. Also note that warm acetone evaporates extremely fast, such that care needs to be taken when taking the sample out of the beaker. Using a spray bottle with acetone is used to facilitate the lift-off, already starting spraying, while taking the sample out avoides having acetone drying in on the sample

- The details of the first resist layer (17.5%wt Copolymer) used for the alignment markers and the ohmics are : 8%wt MMA(methamethyl acrylate) in

MAA(methylacrylic acid) in ethyl-actate. In the Delft cleanroom the bottle is marked as 8%PMMA/MAA (17.5%) Ethyl Lactate .

- The used spinner is programmed to always spin at 500rpm in the first 5s of the spinning recipe.

(a) **Substrate preparation**

Cleaning front side:

- acetone clean (5 min)
- IPA rinse (30 s)
- N_2 (g) dry
- oven 120°C (10 min)

Clean Ga on the back side (necessary in case of wafers from Wegscheider group) :

- 1-2 μm photoresist, e.g. S1813 on front side
- bake on hot plate: 80° (10min)
- 2 min in hot HCl (50°C)
- H_2O rinse (30 s)
- N_2 (g) dry
- acetone (30 min)

Remarks:

- Baking the photoresist to hot (even 120°C) resulted in resist residues which could not be removed, also not with an oxygen plasma strip
- Sonicating the chip is also possible. However care needs to be taken, because GaAs cleaves very easily (it happened to me once in the ultrasonic...).
- Once it was necessary to wipe the surface of the chip with a small wiper (cleanroom 'Q-Tip') to remove residues of unknown origin.

(b) **Alignment markers**

Preparation:

- acetone rinse (2 min)
- IPA rinse (30 s)
- N_2 (g) dry

Resist:

- first layer: 17.5%wt Copolymer: $\approx$ 350nm, 2500 rpm (55s)
- bake on hot plate 175°C (10 min)
- second layer: 2% wt PMMA 950K in anisole: 100nm, 1500 rpm (55s)
- bake on hot plate 175°C (10 min)

Exposure:

- e-beam dose: $650\mu C/cm^2$ at 100kV
- spot size 100nm, beam current 200nA

Developing:

- 1 : 3 MIBK / IPA (1min)
- IPA stop (1 min)
- N_2 (g) dry

Evaporation:

- 50 nm Ti, rate 0.1 nm/s
- 150 nm Au, rate 0.1-0.2 nm/s

Lift-off:

- cold acetone 6h or warm acetone (53°C) 3h / acetone spray
- IPA rinse (30 s)
- N_2 (g) dry

(c) **Mesa etching**

Preparation:

- acetone rinse (2 min)
- IPA rinse (30 s)
- N_2 (g) dry

Resist:

- 2% wt PMMA 950K in anisole: 90nm, 2000 rpm (55s)
- bake on hot plate 175°C (10 min)

Exposure:

- e-beam dose: $550\mu C/cm^2$ at 100kV
- spot size 90nm / beam current 160nA

Developing:

- 1 : 3 MIBK / IPA (1min)
- IPA stop (1 min)

- N_2 (g) dry

Etching:

- surface oxide removal: 1:5 H_2SO_4/H_2O (30s)
- H_2O rinse (30s)
- wet etch in 1:5:25 $H_2O_2/H_2SO_4/H_2O$, etchant cooled to 10°C, rate 3nm/s
- H_2O rinse (30s)
- IPA rinse (30s)
- N_2 (g) dry

Remarks:

- The etch rate can vary for different wafers and is also quite sensitive to how precise the etchant is mixed. Also if the H_2O_2 is already old, its concentration might have changed. Etching a pure GaAs chip first, makes sure, that the etchant is mixed properly. The etch is then typically done in several steps, while checking with a profilometer in between the steps. The aim is to etch as far as the 2DEG lies, which in the wafers used here is typically around 100nm.
- Care needs to be taken when the sample is taken out of the beaker filled with water or acid. The surface adhesion is much higher than of e.g. IPA, so the sample 'sticks' to the liquid surface. Also when rinsing the sample in water or moving it in the acid gentle movements are recommended, since parts of the resist can move otherwise.
- The etchant is cooled to 10°C to reduce the etch rate. The etch rate can also be changed by changing the mixture, especially by reducing the H_2O_2 content. If doing so, one should be aware of the fact, that depending on the mixture, the $H_2O_2/H_2SO_4/H_2O$ etchant can give an anisotropic etch resulting in an undercut in one of the crystallographic directions. More details on this can be found in [204].

(d) **Ohmic contacts**

Preparation:

- acetone rinse (2 min)
- IPA rinse (30 s)
- N_2 (g) dry

Resist:

- first layer: 17.5%wt Copolymer: 350nm, 2500 rpm (55s)

- bake on hot plate 175°C (10 min)
- second layer: 2% wt PMMA 950K in anisole: 100nm, 1500 rpm (55s)
- bake on hot plate 175°C (10 min)

Exposure:

- e-beam dose $650\mu C/cm^2$ at 100kV
- spot size 100nm, beam current 200nA

Developing:

- $1:3$ MIBK / IPA (1min)
- IPA stop (1 min)
- N_2 (g) dry

Evaporation:

- 5 nm Ni, rate 0.1 nm/s
- 150 nm AuGe, rate 0.1nm/s
- 25 nm Ni, rate 0.2 nm/s

Lift-off:

- cold acetone 6h or warm acetone (53°C) 3h / acetone spray
- IPA rinse (30 s)
- N_2 (g) dry

Rapid thermal annealing:

- ramp from room temperature to 440°C in 40s, forming gas atmosphere ($90\%N_2$,$10\%H_2$)
- stay at 440°C for 60s, forming gas atmosphere
- cool down from 440°C to 80°C in $\approx$ 30s, N_2 purge

Remarks:

- The rapid thermal annealer uses a pyroelement, which measures the temperature by detecting the thermal radiation from the carbon holder on which the sample is loaded. The pyroelement is only reliably calibrated above $\approx$ 300°C.

(e) **Fine gates**

Preparation:

- oxygen plasma strip (10s)
- acetone rinse (2 min)
- IPA rinse (30 s)

- N_2 (g) dry

Resist:

- 2% wt PMMA 950K in anisole: 90nm, 2000rpm (55s)
- bake on hot plate 175°C (10 min)

Exposure:

- e-beam dose: $750\mu C/cm^2$, 1.7 times higher dose for plunger and thin part of topgate
- spot size: smallest available (around 20nm with an estimated spot size 2-3nm) / beam current 400pA, resolution in the pattern file: 2nm, beamstepsize: 2nm

Developing:

- $1 : 3$ MIBK / IPA (1min)
- IPA stop (1 min)
- N_2 (g) dry

Surface oxide removal:

- surface oxide removal: 1:5 H_2SO_4/H_2O (30s)
- H_2O rinse (30s)
- IPA rinse (20s)
- N_2 (g) dry

Evaporation:

- 10 nm Ti, rate 0.1nm/s
- 20 nm Au, rate 0.1-0.2nm/s

Lift-off:

- cold acetone 6h or warm acetone (53°C) 3h / acetone spray
- IPA rinse (30 s)
- N_2 (g) dry

Remarks:

- The plunger gates and the tip of the top gate have the smallest designed dimensions of 20nm. After lithography they typically have an actual width of about 30-40nm. The width is dependent on the dose, the height alignment of the ebeam and how well the beam is focused. In the ebeam pattern generator, used to make the samples described in this thesis, the edge of a premade alignment marker is used to focus the beam. The marker is on the holder on which the sample is mounted. If this alignment marker is already degraded by focusing

the beam from previous writing jobs, with much higher beam currents, the beam is focused only very poorly resulting in a large spot size. Using an uncontaminated alignment marker improved the yield for writing the fine gates and also makes the writing result much less sensitive to the exact chosen dose.

(f) **Large gates**

Preparation:

- acetone rinse (2 min)
- IPA rinse (30 s)
- N_2 (g) dry

Resist:

- first layer: 500nm OEBR-1000 (200cp), 3500 rpm (55s)
- bake on hot plate 175°C (30 min)
- second layer:2% wt PMMA 950K in anisole: 90nm, 2000rpm (55s)
- bake on hot plate 175°C (10 min)

Exposure:

- e-beam dose: $750\mu C/cm^2$
- spot size: 20nm/ beam current: 550 pA

Developing:

- 1 : 3 MIBK / IPA (1min)
- IPA stop (1 min)
- N_2 (g) dry

Evaporation:

- 50 nm Ti, rate: 0.1nm/s
- 400 nm Au, rate: 0.1-0.2 nm/s

Lift-off:

- cold acetone 6h or warm acetone (53°C) 3h / acteone spray
- IPA rinse (30 s)
- N_2 (g) dry

Remark:

- That the given spinning speed for the OEBR-1000 (200cp) resist is faster than reported in [109] might be related to the fact that the used resist is already 7 years old.

Bibliography

[1] R. P. Feynman, "Simulating physics with computers," *International Journal of Theoretical Physics*, vol. 21, pp. 467–488, 1982.

[2] S. Lloyd, "Universal Quantum Simulators," *Science*, vol. 273, pp. 1073–1078, 1996.

[3] A. K. Ekert, "Quantum cryptography based on Bell's theorem," *Phys. Rev. Lett.*, vol. 67, pp. 661–663, 1991.

[4] P. W. Shor, "Algorithms for quantum computation: discrete logarithms and factoring," *Proceedings of 35th Annual Symposium on Foundations of Computer Science, IEEE Press*, pp. 124–134, 1994.

[5] L. K. Grover, "Quantum mechanics helps in searching for a needle in a haystack.," *Phys. Rev. Lett.*, vol. 79, pp. 325–328, 1997.

[6] P. W. Shor, "Fault-tolerant quantum computation," *Proceedings of 37th Annual Symposium on Foundations of Computer Science, IEEE Press*, pp. 56–67, 1996.

[7] J. Cirac and P. Zoller, "Quantum Computations with Cold Trapped Ions," *Phys. Rev. Lett.*, vol. 74, no. 20, pp. 4091–4094, 1995.

[8] G. Brennen, C. Caves, P. Jessen, and I. Deutsch, "Quantum logic gates in optical lattices," *Phys. Rev. Lett.*, vol. 82, no. 5, pp. 1060–1063, 1999.

[9] Q. A. Turchette, C. J. Hood, W. Lange, H. Mabuchi, and H. J. Kimble, "Measurement of conditional phase shifts for quantum logic," *Phys. Rev. Lett.*, vol. 75, pp. 4710–4713, Dec 1995.

[10] I. Chuang, N. Gershenfeld, and M. Kubinec, "Experimental Implementation of Fast Quantum Searching," *Phys. Rev. Lett.*, vol. 80, no. 15, pp. 3408–3411, 1998.

[11] E. Knill, R. Laflamme, G. Milburn, *et al.*, "A scheme for efficient quantum computation with linear optics," *Nature*, vol. 409, no. 6816, pp. 46–52, 2001.

[12] R. Prevedel, P. Walther, F. Tiefenbacher, P. Bohi, R. Kaltenbaek, T. Jennewein, and A. Zeilinger, "High-speed linear optics quantum computing using active feed-forward," *Nature*, vol. 445, p. 65, 2007.

[13] J. Mooij, T. Orlando, L. Levitov, L. Tian, C. van der Wal, and S. Lloyd, "Josephson Persistent-Current Qubit," *Science*, vol. 285, no. 5430, pp. 1036–1039, 1999.

[14] B. E. Kane, "A silicon-based nuclear spin quantum computer," *Nature*, vol. 393, p. 133, 1998.

[15] D. Loss and D. P. DiVincenzo, "Quantum computation with quantum dots," *Phys. Rev. A*, vol. 57, p. 120, 1998.

[16] A. Imamoglu, D. D. Awschalom, G. Burkard, D. P. DiVincenzo, D. Loss, M. Sherwin, and A. Small, "Quantum information processing using quantum dot spins and cavity qed," *Phys. Rev. Lett.*, vol. 83, pp. 4204–4207, Nov 1999.

[17] R. Vrijen, E. Yablonovitch, K. Wang, H. W. Jiang, A. Balandin, V. Roychowdhury, T. Mor, and D. DiVincenzo, "Electron-spin-resonance transistors for quantum computing in silicon-germanium heterostructures," *Phys. Rev. A*, vol. 62, p. 012306, Jun 2000.

[18] F. Jelezko, T. Gaebel, I. Popa, A. Gruber, and J. Wrachtrup, "Observation of coherent oscillations in a single electron spin," *Phys. Rev. Lett.*, vol. 92, p. 076401, 2004.

[19] J. Chiaverini, D. Leibfried, T. Schaetz, M. Barrett, R. Blakestad, J. Britton, W. Itano, J. Jost, E. Knill, C. Langer, *et al.*, "Realization of quantum error correction," *Nature*, vol. 432, no. 7017, pp. 602–605, 2004.

[20] H. Haffner, W. Hansel, C. Roos, J. Benhelm, D. Chek-al Kar, M. Chwalla, T. Korber, U. Rapol, M. Riebe, P. Schmidt, *et al.*, "Scalable multiparticle entanglement of trapped ions.," *Nature*, vol. 438, no. 7068, pp. 643–6, 2005.

[21] W. Hensinger, S. Olmschenk, D. Stick, D. Hucul, M. Yeo, M. Acton, L. Deslauriers, C. Monroe, and J. Rabchuk, "T-junction ion trap array for two-dimensional ion shuttling, storage, and manipulation," *Applied Physics Letters*, vol. 88, p. 034101, 2006.

[22] J. Maze, P. Stanwix, J. Hodges, S. Hong, J. Taylor, P. Cappellaro, L. Jiang, M. Dutt, E. Togan, A. Zibrov, *et al.*, "Nanoscale magnetic sensing with an individual electronic spin in diamond," *Nature*, vol. 455, no. 7213, pp. 644–647, 2008.

[23] G. Balasubramanian, I. Chan, R. Kolesov, M. Al-Hmoud, J. Tisler, C. Shin, C. Kim, A. Wojcik, P. Hemmer, A. Krueger, *et al.*, "Nanoscale imaging magnetometry with diamond spins under ambient conditions," *Nature*, vol. 455, no. 7213, pp. 648–651, 2008.

[24] M. Baibich, J. Broto, A. Fert, F. Van Dau, F. Petroff, P. Etienne, G. Creuzet, A. Friederich, and J. Chazelas, "Giant magnetoresistance of (001) Fe/(001) Cr magnetic superlattices," *Phys. Rev. Lett.*, vol. 61, no. 21, pp. 2472–2475, 1988.

[25] G. Binasch, P. Gr
"unberg, F. Saurenbach, and W. Zinn, "Enhanced magnetoresistance in layered magnetic structures with antiferromagnetic interlayer exchange," *Phys. Rev. B*, vol. 39, no. 7, pp. 4828–4830, 1989.

[26] T. Fujisawa, Y. Tokura, and Y. Hirayama, "Energy relaxation process in a quantum dot studied by DC current and pulse-excited current measurements," *Physica B*, vol. 298, no. 1-4, pp. 573–579, 2001.

[27] M. Field, C. G. Smith, M. Pepper, D. A. Ritchie, J. E. F. Frost, G. A. C. Jones, and D. G. Hasko, "Measurements of coulomb blockade with a noninvasive voltage probe," *Phys. Rev. Lett.*, vol. 70, pp. 1311–1314, Mar 1993.

[28] W. Lu, Z. Ji, L. Pfeiffer, K. West, and A. Rimberg, "Real-time detection of electron tunnelling in a quantum dot," *Nature*, vol. 423, no. 6938, pp. 422–425, 2003.

[29] L. Vandersypen, J. Elzerman, R. Schouten, L. van Beveren, R. Hanson, and L. Kouwenhoven, "Real-time detection of single-electron tunneling using a quantum point contact," *Applied Physics Letters*, vol. 85, p. 4394, 2004.

[30] J. M. Elzerman, R. Hanson, L. H. W. van Beveren, B. Witkamp, L. M. K. Vandersypen, and L. P. Kouwenhoven, "Single-shot read-out of an individual electron spin in a quantum dot," *Nature*, vol. 430, p. 431, 2004.

[31] T. Fujisawa, D. Austing, Y. Tokura, S. Tarucha, and Y. Hirayama, "Allowed and forbidden transitions in artificial hydrogen and helium atoms," *Nature*, vol. 419, no. 6904, pp. 278–281, 2002.

[32] J. R. Petta, A. C. Johnson, J. M. Taylor, E. A. Laird, A. Yacoby, M. D. Lukin, C. M. Marcus, M. P. Hanson, and A. C. Gossard, "Coherent manipulation of coupled electron spins in semiconductor quantum dots," *Science*, vol. 309, pp. 2180–2184, 2005.

[33] F. H. L. Koppens, C. Buizert, K.-J. Tielrooij, I. T. Vink, K. C. Nowack, T. Meunier, L. P. Kouwenhoven, and L. M. K. Vandersypen, "Driven coherent oscillations of a single electron spin in a quantum dot," *Nature*, vol. 442, p. 766, 2006.

[34] W. Van der Wiel, S. De Franceschi, J. Elzerman, T. Fujisawa, S. Tarucha, and L. Kouwenhoven, "Electron transport through double quantum dots," *Reviews of Modern Physics*, vol. 75, no. 1, pp. 1–22, 2002.

[35] R. Hanson, L. P. Kouwenhoven, J. R. Petta, S. Tarucha, and L. M. K. Vandersypen, "Spins in few-electron quantum dots," *Rev. Mod. Phys.*, vol. 79, p. 1217, 2007.

[36] J. H. Davies, *The physics of low-dimensional semiconductors : an introduction.* Cambridge University Press, 1998.

[37] O. N. Jouravlev and Y. V. Nazarov, "Electron transport in a double quantum dot governed by a nuclear magnetic field," *Phys. Rev. Lett.*, vol. 96, p. 176804, 2006.

[38] W. A. Coish and D. Loss, "Hyperfine interaction in a quantum dot: Non-markovian electron spin dynamics," *Phys. Rev. B*, vol. 70, p. 195340, 2004.

[39] R. de Sousa and S. Das Sarma, "Theory of nuclear-induced spectral diffusion: Spin decoherence of phosphorus donors in Si and GaAs quantum dots," *Phys. Rev. B*, vol. 68, p. 115322, 2003.

[40] D. Paget, G. Lampel, B. Sapoval, and V. I. Safarov, "Low field electron-nuclear spin coupling in gallium arsenide under optical pumping conditions," *Phys. Rev. B*, vol. 15, p. 5780, 1977.

[41] F. H. L. Koppens, J. A. Folk, J. M. Elzerman, R. Hanson, L. H. W. van Beveren, I. T. Vink, H. P. Tranitz, W. Wegscheider, L. P. Kouwenhoven, and L. M. K. Vandersypen, "Control and detection of singlet-triplet mixing in a random nuclear field," *Science*, vol. 309, pp. 1346–1350, 2005.

[42] J. Inarrea, G. Platero, and A. MacDonald, "Double-dot transport in the spin blockade regime," *Arxiv:cond-mat/0609323*, 2006.

[43] C. P. Slichter, *Principles of Magnetic Resonance, 3rd ed.* Springer-Verlag, Berlin, 1990.

[44] A. Leggett, S. Chakravarty, A. Dorsey, M. Fisher, A. Garg, and W. Zwerger, "Dynamics of the dissipative two-state system," *Reviews of Modern Physics*, vol. 59, no. 1, pp. 1–85, 1987.

[45] J. M. Martinis, S. Nam, J. Aumentado, K. M. Lang, and C. Urbina, "Decoherence of a superconducting qubit due to bias noise," *Phys. Rev. B*, vol. 67, no. 9, p. 094510, 2003.

[46] G. Ithier, E. Collin, P. Joyez, P. J. Meeson, D. Vion, D. Esteve, F. Chiarello, A. Shnirman, Y. Makhlin, J. Schriefl, and G. Schön, "Decoherence in a superconducting quantum bit circuit," *Phys. Rev. B*, vol. 72, no. 13, p. 134519, 2005.

[47] A. A. Clerk, M. H. Devoret, S. M. Girvin, F. Marquardt, and R. J. Schoelkopf, "Introduction to quantum noise, measurement and amplification," *arXiv:0810.4729*, 2008.

[48] L. M. K. Vandersypen and I. L. Chuang, "Nmr techniques for quantum control and computation," *Rev. Mod. Phys.*, vol. 76, p. 1037, 2004.

[49] L. Thomas, "The motion of a spinning electron," *Nature*, vol. 117, p. 514, 1926.

[50] J. J. Sakurai, *Modern quantum mechanics - Revised version*. Addison-Wesley, 1994.

[51] G. Dresselhaus, "Spin-orbit coupling effects in zinc blende structures," *Phys. Rev.*, vol. 100, pp. 580–586, 1955.

[52] R. Winkler, *Spin-Orbit Coupling Effects in Two-Dimensional Electron and Hole Systems*, vol. 191/2003 of *Springer Tracts in Modern Physics*. Springer Berlin / Heidelberg, 2003.

[53] Y. A. Bychkov and E. I. Rashba, "Oscillatory effects and the magnetic-susceptibility of carriers in inversion-layers," *J. Phys. C*, vol. 17, pp. 6039–6045, 1984.

[54] Y. A. Bychkov and E. I. Rashba, "Properties of a 2d electron-gas with lifted spectral degeneracy," *JETP Lett.*, vol. 39, p. 78, 1984.

[55] D. M. Zumbühl, J. B. Miller, C. M. Marcus, K. Campman, and A. C. Gossard, "Spin-orbit coupling, antilocalization, and parallel magnetic fields in quantum dots," *Phys. Rev. Lett.*, vol. 89, no. 27, p. 276803, 2002.

[56] J. Luo, H. Munekata, F. F. Fang, and P. J. Stiles, "Effects of inversion asymmetry on electron energy band structures in gasb/inas/gasb quantum wells," *Phys. Rev. B*, vol. 41, no. 11, pp. 7685–7693, 1990.

[57] P. D. Dresselhaus, C. M. A. Papavassiliou, R. G. Wheeler, and R. N. Sacks, "Observation of spin precession in gaas inversion layers using antilocalization," *Phys. Rev. Lett.*, vol. 68, no. 1, pp. 106–109, 1992.

[58] G. M. Minkov, A. V. Germanenko, O. E. Rut, A. A. Sherstobitov, L. E. Golub, B. N. Zvonkov, and M. Willander, "Weak antilocalization in quantum wells in tilted magnetic fields," *Phys. Rev. B*, vol. 70, no. 15, p. 155323, 2004.

[59] B. Jusserand, D. Richards, H. Peric, and B. Etienne, "Zero-magnetic-field spin splitting in the gaas conduction band from raman scattering on modulation-doped quantum wells," *Phys. Rev. Lett.*, vol. 69, no. 5, pp. 848–851, 1992.

[60] Y. Kato, R. C. Myers, A. C. Gossard, and D. D. Awschalom, "Coherent spin manipulation without magnetic fields in strained semiconductors," *Nature*, vol. 427, p. 50, 2003.

[61] L. Meier, G. Salis, I. Shorubalko, E. Gini, S. Schon, and K. Ensslin, "Measurement of rashba and dresselhaus spin-orbit magnetic fields," *Nature Phys.*, vol. 3, p. 650, 2008.

[62] M. Flatté, J. Byers, and W. Lau, "Spin dynamics in semiconductors," in *Semiconductor Spintronics and Quantum Computation, NanoScience and Technology* (D. Awschalom, D. Loss, and N. Samarth, eds.), Springer, Berlin, 2002.

[63] I. Zutic, J. Fabian, and S. Das Sarma, "Spintronics: Fundamentals and applications," *Rev. Mod. Phys.*, vol. 76, p. 323, 2004.

[64] M. I. Dyakonov and V. I. Perel, "Spin relaxation of conduction electrons in noncentrosymmetric semiconductors," *Sov. Phys. Solid State*, vol. 13, no. 12, pp. 3023–3026, 1972.

[65] R. J. Elliott, "Theory of the Effect of Spin-Orbit Coupling on Magnetic Resonance in Some Semiconductors," *Phys. Rev.*, vol. 96, pp. 266–279, 1954.

[66] A. V. Khaetskii and Y. V. Nazarov, "Spin relaxation in semiconductor quantum dots," *Phys. Rev. B*, vol. 61, pp. 12639–12642, 2000.

[67] A. V. Khaetskii and Y. V. Nazarov, "Spin-flip transitions between Zeeman sublevels in semiconductor quantum dots," *Phys. Rev. B*, vol. 64, p. 125316, 2001.

[68] L. M. Woods, T. L. Reinecke, and Y. Lyanda-Geller, "Spin relaxation in quantum dots," *Phys. Rev. B*, vol. 66, p. 161318, 2002.

[69] V. N. Golovach, A. Khaetskii, and D. Loss, "Phonon-induced decay of the electron spin in quantum dots," *Phys. Rev. Lett.*, vol. 93, p. 016601, 2004.

[70] L. Levitov and E. Rashba, "Dynamical spin-electric coupling in a quantum dot," *Phys. Rev. B*, vol. 67, no. 11, p. 115324, 2003.

[71] S. Debald and C. Emary, "Spin-Orbit-Driven Coherent Oscillations in a Few-Electron Quantum Dot," *Phys. Rev. Lett.*, vol. 94, p. 226803, 2005.

[72] C. Flindt, A. S. Sorensen, and K. Flensberg, "Spin-Orbit Mediated Control of Spin Qubits," *Phys. Rev. Lett.*, vol. 97, p. 240501, 2006.

[73] V. N. Golovach, M. Borhani, and D. Loss, "Electric Dipole Induced Spin Resonance in Quantum Dots," *Phys. Rev. B*, vol. 74, p. 165319, 2006.

[74] F. Marquardt and V. A. Abalmassov, "Spin relaxation in a quantum dot due to Nyquist noise," *Phys. Rev. B*, vol. 71, p. 165325, 2005.

[75] M. Borhani, V. N. Golovach, and D. Loss, "Spin decay in a quantum dot coupled to a quantum point contact," *Phys. Rev. B*, vol. 73, p. 155311, 2006.

[76] N. W. Ashcroft and N. D. Mermin, *Solid State Physics*. Saunders, New York, 1974.

[77] M. Kroutvar, Y. Ducommun, D. Heiss, M. Bichler, D. Schuh, G. Abstreiter, and J. J. Finley, "Optically programmable electron spin memory using semiconductor quantum dots," *Nature*, vol. 432, p. 81, 2004.

[78] S. Amasha, K. MacLean, I. Radu, D. M. Zumbuhl, M. A. Kastner, M. P. Hanson, and A. C. Gossard, "Measurements of the spin relaxation rate at low magnetic fields in a quantum dot," *cond-mat/0607110*, 2006.

[79] A. Abragam, *The Principles of Nuclear Magnetism, Clarendon*. Oxford, 1961.

[80] E. Fermi, "Ueber die magnetischen Momente der Atomkerne," *Zeitschrift fuer Physik*, vol. 60, no. 5-6, pp. 320–333, 1930.

[81] F. Meier and B. P. Zakharchenya, *Optical orientation. Modern problems in condensed matter sciences*. North-Holland, 1984.

[82] W. A. Coish, D. Loss, E. A. Yuzbashyan, and B. L. Altshuler, "Quantum versus classical hyperfine-induced dynamics in a quantum dot," *Journal of Applied Physics*, vol. 101, no. 8, p. 081715, 2007.

[83] I. A. Merkulov, A. L. Efros, and M. Rosen, "Electron spin relaxation by nuclei in semiconductor quantum dots," *Phys. Rev. B*, vol. 65, p. 205309, 2002.

[84] A. V. Khaetskii, D. Loss, and L. Glazman, "Electron Spin Decoherence in Quantum Dots due to Interaction with Nuclei," *Phys. Rev. Lett.*, vol. 88, p. 186802, 2002.

[85] J. Taylor, J. Petta, A. Johnson, A. Yacoby, C. Marcus, and M. Lukin, "Relaxation, dephasing, and quantum control of electron spins in double quantum dots," *Phys. Rev. B*, vol. 76, no. 3, p. 35315, 2007.

[86] P. F. Braun, X. Marie, L. Lombez, B. Urbaszek, T. Amand, P. Renucci, V. K. Kalevich, K. V. Kavokin, O. Krebs, P. Voisin, and Y. Masumoto, "Direct Observation of the Electron Spin Relaxation Induced by Nuclei in Quantum Dots," *Phys. Rev. Lett.*, vol. 94, p. 116601, 2005.

[87] M. V. G. Dutt, J. Cheng, B. Li, X. D. Xu, X. Q. Li, P. R. Berman, D. G. Steel, A. S. Bracker, D. Gammon, S. E. Economou, R. B. Liu, and L. J. Sham, "Stimulated and spontaneous optical generation of electron spin coherence in charged gaas quantum dots," *Phys. Rev. Lett.*, vol. 94, p. 227403, 2005.

[88] A. C. Johnson, J. R. Petta, J. M. Taylor, A. Yacoby, M. D. Lukin, C. M. Marcus, M. P. Hanson, and A. C. Gossard, "Triplet-singlet spin relaxation via nuclei in a double quantum dot," *Nature*, vol. 435, p. 925, 2005.

[89] A. V. Khaetskii, D. Loss, and L. Glazman, "Electron spin evolution induced by interaction with nuclei in a quantum dot," *Phys. Rev. B*, vol. 67, p. 195329, 2003.

[90] R. Hanson, L. P. Kouwenhoven, J. R. Petta, S. Tarucha, and L. M. K. Vandersypen, "Spins in few-electron quantum dots," *Reviews of Modern Physics*, vol. 79, no. 4, p. 1217, 2007.

[91] J. Schliemann, A. V. Khaetskii, and D. Loss, "Spin decay and quantum parallelism," *Phys. Rev. B*, vol. 66, p. 245303, 2002.

[92] D. Klauser, W. A. Coish, and D. Loss, "Nuclear spin state narrowing via gate-controlled Rabi oscillations in a double quantum dot," *Phys. Rev. B*, vol. 73, p. 205302, 2006.

[93] D. Stepanenko, G. Burkard, G. Giedke, and A. Imamoglu, "Enhancement of Electron Spin Coherence by Optical Preparation of Nuclear Spins," *Phys. Rev. Lett.*, vol. 96, p. 136401, 2006.

[94] O. Cakir and T. Takagahara, "Quantum Dynamics of Electron-Nuclei Coupled System in a Double Quantum Dot," *Arxiv preprint cond-mat/0609217*, 2006.

[95] G. Giedke, J. M. Taylor, D. DAlessandro, M. D. Lukin, and A. Imamoglu, "Quantum measurement of a mesoscopic spin ensemble," *Phys. Rev. A*, vol. 74, p. 32316, 2006.

[96] D. Reilly, J. Taylor, J. Petta, C. Marcus, M. Hanson, and A. Gossard, "Suppressing Spin Qubit Dephasing by Nuclear State Preparation," *Science*, vol. 321, no. 5890, p. 817, 2008.

[97] E. A. Laird, C. Barthel, E. I. Rashba, C. M. Marcus, M. P. Hanson, and A. C. Gossard, "Hyperfine-mediated gate-driven electron spin resonance," *Phys. Rev. Lett.*, vol. 99, no. 24, p. 246601, 2007.

[98] S. I. Erlingsson, Y. V. Nazarov, and V. I. Falko, "Nucleus-mediated spin-flip transitions in GaAs quantum dots," *Phys. Rev. B*, vol. 64, p. 195306, 2001.

[99] S. I. Erlingsson and Y. V. Nazarov, "Hyperfine-mediated transitions between a Zeeman split doublet in GaAs quantum dots: The role of the internal field," *Phys. Rev. B*, vol. 66, p. 155327, 2002.

[100] S. I. Erlingsson and Y. V. Nazarov, "Evolution of localized electron spin in a nuclear spin environment," *Phys. Rev. B*, vol. 70, p. 205327, 2004.

[101] V. A. Abalmassov and F. Marquardt, "Electron-nuclei spin relaxation through phonon-assisted hyperfine interaction in a quantum dot," *Phys. Rev. B*, vol. 70, p. 75313, 2004.

[102] N. Shenvi and K. Rogerio de Sousa, "Universal Scaling of Hyperfine-Induced Electron Spin Echo Decay," *Phys. Rev. B*, vol. 71, p. 224411, 2005.

[103] W. Yao, R. B. Liu, and L. J. Sham, "Theory of electron spin decoherence by interacting nuclear spins in a quantum dot," *Phys. Rev. B*, vol. 74, p. 195301, 2006.

[104] C. Deng and X. Hu, "Analytical solution of electron spin decoherence through hyperfine interaction in a quantum dot," *Phys. Rev. B*, vol. 73, p. 241303(R), 2006.

[105] R. G. Shulman, B. J. Wyluda, and H. J. Hrostowski, "Nuclear Magnetic Resonance in Semiconductors. III. Exchange Broadening in GaAs and InAs," *Phys. Rev.*, vol. 109, p. 808, 1958.

[106] R. de Sousa and S. Das Sarma, "Electron spin coherence in semiconductors: Considerations for a spin-based solid-state quantum computer architecture," *Phys. Rev. B*, vol. 67, p. 33301, 2003.

[107] W. Witzel and S. Das Sarma, "Quantum theory for electron spin decoherence induced by nuclear spin dynamics in semiconductor quantum computer architectures: Spectral diffusion of localized electron spins in the nuclear solid-state environment," *Phys. Rev. B*, vol. 74, no. 3, p. 35322, 2006.

[108] A. Holleitner, "Fabrication of coupled quantum dots for multiport access," *Applied Physics Letters*, vol. 82, no. 12, p. 1887, 2003.

[109] L. Willems van Beveren, *Electron spins in few-electron lateral quantum dots.* PhD thesis, Delft University of Technology, 2006. online available from http://www.library.tudelft.nl/dissertations/.

[110] F. H. L. Koppens, *Coherence and Control of a Single Electron Spin in a Quantum Dot.* PhD thesis, Delft University of Technology, 2007. online available from http://www.library.tudelft.nl/dissertations/.

[111] A. S. Bracker, E. A. Stinaff, D. Gammon, M. E. Ware, J. G. Tischler, A. Shabaev, A. L. Efros, D. Park, D. Gershoni, V. L. Korenev, and I. A. Merkulov, "Optical Pumping of the Electronic and Nuclear Spin of Single Charge-Tunable Quantum Dots," *Phys. Rev. Lett.*, vol. 94, p. 47402, 2005.

[112] B. Herzog and E. L. Hahn, "Transient Nuclear Induction and Double Nuclear Resonance in Solids," *Phys. Rev.*, vol. 103, p. 148, 1956.

[113] J. P. Gordon and K. D. Bowers, "Microwave spin echoes from donor electrons in silicon," *Phys. Rev. Lett.*, vol. 1, no. 10, pp. 368–370, 1958.

[114] W. A. Coish, J. Fischer, and D. Loss, "Exponential decay in a spin bath," *Phys. Rev. B*, vol. 77, no. 12, p. 125329, 2008.

[115] A. Greilich, D. R. Yakovlev, A. Shabaev, A. L. Efros, I. A. Yugova, R. Oulton, V. Stavarache, D. Reuter, A. Wieck, and M. Bayer, "Mode Locking of Electron Spin Coherences in Singly Charged Quantum Dots," *Science*, vol. 313, pp. 341–345, 2006.

[116] C. Poole, *Electron Spin Resonance, 2nd ed.* Wiley, New York, 1983.

[117] M. Xiao, I. Martin, E. Yablonovitch, and H. W. Jiang, "Electrical detection of the spin resonance of a single electron in a silicon field-effect transistor," *Nature*, vol. 430, p. 435, 2004.

[118] D. Rugar, R. Budakian, H. J. Mamin, and B. W. Chui, "Single spin detection by magnetic resonance force microscopy," *Nature*, vol. 430, p. 329, 2004.

[119] H.-A. Engel and D. Loss, "Detection of single spin decoherence in a quantum dot via charge currents," *Phys. Rev. Lett.*, vol. 86, p. 4648, 2001.

[120] H.-A. Engel and D. Loss, "Single-spin dynamics and decoherence in a quantum dot via charge transport," *Phys. Rev. B*, vol. 65, p. 195321, 2002.

[121] K. Ono, D. G. Austing, Y. Tokura, and S. Tarucha, "Current rectification by pauli exclusion in a weakly coupled double quantum dot system," *Science*, vol. 297, p. 1313, 2002.

[122] A. C. Johnson, J. R. Petta, C. M. Marcus, M. P. Hanson, and A. C. Gossard, "Singlet-triplet spin blockade and charge sensing in a few-electron double quantum dot," *Phys. Rev. B*, vol. 72, p. 165308, 2005.

[123] J. M. Elzerman, R. Hanson, J. S. Greidanus, L. H. Willems van Beveren, S. De Franceschi, L. M. K. Vandersypen, S. Tarucha, and L. P. Kouwenhoven, "Few-electron quantum dot circuit with integrated charge read out," *Phys. Rev. B*, vol. 67, p. 161308, 2003.

[124] R. Hanson, B. Witkamp, L. M. K. Vandersypen, L. H. Willems van Beveren, J. M. Elzerman, and L. P. Kouwenhoven, "Zeeman energy and spin relaxation in a one-electron quantum dot," *Phys. Rev. Lett.*, vol. 91, p. 196802, 2003.

[125] R. M. Potok, J. A. Folk, C. M. Marcus, V. Umansky, M. Hanson, and A. C. Gossard, "Spin and Polarized Current from Coulomb Blockaded Quantum Dots," *Phys. Rev. Lett.*, vol. 91, p. 16802, 2003.

[126] L. H. Willems van Beveren, R. Hanson, I. T. Vink, F. H. L. Koppens, L. P. Kouwenhoven, and L. M. K. 3, "Spin filling of a quantum dot derived from excited-state spectroscopy," *New Journal of Physics*, vol. 7, p. 182, 2005.

[127] A. Kogan, S. Amasha, D. Goldhaber-Gordon, G. Granger, M. A. Kastner, and H. Shtrikman, "Measurements of Kondo and Spin Splitting in Single-Electron Transistors," *Phys. Rev. Lett.*, vol. 93, p. 166602, 2004.

[128] K. Ono and S. Tarucha, "Nuclear-Spin-Induced Oscillatory Current in Spin-Blockaded Quantum Dots," *Phys. Rev. Lett.*, vol. 92, p. 256803, 2004.

[129] M. S. Rudner and L. S. Levitov, "Self-Polarization and Cooling of Spins in Quantum Dots," *Phys. Rev. Lett.*, vol. 99, p. 036602, 2007.

[130] F. Koppens, D. Klauser, W. Coish, K. Nowack, L. Kouwenhoven, D. Loss, and L. Vandersypen, "Universal phase shift and nonexponential decay of driven single-spin oscillations," *Phys. Rev. Lett.*, vol. 99, no. 10, p. 106803, 2007.

[131] F. Qassemi, W. A. Coish, and F. K. Wilhelm, "Stationary and transient leakage current in the pauli spin blockade," *Phys. Rev. Lett.*, vol. 102, no. 17, p. 176806, 2009.

[132] W. M. Witzel and S. D. Sarma, "Multiple-pulse coherence enhancement of solid state spin qubits," *Phys. Rev. Lett.*, vol. 98, no. 7, p. 077601, 2007.

[133] W. Yao, R.-B. Liu, and L. J. Sham, "Restoring coherence lost to a slow interacting mesoscopic spin bath," *Phys. Rev. Lett.*, vol. 98, no. 7, p. 077602, 2007.

[134] F. H. L. Koppens, K. C. Nowack, and L. M. K. Vandersypen, "Spin echo of a single electron spin in a quantum dot," *Phys. Rev. Lett.*, vol. 100, no. 23, p. 236802, 2008.

[135] G. Burkard, D. Loss, and D. P. DiVincenzo, "Coupled quantum dots as quantum gates," *Phys. Rev. B*, vol. 59, pp. 2070–2078, Jan 1999.

[136] A. Greilich, A. Shabaev, D. R. Yakovlev, A. L. Efros, I. A. Yugova, D. Reuter, A. D. Wieck, and M. Bayer, "Nuclei-Induced Frequency Focusing of Electron Spin Coherence," *Science*, vol. 317, no. 5846, pp. 1896–1899, 2007.

[137] D. J. Reilly, J. M. Taylor, J. R. Petta, C. M. Marcus, M. P. Hanson, and A. C. Gossard, "Suppressing Spin Qubit Dephasing by Nuclear State Preparation," *Science*, vol. 321, no. 5890, pp. 817–821, 2008.

[138] D. J. Reilly, J. M. Taylor, E. A. Laird, J. R. Petta, C. M. Marcus, M. P. Hanson, and A. C. Gossard, "Measurement of temporal correlations of the overhauser field in a double quantum dot," *Phys. Rev. Lett.*, vol. 101, no. 23, p. 236803, 2008.

[139] J. Baugh, Y. Kitamura, K. Ono, and S. Tarucha, "Large nuclear Overhauser fields detected in vertically-coupled double quantum dots," *Phys. Rev. Lett.*, vol. 99, p. 096804, 2007.

[140] S. Foletti, J. Martin, M. Dolev, D. Mahalu, V. Umansky, and A. Yacoby, "Dynamic nuclear polarization using a single pair of electrons," *arXiv:0801.3613*, 2008.

[141] A. I. Tartakovskii, T. Wright, A. Russell, V. I. Fal'ko, A. B. Van'kov, J. Skiba-Szymanska, I. Drouzas, R. S. Kolodka, M. S. Skolnick, P. W. Fry, A. Tahraoui, H.-Y. Liu, and M. Hopkinson, "Nuclear spin switch in semiconductor quantum dots," *Phys. Rev. Lett.*, vol. 98, no. 2, p. 026806, 2007.

[142] P. Maletinsky, C. W. Lai, A. Badolato, and A. Imamoglu, "Nonlinear dynamics of quantum dot nuclear spins," *Phys. Rev. B*, vol. 75, no. 3, p. 035409, 2007.

[143] P.-F. Braun, B. Urbaszek, T. Amand, X. Marie, O. Krebs, B. Eble, A. Lemaitre, and P. Voisin, "Bistability of the nuclear polarization created through optical pumping in in[sub 1 - x]ga[sub x]as quantum dots," *Phys. Rev. B*, vol. 74, no. 24, p. 245306, 2006.

[144] F. H. L. Koppens, C. Buizert, I. T. Vink, K. C. Nowack, T. Meunier, L. P. Kouwenhoven, and L. M. K. Vandersypen, "Detection of single electron spin resonance in a double quantum dot," *J. Appl. Phys.*, vol. 101, p. 081706, 2007.

[145] J. Danon, I. T. Vink, F. H. L. Koppens, K. C. Nowack, L. M. K. Vandersypen, and Y. V. Nazarov, "Multiple nuclear polarization states in a double quantum dot," *Phys. Rev. Lett.*, vol. 103, no. 4, p. 046601, 2009.

[146] J. Danon and Y. V. Nazarov, "Nuclear tuning and detuning of the electron spin resonance in a quantum dot: Theoretical consideration," *Phys. Rev. Lett.*, vol. 100, no. 5, p. 056603, 2008.

[147] M. S. Rudner and L. S. Levitov, "Electrically driven reverse overhauser pumping of nuclear spins in quantum dots," *Phys. Rev. Lett.*, vol. 99, no. 24, p. 246602, 2007.

[148] A. Overhauser, "Polarization of nuclei in metals," *Physical Review*, vol. 92, no. 2, pp. 411–415, 1953.

[149] F. H. L. Koppens, C. Buizert, K.-J. Tielrooij, I. T. Vink, K. C. Nowack, T. Meunier, L. P. Kouwenhoven, and L. M. K. Vandersypen, "Driven coherent oscillations of a single electron spin in a quantum dot," *Nature*, vol. 442, p. 766, 2006.

[150] N. G. van Kampen, *Stochastic Processes in Physics and Chemistry*. North-Holland, Amsterdam, 1990.

[151] D. Awschalom, D. Loss, and N. Samarth, *Semiconductor Spintronics and Quantum Computation*. Springer, 2002.

[152] B. Simovič, P. Studerus, S. Gustavsson, R. Leturcq, K. Ensslin, R. Schuhmann, J. Forrer, and A. Schweiger, "Design of Q-band loop-gap resonators at frequencies of 34–36 GHz for single electron spin spectroscopy in semiconductor nanostructures," *Review of Scientific Instruments*, vol. 77, p. 064702, 2006.

[153] Y. Tokura, W. G. Van der Wiel, T. Obata, and S. Tarucha, "Coherent single electron spin control in a slanting zeeman field," *Phys. Rev. Lett.*, vol. 96, p. 047202, 2006.

[154] Y. Kato, R. C. Myers, D. C. Driscoll, A. C. Gossard, J. Levy, and D. D. Awschalom, "Gigahertz electron spin manipulation using voltage-controlled g-tensor modulation," *Science*, vol. 299, p. 1201, 2003.

[155] G. Salis, Y. Kato, K. Ensslin, D. C. Driscoll, A. C. Gossard, and D. D. Awschalom, "Electrical control of spin coherence in semiconductor nanostructures," *Nature*, vol. 414, p. 619, 2001.

[156] M. Schulte, J. G. S. Lok, G. Denninger, and W. Dietsche, "Electron spin resonance on a two-dimensional electron gas in a single alas quantum well," *Phys. Rev. Lett.*, vol. 94, no. 13, p. 137601, 2005.

[157] J. D. Walls, "Parametric spin excitations in lateral quantum dots," 2007.

[158] See later in this chapter.

[159] T. H. Stoof and Y. V. Nazarov, "Time-dependent resonant tunneling via two discrete states," *Phys. Rev. B*, vol. 53, no. 3, pp. 1050–1053, 1996.

[160] R. E. Williams, *Modern GaAs processing methods*. The Artech House microwave library, Boston Artech House, 1990.

[161] R. Winkler. private communication.

[162] S. Frolov, S. Lüscher, W. Yu, Y. Ren, J. Folk, and W. Wegscheider, "Ballistic spin resonance," *Nature*, vol. 458, no. 7240, pp. 868–871, 2009.

[163] C. Barthel, D. J. Reilly, C. M. Marcus, M. P. Hanson, and A. C. Gossard, "Rapid single-shot measurement of a singlet-triplet qubit," *Phys. Rev. Lett.*, vol. 103, p. 160503, 2009.

[164] J. Elzerman, R. Hanson, L. van Beveren, L. Vandersypen, and L. Kouwenhoven, "Excited-state spectroscopy on a nearly closed quantum dot via charge detection," *Applied Physics Letters*, vol. 84, p. 4617, 2004.

[165] S. Amasha, K. MacLean, I. P. Radu, D. M. Zumbühl, M. A. Kastner, M. P. Hanson, and A. C. Gossard, "Spin-dependent tunneling of single electrons into an empty quantum dot," *Phys. Rev. B*, vol. 78, no. 4, p. 041306, 2008.

[166] S. Foletti, H. Blum, D. Mahalu, V. Umansky, and A. Yacoby, "Universal quantum control of two-electron spin quantum bits using dynamic nuclear polarization," *Nature Physics*, vol. published online, p. 11 October 2009, 2009.

[167] M. Pioro-Ladriere, T. Obata, Y. Tokura, Y. Shin, T. Kubo, K. Yoshida, T. Taniyama, and S. Tarucha, "Electrically driven single-electron spin resonance in a slanting zeeman field," *Nature Physics*, vol. 4, no. 10, pp. 776–779, 2008.

[168] V. recent work in the group of S. Tarucha (Tokyo). Unpublished.

[169] J. R. Petta, J. M. Taylor, A. C. Johnson, A. Yacoby, M. D. Lukin, C. M. Marcus, M. P. Hanson, and A. C. Gossard, "Dynamic nuclear polarization with single electron spins," *Phys. Rev. Lett.*, vol. 100, no. 6, p. 067601, 2008.

[170] D. J. Reilly, J. M. Taylor, J. R. Petta, C. M. Marcus, M. P. Hanson, and A. C. Gossard, "Exchange control of nuclear spin diffusion in a double quantum dot," 2008.

[171] N. Shaji, C. Simmons, M. Thalakulam, L. Klein, H. Qin, H. Luo, D. Savage, M. Lagally, A. Rimberg, R. Joynt, *et al.*, "Spin blockade and lifetime-enhanced

transport in a few-electron Si/SiGe double quantum dot," *Nature Physics*, vol. 4, no. 7, pp. 540–544, 2008.

[172] C. Simmons, M. Thalakulam, N. Shaji, L. Klein, H. Qin, R. Blick, D. Savage, M. Lagally, S. Coppersmith, and M. Eriksson, "Single-electron quantum dot in Si/ SiGe with integrated charge sensing," *Applied Physics Letters*, vol. 91, p. 213103, 2007.

[173] C. Simmons, M. Thalakulam, B. Rosemeyer, B. Van Bael, E. Sackmann, D. Savage, M. Lagally, R. Joynt, M. Friesen, S. Coppersmith, and M. Eriksson, "Charge sensing and controllable tunnel coupling in a Si/SiGe double quantum dot," *Nano Letters*, vol. 9, pp. 3234–3238, 2009.

[174] R. R. Hayes, A. A. Kiselev, M. G. Borselli, S. S. Bui, E. T. Croke III, P. W. Deelman, B. M. Maune, I. Milosavljevic, J.-S. Moon, R. S. Ross, A. E. Schmitz, M. F. Gyure, and A. T. Hunter, "Lifetime measurements (t1) of electron spins in si/sige quantum dots," 2009.

[175] D. Culcer, X. Hu, and S. D. Sarma, "Dephasing of si spin qubits due to charge noise," *Applied Physics Letters*, vol. 95, no. 7, p. 073102, 2009.

[176] Y. Hu, H. Churchill, D. Reilly, J. Xiang, C. Lieber, and C. Marcus, "A Ge/Si heterostructure nanowire-based double quantum dot with integrated charge sensor," *Nature Nanotechnology*, vol. 2, no. 10, pp. 622–625, 2007.

[177] N. Mason, M. Biercuk, and C. Marcus, "Local gate control of a carbon nanotube double quantum dot," *Science*, vol. 303, no. 5658, p. 655, 2004.

[178] S. Sapmaz, C. Meyer, P. Beliczynski, P. Jarillo-Herrero, and L. P. Kouwenhoven, "Excited state spectroscopy in carbon nanotube double quantum dots," *Nano Letters*, vol. 6, p. 1350, 2006.

[179] H. Churchill, A. Bestwick, J. Harlow, F. Kuemmeth, D. Marcos, C. Stwertka, S. Watson, and C. Marcus, "Electron–nuclear interaction in 13C nanotube double quantum dots," *Nature Physics*, vol. 5, no. 5, pp. 321–326, 2009.

[180] J. Cao, Q. Wang, and H. Dai, "Electron transport in very clean, as-grown suspended carbon nanotubes," *Nature Materials*, vol. 4, no. 4, pp. 745–749, 2005.

[181] G. Steele, G. Gotz, and L. Kouwenhoven, "Tunable few-electron double quantum dots and Klein tunnelling in ultraclean carbon nanotubes," *Nature Nanotechnology*, vol. 4, no. 6, pp. 363–367, 2009.

[182] F. Kuemmeth, S. Ilani, D. Ralph, and P. McEuen, "Coupling of spin and orbital motion of electrons in carbon nanotubes," *NATURE-LONDON-*, vol. 452, no. 7186, p. 448, 2008.

[183] D. V. Bulaev, B. Trauzettel, and D. Loss, "Spin-orbit interaction and anomalous spin relaxation in carbon nanotube quantum dots," *Phys. Rev. B*, vol. 77, no. 23, p. 235301, 2008.

[184] B. Trauzettel, D. Bulaev, D. Loss, and G. Burkard, "Spin qubits in graphene quantum dots," *Nature Physics*, vol. 3, no. 3, pp. 192–196, 2007.

[185] F. Molitor, S. Dröscher, J. Güttinger, A. Jacobsen, C. Stampfer, T. Ihn, and K. Ensslin, "Transport through graphene double dots," *Applied Physics Letters*, vol. 94, no. 22, p. 222107, 2009.

[186] J. Taylor, H. Engel, W. Dur, A. Yacoby, C. Marcus, P. Zoller, and M. Lukin, "Fault-tolerant architecture for quantum computation using electrically controlled semiconductor spins," *Nature Physics*, vol. 1, no. 3, p. 177, 2005.

[187] D. Stepanenko and G. Burkard, "Quantum gates between capacitively coupled double quantum dot two-spin qubits," *Phys. Rev. B*, vol. 75, no. 8, p. 085324, 2007.

[188] E. Laird, *Electronic control of spin qubits.* PhD thesis, Harvard University, 2009. online available from http://marcuslab.harvard.edu.

[189] Ł. Cywiński, W. Witzel, and S. Das Sarma, "Electron spin dephasing due to hyperfine interactions with a nuclear spin bath," *Phys. Rev. Lett.*, vol. 102, no. 5, p. 57601, 2009.

[190] W. Coish, J. Fischer, and D. Loss, "Exponential decay in a spin bath," *Phys. Rev. B*, vol. 77, no. 12, p. 125329, 2008.

[191] V. recent work in the group of A. Yacoby (Harvard). Unpublished.

[192] M. Nielsen and I. Chuang, *Quantum computation and information.* Cambridge University Press, Cambridge, UK, 2000.

[193] W. Coish and D. Loss, "Exchange-controlled single-electron-spin rotations in quantum dots," *Phys. Rev. B*, vol. 75, no. 16, p. 161302, 2007.

[194] D. DiVincenzo, D. Bacon, J. Kempe, G. Burkard, and K. Whaley, "Universal quantum computation with the exchange interaction," *Nature*, vol. 408, no. 6810, pp. 339–342, 2000.

[195] W. Coish and D. Loss, "Singlet-triplet decoherence due to nuclear spins in a double quantum dot," *Phys. Rev. B*, vol. 72, no. 12, p. 125337, 2005.

[196] X. Hu and S. Das Sarma, "Charge-fluctuation-induced dephasing of exchange-coupled spin qubits," *Phys. Rev. Lett.*, vol. 96, no. 10, p. 100501, 2006.

144

[197] M. Stopa and C. M. Marcus, "Magnetic field control of exchange and noise immunity in double quantum dots," *Nano Letters*, vol. 6, no. 8, p. 1778, 2008.

[198] C. Buizert, F. Koppens, M. Pioro-Ladrière, H. Tranitz, I. Vink, S. Tarucha, W. Wegscheider, and L. Vandersypen, "InSitu Reduction of Charge Noise in GaAs/Al_ {x} Ga_ {1-x} As Schottky-Gated Devices," *Phys. Rev. Lett.*, vol. 101, no. 22, p. 226603, 2008.

[199] D. Schr
"oer, A. Greentree, L. Gaudreau, K. Eberl, L. Hollenberg, J. Kotthaus, and S. Ludwig, "Electrostatically defined serial triple quantum dot charged with few electrons," *Phys. Rev. B*, vol. 76, no. 7, p. 75306, 2007.

[200] L. Gaudreau, A. Kam, G. Granger, S. A. Studenikin, P. Zawadzki, and A. S. Sachrajda, "A tuneable few electron triple quantum dot," 2009.

[201] L. Childress, A. S. Sørensen, and M. D. Lukin, "Mesoscopic cavity quantum electrodynamics with quantum dots," *Phys. Rev. A*, vol. 69, p. 042302, Apr 2004.

[202] M. Trif, V. N. Golovach, and D. Loss, "Spin dynamics in inas nanowire quantum dots coupled to a transmission line," *Phys. Rev. B*, vol. 77, no. 4, p. 045434, 2008.

[203] D. DiVincenzo, "The physical implementation of quantum computation," *Fortschr. Phys.*, vol. 48, p. 771, 2000.

[204] R. Williams, *Modern GaAs processing techniques.* Artech House, 1990.

Summary

Electrical manipulation and detection of single electron spins in quantum dots

This thesis describes a series of experiments aimed at understanding and controlling the behavior of the spin of single electrons, confined in so-called quantum dots. A quantum dot is a small electrostatic trap for electrons, which can be realized in a semiconductor, and contains a controllable number of electrons. This work is motivated by the prospects of using the electron spin in such a quantum dot as a quantum bit (qubit), the computational unit of a quantum computer. The envisioned basis states (logical 0 and 1) of the qubit are the two possible orientations of the spin in a magnetic field: 'spin-up' (parallel to the field) and 'spin-down' (anti-parallel to the field). Due to the tiny magnetic moment associated with a single electron spin it is expected that a qubit encoded in these two possible spin states will be well protected against interactions with the environment. While the measured relaxation times seemed promising, experiments, exploring how long a superposition of 'spin-up' and 'spin-down' survives, show, that an electron spin in a quantum dot is subject to rapid decoherence.

The quantum dot devices studied in this work are defined in a two-dimensional electron gas (2DEG) of a GaAs/AlGaAs heterostructure, by applying negative voltages to metallic gate electrodes fabricated on top of the heterostructure. The progress made on controlling single electron spins in these quantum dots allows for a quantitative understanding of the timescales and mechanisms by which the spin loses phase coherence. This is the focus of the first part of this thesis. Manipulation of the electron spin is realized by employing the traditional technique of electron spin resonance (ESR), where a small oscillating magnetic field is applied perpendicular to the larger static magnetic field. When the frequency of the oscillating magnetic field matches the precession frequency of the spin in the static field, the spin directions evolves from 'spin-up' to 'spin-down' and back again. By applying bursts of the oscillating field, the spin can be rotated to point into any desired direction, that is, it can be prepared in any superposition state. This ability allows to perform a so-called Ramsey experiment, which is used to reveal the timescale on which the information about the phase in a superposition state is lost. The experiment involves a rotation of the spin from, for example spin-up to a su-

perposition state, and after a short waiting time, rotating back to up. The second rotation is only successful if the phase of the superposition state has been preserved. The chance to find spin-down instead after the second rotation increases with the degree that the phase information is lost. The experiment shows that the phase-information is already lost after about 30 nanoseconds. The source of this fast dephasing is identified to be the coupling of the electron spin to the nuclear spins in the quantum dot host material. The electron spin interacts through the hyperfine interaction with roughly a million randomly fluctuating nuclear spins, which act as a small but unknown effective magnetic field. The precession of the electron spin in this random field causes the observed rapid dephasing. This precession can be reversed to a large extent via a spin-echo technique, in which after a time τ the spin is rotated by 180°, which effectively reverses the time evolution during the time after the pulse and results in a refocussing of the spin after another time τ. Using this technique the decoherence time is extended to about 500 nanoseconds.

Since the coherence properties of the electron spin depends on the dynamics of the nuclear spin bath, it is desirable to gain control over the nuclear spin bath. The hyperfine interaction coupling the electron spin and nuclear spins in fact works both ways: the electron spin also affects the nuclear spins. Recently, several experiments have shown that the electron spin dynamics can give rise to dynamical nuclear spin pumping and polarization in a quantum dot. In this thesis observation of electron-nuclear feedback is reported, when the electron spin is driven by electron spin resonance. The nuclear magnetic field adjusts itself such that the electron spin resonance condition remains satisfied while changing external control parameters like the external magnetic field and excitation frequency. From simple theoretical arguments one can conclude that the randomness of the nuclear field has been reduced at least by a factor of 10 in the discussed experiment.

The experiment mentioned so far were enabled by control of the electron spin through electron spin resonance induced by an oscillating magnetic field. In the second part of this thesis it is shown that electron spin resonance can also be induced by applying an oscillating electric field. Due to the moving of the electron induced by the applied electric field the spin feels an effective magnetic field originating from the spin-orbit coupling in the semiconductor host material. In a semiconductor this magnetic field is related to the crystal structure as well as the trapping potential in the semiconductor. For an electron trapped in a quantum dot, this effective field depends on the location of the electron. Via an oscillating electric field the electron's position oscillates and in this way its spin experiences an oscillating magnetic field. In combination with a static magnetic field we demonstrated control of single electron spin states via oscillating electric fields. The advantage of this method is that electric fields can be generated much more easily, simply by exciting a local gate electrode. In addition, this method allows for greater spatial selectivity, which is important for local addressing of individual spins. Finally generating an oscillating electric field results in less ohmic heating on-chip compared to generating an

oscillating magnetic field.

In the last part of this thesis the progress of an experiment is summarized in which we attempt to integrate different techniques developed for implementing qubits using electron spins in quantum dots in a single experiment. This would enable simple two-qubit experiments like exploring two-spin entanglement or realization of a CNOT gate. The first step is to realize a read-out of the joined spin state of two electrons in two adjacent quantum dots. This is possible by extending a read-out principle, which has been successfully applied to read out the state of a single spin, to the case of two spins in a double quantum dot When this thesis went to press, all major problems to perform this read-out have been solved. Though not yet in this thesis, it is likely that the read-out is realized soon.

<div align="right">

Katja Nowack
November 2009

</div>

Samenvatting

Electrische manipulatie en detectie van enkele elektronenspins in quantum dots

Dit proefschrift beschrijft een reeks experimenten, die tot doel hebben het gedrag van de spin van enkele elektronen, opgesloten in een halgeleider quantum dot, te begrijpen en onder controle te krijgen. Een quantum dot is een soort elektrische val voor elektronen, welke in een halfgeleider gemaakt kan worden, en is gevuld is met een regelbaar aantal elektronen. De motivatie voor dit onderzoek is de mogelijke toepassing van de spin van een elektron als quantum bit (of qubit), de elementaire rekeneenheid van een quantum computer. De beoogde basistoestanden van de qubit (de logische 0 en 1) zijn de twee mogelijke richtingen van de spin in een magnetisch veld: 'spin-op' (parallel aan het magnetische veld) en 'spin-neer' (antiparallel aan het magnetische veld). Omwille van het extreem kleine magnetisch moment van een elektron spin is de verwachting dat een qubit gecodeerd in de twee spin toestanden relatief ongevoelig is voor verstoringen uit de omgeving. Metingen van de relaxatietijden leken hoopgevend, maar andere experimenten, welke onderzoeken hoe lang een superpositie van 'spin-op' en 'spin-neer' blijft bestaan, laten zien dat de spin van een elektron opgesloten in een quantum echter zeer snele decoherentie vertoont.

De in dit werk bestudeerde quantum dots zijn gedefinieerd in een tweedimensionaal elektronengas (2DEG) van een GaAs/AlGaAs heterostructuur door negatieve spanningen aan te brengen op metallische elektroden bovenop de heterostructuur. De vooruitgang in het controleren van enkele elektronen spins in deze quantum dots maakt het mogelijk om een kwantitatief begrip te verkrijgen over de tijdschalen en de mechanismes welke de decoherentie veroorzaken. Dit is de focus van het eerst deel van het proefschrift. We manipuleren een enkele spin via de techniek van elektronenspin resonantie (ESR) waarbij een zwak wisselend magneetveld wordt aangelegd loodrecht op een sterker statisch magneetveld. Als de frequentie van het wisselende veld gelijk is aan de precessiefrequentie van de spin in het statische veld, zal de spin van spin-op naar spin-neer en weer terug naar spin-op evolueren. Door het wisselende magneetveld gedurende korte tijd aan te schakelen kan de spin in iedere gewenste richting worden gedraaid, of mutatis mutandis, in iedere gewenste superpositie toestand worden gebracht. Dit maakt het mogelijk om een zogenaamd Ramsey experiment door te voeren, hetwelke toestaat om de snelheid te meten waarmee

faseinformatie van de superpositietoestand verloren gaat. De spin wordt in dit experiment door een rotatie van bijvoorbeeld spin-op in een superpositie gebracht en na een korte wachttijd weer teruggeroteerd naar spin-op. De tweede rotatie kan alleen accuraat worden doorgevoerd wanneer de fase-informatie van de superpositie toestand behouden is gebleven. De kans om een spin-neer na de tweede rotatie te meten groeit naarmate de faseinformatie meer is verloren gegaan. Het Ramsey experiment toont aan dat de faseinformatie al na zo'n 30 nanoseconden verloren gaat. De bron van deze snelle defasering is de koppeling van de elektronenspin met de kernspins in het materiaal waarvan de quantum dot is gemaakt. De elektronenspin ondergaat een wisselwerking met ongeveer een miljoen willekeurig fluctuerende kernspins via de hyperfijnwisselwerking. De kerspins manifesteren zich als als een klein maar willekeurig georiënteerd magnetisch veld. De precessie van de spin rond dit willekeurige veld veroorzaakt de snelle defasering, die wij hebben gemeten. Deze precessie hebben we voor een groot deel ongedaan gemaakt met een spin-echo techniek, waarbij de spin na een tijd τ om 180° gedraaid wordt, wat effectief de tijdsevolutie in de tijd na de puls omdraait en tot een herstel leidt na nog eens een tijd τ. Met deze techniek kan de decoherentie worden vertraagd tot een tijdsduur van ongeveer 500 nanoseconden.

Aangezien de coherentie van de elektronen spin afhankelijk is van de dynamica van de kernspins in zijn omgeving is het wenselijk dat er controle over deze kernspins kan worden verkregen. De hyperfijnwisselwerking werkt twee kanten op: de elektronenspin benvloedt op zijn beurt ook de kernspins. Recente experimenten hebben aangetoond dat de dynamica van de elektron spin aanleiding kan geven tot het pompen en polariseren van de kernspins in een quantum dot. In deze thesis wordt de observatie gerapporteerd van een terugkoppeling van de elektron spin naar de kernspins wanneer de elektronen spin wordt aangedreven op resonantie. Het kernveld past zich dynamisch aan zodat dusdanig de elektron spin resonantieconditie vervuld blijft en dit terwijl externe controle parameters, waaronder het externe magnetische veld en de excitatie frequentie, worden aangepast. Op basis van eenvoudige theoretische argumenten kunnen we concluderen dat in dit experiment de willekeur in het kernveld werd gereduceerd met minstens een factor 10.

In de experimenten die tot dusver werden vermeld werd gebruik gemaakt van een wisselend magnetisch veld voor manipulatie van het elektron via elektron spin resonantie. In het tweede deel van de thesis wordt aangetoond dat de elektron spin resonantie ook kan worden geïnduceerd door het aanleggen van een oscillerend elektrisch veld. Door de beweging van het electron aangedreven door het aangeboden elektrische veld "voelt" de spin een effectief magneetveld. In de halfgeleider is dit effectieve magneetveld gerelateerd aan de kristalstructuur alsmede de potentiaal die het tweedimensionale elektrongas definieert. Voor het elektron in de quantum dot geldt dat dit effectieve magnetische veld afhankelijk is van de positie van het elektron. Onder invloed van het wisselende elektrisch veld oscilleert de positie van het elektron en ervaart de spin van het elektron op die manier een oscillerend effectief

magnetisch veld. In combinatie met een statisch extern magneetveld hebben we op deze wijze enkel en alleen gebruik makende van elektrische velden controle over de spin gedemonstreerd. Het voordeel van deze methode is dat elektrische velden in de praktijk eenvoudiger te realiseren zijn dan wisselende magnetische velden en dat deze methode het ook mogelijk maakt een spin lokaal aan te sturen. Tenslotte gaat de opwekking van elektrische velden op een chip gepaard met minder opwarming dan de opwekking van magnetische velden.

In het laatste onderdeel van deze thesis vatten we de voortgang van een experiment samen waarin wordt getracht om de verschillende technieken te combineren die werden ontwikkeld voor de implementatie van qubits op basis van elektronen spins. Deze combinatie van technieken zal de voltrekking van eenvoudige 2-qubit experimenten mogelijk maken, waaronder de realisatie van een CNOT poort. De eerste stap is de realisatie van de gecombineerde uitlezing van de spintoestand van twee elektronen in twee naburige quantum dots. Dit is mogelijk door een uitleesmethode, die succesvol werd aangewend voor het uitlezen van de spintoestand van een individuele spin, uit te breiden naar twee spins in een dubbele quantum dot. Op het moment dat deze thesis ter perse ging waren alle voornaamste problemen om de uitlezing te realiseren opgelost. Hoewel deze uitlezing nog geen integraal onderdeel van deze thesis uitmaakt is de verwachting dat de uitlezing op korte termijn zal kunnen worden gedemonstreerd.

<div align="right">

Katja Nowack
November 2009

</div>

Curriculum Vitae

Katja Carola Nowack

October 17, 1979	Born in Krefeld, Germany.
1991 – 1997	Erasmus von Rotterdam Gymnasium, Viersen, Germany.
1999 – 2005	Studies of physics (*cum laude*), RWTH Aachen, Germany. Diploma thesis in the group of prof. dr. Schoeller, under supervision of prof. dr. Maarten Wegewijs. "*Tunneling through a single molecule with vibrational excitations*".
2005 – 2009	PhD research at Delft University of Technology under supervision of prof. dr. ir. L. M. K. Vandersypen. "*Electrical manipulation and detection of single electron spins in quantum dots*".

List of publications

1. *Locking electron spins into resonance by electron-nuclear feedback*
   I. T. Vink, K. C. Nowack, F. H. L. Koppens, J. Danon, Yu. V. Nazarov
   and L. M. K. Vandersypen,
   Nature Physics **5**, 764 (2009)

2. *Multiple nuclear polarization states in a double quantum dot*
   J. Danon, I. T. Vink, F. H. L. Koppens, K. C. Nowack, L. M. K. Vandersypen and
   Yu. V. Nazarov,
   Physical Review Letters **103**, 046601 (2009)

3. *Spin Echo of a Single Electron Spin in a Quantum Dot*
   F. H. L. Koppens, K. C. Nowack and L. M. K. Vandersypen,
   Physical Review Letters **100**, 236802 (2008)

4. *Coherent Control of a Single Electron Spin with Electric Fields*
   K. C. Nowack, F. H. L. Koppens, Yu. V. Nazarov and L. M. K. Vandersypen,
   Science **318**, 1430 (2007)

5. *Universal Phase Shift and Nonexponential Decay of Driven*
   Single-Spin Oscillations
   F. H. L. Koppens, D. Klauser, W. A. Coish, K. C. Nowack, L. P. Kouwenhoven, D.
   Loss and L. M. K. Vandersypen,
   Physical Review Letters **99**, 106803 (2007)

6. *Detection of single electron spin resonance in a double quantum dot*
   F. H. L. Koppens, C. Buizert, I. T. Vink, K. C. Nowack, T. Meunier,
   L. P. Kouwenhoven and L. M. K. Vandersypen,
   Journal of Applied Physics **101**, 081706 (2007)

7. *Driven coherent oscillations of a single electron spin in a quantum dot*
   F. H. L. Koppens, C. Buizert, K. J. Tielrooij, I. T. Vink, K. C. Nowack,
   T. Meunier, L. P. Kouwenhoven and L. M. K. Vandersypen,
   Nature **442**, 766 (2006)

8. *Single Electron Tunneling in Small Molecules*
   M. R. Wegewijs, M. H. Hettler, C. Romeike, A. Thielmann, K. Nowack
   and J. Koenig,
   Introducing Molecular Electronics, Lecture Notes in Physics **680**
   (Springer, Berlin, 2005)

9. *Nuclear wavefunction interference in single-molecule electron transport*
   M. R. Wegewijs and K. C. Nowack,
   New Journal of Physics **7**, 239 (2005)

10. *Vibration-assisted tunneling through competing molecular states*
    K. C. Nowack and M. R. Wegewijs,
    preprint: cond-mat/0506552